

**Spin- and angle-resolved
photoemission spectroscopy on
unconventional superconductor
strontium ruthenate**

by

Christian Neil Veenstra

B.Sc., M^cMaster University, 2005
M.Sc., The University of British Columbia, 2007

A THESIS SUBMITTED IN PARTIAL FULFILLMENT OF
THE REQUIREMENTS FOR THE DEGREE OF

DOCTOR OF PHILOSOPHY

in

The Faculty of Graduate Studies

(Physics)

THE UNIVERSITY OF BRITISH COLUMBIA

(Vancouver)

January 2013

© Christian Neil Veenstra 2013

Abstract

This thesis represents two bodies of work: a detailed look at what angle-resolved photoemission spectroscopy (ARPES) measures, as well as ARPES and circularly polarized photon spin- and angle-resolved photoemission spectroscopy (CPS-ARPES) measurements on the unconventional superconductor Sr_2RuO_4 .

In the first part I present a study of both established methods of ARPES analysis and some new variations on model spectral functions. This modelling was done in a realistic regime, yet far from the limits often assumed. Away from these limits I show that any “effective coupling” inferred from quasiparticle renormalizations differs drastically and unpredictably from the true coupling. Conversely, I show that perturbation theory retains good predictive power where expected, that the momentum dependence of the self-energy can be revealed via the relationship between velocity renormalization and quasiparticle strength, and that it is often possible to infer the self-energy and bare electronic structure through lineshape analysis.

In the second part I present experimental ARPES and CPS-ARPES data on Sr_2RuO_4 . Newly discovered and unexplained ARPES features are characterized and compared with a variety of different possible structural distortions through bulk and slab local-density approximation (LDA) band structure calculations. I thereby rule out phases driven by electronic interaction, such as Dirac- or Rashba-type surface states, and instead find that there exists a progressive structural modulation whereby both the surface and (at a minimum) sub-surface layers exhibit a $(\sqrt{2} \times \sqrt{2})\text{R}45^\circ$ reconstruction.

Through CPS-ARPES on Sr_2RuO_4 I also directly demonstrate that the effects of spin-orbit (SO) coupling are not limited to a modification of the

Abstract

band structure, but fundamentally entangle the spin and spatial parts of the wave-function. This must drive the superconducting state in Sr_2RuO_4 to be even more unconventional than is generally assumed, with mixing between singlet and triplet states that varies around the Fermi surface, and thereby offers a possible resolution to a number of experiments that clash with the categorization of Sr_2RuO_4 as a hallmark spin-triplet chiral p -wave superconductor.

Preface

I have published, as first author, almost all of the work presented here. That which is not published was either used to support these publications or is in preparation for publication. That is not to say that I produced this work alone; here I will detail the relative contributions of my co-authors to all chapters and manuscripts.

Chapter 2 – Spectral function analysis

Portions of Chapter 2 and Appendices A and D have been published in Refs. 1 and 2. In these publications, as in these chapters, I was responsible for writing and preparing the manuscript, figures, and derivations, as well as managing collaboration and feedback from the co-authors. I was also responsible for all data analysis, including writing all software to perform this analysis. G. L. Goodvin, a fellow student and co-author, was primarily responsible for creating a code library that applied the momentum average approximation to the two model systems studied here, which he used in his own publications [3, 4]. I wrote a software interface to this library to generate the large quantity of simulated data required for analysis. M. Berciu, as Goodvin’s supervisor and a member of my advisory committee, and A. Damascelli, as my supervisor, provided direction and oversight to guide the project. A. Damascelli provided guidance particularly on experimental aspects and how people have performed similar analysis in the past, while M. Berciu provided guidance on theoretical aspects in addition to insight on the momentum average approximation which she devised [5].

Chapter 3 – Chamber characterization

Chapter 3 is based on analysis and experiments done to characterize the in-house angle-resolved photoemission spectroscopy (ARPES) system at UBC, as well as specifically to characterize the data found in Chapter 4. Although many people have assisted in the characterization of the system, all work presented in this chapter is my own, with three exceptions: the electron gun data presented in § 3.1.2 was taken by G. Levy; the gold Fermi edge data presented in Fig. 3.8 panel (a) was taken by B. Ludbrook, as it corresponds with data on Sr_2RuO_4 used in Chapter 4, as described below; and the gas cell photoemission data presented in Fig. 3.9 was taken by SPECS, the manufacturer of our analyzer. I performed all the analysis presented on these data sets and wrote most of software to do so (see last section of this preface: **Software for ARPES data preparation**).

Chapter 4 – ARPES on Sr_2RuO_4

Chapter 4 and Appendix B are based on work and experiments conducted with the ARPES group at UBC using our in-house spectroscopy system, a system I have played a large role in helping to build and characterize over the past seven years. Portions of Chapter 4 and Appendix B have been submitted for publication [6]. The long co-author list represents two distinct groups: C. N. Veenstra, Z.-H. Zhu, B. Ludbrook, G. Levy, A. Nicolaou, J. A. Rosen, and R. Comin (in addition to others) have assisted with the construction and/or ongoing maintenance and characterization of the system used under the direction of A. Damascelli, while S. Kittaka and Y. Maeno grew the samples. Z.-H. Zhu, under the direction of I. S. Elfimov, was responsible for running the local-density approximation (LDA) calculations. In this publication, as in this chapter, I was responsible writing and preparing the manuscript and figures, as well as managing collaborations with the co-authors. Additionally, I performed all the data analysis and wrote much of the software required to do so (see last section of this preface: **Software for ARPES data preparation**). Most, but not all, of the data presented in this chapter was also physically taken by me using samples I

had prepared – the exception being the data presented in Fig. 4.3 panels (d,e) and Fig. 4.4 panels (b,c,d), which are based on the same data set that was taken by B. Ludbrook using a sample I had polished and prepared to be free of ruthenium metal inclusions. B. Ludbrook and Z.-H. Zhu also took additional data on Sr_2RuO_4 , including some as a function of potassium doping. This additional data, while helpful to piece together an overall picture of what was going on, was not presented in [6], nor is it discussed in this thesis. M. Capsoni, as a summer student working with our group under my direction, also assisted me in taking some of the data presented here and additional data not presented.

Chapter 5 – CPS-ARPES on Sr_2RuO_4

Chapter 5 and Appendix C are based on work performed at the Swiss Light Source Complete Photoemission Experiment (COPHEE) endstation. Portions of Chapter 5 appear in a manuscript under preparation for submission. C. N. Veenstra, Z.-H. Zhu, B. Ludbrook, and A. Nicolaou were the group that travelled together from UBC to COPHEE to perform the measurements during one week of beamtime. Owing to the long acquisition times necessary (data used to make Fig. 5.6, for example, took 16 hours) and close group environment of a short beamtime, it is only fair to say that everybody was responsible for all data taken. Although I led this group during the beamtime, everybody also took part in discussions regarding best courses of action, and in this regard Z.-H. Zhu was particularly helpful. M. Raichle, a postdoctoral fellow working with our group, had been in charge of the project idea before I took over and even led some measurements on Sr_2RuO_4 at COPHEE with a similar goal. Although the project did not succeed at that time, reviewing Raichle's data and the avenues previously explored was very helpful in forming a new plan. B. Slomski and G. Landolt were graduate students who, under the direction J. H. Dil, were ultimately responsible for the well-being of the COPHEE system and directed us on physically running experiments there, in addition to providing valuable insight into how the system works. S. Kittaka and Y. Maeno were responsible for sample growth. I. S. Elfimov,

M. W. Haverkort, and A. Damascelli all served in a supervisory role on this project and have provided much valuable insight. M. W. Haverkort, in particular, has provided an exceptional amount of guidance on the theoretical side of the work and also wrote the software libraries I used that execute the LMTO/NMTO+SO method on Sr_2RuO_4 , provide the quantum operators on the correct basis, and allow for the illustration of orbital character.

For this manuscript and chapter I have prepared most of the text and all of the figures; § 5.3 was originally drafted by M. W. Haverkort. I performed all of the analysis on the circularly polarized photon spin- and angle-resolved photoemission spectroscopy (CPS-ARPES) data and also wrote the software to do so.

Software for ARPES data preparation

I wrote all of the software to perform the data analysis presented in this thesis; however, (as mentioned above for Chapters 3 and 4) some aspects of the software required for ARPES data preparation were co-authored with other members of the ARPES group at UBC. In order to analyze ARPES data, our group wrote a full object-oriented software suite in the Interactive Data Language (IDL), with many command-driven tools but with a graphical user interface (GUI) for most steps. This effort was undertaken largely by G. Levy, J. A. Rosen, and me. Each of us developed most of our own code regarding data management, workflow, and analysis, with many core routines (or pieces of them) for data preparation shared and often co-authored. In total this suite involved 138 000 lines of code¹, which could be roughly divided as 20k managed by Rosen, 86k managed by Levy², 2k produced by summer students, and 30k that I managed – although there has been a lot of intermingling, particularly between Levy and me. This total naturally also includes many routines not directly used for this thesis, including software for low-energy electron diffraction (LEED) and x-ray photoelectron spectroscopy (XPS) analysis.

¹As counted by CLOC 1.56; this does not include blank lines or comments.

²Levy's code base also includes many libraries for quickly building GUI interfaces, modified to suit our own purposes.

Table of Contents

Abstract	ii
Preface	iv
Table of Contents	viii
List of Tables	xii
List of Figures	xiii
List of Abbreviations and Symbols	xvii
Acknowledgements	xxi
1 Introduction	1
1.1 A quantum many-body problem	1
1.2 ARPES and spectral function analysis	1
1.3 ARPES on Sr_2RuO_4	3
1.4 CPS-ARPES, Spin-orbit coupling, and superconductivity in Sr_2RuO_4	4
2 Spectral function analysis	6
2.1 The models	9
2.1.1 The Hamiltonian	11
2.1.2 An example spectral function	12
2.2 Quasiparticle analysis	13
2.2.1 Quasiparticle dispersion, velocity, mass, strength, and their renormalizations	14

Table of Contents

2.2.2	Renormalization as a function of coupling strength . . .	19
2.2.3	Renormalizations for different phonon energies	21
2.2.4	Renormalizations in different dimensions	24
2.2.5	Perturbation theory predictions near $\lambda = 0$	24
2.2.6	Verifying momentum independence of the self-energy	29
2.3	Self-energy analysis	30
2.3.1	Momentum-independent self-energies	31
2.3.2	Momentum-dependent self-energies	37
2.4	Conclusions	40
3	Chamber characterization	41
3.1	Angular resolution	43
3.1.1	Setup	43
3.1.2	Electron gun tests	43
3.1.3	Sample tests	49
3.1.4	Conclusions	50
3.2	Energy resolution	51
3.3	Event counting	56
3.4	Functional forms and a comparison of different measures . . .	60
4	ARPES on Sr_2RuO_4	62
4.1	Bulk band structure, Fermi surface, and “extra” bands	63
4.1.1	Additional features found	67
4.1.2	Exploring the 3K phase	71
4.1.3	Time-dependent surface degradation and dispersion analysis	76
4.1.4	Polarization dependence	84
4.1.5	A comparison with folded features in the cuprates . . .	87
4.2	LDA calculations and structural distortions	87
4.2.1	Preliminary bulk calculations	89
4.2.2	Slab choice	93
4.2.3	Slab results	95
4.3	Conclusions	97

Table of Contents

5	CPS-ARPES on Sr_2RuO_4	98
5.1	Single-particle predictions – entanglement at the Fermi energy	99
5.2	Measuring spin–orbital entanglement	103
5.2.1	States measured	103
5.2.2	ARPES results	105
5.2.3	CPS-ARPES results	105
5.3	Implications for pairing	112
5.4	Conclusion	117
6	Conclusion	118
	Bibliography	123

Appendices

A	Spectral function analysis	137
A.1	Calculating renormalizations from perturbation theory	137
A.2	Kramers–Kronig bare-band fitting	138
B	ARPES data preparation	143
B.1	Angle (slit) correction	146
B.2	Energy (gold) correction	146
B.3	Angle to k -space mapping	147
C	CPS-ARPES data preparation	150
C.1	How polarization is measured	150
C.2	Polarization from a toy model – what’s in a wiggle?	155
D	Software routines	164
D.1	Monte Carlo integration using the GNU VEGAS algorithm	164
D.1.1	shared.h	165
D.1.2	Holstein.cpp	165
D.1.3	Breathing.cpp	166

Table of Contents

D.1.4	Integrator.cpp	167
D.1.5	makefile	182
D.1.6	do_them_all	184

List of Tables

4.1	A comparison between Fermi surface volumes, velocities, and their renormalizations as measured by ARPES, LDA+spin-orbit (SO), and dHvA for Sr_2RuO_4	80
-----	--	----

List of Figures

2.1	Spectral function and self-energies of the Holstein polaron, for different microscopic couplings	9
2.2	Example spectral function and quasiparticle dispersion, velocity, mass, and renormalization for the Holstein model in 1D	17
2.3	Example spectral function and quasiparticle dispersion, velocity, mass, and renormalization for coupling to a single breathing mode in 1D	18
2.4	Effective coupling as a function of true coupling for both the Holstein model and coupling to a single breathing mode in 1D	20
2.5	Effective coupling as a function of true coupling, over a range of phonon energies	22
2.6	Effective coupling as a function of true coupling, over a range of dimensionalities	23
2.7	$\partial\lambda_{\text{eff}}/\partial\lambda _{k=0,\lambda=0}$ as a function of phonon energy, for the Holstein model	26
2.8	$\partial\lambda_{\text{eff}}/\partial\lambda _{k=0,\lambda=0}$ as a function of phonon energy, for coupling to a breathing mode	27
2.9	Diagrammatic description of MDC self-energy analysis	33
2.10	MDC self-energy analysis performed on the Holstein model at low coupling	34
2.11	Deviation between known self-energy and that extracted by MDC self-energy analysis as a function of coupling strength .	35
2.12	MDC self-energy analysis performed on the coupling to a breathing mode model at low and high coupling	38

List of Figures

3.1	Illustration of slit array and slit array data	42
3.2	Angular resolution tests in WAM, using an electron gun . . .	44
3.3	Angular resolution tests in LAD, using an electron gun	45
3.4	Angular resolution tests in WAM, on Sr_2RuO_4	47
3.5	Angular resolution tests in LAD, on Sr_2RuO_4	48
3.6	Illustration of energy discrimination through the hemispher- ical analyzer	52
3.7	Energy resolution test in LAD, on gold	53
3.8	Energy resolution test in WAM, on gold	54
3.9	Gas cell photoemission showing the form of single electron events	57
3.10	Before and after images for a single event filter	58
3.11	A comparison of Gaussian and Lorentzian functions	61
4.1	Bulk band structure of Sr_2RuO_4	64
4.2	Laue diffraction on Sr_2RuO_4	65
4.3	Expected vs. measured Fermi surface of Sr_2RuO_4	68
4.4	MDC cuts on the Fermi surface of Sr_2RuO_4	69
4.5	Orientation of the single crystal for measurements with and without the 3K phase	72
4.6	Polarized light microscopy image of the 3K phase	74
4.7	ARPES FS both with and without 3K phase	75
4.8	Time evolution of near- E_F features in Sr_2RuO_4	78
4.9	Band maps for time evolution of near- E_F features in Sr_2RuO_4	79
4.10	Polarization dependence of the ARPES FS of Sr_2RuO_4	82
4.11	Polarization dependence of selected FS features of Sr_2RuO_4 .	83
4.12	Bulk band structure of Sr_2RuO_4 , with incremental octahedra rotations	90
4.13	Bulk band structure of Sr_2RuO_4 , with buckling in oxygen octahedra	91
4.14	Bulk band structure of Sr_2RuO_4 , with electronic interaction U	92
4.15	Crystal structure of Sr_2RuO_4 , as used for LDA+SO slab cal- culations	94

List of Figures

4.16	Results of LDA+SO slab calculations	96
5.1	Band structure of Sr_2RuO_4 and expectation values of $\langle \vec{l} \cdot \vec{s} \rangle$.	100
5.2	Orbital character as well as expectation value of $\langle \vec{l} \cdot \vec{s} \rangle$ and its components around the Fermi surface sheets of Sr_2RuO_4 .	101
5.3	Illustration of the states measured by CPS-ARPES	104
5.4	Spin-integrated ARPES on Sr_2RuO_4 at the Γ point, per- formed at UBC	106
5.5	CPS-ARPES on Sr_2RuO_4 at the Γ point, performed at COPHEE, with 24 eV photon energy	108
5.6	CPS-ARPES on Sr_2RuO_4 at the Γ point, performed at COPHEE, with 56 eV photon energy	109
5.7	CPS-ARPES on Sr_2RuO_4 at the Γ point, performed at COPHEE, with 56 eV photon energy over an extended energy range . . .	110
5.8	Orbitals illustrated in real space around the Fermi surface sheets in Sr_2RuO_4	113
5.9	Orbitals illustrated in greater detail, for selected k -points in Sr_2RuO_4	114
5.10	$\langle \vec{s}_{\mathbf{k}} \cdot \vec{s}_{-\mathbf{k}} \rangle$ around the Fermi surface sheets in Sr_2RuO_4	116
A.1	Tail extrapolation for use in KK transformations	140
B.1	An illustration of ARPES data preparation workflow	144
B.2	A screen shot of IDL while defining peak positions in prepa- ration for correcting angular distortions	145
B.3	A screen shot of IDL during the angle-to-momentum space transformation	148
C.1	Mott detector setup at COPHEE	151
C.2	Raw detector data from CPS-ARPES measurements	153
C.3	Spin-polarized photoemission from a model SO-split system .	156
C.4	Peak splitting simulation example, varying splitting	157
C.5	Peak splitting simulation example, varying peak width	158
C.6	Peak splitting simulation example, varying background	159

List of Figures

C.7	Peak splitting simulation example, varying splitting with background	160
C.8	Peak splitting simulation example, varying width with background	161

List of Abbreviations and Symbols

Acronyms

ARPES	angle-resolved photoemission spectroscopy
a.u.	arbitrary units
BCT	body-centred tetragonal
BZ	Brillouin zone
COPHEE	Complete Photoemission Experiment
CPS-ARPES	circularly polarized photon spin- and angle-resolved photoemission spectroscopy
dHvA	de Haas–van Alphen
EDC	energy distribution curve
FS	Fermi surface
FWHM	full width at half maximum
GUI	graphical user interface
HWHM	half width at half maximum
IDL	Interactive Data Language
KK	Kramers–Kronig

Frequently used symbols

KKBF	Kramers–Kronig bare-band fitting
LAD	low-angular-dispersion mode
LDA	local-density approximation
LEED	low-energy electron diffraction
LMTO	linear muffin-tin orbital
LSDA	local-spin-density approximation
MA	momentum average approximation; $MA^{(n)}$ refers to the n terms kept exactly [4, 5], while $MA^{(v,n)}$ includes variational considerations [3].
MDC	momentum distribution curve
NMTO	order-N muffin-tin orbital
SARPES	spin- and angle-resolved photoemission spectroscopy
SO	spin-orbit
SPECS	SPECS Surface Nano Analysis GmbH
TB	tight-binding
UBC	University of British Columbia
WAM	wide-angle mode
XPS	x-ray photoelectron spectroscopy

Frequently used symbols

\oplus (\ominus) is used to designate circular plus (minus) polarization of light.

$'$ primes are used to denote real/imaginary parts in Chapter 2, folded features in Chapter 4, and the detector space coordinate system in Appendix C.

Frequently used symbols

α a FS-crossing band in Sr_2RuO_4 ; see Fig. 4.1.

β a FS-crossing band in Sr_2RuO_4 ; see Fig. 4.1.

γ a FS-crossing band in Sr_2RuO_4 ; see Fig. 4.1.

Γ the origin in the momentum space BZ; see Fig. 4.1.

δ a band that can sometimes be predicted to cross the FS in Sr_2RuO_4 for certain lattice distortions but that is not observed to do so; see Fig. 4.1.

$\varepsilon_{\mathbf{k}}^b$ the “bare-band” single-particle electronic dispersion, as would be found with no interactions, as a function of momentum \mathbf{k} ; see Eq. 2.1 in general or Fig. 2.2 and Eq. 2.3 for the models used in Chapter 2.

$\varepsilon_{\mathbf{k}}^q$ the quasiparticle dispersion, identified as the EDC peak location in the spectral function as a function of momentum \mathbf{k} ; see Fig. 2.2.

$\varepsilon_{\mathbf{k}}^{pert}$ the quasiparticle dispersion, as predicted by perturbation theory; see Fig. 2.2 and Eqs. 2.8 and 2.9.

$\Sigma(\mathbf{k}, \omega)$ the self-energy, or its real (Σ') or imaginary (Σ'') part; see Eqs. 2.1 and 2.10.

λ the dimensionless coupling, $\lambda = \langle |g|^2 \rangle / 2Dt\Omega$; see Eq. 2.6.

λ_{eff} the “effective coupling”, as would be interpreted in the Migdal limit based on quasiparticle renormalization.

ω energy.

Ω phonon energy.

a lattice constant; for Chapter 2 see Eq. 2.7, and for Sr_2RuO_4 see Fig. 4.15.

$A(\mathbf{k}, \omega)$ the spectral function; see Eqs. 2.1.

b a subscript to indicate a bulk-like band; see Fig. 4.3.

D dimension.

E_F the Fermi energy.

E_k kinetic energy; also an analyzer setting for the kinetic energy (as photoemitted) an electron requires to be mapped to the centre of the detector.

E_{pass} pass energy – an analyzer setting for the kinetic energy (inside the analyzer) an electron requires to pass through the centre of the hemispheres. This also controls the energy resolution of the analyzer.

g the coupling term between phonons and electrons in the Hamiltonian; see Eqs. 2.2, 2.4, and 2.5.

\mathbf{k} momentum.

$k_m(\omega)$ momentum location of MDC peak maxima as a function of energy ω ; related to, but not the same as, ε_k .

m_k dispersion mass, defined as $1/m_k = \partial^2 \varepsilon_k / \partial k^2$; see Fig. 2.2.

\mathbf{M} a location in the momentum space BZ; see Fig. 4.1.

s a subscript to indicate a surface-like band; see Fig. 4.3.

t tight-binding hopping; see Eq. 2.7.

T_c critical temperature of a phase transition, usually between superconducting and normal.

v_k dispersion velocity, defined as $v_k = \partial \varepsilon_k / \partial k$; see Fig. 2.2.

\mathbf{X} a location in the momentum space BZ; see Fig. 4.1.

\mathbf{Z} a location in the momentum space BZ; see Fig. 4.1.

$Z_{\mathbf{k}}^q$ quasiparticle strength, where $Z_{\mathbf{k}}^q = \int^q A(\mathbf{k}, \omega) d\omega$ is the integral over the coherent, quasiparticle part of the spectral function only.

Acknowledgements

Many, many people have helped me along my journey to complete this work, but some deserve special mention.

Thank you to my fellow lab mates: Giorgio Levy, Jeff Mottershead, Thomas Roth, David Fournier, Ryan Wicks, Jason Zhu, Bart Ludbrook, Nik Ingle and Riccardo Comin. As well, thanks to Doug Wong and Pinder Dosanjh for technical assistance. After all those years we did it. We built a world-class ARPES system, and it works. Jason, you deserve a second thank-you for your additional support as we wrote our respective theses and publications together up in AMPEL 346.

Thank you as well to those theorists who've taken the time to help me, an experimentalist, understand - Maurits Haverkort, Mona Berciu, Ilya Elfimov, and Glen Goodvin.

Thank you to all the personelle who keep the COPHEE beamline at the Swiss Light Source going, and to Hugo Dil, Bartosz Slomski, and Gabriel Landolt for showing us how to use it. Thanks especially to Hugo, who met with me to discuss the experiment both before and after the beamtime, thereby ensuring its success.

Thank you to Yoshi Maeno and Shunichiro Kittaka; although we've never met, without your samples I would have nothing to measure.

Thank you to Iva Cheung for editing this thesis, and showing me the difference between "which" and "that".

Finally I would like to thank my supervisor, Andrea Damascelli. Thank you for not only coming up with ideas, but also the funding and guidance to see them through.

Chapter 1

Introduction

1.1 A quantum many-body problem

Although the foundations of modern quantum mechanics were laid at the beginning of the 20th century, the “complications” that arise from the nature of the many-body problem in many materials have survived decades of active research and remain a playground for condensed matter physicists. In materials where one can no longer consider each electron to feel only the average effect from a “sea” of its neighbours the complex network of microscopic particle interactions can foster a diverse variety of observable phenomena. From the first discovery of Bardeen–Cooper–Schrieffer superconductivity over a century ago to Mott–Hubbard insulation, colossal magnetoresistance, and unconventional superconductivity, these materials continue to provide fascinating manifestations of quantum mechanics and the many-body problem for theorists and experimentalists alike.

1.2 ARPES and spectral function analysis

By measuring both the angle and energy of photoemitted electrons, angle-resolved photoemission spectroscopy (ARPES) gives access to information about the energy and momentum of the electrons in a material. This makes it a powerful tool in the study of materials where microscopic interactions cannot be ignored [7]. In **Chapter 2** we present a detailed study on the analysis of ARPES data, in particular focusing on quasiparticle renormalizations and self-energy analysis.

In the quasiparticle picture, a simplified model of the complex many-body problem inherent in such materials is constructed through the intro-

duction of quasiparticles, which themselves behave in a more understandable manner. In this picture the quasiparticle – a collection of fundamental particles, excitations, and the interactions between them – will have its own energy–momentum dispersion relation as well as a self-energy. The quasiparticle renormalizations are the ratios between various properties of the quasiparticle dispersion and those of the “bare”-particle (as they would be were the particle not “dressed” by its association with all the interactions included in the collection). The self-energy, a complex quantity, represents the difference in energy between the quasiparticle and bare-particle through the real part, and the inverse lifetime of the quasiparticle through the imaginary part. In materials well-suited to this picture the quasiparticle is not only an abstract theoretical concept, but something whose properties – the quasiparticle dispersion and lineshape – can actually be observed through ARPES and related to the renormalization and self-energy. These are the relationships studied in Chapter 2, where we present a study of quasiparticle renormalization and self-energy analysis. Both established methods of ARPES analysis as well as some new variations are applied to simulated single-electron removal spectral functions, which are generated using two different models of electron-phonon coupling in a filled band system.

The quasiparticle renormalizations found in these simulations are initially surprising when compared to the microscopic coupling found in the Hamiltonian. While these simulations were done in a realistic regime, the filled-band nature of the model is far from the limits often assumed, i.e., where the phonon energy is very small compared with the Fermi energy in a parabolic band and Migdal’s theorem [8], which predicts quasiparticle renormalizations that scale linearly with the microscopic coupling, is valid. Away from these limits we find that the “effective coupling”, as would be inferred from quasiparticle renormalizations directly, will differ drastically and unpredictably from the true coupling. This work helps explain the exceedingly large quasiparticle renormalizations observed in some systems [9–12], which seem implausible when understood using the de-facto standard ARPES interpretation where Migdal’s theorem is assumed to hold. In contrast with Migdal’s theorem, we show that the perturbation theory

predictions for quasiparticle renormalization remain good where expected. Additionally, we find that the momentum dependence of the self-energy can be revealed via the relationship between velocity renormalization and quasiparticle strength.

Through lineshape self-energy analysis on these simulations, we show that (although not strictly valid) it is often possible to infer the self-energy and bare electronic structure through an iterative fitting process – even if the self-energy is momentum dependent, a condition that is generally neglected. We also show that through lineshape alone, when that lineshape is Lorentzian, it is possible to reliably extract the shape of the imaginary part of a momentum-dependent self-energy without reference to the bare-band. Finally, through simulations with a momentum-dependent self-energy, I explore exactly *which* self-energy is extracted by these methods, and find that the self-energy extracted is that which follows a path through energy–momentum space along the observed spectral maximum.

1.3 ARPES on Sr_2RuO_4

In addition to this theoretical background work on typical ARPES analysis, I have helped to construct a new state-of-the-art ARPES system here at UBC. Results pertaining to the characterization of this system are presented in **Chapter 3**. A logical extension of the spectral function analysis work presented in Chapter 2 could have been to apply these methods, particularly the detailed self-energy analysis schemes, to a real material using this ARPES system. This was attempted with the unconventional superconductor Sr_2RuO_4 [13], believed to also be a model Fermi-liquid [14, 15] – a trait that should simplify such analysis. However, this did not turn out to be feasible even with the high resolution of the new ARPES system at UBC. This failure was due to some previously undetected spectral features – an apparent splitting of certain bands – found to exist in Sr_2RuO_4 , which confounded detailed lineshape analysis ³.

³In the meantime (although not discussed in this thesis) another member of our group, B. Ludbrook, has begun measurements on MgB_2 , on which it seems likely that such anal-

These features themselves proved to be quite interesting, and their characterization and the ultimate resolution of their origin forms the entirety of **Chapter 4**. These features were not unnoticed by the rest of the ARPES community, with another group publishing results offering no definitive explanation but suspecting a surface state driven by electronic interactions [16] even as our own publication [6] was under review. However, through a detailed study of the characteristics of these features along with their degradation over time, their polarization dependence, a topological comparison to folding in the Bi-cuprates, and a comparison to local-density approximation (LDA) slab calculations we rule out phases driven by electronic interaction. Instead we find that a structural crystal-lattice distortion already known to be present in the surface must extend to (at a minimum) the sub-surface layer, with an associated progression of electronic states. The different electronic structure from these two layers is thus responsible for the apparent splitting observed. This experience with Sr_2RuO_4 led to a further opportunity to explore more interesting aspects of its electronic structure – directly verifying the effects of spin-orbit coupling, which has the potential to profoundly change the unsolved description of superconductivity in this material.

1.4 CPS-ARPES, Spin-orbit coupling, and superconductivity in Sr_2RuO_4

Spin-orbit (SO) coupling is the well-characterized interaction between an electron's spin and orbital motion owing to relativity and the electric field of the nuclei. Because of this it is well-known to be of importance in the energy of core levels and materials incorporating the $3d$ transition metals. However, in Sr_2RuO_4 (with electronic structure based on the $4d$ transition metal ruthenium), it is only due to degeneracies and the overall proximity in energy of the three Fermi-surface crossing bands (always of a similar energy to the coupling) that it becomes important near the Fermi energy.

ysis will succeed.

By breaking these degeneracies SO coupling modifies the band structure, an effect that has already been observed [17]. A much more important effect, however, is due to the physics that causes these degeneracies to be broken in the first place.

By entangling the spin and spatial descriptions, SO coupling invalidates the standard method of writing the electronic wave-function as a product of independent spin and spatial descriptions. Instead the two are fundamentally intertwined. It is this entanglement that we, for the first time, directly measure in **Chapter 5**. We accomplish this by using circularly polarized light on carefully selected initial states that, owing to selection rules and the predictions of their SO entanglement, will generate spin-polarized photoemission. These experiments were performed at the Complete Photoemission Experiment (COPHEE) beamline at the Swiss Light Source, which can perform spin- and angle-resolved photoemission spectroscopy (SARPES) with circularly polarized light (CPS-ARPES).

We also, by calculating the wave-functions on the minimal basis of ruthenium d and oxygen p orbitals and adding SO coupling as a local term in the Hamilton, explicitly calculate some of the effects of SO coupling for both single electrons and possible pairings. We show this entanglement must necessarily drive the superconducting state in Sr₂RuO₄ to be even more unconventional than is generally assumed, by allowing mixing between singlet, triplet, and other spin states. This mixing varies around the Fermi surface, and offers a possible resolution to a small number of experiments that clash with the broader categorization of Sr₂RuO₄ as a hallmark spin-triplet chiral p -wave superconductor.

Chapter 2

Spectral function analysis

The many-body problem allows relatively simple interactions to transform into a wide range of exciting yet often complicated phenomena. The quasiparticle picture simplifies these complications by grouping fundamental particles and excitations together into quasiparticles, which themselves behave in a more understandable manner. In this picture the real part of the self-energy represents the energy difference from the bare-particle energy, and the imaginary part the inverse lifetime of the combined excitation. Angle-resolved photoemission spectroscopy (ARPES) is a well-established tool for the investigation of such electronic systems, as it provides access to the electron-removal part of the momentum-resolved spectral function $A(\mathbf{k}, \omega)$ [7], which is generally written in the following form:

$$A(\mathbf{k}, \omega) = -\frac{1}{\pi} \frac{\Sigma''(\mathbf{k}, \omega)}{[\omega - \varepsilon_{\mathbf{k}}^b - \Sigma'(\mathbf{k}, \omega)]^2 + [\Sigma''(\mathbf{k}, \omega)]^2}. \quad (2.1)$$

The analysis of this extremely rich data source can be both difficult and rewarding, as it depends on both the interaction self-energy $\Sigma(\mathbf{k}, \omega) = \Sigma'(\mathbf{k}, \omega) + i\Sigma''(\mathbf{k}, \omega)$, as well as the single-particle electronic dispersion $\varepsilon_{\mathbf{k}}^b$ (the so-called bare-band). A variety of approaches to analyzing this spectral function have been utilized and often focus on analysis of either quasiparticle dispersions and their path through (\mathbf{k}, ω) space, or lineshape and its implications for the structure of the self-energy. Both methods generally cut the spectral function into curves constant in either momentum [generating a series of energy distribution curves (EDCs)] or energy [for a series of momentum distribution curves (MDCs)]. In this chapter, using simulations that have no experimental limitations, we will perform quasiparticle analysis on EDCs (which allows the identification of a quasiparticle peak in

each \mathbf{k} slice, thereby forming a quasiparticle dispersion, $\varepsilon_{\mathbf{k}}^q$) and self-energy analysis on MDCs (as self-energies often show weak momentum and strong energy dependence, allowing more straightforward approximation for slices of constant energy).

In quasiparticle analysis one can estimate properties such as the dispersion's velocity $v_{\mathbf{k}}^q = \partial\varepsilon_{\mathbf{k}}^q/\partial\mathbf{k}$; effective mass $m_{\mathbf{k}}^q$, where $1/m_{\mathbf{k}}^q = \partial^2\varepsilon_{\mathbf{k}}^q/\partial\mathbf{k}^2$; and quasiparticle strength $Z_{\mathbf{k}}^q$, where $Z_{\mathbf{k}}^q = \int^q A(\mathbf{k}, \omega)d\omega$ is the integral over the coherent part of the spectral function (this is the quasiparticle weight only, which in somewhat loose terminology is often referred to as *quasiparticle coherence* [7]). If the bare-band dispersion $\varepsilon_{\mathbf{k}}^b$ is known, the renormalization of these properties can also be calculated. This concept has been used to generate an “effective coupling” (which we will denote λ_{eff} but which is often denoted simply as λ in ARPES literature) in the analysis of many complex systems, often through the so-called mass enhancement factor $m_{\mathbf{k}}^b/m_{\mathbf{k}}^q = v_{\mathbf{k}}^q/v_{\mathbf{k}}^b = Z_{\mathbf{k}}^q = 1/(1+\lambda_{\text{eff}})^4$. This factor has become a de facto standard in ARPES analysis [7, 15, 18–20], since, in the Migdal/Eliashberg limit after few approximations, it is equivalent to the true dimensionless microscopic coupling found in the Hamiltonian (denoted by λ here and in theoretical literature) and is expected to manifest itself in a variety of different measurements [21, 22]. However, the large values sometimes measured for these renormalizations and effective couplings via ARPES (see, for example, Refs. 9–12), should raise the question of this scheme's universal utility [23–28] and the applicability of the limits implied by such analysis to the systems being measured [1, 29–31].

Another common goal of spectral function analysis is to extract the self-energy. In most circumstances, under the assumption of \mathbf{k} -independence of the self-energy, MDCs cuts through Eq. 2.1 reduce to a simple Lorentzian form, thus allowing a measurement of $\Sigma'(\omega)$ and $\Sigma''(\omega)$ through ARPES [19, 23, 32–36]. However, not only do these methods hinge on some assumptions and/or approximations for the bare-band $\varepsilon_{\mathbf{k}}^b$, but more fundamentally the

⁴Here we use the equals sign between different renormalization quantities, as is often assumed in ARPES literature, but, as we will show, these quantities are in general not equivalent.

problem of how momentum dependence in $\Sigma'(\mathbf{k}, \omega)$ and $\Sigma''(\mathbf{k}, \omega)$ affects this analysis is unaddressed – even though it is known that a Lorentzian lineshape does not guarantee a momentum-independent self-energy [37].

In this chapter we present a careful study of established methods and present some new variations using one of the most studied interactions – that of electrons and phonons. This work resulted in two publications [1, 2]. We generate self-energies and spectral functions, where the inclusion of momentum dependence and all energy scales are controlled using the least complicated electron–phonon interaction models possible. We do this in a filled-band system – far from the asymptotic limit often assumed, i.e., where the phonon energy is very small compared with the Fermi energy in a parabolic band and Migdal’s theorem [8] predicting $(1 + \lambda)$ quasiparticle renormalizations is valid. These spectral functions are examined over a wide range of parameter space through techniques often used in ARPES. Analyzing over 1200 simulations we consider variations of the microscopic coupling strength (§ 2.2.2), phonon energy (§ 2.2.3), and dimensionality (§ 2.2.4) for two models: a momentum-independent Holstein model and momentum-dependent coupling to a breathing mode phonon. In this limit we find that any “effective coupling”, λ_{eff} , inferred from the quasiparticle renormalizations differs from the microscopic dimensionless coupling characterizing these Hamiltonians, λ , and could drastically either over- or underestimate it, depending on the particular parameters and model. Conversely, we show that perturbation theory retains good predictive power for low coupling and small momenta (§ 2.2.5) and that the momentum dependence of the self-energy can be revealed via the relationship between velocity renormalization and quasiparticle strength (§ 2.2.6). Additionally in § 2.3 we show that (although not strictly valid) it is often possible to infer the self-energy and bare electronic structure through self-consistent Kramers–Kronig bare-band fitting (KKBF) and also that through lineshape alone, when the lineshape is Lorentzian, it is possible to reliably extract the shape of the imaginary part of a momentum-dependent self-energy without reference to the bare-band.

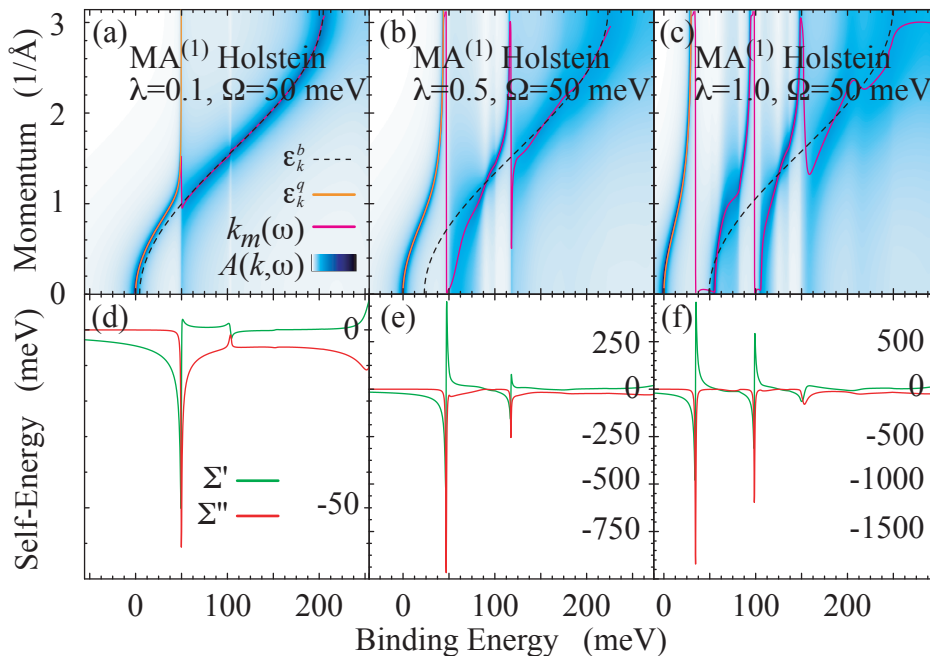


Figure 2.1: The spectral function (a–c) and self-energies (d–f) for the 1D momentum-independent Holstein polaron model calculated with MA⁽¹⁾ for $\Omega = 50$ meV and different microscopic couplings, with the bare-band ε_k^b , quasiparticle band ε_k^q , and $k_m(\omega)$ path shown.

2.1 The models

We use single-electron addition to an empty band to simulate photoemission from a completely filled system, at 0 Kelvin. Note that this case can be exactly mapped onto that of a single particle added to an empty band through particle–hole symmetry, which essentially amounts to the replacement $\omega \rightarrow -\omega$. This is an ideal test case, as it provides the simplest possible description of electron–phonon coupling and is uncomplicated by further interactions such as strong correlations between electrons (as in, for example, Ref. 38), or even a Fermi sea, which would add yet another energy scale to the problem (as in, for example, Refs. 39, 40). The chemical potential in our treatment is then the top of the first electron removal state, labelled as 0 binding energy on all plots. For momentum-independent study we will use

2.1. The models

spectral functions and self-energies generated with the momentum average approximation $\text{MA}^{(1)}$ [4, 5]. Since $\text{MA}^{(1)}$ has been shown to be accurate everywhere in parameter space [4], it will enable us to study $A(\mathbf{k}, \omega)$ and $\Sigma(\omega)$ over a broad range of electron–phonon coupling and phonon energies. For momentum-dependent study we use an extension of this approximation with variational considerations, denoted $\text{MA}^{(v,n)}$ [3]. Although generally accurate everywhere in parameter space, for reasons specific to this approximation, details studied through EDC quasiparticle analysis are best realized through $\text{MA}^{(v,1)}$, and MDC-based self-energy analysis is best realized through $\text{MA}^{(v,0)}$. In all cases the spectral function remains entirely self-consistent with the associated self-energy⁵.

Our test case for a momentum-independent self-energy is the simplest possible in momentum space – namely, the Holstein polaron [42]: momentum-independent coupling between a single dispersionless phonon mode and tight-binding electrons. In reality, however, even for the Holstein model, the self-energy is weakly dependent on momentum, which can be seen at the $\text{MA}^{(2)}$ level of approximation [4]. We overcome this complication by choosing the momentum-independent self-energy from the $\text{MA}^{(1)}$ level in order to see how well these methods work for a truly momentum-independent self-energy. For strongly momentum-dependent self-energy study we will model coupling to a single optical mode, where the phonons live on half-integer lattice sites in between the electron sites and modify the on-site energy of their neighbours. In 2D this describes lattice vibrations in a CuO_2 -like plane, where the motion of the O ions is the most important vibrational degree of freedom; this has been the topic of many ARPES studies [11, 32–34]. Throughout this chapter we will refer to this as the breathing mode model.

⁵With more terms kept exactly, $\text{MA}^{(v,1)}$ should show overall improvement over $\text{MA}^{(v,0)}$; however, for reasons that are not understood, it does so only in the quasiparticle regime – conversely the continuum of $A(k, \omega)$ below the quasiparticle band is worsened; toward the Brillouin zone edge it is pushed further down in energy than exact diagonalization results indicate it should be [3, 41]. We use the lower-order $\text{MA}^{(v,0)}$ for the MDC-based self-energy analysis, as this analysis uses $A(k, \omega)$ in both the continuum and quasiparticle regime.

2.1.1 The Hamiltonian

We may write both these models in the following form in momentum space:

$$\mathcal{H} = \sum_{\mathbf{k}} \varepsilon_{\mathbf{k}}^b c_{\mathbf{k}}^{\dagger} c_{\mathbf{k}} + \Omega \sum_{\mathbf{Q}} b_{\mathbf{Q}}^{\dagger} b_{\mathbf{Q}} + \sum_{\mathbf{k}, \mathbf{Q}} \frac{g_{\mathbf{Q}}}{\sqrt{N}} c_{\mathbf{k}-\mathbf{Q}}^{\dagger} c_{\mathbf{k}} (b_{\mathbf{Q}}^{\dagger} + b_{-\mathbf{Q}}). \quad (2.2)$$

The terms describe, in order, an electron with dispersion

$$\varepsilon_{\mathbf{k}}^b = -2t \sum_{i=1}^D \cos(k_i a) \quad (2.3)$$

in D dimensions, an optical phonon with energy Ω and momentum \mathbf{Q} , and the on-site momentum-dependent electron–phonon coupling $g_{\mathbf{Q}}$ [for N sites with periodic boundary conditions; $c_{\mathbf{k}}^{\dagger}$ ($c_{\mathbf{k}}$) and $b_{\mathbf{k}}^{\dagger}$ ($b_{\mathbf{k}}$) are the usual electron and phonon creation (annihilation) operators]. For the Holstein case

$$g_{\mathbf{Q}} \equiv g \quad (2.4)$$

is a constant, while for coupling to the breathing mode

$$g_{\mathbf{Q}} \equiv -i\sqrt{2}g \sum_{i=1}^D \sin(Q_i a/2), \quad (2.5)$$

which has an average value of $\langle |g_{\mathbf{Q}}|^2 \rangle = g^2$ across the Brillouin zone⁶. This allows us to define the same dimensionless coupling for both models:

$$\lambda = \frac{\langle |g|^2 \rangle}{2Dt\Omega}, \quad (2.6)$$

⁶In most implementations, the coupling is found via a scattering integral around the Fermi surface [21], which for the breathing mode model would be zero at all coupling strengths. We take the Brillouin zone as a sensible alternative in this case (the choice is irrelevant for the momentum-independent Holstein coupling).

2.1. The models

the ratio between lattice deformation energy $-g^2/\Omega$ and free-electron ground-state energy $-2Dt$. For this thesis we set

$$\begin{aligned} a &= \hbar = 1, \\ t &= 50 \text{ meV}, \end{aligned} \tag{2.7}$$

such that the 1D bandwidth is 200 meV and the Brillouin zone is $2\pi\text{\AA}^{-1}$ wide. Also note that an additional constant 1 meV full width at half maximum (FWHM) Lorentzian broadening is used, similar to an impurity scattering, to allow the numerical resolution of the sharpest features in $A(k, \omega)$.

2.1.2 An example spectral function

The spectral function calculated with MA⁽¹⁾ for the Holstein problem in 1D, with $\Omega = 50$ meV and $\lambda = 0.1, 0.5, 1.0$, is presented as a false-colour plot in Fig. 2.1(a,b,c), along with the path of peak maxima measured through MDCs [$k_m(\omega)$] and EDCs (ε_k^q) compared with the bare-band dispersion ε_k^b . In the bottom panels (d,e,f) of Fig. 2.1 we present the real, $\Sigma'(\omega)$, and imaginary, $\Sigma''(\omega)$, parts of the self-energy for this momentum-independent model. Here each ε_k^q is a true (and the lowest) pole of the Green's function (it has zero width, hence an infinite lifetime) and is only resolved numerically owing to the impurity scattering inserted in the energy direction. One can see from Eq. 2.1 that the peak width should go roughly like $\Sigma''(k, \omega)$, and it is reassuring to see in Fig. 2.1(d,e,f) that the imaginary part of the self-energy is indeed zero near ε_k^q . The pole structure ε_k^q is also distinct from that of k_m , the path of peak maxima observed during MDC analysis; not only are they fundamentally different (as one is a function of ω and the other of k), but the path of peak maxima observed when cutting $A(k, \omega)$ in energy vs. momentum will not necessarily overlap, as has already been noted in the literature [15, 43].

For small couplings [Fig. 2.1 panel (a)] most of the spectral weight remains along ε_k^b , with only a small feature formed at energy Ω below the top of the band. With experimental resolution such a feature might appear only as a ‘‘kink’’ in a quasiparticle dispersion; however, from looking at the

2.2. Quasiparticle analysis

self-energy [panel (d)] one can see that a distinction between ε_k^b and $k_m(\omega)$ should be made at this feature. The lowest pole, where $\Sigma''(\omega) \approx 0$ and which we will identify as the quasiparticle, exists only between the top of the band and Ω . This pole forms a narrow dispersion, ε_k^q , of bandwidth approximately Ω , although for k near the zone edge the electron spectral weight is very weak owing to its significant phonon character. The $k_m(\omega)$ path of MDC peak maxima, however, does not follow this quasiparticle dispersion but instead carries on close to the original bare-band ε_k^b into what we will identify as the continuum, owing to its broader structure and finite Σ'' .

As the coupling is increased [Fig. 2.1 panels (b,c)], this distinction becomes increasingly evident; the quasiparticle band gains spectral weight toward the zone boundary and becomes better defined. Also, its bandwidth narrows, becoming less than Ω , as the quasiparticle mass increases and the quasiparticle velocity decreases. At the same time the spectral weight in the continuum becomes more spread out at deep energies, and new quasiparticle-like features begin to appear at the top of the continuum. At very large coupling (not shown) these additional features and the quasiparticle will eventually form a ladder of states with flat dispersions, although this coupling regime is well beyond the scope of this thesis.

2.2 Quasiparticle analysis

As can be seen in Fig. 2.1, quasiparticle renormalizations do increase as the microscopic coupling increases. This monotonicity has led to widespread acceptance of measuring coupling through the quasiparticle mass, velocity, or strength renormalizations observed with ARPES, often without reference as to whether or not the system should be expected to fall in the Migdal/Eliashberg framework. In this section we use our simple models to demonstrate that this scheme is not universal and to make other observations by performing quasiparticle analysis, as is typically done with ARPES data (Figs. 2.2 and 2.3), on ~ 1200 generated spectral functions. These allow us to explore a range of couplings (Fig. 2.4), parameters (Fig. 2.5), and di-

dimensionality (Fig. 2.6) on models that provide both momentum-dependent and momentum-independent self-energies. Following a discussion of these results we will follow the mass renormalization behaviour as $\lambda \rightarrow 0$ for $\mathbf{k} \sim 0$ in detail through perturbation theory in § 2.2.5, the predictions for which are also plotted in Figs. 2.2, 2.3, and 2.4 for later comparison. Finally, in § 2.2.6, we will show that it is possible to determine whether or not the self-energy is momentum dependent from quasiparticle analysis.

2.2.1 Quasiparticle dispersion, velocity, mass, strength, and their renormalizations

In order to perform quasiparticle analysis we generate an entire spectral function for each combination of the following parameters: model, dimensionless coupling $\lambda = \langle |g|^2 \rangle / 2Dt\Omega$, phonon energy scale $\Omega/2t$, dimensionality D , and (for 2 and 3D) the desired cut through momentum space. For all simulations the form of the bare-band is not changed, and the hopping is set to a constant of $t = 50$ meV to give physically familiar values, a bandwidth of 200 meV in the 1D case. (To consider other bandwidths, one should simply scale the bandwidth, phonon energy, and coupling together, as seen in the Hamiltonian, Eq. 2.2). On each of the ~ 1200 generated spectral functions the quasiparticle dispersion is found by fitting a Lorentzian peak with linear background to each EDC within the quasiparticle regime. The inclusion of a linear background allows any spectral weight from the continuum that has bled in to be excluded (a problem especially at low couplings and high dimensions). We illustrate this analysis in Figs. 2.2 and 2.3, where for the Holstein and coupling to breathing mode models (respectively), we present the spectral function $A(k, \omega)$ for a mid-range coupling $\lambda = 0.5$ and phonon energy $\Omega = 50$ meV, as well as dispersions found from the Lorentzian fits ε_k^q , perturbation theory prediction ε_k^{pert} , and the bare electronic structure ε_k^b [panel (a)]. Also shown are the velocities [v_k^q , v_k^{pert} , and v_k^b in panel (b)], inverse masses [$1/m_k^q$, $1/m_k^{pert}$, and $1/m_k^b$ in panel (c)], the corresponding renormalization ratios (v_k^b/v_k^q , m_k^q/m_k^b , and their perturbation theory predictions), the inverse quasiparticle strength $1/Z_k^q$, and bandwidth renormal-

2.2. Quasiparticle analysis

ization Ω/W^q [panel (d); see caption for definitions]. In Fig. 2.2 the results are for the Holstein model with a momentum-independent self-energy, while Fig. 2.3 is for coupling to a breathing mode, which yields a momentum-dependent self-energy.

Figs. 2.2 and 2.3(d) show that the velocity, mass, and spectral weight renormalizations are all functions of momentum, which raises concerns if one wishes to compare them with the bandwidth renormalization Ω/W^q or an “expected” renormalization factor of $(1 + \lambda)$, which are both constant. Although they do cross at certain values of k , this is merely accidental, and none match at the top of the band – our “Fermi surface”. More problematic is that the mass renormalization must necessarily contain a divergence if the inflection point of ε_k^b is different from ε_k^q , where $1/m_k^q$ vanishes (emphasized by the horizontal dashed line). Similarly, in the case of momentum-dependent coupling [panel (e)], it can be seen that the quasiparticle dispersion ε_k^q is not even monotonic, causing another divergence when v_k^q vanishes in the middle of the dispersion. (This non-monotonic dispersion is a direct consequence of the structure of the polaronic cloud, which causes a larger second-nearest-neighbour hopping and is discussed at length in Ref. 41.) Because of this momentum dependence, any estimation of λ drawn from v_k^b/v_k^q , m_k^q/m_k^b , or $1/Z_k^q$ would depend heavily on the momentum chosen; if either of v_k^b/v_k^q or m_k^q/m_k^b were used close to their divergences, the estimated value could be off by an unlimited amount. Even Ω/W^q , although constant in k , does not match the value of $(1 + \lambda)$ for either the momentum-independent or momentum-dependent case. From Figs. 2.2 and 2.3 we draw the conclusion that none of the renormalization quantities gives a good direct estimate of the dimensionless coupling $\lambda = \langle |g^2| \rangle / 2t\Omega$. Further, we find that, with the exception of the quasiparticle strength and velocity renormalization in the Holstein model only (which we will return to in § 2.2.6), the renormalizations do not even match each other – even though the models were kept as similar and simple as possible. This indicates that making even qualitative comparisons of “coupling” from experiments on different materials (or even different experiments on the same material) through these renormalization parameters may not be meaningful. However, modelling of the parameters

2.2. Quasiparticle analysis

in question from the original Hamiltonian via perturbation theory might be a start, as these results show much closer agreement near $k = 0$ despite the relatively high (for perturbation theory) coupling. (We will return to discuss perturbation theory later in § 2.2.5.)

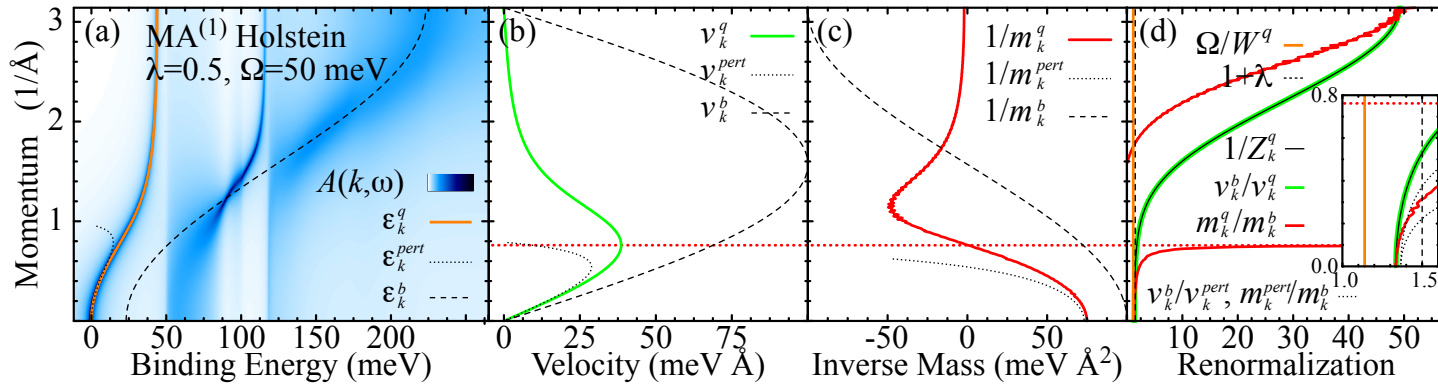


Figure 2.2: (a) $A(k, \omega)$ calculated for the momentum-independent Holstein self-energy in 1D with MA⁽¹⁾ for $\Omega = 50$ meV and $\lambda = 0.5$; the quasiparticle dispersion ε_k^q , perturbation theory (about $k = 0$) prediction ε_k^{pert} , and bare-band ε_k^b are also shown. (b) Quasiparticle (v_k^q), perturbation theory (v_k^{pert}), and bare-band (v_k^b) velocities, as well as (c) corresponding inverse masses, $1/m_k^q$, $1/m_k^{pert}$, and $1/m_k^b$, according to the definitions $v_k = \partial\varepsilon_k/\partial k$ and $1/m_k = \partial^2\varepsilon_k/\partial k^2$. (d) Momentum-dependent quasiparticle renormalization as obtained from v_k^b/v_k^q , m_k^q/m_k^b , as well as the inverse quasiparticle strength $1/Z_k^q$, where $Z_k^q = \int^q A(k, \omega) d\omega$ is the quasiparticle-only integrated spectral weight; in the inset, these quantities are compared near $k=0$ with the renormalization factors Ω/W^q and $(1+\lambda)$, obtained from quasiparticle bandwidth W^q (defined as the energy difference between top and bottom of the quasiparticle band) and dimensionless coupling $\lambda = g^2/2t\Omega$, as well as the perturbation theory prediction for mass and velocity renormalizations (shown with the same line style but which can be distinguished by their proximity to the quasiparticle curves). In subsequent figures (2.4, 2.5, 2.6) the quantity plotted is the effective coupling, λ_{eff} that would be implied by these renormalizations in the Migdal limit; this simply amounts to subtracting 1 from the renormalization. The noise is due to the finite simulation grid and subsequent lineshape fitting; slight variations in peak position are exaggerated by taking the derivative numerically, and therefore they are most visible in m_k^q .

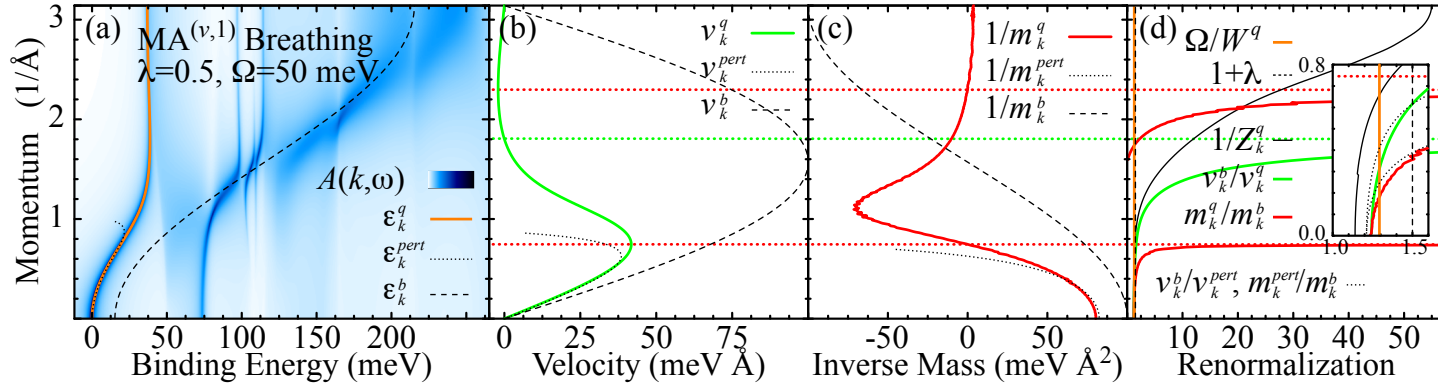


Figure 2.3: (a) $A(k, \omega)$ calculated for a momentum-dependent self-energy from coupling to a single breathing mode in 1D with $\text{MA}^{(v,1)}$ for $\Omega = 50$ meV and $\lambda = 0.5$; the quasiparticle dispersion, its perturbation theory prediction, and the bare-band are also shown. (b) Quasiparticle, perturbation theory, and bare-band velocities, as well as (c) corresponding inverse masses. (d) Momentum-dependent quasiparticle renormalization for these quantities, as well as the inverse quasiparticle strength, quasiparticle bandwidth, dimensionless coupling, and perturbation theory predictions; these are shown in greater detail near $k = 0$ in the inset. All definitions are identical to those in Fig. 2.2, where $\lambda = \langle |g|^2 \rangle / 2t\Omega$ is the average of the coupling across the Brillouin zone.

2.2.2 Renormalization as a function of coupling strength

Despite their differences from each other and their momentum dependence, however, these renormalizations do monotonically increase as the microscopic coupling increases (as previously observed in Fig. 2.1) which naturally leads one to wonder how, precisely, these quantities scale with λ as well as Ω in our different models, so that one might be able to capture the trend if the material and measured quantity were held constant – for example, in an experiment performed as a function of doping, if that doping does not cause structural distortions. In Fig. 2.4 we will follow the “effective coupling”, λ_{eff} (which is simply the observed renormalization minus 1), that each of these renormalization quantities would predict using the Migdal/Eliashberg framework as a function of λ , as well as renormalizations found using the perturbation theory results around $k = 0$ (Eqs. 2.8 and 2.9), for both momentum-independent [panel (a)] and momentum-dependent [panel (b)] self-energies. In Fig. 2.5 we plot a selection of these quantities in the same fashion, for a range of phonon energies. For the momentum-dependent quantities we must choose a k value: we plot v_0^b/v_0^q , m_0^q/m_0^b , and $1/Z_0^q$ at $k = 0$ (our “Fermi surface”), as well as $v_{k_i}^b/v_{k_i}^q$ and $1/Z_{k_i}^q$ at the inflection point $k = k_i$ of the quasiparticle band ε_k^q , where $m_{k_i}^q/m_{k_i}^b$ diverges.

In Fig. 2.4 we find that the predictions from all quantities scale monotonically with the microscopic coupling and are concave up. In the low-coupling regime (below about $\lambda = 0.3$) the perturbation theory results match the simulations – however, nowhere does λ_{eff} match λ from the Hamiltonian. At small coupling values, using this model, many renormalization quantities would drastically underestimate the true microscopic coupling, by a factor ranging from infinite (Ω/W near $\lambda = 0$, where it is not renormalized in the Holstein model) to ~ 6 ($1/Z_{k_i}^q$ near $\lambda = 0.1$, breathing mode). Conversely, at larger coupling values ($\lambda \sim 2$) all quantities would *overestimate* the true microscopic coupling, with factors ranging from ~ 4 (Ω/W , Holstein) to ~ 22 ($v_{k_i}^b/v_{k_i}^q$, breathing mode). We also find that, depending on the coupling or model, the relative renormalization strength of quantities changes – for the momentum-independent model Ω/W is renormalized the least, whereas

2.2. Quasiparticle analysis

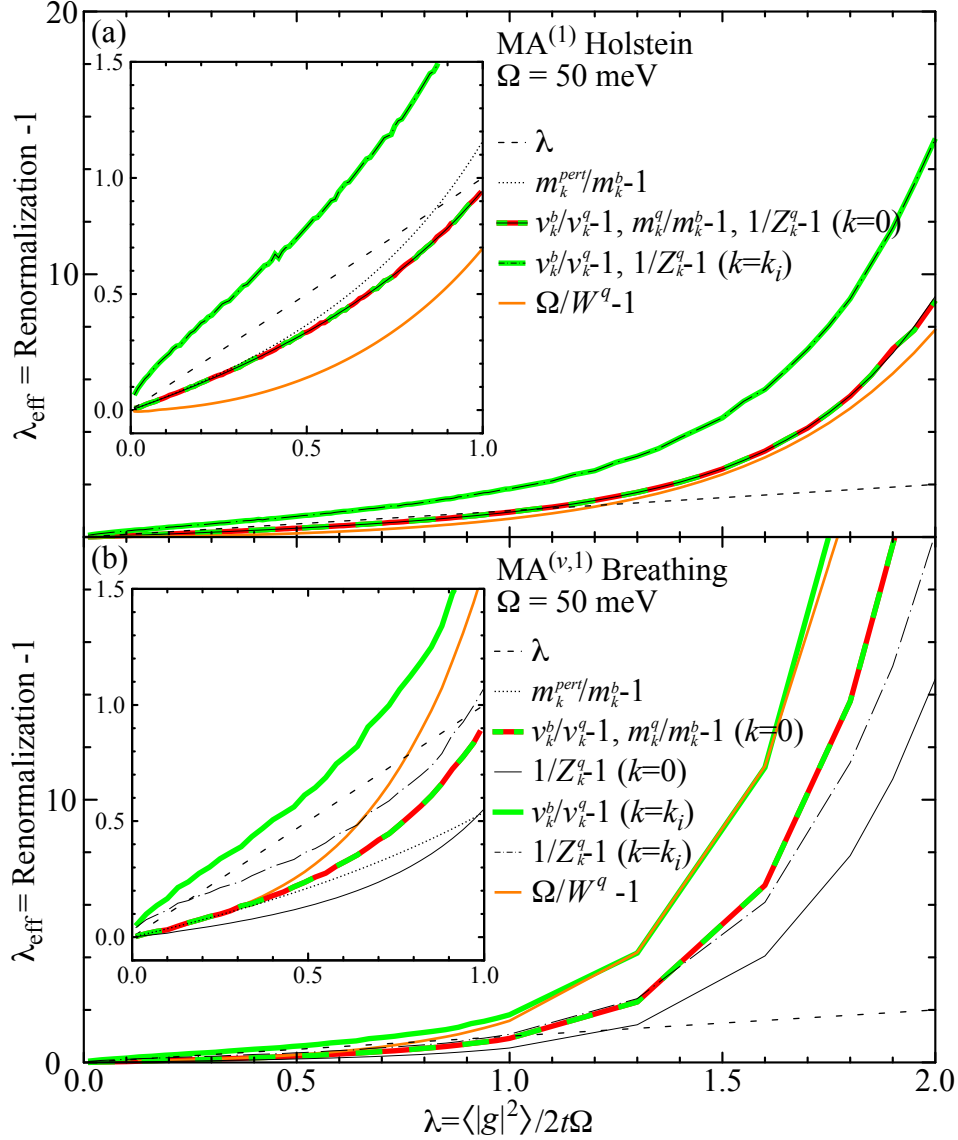


Figure 2.4: Effective coupling, λ_{eff} (as would be interpreted in the Migdal limit from the renormalization parameters as defined in Fig. 2.2), plotted vs. the true dimensionless coupling $\lambda = \langle |g|^2 \rangle / 2t\Omega$; where g is a constant for the Holstein model (a), and $g_Q \equiv -i\sqrt{2}g \sin(Qa/2)$ for the breathing mode model (b). Also shown, in the insets only, are the predictions for observed effective coupling found via the mass renormalizations in perturbation theory (Eqs. 2.8 and 2.9) for the low-coupling regime at $k = 0$. Note that the noise in v and $1/Z$ at $k = k_i$ originates from the numerical determination of the inflection point k_i .

in the momentum-dependent model $1/Z_0^q$ shows the least renormalization. This indicates, yet again, that comparing different materials via renormalizations is not feasible, nor is comparing different renormalizations on the same material without a detailed model. We note again that, in the Holstein model only, quasiparticle strength and velocity renormalization are identical for all couplings at both $k = 0$ and $k = k_i$ (as previously seen in Fig. 2.2, where they are shown to be identical at *all* momenta, contrasted against Fig. 2.3, where they do not match), which will be explored further in § 2.2.6.

2.2.3 Renormalizations for different phonon energies

In Fig. 2.5 we follow the same quantities for a variety of phonon energies, allowing Ω to vary from 1/16 to 3/4 of the bare-band width for both models (although inverse quasiparticle weight is omitted from the breathing mode plots for clarity). First we note that there are some qualitative similarities, but just as many differences. In all these 1D cases the concavity increases as phonon energy decreases, so that by the mid-coupling regime ($\lambda \approx 1$) we recover the expected dependence – phonons that are easier (require less energy) to excite renormalize the band more. However, in the low-coupling regime we do not find this dependence (later seen again in Figs. 2.7 and 2.8 and in agreement with Eqs. 2.8 and 2.9). For both models the bandwidth [panels (a, d)] shows the opposite behaviour for low coupling, with a transition near $\lambda = 0.8$. Still considering the low-coupling regime, mass and velocity renormalizations show little dependence on the phonon energy for the breathing mode model yet strong dependence in the Holstein case. Again we find that the renormalizations and their corresponding “effective couplings” vary widely from each other and depend on the model and parameters chosen – sometimes in counterintuitive ways (with the exception of quasiparticle strength and velocity renormalization, which again overlap for the Holstein model).

2.2. Quasiparticle analysis

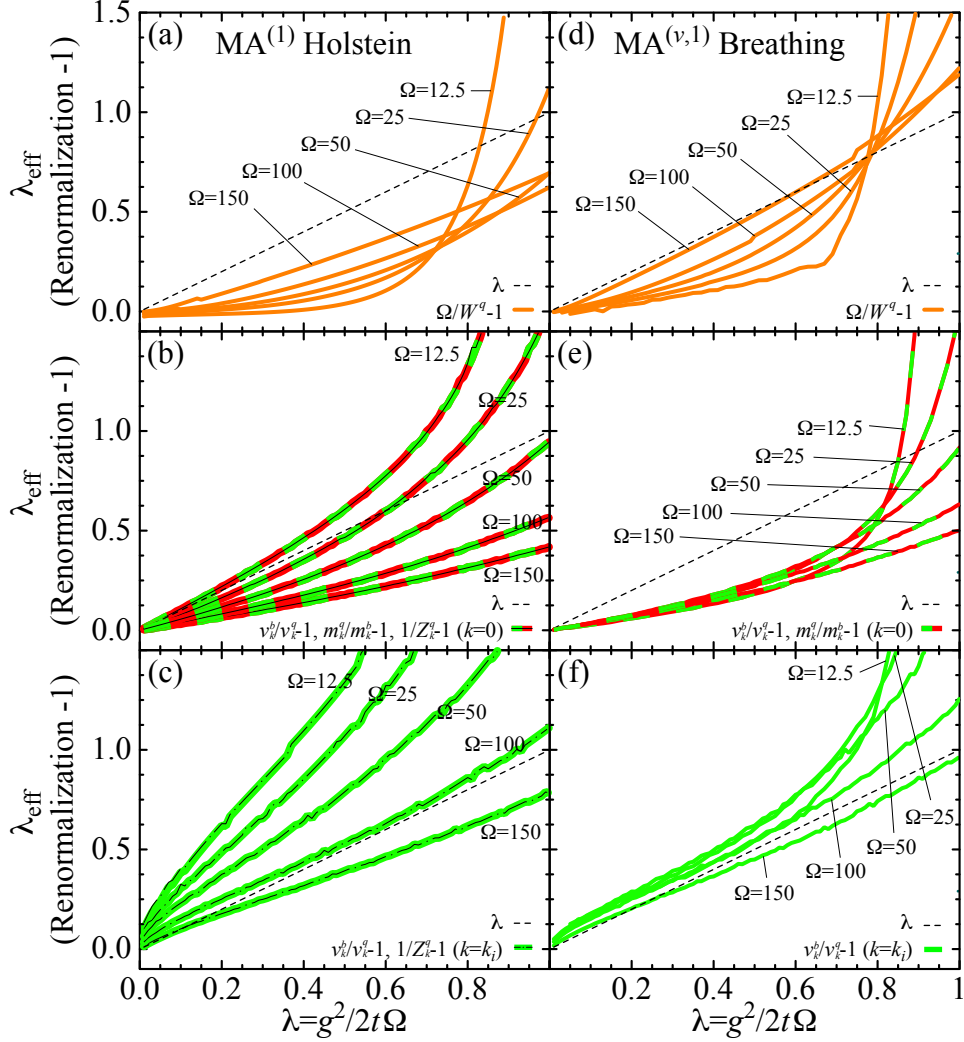


Figure 2.5: Effective coupling, λ_{eff} , (as would be interpreted in the Migdal limit from the renormalization parameters defined in Fig. 2.2) from the Holstein model (a–c) and breathing mode model (d–f) plotted vs. the true dimensionless coupling $\lambda = g^2/2t\Omega$ for a range of phonon energies Ω labelled in meV. In panels (b, c) those from multiple renormalization parameters (which lie directly on top of each other) are all plotted, whereas in (e, f) those from inverse quasiparticle weight do not fall on any other curve and are therefore omitted for clarity. The slope at $\lambda = 0$ in panels (b, e) is the quantity plotted in Figs. 2.7 and 2.8. Note that the noise in panels (c, f) originates mostly from the numerical determination of the inflection point k_i , while in (a, d) it stems mostly from variations in fitting the quasiparticle peak location at high momentum, where it has less weight.

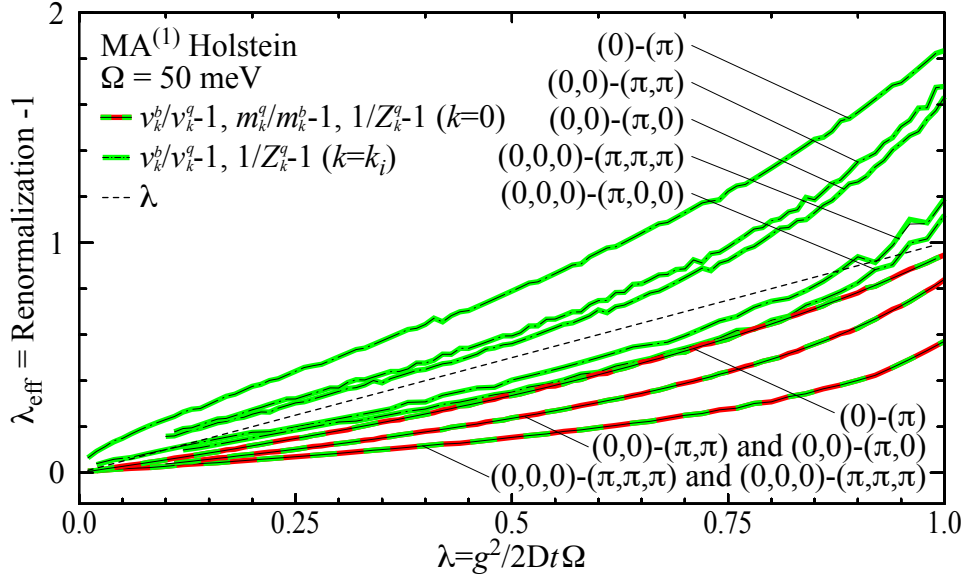


Figure 2.6: Effective coupling, λ_{eff} , (as would be interpreted in the Migdal limit from the mass and velocity renormalization parameters defined in Fig. 2.2) from the Holstein model and plotted vs. the true dimensionless coupling $\lambda = g^2/2Dt\Omega$ for different dimensionalities and high-symmetry cuts. Note that the noise in v and $1/Z$ at $k = k_i$ originates from the numerical determination of the inflection point k_i .

2.2.4 Renormalizations in different dimensions

The final parameter to be varied is dimensionality, which we explore briefly with Fig. 2.6 for the Holstein Hamiltonian in the low-coupling regime only. Here we find that, for a fixed dimensionality and phonon energy where $\Omega \sim t$, the renormalizations as a function of λ look qualitatively similar. The various renormalized quantities increase monotonically yet remain distinct from the microscopic coupling as well as each other (with the exception of quasiparticle strength and velocity renormalization, which are again the same), with details that depend on phonon energy and dimensionality. We feel it is important to note, however, that at larger couplings not explored here other studies on the dynamics of the Holstein (and momentum-dependent Su–Schrieffer–Heeger) models have found more complicated behaviour in higher dimensions, where a critical coupling value marks a drastic change in quasiparticle properties, which is most prominent as $\Omega \rightarrow 0$ [44–47]. Although interesting, this type of behaviour would not simplify quasiparticle renormalization analysis on such a system and is not investigated here.

2.2.5 Perturbation theory predictions near $\lambda = 0$

So far we have shown that, while the slope may not be 1, the renormalization curves could all still be reasonably well approximated as *linear* in λ in the very-low-coupling regime and that perturbation theory makes an excellent prediction for them near $k = 0$. This allows us to follow this slope continuously through parameter space with perturbation theory than by simulating even larger numbers of spectral functions. It is worth noting that in the classic implementation of the $(1 + \lambda)$ effective coupling scheme (see Ref. 22), perturbation theory is discussed but dismissed as a possible avenue, because the resulting corrections are too large for perturbation theory to be valid. However, in that instance, some approximations are made to ease completion of the integrals – these approximations eliminate the possibility of the arbitrarily small couplings we have used here. In our case the lowest non-zero order in the phonon–electron interaction term from Eq. 2.2 is the second (see Appendix § A.1), and in 1D we find that for both models it is possible

2.2. Quasiparticle analysis

to complete the integrals without further approximation. In the Holstein case the energy dispersion should be modified from $\varepsilon_k^b = -2t \cos(ka)$ to

$$\varepsilon_k^{pert} \approx -2t \left(\cos(ka) + \lambda \frac{\frac{\Omega}{2t}}{\sqrt{(\cos(ka) + \frac{\Omega}{2t})^2 - 1}} \right), \quad (2.8)$$

which agrees with the results calculated for the quasiparticle residue at $k = 0$ in Ref. 48. For the breathing mode model we find that the dispersion becomes

$$\begin{aligned} \varepsilon_k^{pert} &\approx -2t \left(\cos(ka) + \lambda \frac{\Omega}{2t} \mathcal{F} \left(\frac{\Omega}{2t}, k \right) \right), \\ \mathcal{F} \left(\frac{\Omega}{2t}, k \right) &\equiv \cos(ka) + \frac{\sin^2(ka) - \frac{\Omega}{2t} \cos(ka)}{\sqrt{(\cos(ka) + \frac{\Omega}{2t})^2 - 1}}. \end{aligned} \quad (2.9)$$

This demonstrates that, at the very least, we should expect the renormalizations to depend not solely on the dimensionless coupling $\lambda = g^2/2t\Omega$ but also on the other relevant energy scale in the problem – the ratio of phonon energy to bandwidth. By taking derivatives of these dispersions we can also find the predicted mass and velocity renormalizations. In Figs. 2.2 and 2.3 we plot the predicted dispersion, derivatives, and renormalizations contrasted against the simulated spectral function and find close but not perfect agreement for both models near $k = 0$ (but failing at large momenta), despite the relatively high coupling ($\lambda = 0.5$). As seen in Fig. 2.4 (and later in Figs. 2.7 and 2.8), near $k = 0$ for vanishing λ there is perfect agreement within our measurement accuracy; perturbation theory begins to show signs of failure near $\lambda \approx 0.25$. In higher dimensions we did not complete the integrals exactly but instead used the VEGAS Monte Carlo integration algorithm (see Appendix §D.1) to evaluate them numerically [49–51]. Using this routine for all dimensionalities allowed us to validate the results by comparing them with these known solutions for 1D for both models and the results found in Refs. 44, 48 for the Holstein model in one

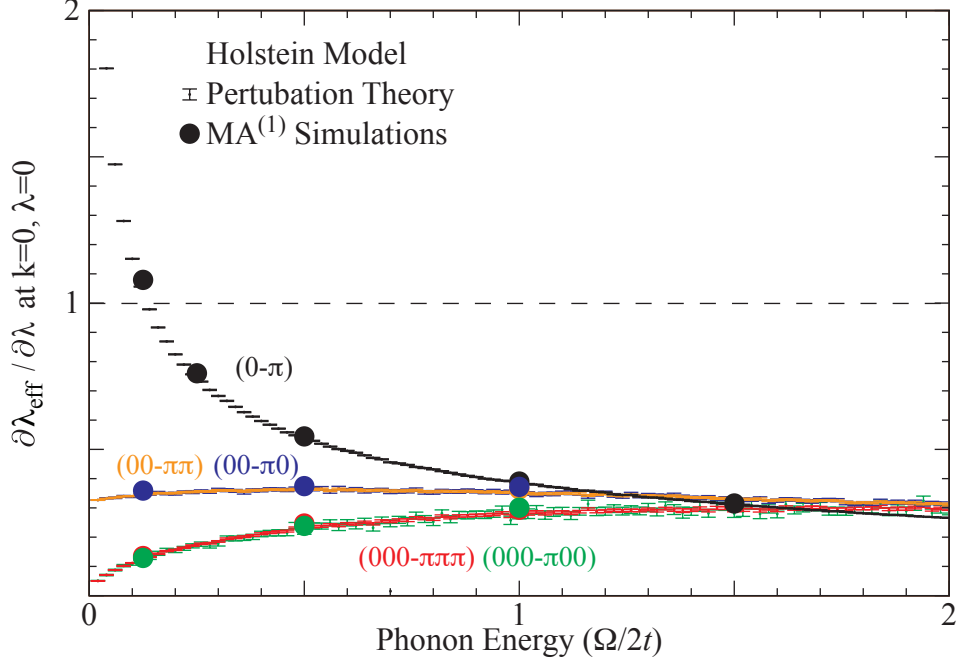


Figure 2.7: Rate of change in observed effective coupling, λ_{eff} , per change in true dimensionless coupling, λ , defined as $\partial\lambda_{\text{eff}}/\partial\lambda|_{k=0, \lambda=0}$ (where $\lambda_{\text{eff}} \equiv m_k^q/m_k^b - 1$ is as predicted by perturbation theory and measured from simulated spectral functions, and $\lambda = \langle |g|^2 \rangle / 2Dt\Omega$), plotted as a function of the phonon energy for the Holstein model. If the Migdal limit holds, this derivative would be a constant, 1, for all values of $\Omega/2t$. For $D > 1$ cuts from the Γ point to both the corner and face of the Brillouin zone were considered, as labelled. Vertical error in the results from simulated spectral functions is comparable to symbol size and results from approximating the slope at $\lambda = 0$ from the finite data points in Figs. 2.5 and 2.6, as well as similar simulation sets not shown. Uncertainty in the perturbation theory results stems from the numeric Monte Carlo integration used to determine the perturbation energies, taken from the distribution of independent subsets of total points evaluated, and is higher for non-diagonal cuts because of the narrower bandwidth in that direction. The curves predicted by Ref. 44 for the Holstein model in one and two dimensions are not shown, as they would be hidden by symbols, but fall exactly onto the perturbation theory results.

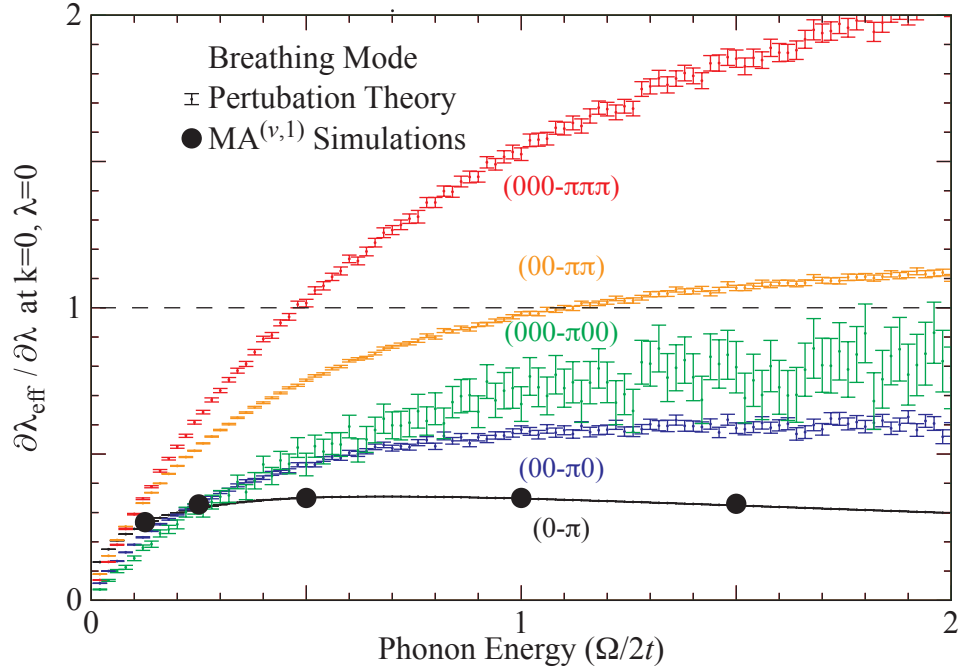


Figure 2.8: Rate of change in observed effective coupling, λ_{eff} , per change in true dimensionless coupling, λ , as a function of the phonon energy (as defined in Fig. 2.7) for coupling to a breathing mode.

2.2. Quasiparticle analysis

and two dimensions, where they show perfect agreement (once corrected for a slightly different definition of λ in 2D).

In Figs. 2.7 (for Holstein) and 2.8 (for coupling to a breathing mode) we show how the renormalization with the dimensionless coupling parameter λ near $k = 0$, $\lambda = 0$ (and hence the observed effective coupling, λ_{eff}) varies as a function of the other energy scale $\Omega/2t$ for both models in one, two and three dimensions, and how this matches nearly perfectly against measurements of the same quantity on the simulations. Interestingly, despite spectral functions that have outwardly similar characteristics [as seen, for example, comparing panel (a) in Fig. 2.2 vs. Fig. 2.3 or Fig. 2.10 vs. Fig. 2.12], we find that neither model would be well approximated by a $\lambda_{\text{eff}} = \lambda$ scheme, which is shown as the dashed line along 1. Additionally, we find a drastic difference in how the actual renormalizations vary with phonon energy depending on the model. The 1D Holstein model shows a perhaps expected dependence: phonons that require very little energy to excite have a dramatic effect on the electronic renormalization (blowing up as $\Omega \rightarrow 0$), but as the phonon energy increases, the mode has progressively less effect. In the 2D case, however, we find very limited dependence on phonon energy, with a curve that is almost flat and could therefore be rescaled to match if λ was chosen to be defined appropriately. In 3D we find the opposite of the 1D case, in that the renormalization vanishes as $\Omega \rightarrow 0$. These very different limits are directly related to the bare-electron density of states at the band-edge and its strong dependence on dimensionality [44]. In all dimensions we find that the renormalization is isotropic (as one might expect from an isotropic coupling) and that it asymptotically approaches a similar value for large phonon energies – reminiscent of a renormalization that depends solely on λ , if only for $\Omega/2t \gg 1$. In stark contrast, however, the more realistic breathing mode model shows entirely different behaviour. For all dimensionalities the overall functional form is similar for $\Omega \rightarrow 0$, where mass renormalizations vanish. This low-energy behaviour may be expected, as for weak coupling and energies close to $k = 0$ in the bare-band, the electron couples mostly to $q \approx 0$ phonons – and in this model such coupling vanishes, $g(q \rightarrow 0) \rightarrow 0$. As the phonon energy increases, however, we dis-

cover that the renormalization is anisotropic, with stronger renormalization along the diagonal cut (as may be expected for an anisotropic coupling), and we find a coupling that gets stronger as dimensionality increases (opposite of the Holstein case). We also find that the renormalizations do not asymptotically approach any fixed value for large phonon energies, as they did for the Holstein case.

Overall we find that there is much variability in quasiparticle analysis, to the point that one cannot make a general rule about renormalizations in this regime. There are, however, two common threads. The first is that, for both our models, perturbation theory works in the low-coupling regime: it correctly predicts the quasiparticle band structure near $k = 0$ for all combinations of parameters tested, although it fails at higher momenta (as seen in Figs. 2.2 and 2.3). The second, and perhaps more interesting, hints at something that may be quantitatively gained through quasiparticle analysis – without even requiring a more detailed model on which to attempt perturbation theory or other tools – and that we explore in the following section.

2.2.6 Verifying momentum independence of the self-energy

In Figs. 2.2, 2.3, 2.4, 2.5, and 2.6 one observes that, in the momentum-independent case only, v_k^b/v_k^q and $1/Z_k^q$ lie precisely on top of each other for all values and match m_k^q/m_k^b at $k = 0$. Although the velocity and mass renormalizations at $k = 0$ are simply a consequence of derivatives following each other near an extremum, the relationship between velocity renormalization and quasiparticle strength has implications for the structure of the self-energy, as will be discussed in detail here.

By definition, the Green's function is:

$$G(k, \omega) = \frac{1}{\omega - \varepsilon_k^b - \Sigma(k, \omega) + i\eta}. \quad (2.10)$$

In the infinite-lifetime quasiparticle regime the self-energy should be purely real, with any broadening coming solely from the small impurity scattering,

2.3. Self-energy analysis

η . We may then identify the implicitly defined quasiparticle dispersion as $\varepsilon_k^q = \varepsilon_k^b + \Sigma(k, \omega)|_{\omega=\varepsilon_k^q}$ and, since we are interested in an EDC, expand the self-energy about $\omega = \varepsilon_k^q$ to first order in energy. Taking $-1/\pi$ times the imaginary part yields the spectral function:

$$A(k, \omega) \approx \frac{1}{\pi} \frac{\eta}{\eta^2 + (\omega - \varepsilon_k^q)^2 (1 - \frac{\partial \Sigma(k, \omega)}{\partial \omega}|_{\omega=\varepsilon_k^q})^2}. \quad (2.11)$$

We can see that, cut along energy in the quasiparticle regime, the spectral function will be a Lorentzian at ε_k^q , with width given by η and with weight $Z_k = 1/(1 - \frac{\partial \Sigma(k, \omega)}{\partial \omega}|_{\omega=\varepsilon_k^q})$. This relationship between quasiparticle weight and the energy derivative of the self-energy is often derived and is usually associated directly with the success of an effective coupling scheme [21, 22], but we do *not* make that association here. Velocity renormalization is simply the ratio of momentum derivatives of the bare, v_k^b , and quasiparticle $v_k^q = v_k^b + \frac{\partial \Sigma(k, \omega)}{\partial \omega}|_{\omega=\varepsilon_k^q} v_k^q + \frac{\partial \Sigma(k, \varepsilon_k^q)}{\partial k}$ bands, which reduces to:

$$\frac{v_k^b}{v_k^q} = \frac{1}{Z_k} - \frac{\partial \Sigma(k, \varepsilon_k^q)}{\partial k} \frac{1}{v_k^q}. \quad (2.12)$$

We see that, for momentum-independent self-energies, the velocity renormalization must follow the inverse spectral weight. This means that the renormalization quantities can be used to conclusively check the momentum dependence of the self-energy, in the quasiparticle regime. Whether or not the self-energy is momentum dependent is of great importance to MDC self-energy analysis, on which we focus in the rest of the chapter.

2.3 Self-energy analysis

Since quasiparticle analysis fails to reveal the true microscopic coupling through renormalizations, we look toward other options for spectral function analysis. In this section we describe how it is possible to estimate the self-energy through the analysis of MDC lineshapes. We will begin, for simplicity, with a description for momentum-independent self-energy in § 2.3.1

and move on to describe the implications of momentum dependence on the procedure in § 2.3.2.

2.3.1 Momentum-independent self-energies

Cases of a momentum-independent self-energy can be verified through quasi-particle analysis; as seen in § 2.2.6, Eq. 2.12, the *overlap* of v_k^b/v_k^q and $1/Z_k^q$ is possible only when the self-energy is *momentum independent* along the quasiparticle dispersion. Although the quasiparticle dispersion and the path of MDC peak maxima where MDC analysis is carried out may vary, in practice they are often very close in the quasiparticle regime. One must always keep in mind that although a momentum-independent self-energy causes a Lorentzian MDC lineshape, Lorentzian lineshape alone is not sufficient to conclude that $\Sigma(k, \omega) = \Sigma(\omega)$ [37].

In cases where the self-energy is momentum independent, we may analyze $A(k, \omega)$ in terms of MDCs at constant energy $\omega = \tilde{\omega}$, where the self-energy may then also be considered a constant. Under this condition, as long as ε_k^b can be linearized in the vicinity of the MDC peak maximum observed at $k = k_m$, the MDC lineshape will be Lorentzian. By Taylor expanding ε_k^b about an MDC peak maximum at $k = k_m$, i.e., $\varepsilon_k^b = \varepsilon_{k_m}^b + v_{k_m}^b \cdot (k - k_m) + \dots$; ignoring higher-order terms (which must be negligible if the curve appears Lorentzian); and noticing that $\varepsilon_{k_m}^b + \Sigma'_{\tilde{\omega}} - \tilde{\omega} = 0$ will implicitly define the observed peak maximum, we can rewrite Eq. 2.1 as

$$A_{\tilde{\omega}}(k) \simeq \frac{A_0}{\pi} \frac{\Delta k_m}{(k - k_m)^2 + (\Delta k_m)^2}, \quad (2.13)$$

with

$$\begin{aligned} \Delta k_m &= -\Sigma''_{\tilde{\omega}}/v_{k_m}^b = \text{HWHM}, \\ A_0 &= 1/v_{k_m}^b = \int A_{\tilde{\omega}}(k) dk. \end{aligned} \quad (2.14)$$

Here Δk_m is the half width at half maximum (HWHM) of a Lorentzian of weight A_0 . For each constant energy cut, $\omega = \tilde{\omega}$, the observed peak

2.3. Self-energy analysis

maximum is labelled k_m . The self-energies are then easily found as

$$\begin{aligned}\Sigma'_{\tilde{\omega}} &= \tilde{\omega} - \varepsilon_{k_m}^b, \\ \Sigma''_{\tilde{\omega}} &= -\Delta k_m v_{k_m}^b.\end{aligned}\tag{2.15}$$

One must be careful visualizing the relationships; although a simple picture might be that the peak, whose width scales with the imaginary self-energy and band velocity, has been “pushed up” by the real self-energy to its observed location at $\tilde{\omega}$, one must remember that these quantities are defined implicitly and evaluated at different locations in the (k, ω) plane: the self-energy is evaluated at $(k_m, \tilde{\omega})$ and the bare-band at $(k_m, \varepsilon_{k_m}^b)$. Of course, these implicit definitions are no trouble if you simply wish to *observe* $A(k, \omega)$ and not *calculate* it based on this simple approximation. These relations are illustrated graphically in Fig. 2.9.

These relationships work exactly where they are applicable – namely, when the self-energy is momentum independent, when k_m is far from a band edge (where $v_{k_m}^b$ must vanish), where the peak shape is truly Lorentzian, and when the peak width is narrow enough that a first-order expansion of ε_k^b is appropriate. Since the convolution of two Lorentzians is another Lorentzian where the peak width is a simple sum of the widths of the original functions, the inserted impurity scattering shows up directly as an addition to the measured $\Sigma''_{\tilde{\omega}}$. (For comparison purposes a constant $\eta = 1$ meV has therefore been subtracted from all plots of $\Sigma''_{\tilde{\omega}}$.) However, these relationships still hinge on knowledge of the bare-band. If ε_k^b is unknown it is possible to fit it, to within an arbitrary energy offset, to any functional form that provides a value and derivative using a Kramers–Kronig bare-band fitting (KKBF) routine (see Appendix § A.2). Alternatively, as previously noted in Ref. 1 and used in Ref. 52, the imaginary part of the self-energy requires knowledge of only $v_{k_m}^b$, which can be obtained directly from $A_0 = 1/v_{k_m}^b$, allowing us to write it as the MDC width/integral ratio:

$$\Sigma''_{\text{ratio}} = -\Delta k_m / A_0\tag{2.16}$$

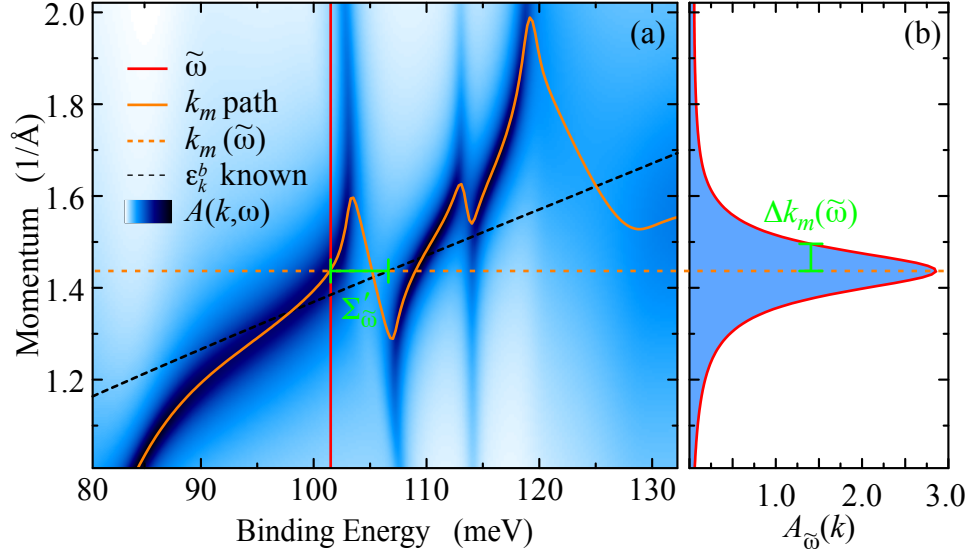


Figure 2.9: Eqs. 2.13 and 2.15 described diagrammatically for a momentum independent self-energy. (a) is a false-colour plot with the bare-band (ε_k^b) and path of peak maxima (k_m path) shown in addition to an example MDC cut at $\tilde{\omega}$ and the peak maximum location for that cut [$k_m(\tilde{\omega})$]. (b) the cut through momentum of $A(k, \omega)$ at constant energy $\tilde{\omega}$, observed to be a Lorentzian, with a peak maximum located at $k_m(\tilde{\omega})$, a HWHM $\Delta k_m(\tilde{\omega})$, and an area $A_0(\tilde{\omega})$. These lineshape properties are related to the self-energy at $\tilde{\omega}$ through the bare-band evaluated at k_m through Eq. 2.15.

2.3. Self-energy analysis

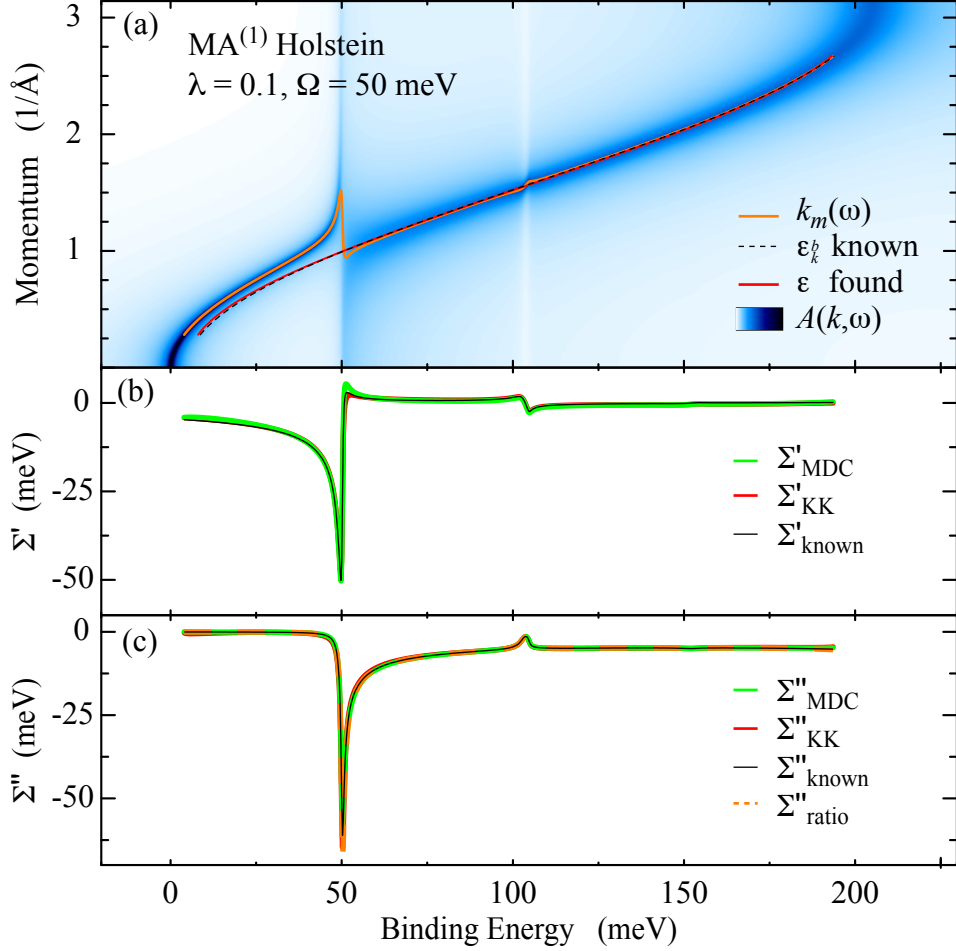


Figure 2.10: (a) $A(k, \omega)$, calculated for the momentum-independent Holstein self-energy with MA⁽¹⁾ for $\Omega = 50$ meV and $\lambda = 0.1$, as a false-colour plot; also shown are the k_m path of MDC maxima along which the analysis is performed, as well as the known bare-band and the third order polynomial approximation found through the KKBF analysis (the arbitrary energy offset introduced through KKBF has been shifted back by hand to allow comparison between the two). (b,c) Real and imaginary parts of the self-energy from the model (Σ_{known}), the bare-band and MDC fitting routine (Σ_{MDC}) as found via Eq. 2.15, and the KK transform of Σ_{MDC} (Σ'_{KK}) and Σ_{MDC} (Σ''_{KK}) used as an internal check in KKBF. In (c) the MDC ratio results, Σ''_{ratio} , as found via Eq. 2.16, are also shown.

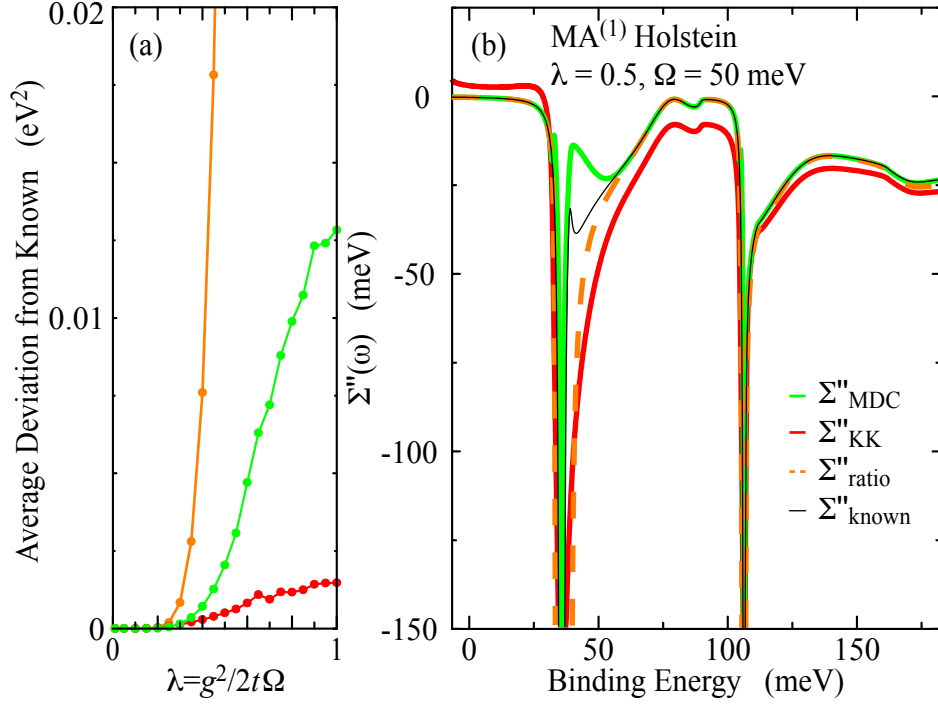


Figure 2.11: (a) Deviation (i.e., average of the squared difference at each k_m) between estimated and known self-energies vs. λ . (b) Various estimates for the imaginary part of the self-energy, defined as in the caption of Fig. 2.10, for $A(k, \omega)$ calculated within MA⁽¹⁾ for $\Omega = 50$ meV and $\lambda = 0.5$.

2.3. Self-energy analysis

This variation allows us to tackle the problem over a larger range of λ , as it does not rely on the KKBF routine to succeed over the entire range in order to ensure the fitness of the Kramers–Kronig transform and fit the bare-band. Eq. 2.16 is free to work over energies where the peak is Lorentzian (i.e., Eq. 2.13 holds) and to fail in others without allowing these failures to block the procedure. Experimentally, when using this ratio, one must be careful that the observed spectra are properly normalized – otherwise, it will be off by a constant multiple – but even if this is not possible the form of the imaginary self-energy should be nevertheless recoverable. It is also possible, in cases of momentum-independent self-energy for which $v_k^b/v_k^q = 1/Z_k^q$ from Eq. 2.12, to find the same ratio using only quasiparticle properties as $\Sigma''_{\text{MDC}} = -v_{k_m}^q \Delta k_m / Z_{k_m}^q$.

The results of both the KKBF and the ratio method, performed as if the bare-band was not known on a momentum-independent self-energy in the low-coupling regime, are presented in Fig. 2.10. The internal self-consistency of the KKBF results is confirmed by the good match between Σ_{MDC} and Σ_{KK} , and the agreement of Σ_{ratio} adds further confidence. These “measured” quantities show good agreement with their known counterparts everywhere Eq. 2.13 is applicable, demonstrating that these methods work well in the low-coupling regime; however, they become progressively less accurate as the coupling increases. In Fig. 2.11(a) we show the progressive failure of the method applied for couplings where λ ranges from 0 to 1, which demonstrates a rapid degeneration of the accuracy of the method outside of the low-coupling regime. Note, however, that the two methods fail in different ways. Σ''_{MDC} tends to fail more globally, whereas Σ''_{ratio} often continues to work almost exactly in some energy regions while failing catastrophically in others. (These regions cause its average deviation, shown in Fig. 2.11, to indicate perhaps a higher degree of failure than deserved.) In Fig. 2.11(b) we demonstrate these differences by showing the results of the methods applied blindly at $\lambda = 0.5$, even though lineshapes show that there are areas where Eq. 2.13 does not apply. One can see how the internal KKBF check has begun to fail, as Σ''_{MDC} and Σ''_{KK} do not match; there are structural differences, and Σ''_{KK} has picked up different offsets in the various flatter parts of

the spectrum, making setting its overall offset difficult. As the disagreement between Σ''_{MDC} and Σ''_{KK} increases with coupling, it will eventually cause the KKBF routine to fail to capture the bare electronic structure. None of the methods reproduce Σ''_{known} near the sharp one-phonon structure; note that Σ''_{MDC} and Σ''_{ratio} overestimate and underestimate it, respectively. Our experience with this model leads us to believe that this behaviour is typical: when the methods fail, they do not tend to fail in identical ways, so that in regions where they do match one can still have confidence that the methods are working.

2.3.2 Momentum-dependent self-energies

The methods previously described to extract the self-energy from the spectral function hinge on the momentum independence of the self-energy in two ways. For fitting lineshape, a momentum-independent self-energy guarantees a Lorentzian lineshape, but the inverse is not true – it is still possible to have a momentum-dependent self-energy that generates a Lorentzian. Additionally, fitting the bare-band relies on the Kramers–Kronig transforms in energy, which are valid only for a fixed momentum. In cases where the momentum dependence is not too strong locally near k_m , however, we have found that it is still possible to gain insight using similar approaches, although even more care must be taken in the interpretation of the results. If, despite momentum dependence, the MDC appears Lorentzian in shape, certain higher-order terms must be small when expanding each of ε_k^b , $\Sigma'(\omega, k)$, and $\Sigma''(\omega, k)$ about k_m . Under this condition we may drop terms of order $(k - k_m)^3$ and higher from the denominator as well as $(k - k_m)$ and higher from the numerator, which also implies we may drop $\partial\Sigma''/\partial k$ and $\partial^2\Sigma''/\partial k^2$ everywhere. We end up with an expression identical to Eq. 2.13, only with new interpretations for the HWHM and the spectral weight of the peak:

2.3. Self-energy analysis

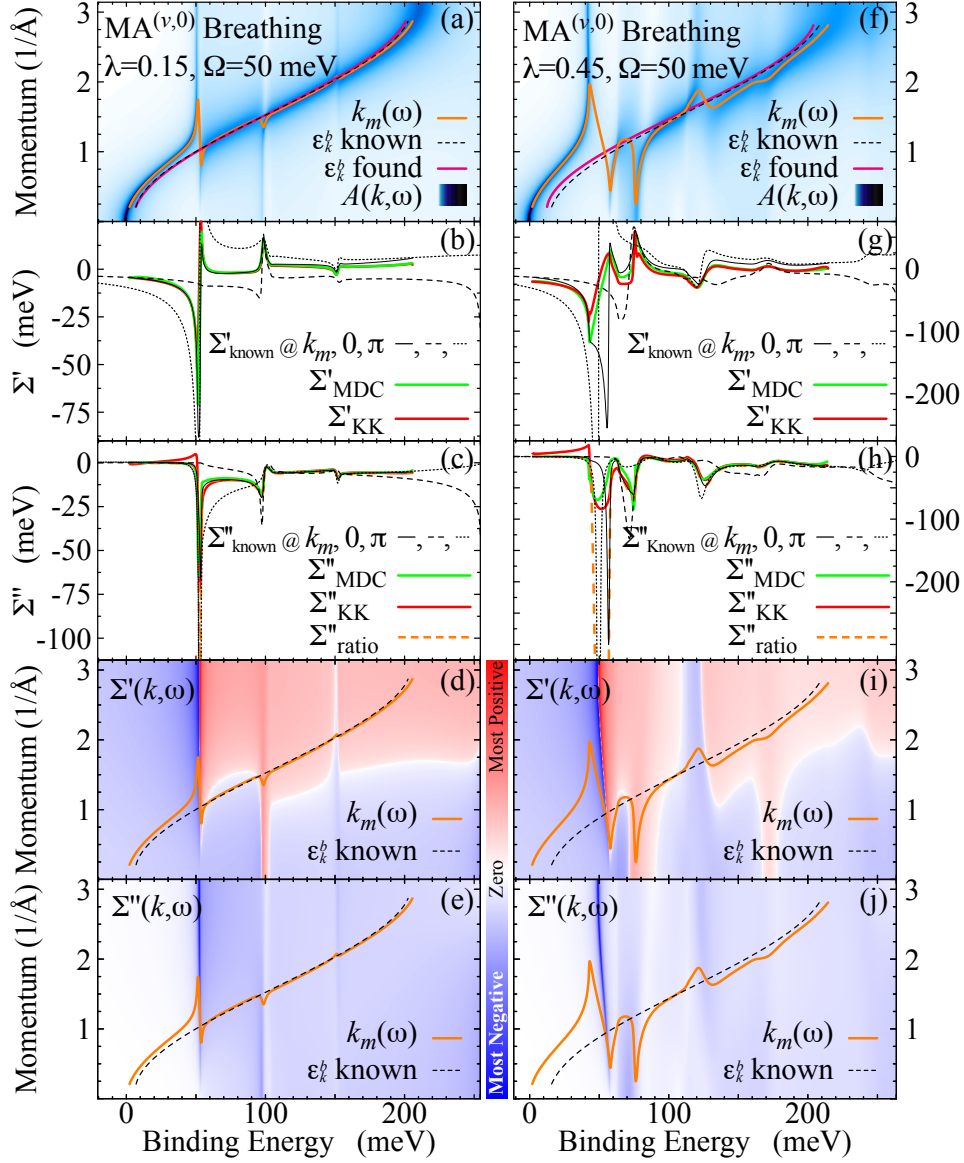


Figure 2.12: (a–c, f–h) $A(k, \omega)$ and self-energies as defined in Fig. 2.10 for momentum-dependent coupling to a single breathing mode. In this instance, as the self-energy is momentum dependent, the known self-energies are plotted along the path of peak maxima ($\Sigma_{\text{Known}}@k_m$) to show good agreement with the derived values, as well as along both edges of the Brillouin zone for comparison ($\Sigma_{\text{Known}}@k = 0$ and $\Sigma_{\text{Known}}@k = \pi$). Finally (d, e, i, j) show the full extent of the energy and momentum dependence of the real and imaginary self-energies as a false-colour plot, with the k_m path superimposed.

2.3. Self-energy analysis

$$\begin{aligned} \Delta k_m &= -\frac{\Sigma''(\tilde{\omega}, k_m)}{v_{k_m}^b + \partial\Sigma'(\tilde{\omega}, k_m)/\partial k}, \\ A_0 = \int A_{\tilde{\omega}}(k)dk &= \frac{1}{v_{k_m}^b + \partial\Sigma'(\tilde{\omega}, k_m)/\partial k}. \end{aligned} \quad (2.17)$$

Now that the self-energies are momentum dependent, it becomes more important to remember that the self-energy extracted using this method will follow the k_m path through (ω, k) space; this path is demonstrated as a false-colour plot in Fig. 2.12 (d, e, i, j). From Eq. 2.17 we find that, in this momentum-dependent case, the ratio check Eq. 2.16 proves to be invaluable, as it removes the possible inaccuracies when strong momentum dependence near k_m in Σ' might provide a Lorentzian lineshape with a misleading width, when viewed from a momentum-independent perspective. In Fig. 2.12 (a–c, f–h) we present the results of both KKBF and the ratio method for a momentum-dependent coupling. From a comparison between the measured and known self-energies on paths through k -space along the zone boundaries and along k_m , we find agreement only along the k_m path, as expected. Further, especially in Fig. 2.12 (h) near the third phonon structure close to ~ 125 meV, one can see how it is possible for Σ''_{MDC} and Σ''_{KK} to agree with each other and yet not correctly predict Σ''_{known} , despite the peak shape being reasonably Lorentzian, owing to sufficient local momentum dependence in the real self-energy [Fig. 2.12 (i)]. In this location we note, however, that Σ''_{ratio} still correctly predicts Σ''_{known} as it is not affected by this local momentum dependence. Overall we find that, in a similar fashion to the momentum-independent case, there is generally good agreement between the found self-energies and the self-energy along the k_m path in the low-coupling regime, and the methods progressively fail as we move into the mid-coupling regime. The available modes of failure are increased: there are more locations where the lineshape is not Lorentzian because of strong local momentum dependence of the self-energy; there are places where it is still Lorentzian but with a misleading width; and the Kramers–Kronig relations are not valid along an arbitrary path through (ω, k) space, which

disrupts the fitness of the KKBF routine. While it is not surprising that the KKBF routine eventually fails for large couplings in the momentum-dependent case, it is interesting that it works at all, as the Kramers–Kronig relations in energy are formally valid only for a fixed momentum, but the measured self-energies follow the k_m path at all couplings. Despite this, as can be seen in Fig. 2.12 (b, c), the Kramers–Kronig relations appear to work relatively well along the k_m path in the low-coupling case. Nevertheless we find that, in this model, failures occur at qualitatively similar couplings when momentum dependence is added.

2.4 Conclusions

The spectral function is an extremely rich data source. We have shown that, despite the allure of extracting the true microscopic coupling through quasi-particle renormalizations of ARPES data with an effective coupling scheme, away from the Migdal limit it is not always possible to do so – and certainly not for cases close to a dispersion maximum. Away from this limit $\lambda_{\text{eff}} \neq \lambda$. However, through careful modelling and the analysis of specific features it may be possible to learn much more. If one can correctly devise a model, it may be possible to predict a given renormalization or even show experimental support for a given model via relationships between renormalization parameters. Through MDC self-energy analysis, we have shown that the self-energy can be extracted along paths through (k, ω) space in the low-coupling regime – and that it is possible still to gain some insight at higher couplings. We have also shown that it is possible to infer the momentum dependence of the self-energy through comparison of renormalization properties. Methods like these, together with detailed models and powerful simulations, will hold the key to more thorough and quantitative analysis of the rich data supplied through ARPES.

Chapter 3

Chamber characterization

A large effort was put toward chamber characterization as part of the commissioning and optimization of the new angle-resolved photoemission spectroscopy (ARPES) system at University of British Columbia (UBC). This chapter will describe efforts undertaken both to characterize the system in general and also specifically to characterize the data presented in Chapter 4. While the analyzer has a variety of angular modes, those used most frequently (by me), and the only ones presented in this thesis, are wide-angle mode (WAM) and low-angular-dispersion mode (LAD). WAM is the mode that admits the largest angular window, $\pm 13^\circ$, and is most useful for mapping entire Fermi surfaces (for example Fig. 4.3), while LAD (as its name suggests), with an acceptance of $\pm 7^\circ$, is most useful for following electronic dispersions (for example Fig. 4.8).

We will begin with measurements to characterize the angular resolution and its dependence on sample position in § 3.1, using both photoemission from samples as well as an electron gun, and will cover energy resolution in § 3.2. Finally, the “resolution” of the final 2D electron detection system is discussed in § 3.3. For clarity, a brief discussion of the functional forms used and a comparison between different measures of “resolution” – full width at half maximum (FWHM) vs. standard deviation vs. resolved width of a Fermi edge – is presented in § 3.4.

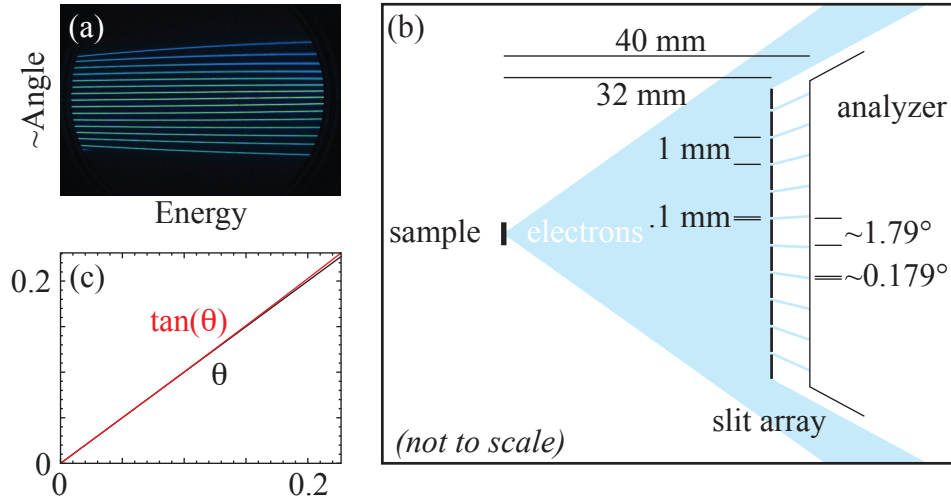


Figure 3.1: Illustration of slit array and slit array data. (a) typical detector image taken with slit array and electron gun, in WAM. (b) illustration of the sample, emitted electrons, slit array, and analyzer, with sample placed at the focal point of the analyzer. (c) plot of $\tan(\theta)$ vs. θ for 0 to .22689 radians, equivalent to the 13° maximum half-acceptance angle of the analyzer. This represents the total deviation from linearity in angular spacing of the electrons that pass the slit array, owing to its being straight with evenly spaced slits (rather than curved, with centre of curvature at the sample). The largest deviation, at the far edge of the scale, is $\tan(\theta_{\max}) - \theta_{\max} \approx .00398 \sim .228^\circ$. Assuming a point source, the angular spacing of slits passing through the centre of the analyzer will be $\sim 1.79^\circ$ with width $\sim 0.179^\circ$, while at the edge of detection (13° from centre) spacing is $\sim 1.71^\circ$ with width $\sim 0.170^\circ$ owing to this effect.

3.1 Angular resolution

3.1.1 Setup

In order to measure the angular resolution of the analyzer in situ, a slit array can be moved in between the sample and the analyzer entrance slit to generate a data set with features evenly spaced in angle, as shown in Fig. 3.1⁷. This can be done using an electron gun (nominal FWHM spot size is $50\ \mu\text{m}$ for the SPECS EQ 22/25 used) scattering from a thin wire (thickness $95\ \mu\text{m}$) or gold target to measure the fundamental limit of angular resolution, or directly with photoemission from the sample measured during an experiment (nominal light source spot size $\sim 500\ \mu\text{m}$). We present results from both these methods here, which yield different estimates for the angular and effective angular resolution attainable with our setup.

3.1.2 Electron gun tests

In order to determine the optimal sample position within the three positional degrees of freedom of the cryostat as built, data was taken as a function of cryostat position using an electron gun (spot size $50\ \mu\text{m}$) on a thin tungsten wire (thickness $95\ \mu\text{m}$) mounted to the bottom of the cryostat. The goal was to optimize the angular resolution by moving the cryostat and thereby find the focal point of the analyzer. Unfortunately, this did not prove feasible for two reasons. Primarily, the angular resolution was not found to depend strongly or reliably on sample position. The lack of reliability was likely related to the second reason – a $95\ \mu\text{m}$ wire is difficult to reproducibly hit with a $50\ \mu\text{m}$ electron beam (especially when moving the cryostat by millimetres), and partial illumination of the wire could also cause a change in perceived resolution. Eventually the optimal cryostat location was physically measured during a chamber venting for routine maintenance, based on the nominal focal point of the analyzer. Both the wire (because of difficulties the wire caused inserting and removing the cryostat) and the electron

⁷This is the same configuration used to correct for image warping in the angular direction (see § B.1).

3.1. Angular resolution

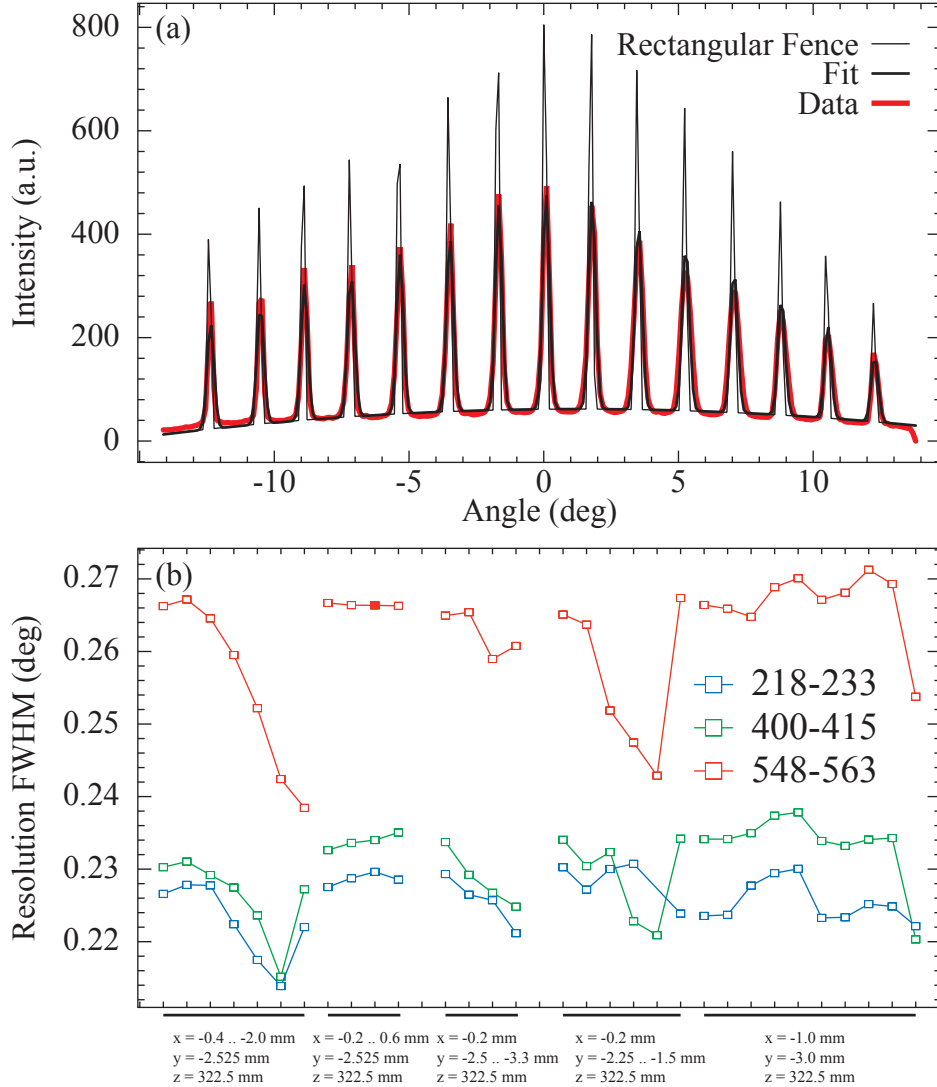


Figure 3.2: Angular resolution tests in WAM, using an electron gun. (a) example angular dispersion of the slit image, integrated from pixels 548–563 (thick red), as well as infinite resolution rectangular fence with background (thin black) and final instrumental broadened fit (thick black). (b) the energy resolution derived from such fits for varying cryostat position, integrated over three detector energy regions: pixels 200–210, typical mid-occupied state (blue); 400–410, typical Fermi edge (green); and 500–510, typically just on the unoccupied side of the Fermi energy (red). Note that the camera used in these measurements has since been upgraded from 640 to 1376 pixels in this direction. The data point corresponding to panel (a) is the filled shape in (b).

3.1. Angular resolution

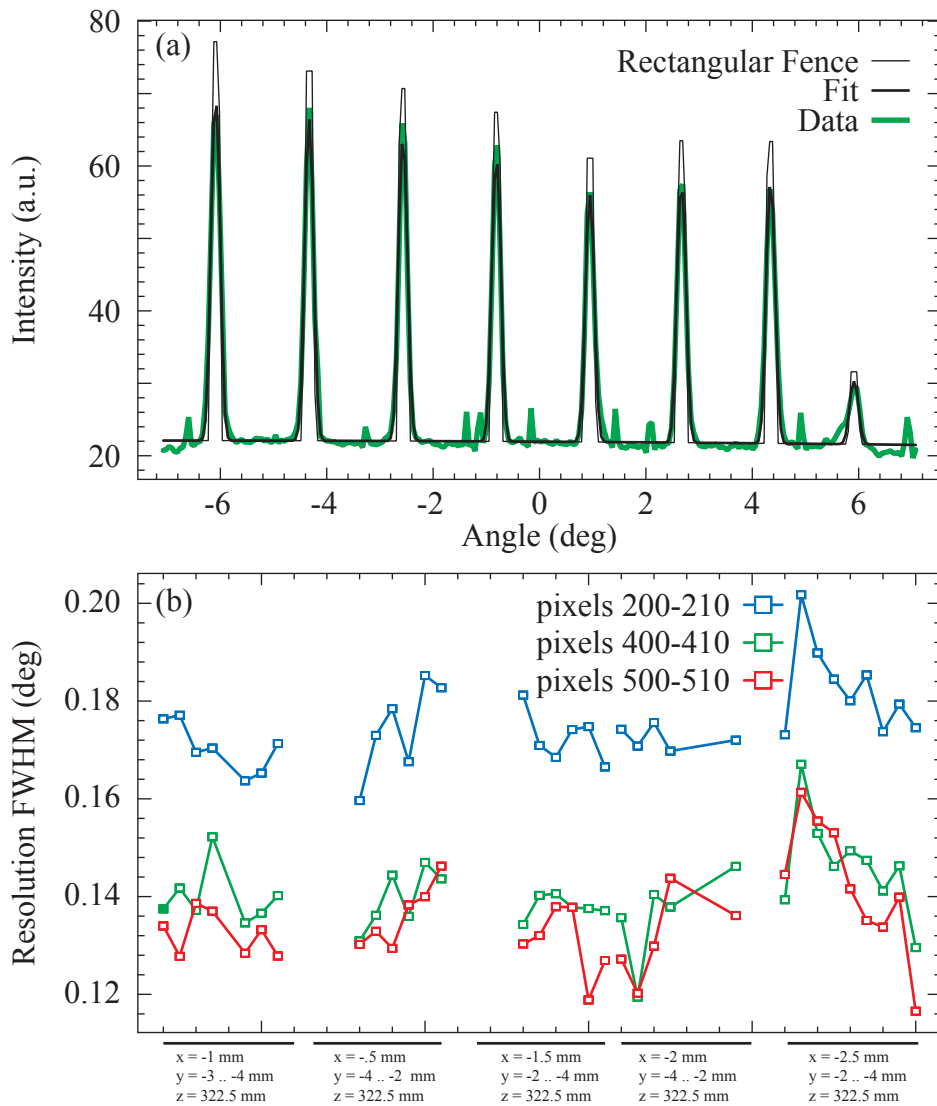


Figure 3.3: Angular resolution tests in LAD, using an electron gun. (a) example angular dispersion of the slit image, integrated from pixels 400–410 (thick green), as well as infinite resolution rectangular fence with background (thin black) and final instrumental broadened fit (thick black). (b) the energy resolution derived from such fits for varying cryostat position, integrated over three detector energy regions: pixels 200–210, typical mid-occupied state (blue); 400–410, typical Fermi edge (green); and 500–510, typically just on the unoccupied side of the Fermi energy (red). Note that the camera used in these measurements has since been upgraded from 640 to 1376 pixels in this direction. The data point corresponding to panel (a) is the filled shape in (b).

3.1. Angular resolution

gun (in order to minimize possible sources of stray fields) have since been removed from the chamber.

Despite failing to precisely determine the focal point (instead discovering that it was not required to be precisely at the focal point), owing to the small spot size of the electron gun this wire-test data set remains a good indicator of the fundamental angular resolution of the analyzer. In order to determine the resolution for each image it was first transformed into angle-space (see § B.1) to reduce warping and to set the scale from pixels to angle⁸. Each image was then least-squares [53] fit to a rectangular “fence” with polynomial background and convolved with a Gaussian resolution. The background, individual rectangle location/height, and instrumental resolution were fit parameters, while the rectangular width was kept fixed at 0.18° , which corresponds to the width expected from a point source with infinite resolution. The result of a single fit is shown in panel (a) of Fig. 3.2 for WAM and Fig. 3.3 for LAD, with the results of all fits shown in (b).

These test results show that the resolution does not strongly depend on sample position relative to the focal point, although there is some variation across the detector. Comparing all measurements near the typical Fermi edge location, where angular resolution is most important, gives $\text{FWHM}_{\text{WAM}} = 0.230 \pm 0.005^\circ$ and $\text{FWHM}_{\text{LAD}} = 0.141 \pm 0.008^\circ$ for the resolution and its standard deviation across the multiple measurements. If we assume that the instrumental resolution combines in quadrature with the electron gun spot size (FWHM 0.050 mm at 32 mm from the slit corresponds to 0.090°), then we obtain

$$\begin{aligned}\text{FWHM}_{\text{WAM}} &= 0.212 \pm 0.005^\circ, \\ \text{FWHM}_{\text{LAD}} &= 0.109 \pm 0.008^\circ.\end{aligned}\tag{3.1}$$

3.1. Angular resolution

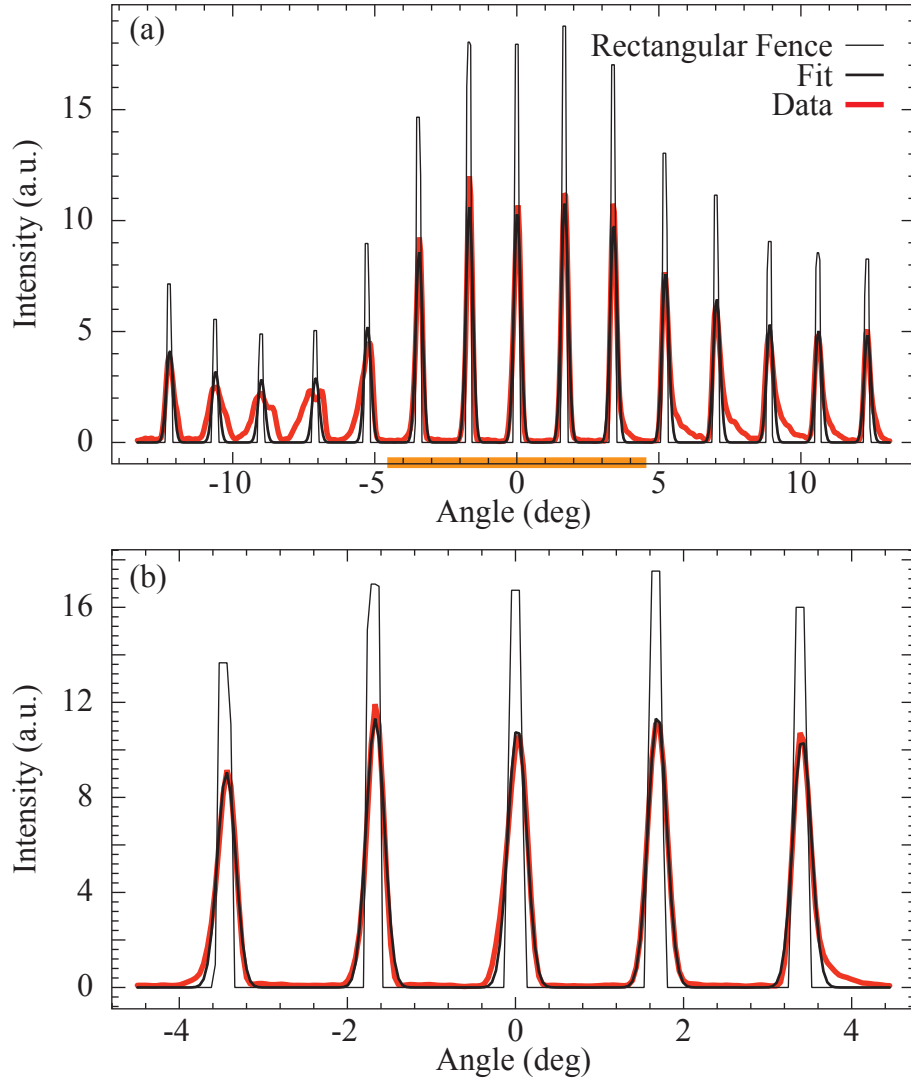


Figure 3.4: Angular resolution tests in WAM, on Sr₂RuO₄, showing the image integrated from -100 to 0 meV (thick red), as well as infinite resolution rectangular fence with background (thin black) and final instrumental broadened fit (thick black). In (a) the full angular width of the detector is shown, while (b) presents a close-up of the centre region.

3.1. Angular resolution

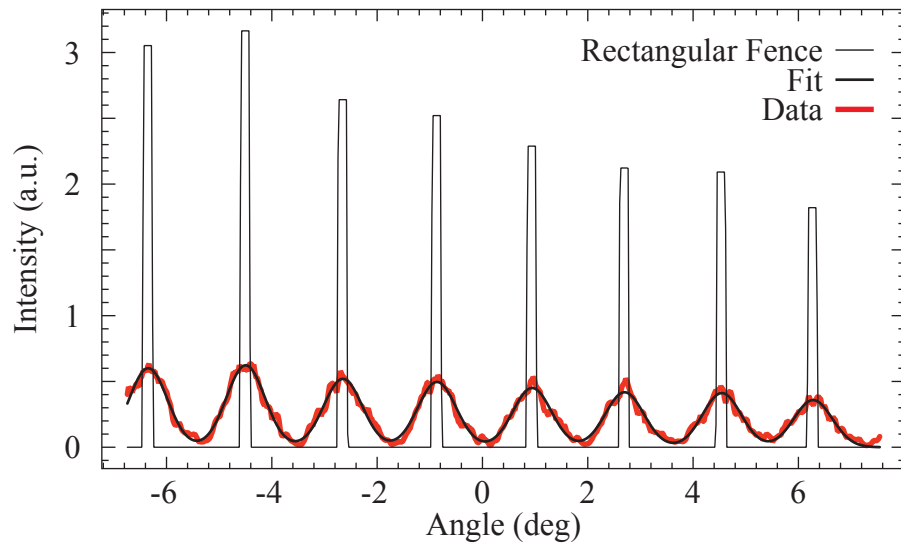


Figure 3.5: Angular resolution tests in LAD, on Sr_2RuO_4 , showing the image integrated from -35 to 0 meV (thick red), as well as infinite resolution rectangular fence with background (thin black) and final instrumental broadened fit (thick black).

3.1.3 Sample tests

Although the angular resolution was not observed to strongly change as a function of position during the electron gun tests, the image warping was. This suggests that, although in principle the analyzer should map all parallel electrons to the same spot on the detector regardless of their point of origin, photon spot ($\sim 500 \mu\text{m}$) and sample (~ 0.5 to 2 mm) size can affect the final angular resolution of ARPES measurements on a real sample. For this reason, and to ensure the accuracy of the pixel-to-angle conversion, slit array measurements are taken for every data set measured. It is useful to make an estimate of the instrumental resolution from these measurements as well.

In Figs. 3.4 and 3.5 we present such tests using data sets presented in Chapter 4 for WAM and LAD, respectively. Comparing panels (a) and (b) in Fig. 3.4 for the WAM test, we find that the apparent angular resolution is not uniform across the detector, which is typical of slit images taken using a real sample in this mode. In Fig. 3.5 we find that the apparent angular resolution in LAD is much worse, despite the narrower acceptance angle, but that it is uniform across the detector. By fitting these data sets, as was done in § 3.1.2, we find the resolutions, with uncertainty based on chi-squared (which is much less reliable than the large data sets used in the electron gun tests), to be

$$\begin{aligned}
 \text{FWHM}_{\text{WAM, whole detector}} &= 0.259 \pm 0.005^\circ, \\
 \text{FWHM}_{\text{WAM, centre region}} &= 0.220 \pm 0.003^\circ, \\
 \text{FWHM}_{\text{LAD}} &= 0.850 \pm 0.005^\circ.
 \end{aligned}
 \tag{3.2}$$

It is interesting that, now with a larger spot size, the apparent angular resolution in WAM has not changed much, whereas in LAD it has changed drastically. Owing to the smaller angular acceptance, which has the effect

⁸Moving to angle space assuming the sample is at the focal point also has the effect of eliminating a change in perceived resolution owing to expansion/contraction of the entire pattern caused by deviation from the true focal point, although it changes the perceived total angular acceptance angle.

of “zooming” in angle space on the detector, one would expect the angular resolution in LAD to be superior to that of WAM; however, when measuring photoemission on actual samples, WAM, in our chamber as built, appears to have superior angular resolution. Although this discrepancy between modes is very reproducible⁹, how it exists is not clear, but it extends from low- to medium- and high-angular-dispersion modes, which (although not fully characterized here) all show visually similar apparent resolutions to LAD. Indeed, given a 500 μm spot size (which is likely, as Sr_2RuO_4 cleaves well and often photoemits from the entire cleaved surface, making the light source the limiting factor) at 32 mm, one should even *expect* a $.895^\circ$ apparent broadening in the slit image, so it is not clear how WAM can do so well.

3.1.4 Conclusions

As mentioned at the beginning of the last section, in principle the analyzer should map all parallel electrons to the same spot on the detector regardless of their point of origin. This means that the apparent resolutions as measured with a large spot size using the slit array (which blocks electrons, creating features in angle that depend on the spot size) do not necessarily reflect the ability of the analyzer to resolve fundamental photoemitted features of the electronic state in a sample (these features are emitted in parallel, from all points on the sample surface). However, it has been observed (especially during the electron gun tests) that the image warping (not just position) changes when moving the sample, indicating that the analyzer does not *quite* map all parallel electrons to the same spot on the detector when they originate from different locations. For this reason the effective resolution will lie somewhere in between the values presented in Eqs. 3.1 and 3.2. It is recommended to always check the apparent angular resolution by analyzing a slit image for every data set.

In practice, as suggested by the apparent resolution in slit-array data measured on real samples, WAM does have a consistently better angular resolution compared with LAD (demonstrated by ability to separate features

⁹Reproducible with photoemission from samples – the electron gun tests have not been repeated, and cannot be repeated without re-installing an electron gun on the chamber.

which are close together in angle space). However, it is still not practical to use WAM to perform dispersion analysis, because it is not possible to set the pass-energy of the analyzer low enough to obtain sufficient energy resolution in this mode; it remains a Fermi surface mapping tool.

3.2 Energy resolution

The discrimination in the energy direction for our system is outlined in Fig. 3.6. The selectable entrance slit allows for finer resolution at the cost of restricting electrons with a small slit or provides higher electron yield at the cost of reduced resolution¹⁰, while the pass energy E_{pass} varies the overall scale of the image (energy/pixel). The energy resolution of the analyzer is therefore controlled by a combination of the pass energy and entrance slit used and nominally obeys the following relation:

$$\text{FWHM}_{\text{Energy Resolution}} = E_{\text{pass}} \cdot \frac{\text{Slit Width}}{300 \text{ mm}}, \quad (3.3)$$

where the (curved) slits available may be selected from 0.8, 0.5, 0.2, and 0.1 mm and the pass energies available depend on both the angular lens mode as well as the kinetic energy chosen.

Along with every data set a measurement is also performed on polycrystalline¹¹ gold, held at sample temperature, in order to measure the energy resolution in situ. This gold sample reference is a part of the cryostat, held a known distance from the sample, allowing for quick and precise switching between sample and gold. Examining the sharpness of the Fermi edge on

¹⁰In addition to size affecting resolution, the entrance slit's *shape* affects the shape of the final image. Experiments presented here were performed with a concentrically curved entrance slit, which causes electrons of the same energy to fall on concentric rings on the detector. Corrections for this effect are discussed in §B.2. A straight slit, available in our analyzer as built, causes electrons of the same energy to fall in rings with twice the curvature. A slit with twice the curvature, not available on our analyzer as built, should cause electrons of the same energy to fall in straight lines on the detector – but would also be more susceptible to non-uniform warping from the non-radial fields caused by the existence of the slit itself. Such warping would be difficult, if not impossible, to properly correct.

¹¹Polycrystalline so it has no angular structure.

3.2. Energy resolution

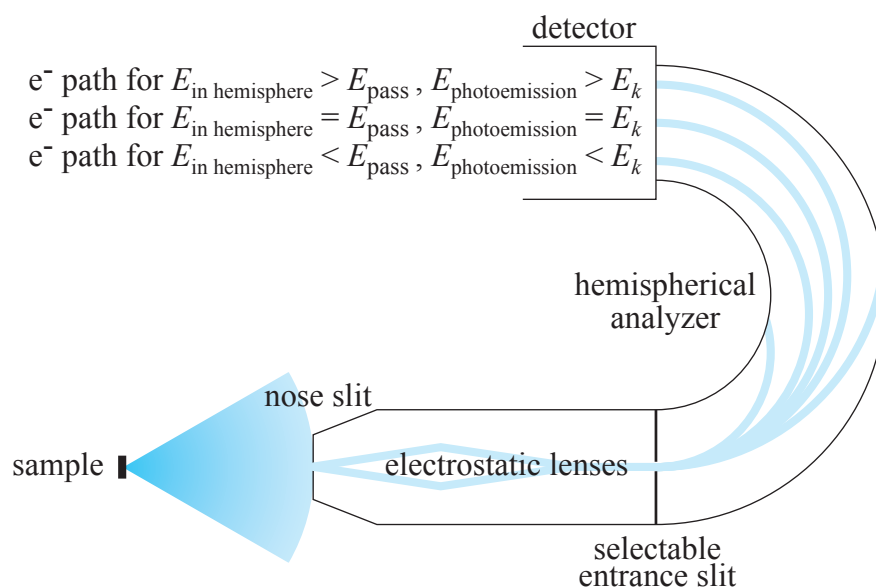


Figure 3.6: Illustration of energy discrimination through the hemispherical analyzer. This view is perpendicular to that which discriminates angle, presented in Fig. 3.1. In this direction electrons first pass through a slit on the analyzer nose, which admits electrons over $\sim 1^\circ$ (as inferred from the apparent angular resolution taken over multiple scans at different sample angles – for example, in Fig. 4.3). These electrons are then focused on the entrance slit to the hemispheres and retarded (or accelerated) such that electrons that entered the lenses with kinetic energy E_k will exit them and enter the hemispheres with energy E_{pass} . Passing through the selectable entrance slit, electrons are then discriminated in energy via the radial field of the hemispheres; electrons with energy E_{pass} will travel through the centre of the hemispheres, while those with more or less energy will drift either to the outside or inside (respectively).

3.2. Energy resolution

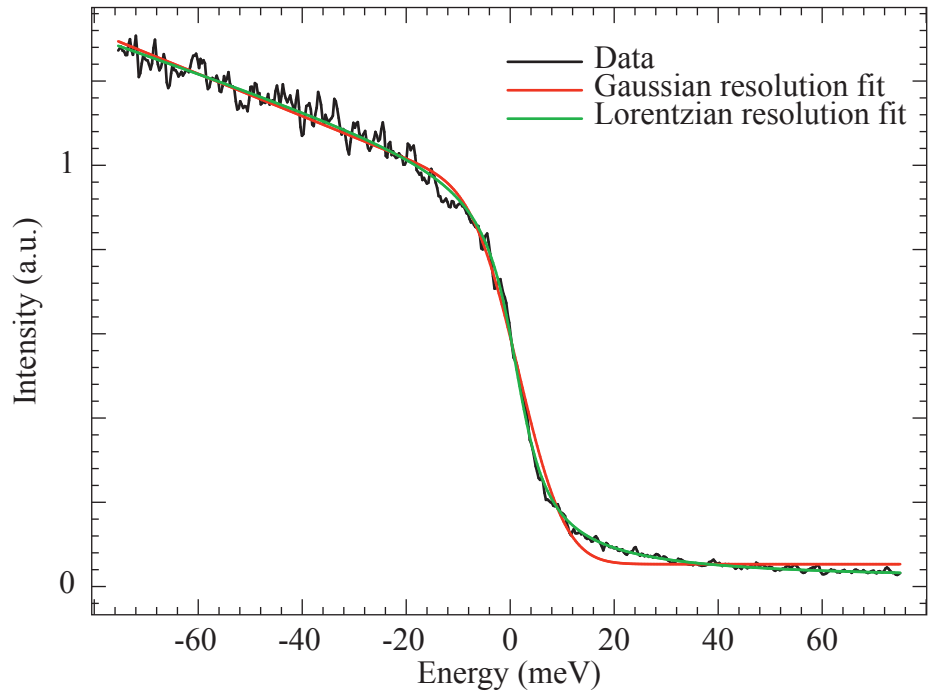


Figure 3.7: Energy resolution test in LAD, on gold at 9.7 K, showing the Fermi edge integrated across the detector after image warping corrections (black) as well as fit results assuming Gaussian (red) and Lorentzian (green) resolutions.

3.2. Energy resolution

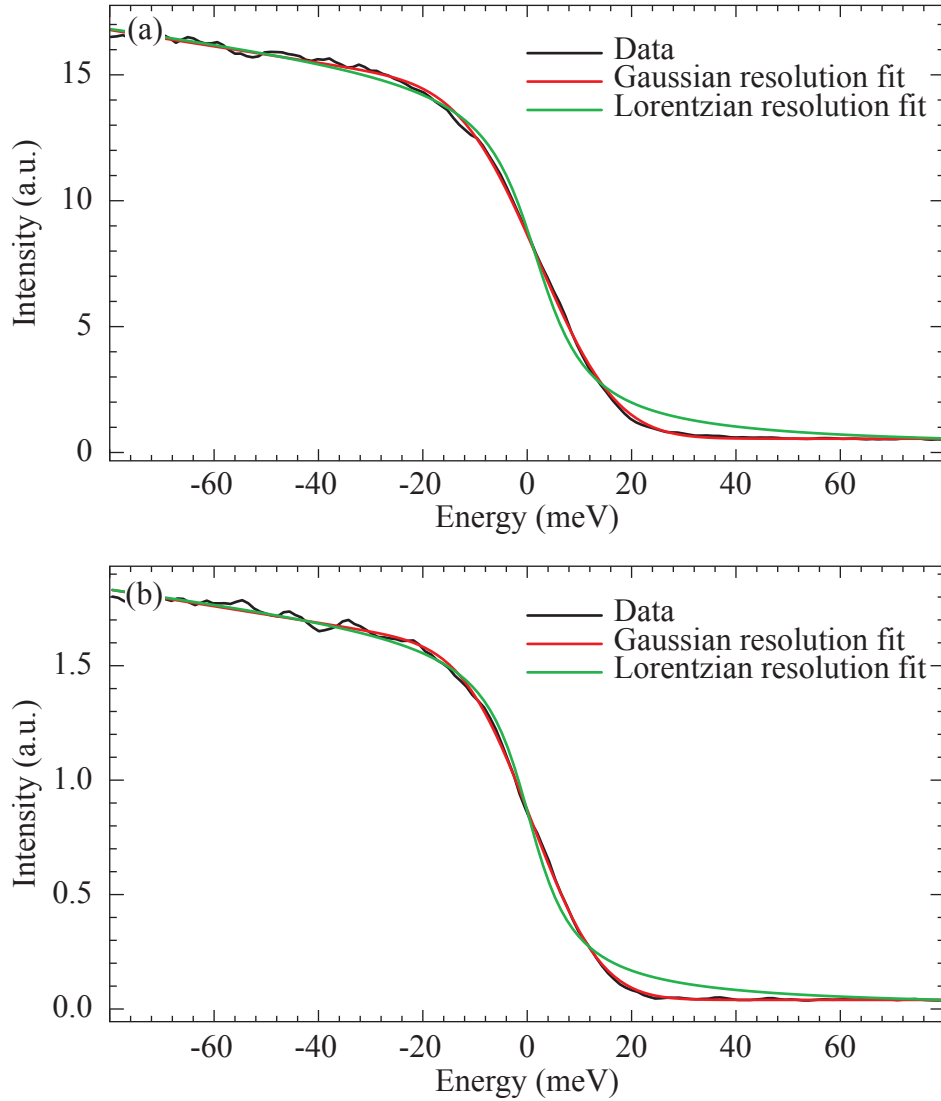


Figure 3.8: Energy resolution test in WAM, on gold, showing the Fermi edge integrated across the detector after image warping corrections (black) as well as fit results assuming Gaussian (red) and Lorentzian (green) resolutions. (a) shows the tests corresponding to data shown in Fig. 4.3 on gold at 8.5 K; (b) shows the tests corresponding to data shown in Fig. 4.10 on gold at 5.0 K.

3.2. Energy resolution

the gold data thereby provides a direct measurement of the instrumental resolution directly at the Fermi energy for the exact analyzer parameters and sample position as used.

The gold data taken to characterize the energy resolution for Figs. 4.8 and 4.9 is presented in Fig. 3.7. This data was taken in LAD, with slit 6 (0.5 mm, curved) and $E_{\text{pass}} = 3 \text{ eV}$; this corresponds to a nominal energy resolution of 5 meV, according to Eq. 3.3. At the sample temperature of 9.7 K ¹² the Fermi edge should have an inherent width from 90% to 10% of 3.67 meV. In order to determine the instrumental resolution, a least-squares [53] fit was performed on the data, where the model function consisted of a linear occupied state times a 9.7 K Fermi function with background, convolved with instrumental resolution of both Gaussian (red curve) and Lorentzian (green curve) form. The background, slope of the occupied states, and instrumental resolution were fit parameters, with the temperature held fixed. From the fit results it appears that the instrumental energy resolution in this mode may be better described by a Lorentzian than a Gaussian form, which is interesting, as Gaussian resolutions are usually assumed. The FWHM resolution values thus extracted were 9 meV, assuming Lorentzian, or 16 meV, assuming Gaussian. By either measure the resolution is greater than that nominally specified in the manual, by a factor of two to three.

In Fig. 3.8 we present some of the gold Fermi edges used to characterize energy resolution for the WAM Fermi surfaces presented in Chapter 4. As for the LAD test the gold image was first corrected and then integrated across the detector. Panel (a) is the measurement taken along with Fig. 4.3, on gold at 8.5 K, while (b) shows that corresponding to Fig. 4.10, on gold at 5.0 K. Both images were taken using slit 6 (0.5 mm, curved) and a pass energy of $E_{\text{pass}} = 12 \text{ eV}$ for a nominal resolution of 20 meV. In this case we find that the Gaussian provides a better-looking fit, although again neither form is perfect. For (a) resolutions found from these fits are 28 meV (15 meV); (b) gives 24 meV (13 meV) for Gaussian (Lorentzian) forms. Other gold measurements taken in WAM give similar results for resolution values and the appearance of Gaussian vs. Lorentzian forms.

¹²9.7 K times the Boltzmann constant is $\sim 0.84 \text{ meV}$.

From these (somewhat limited) measurements it appears that, for nominal energy resolutions ~ 20 meV in WAM, the resolution is close to Gaussian and similar to that expected from the slit selection and analyzer pass energy. However, in LAD and with nominal energy resolutions ~ 5 meV, the energy resolution may not be as expected in either form or width. Regardless of specified resolution, it is good practice to verify the resolution with a gold measurement for every data set.

3.3 Event counting

The final electron detection of our system consists of a double-layer multichannel plate¹³ to amplify the electron signal, followed by a phosphor screen and digital camera. An electron entering the multichannel plate sets off a cascade of further electrons, which lights the phosphor screen and is ultimately recorded by the camera.

An image highlighting the properties of single-electron events is presented in Fig. 3.9 (this data was taken using gas cell photoemission by SPECS to test energy resolution during the initial analyzer commissioning). Ideally, each electron that hits the detector would be recorded as a single event at a precise location. However, owing to variations (perhaps in how far electrons make it into the multichannel plate before triggering a cascade) the overall scale of each electron event is generally recorded with a different brightness, which can be seen in the inset of panel (a) and again in Fig. 3.10(a). Further, each event generates a dim halo with a diameter of approximately 20 pixels¹⁴. This halo can be seen in Fig. 3.9 (a) around the main spectral feature and also in (b) as the “tails” extending on both sides of the integrated image. Although the origin of these tails was initially unclear, they have remained with similar size on both cameras used on the system and additionally could be observed to occur around the large number of events generated by a flaw that later developed on the multichannel plate

¹³Arranged in a chevron shape, such that electrons cannot pass all the way through without hitting the side of a channel.

¹⁴Diameter ~ 20 pixels on the old 640×480 camera, which has since been upgraded.

3.3. Event counting

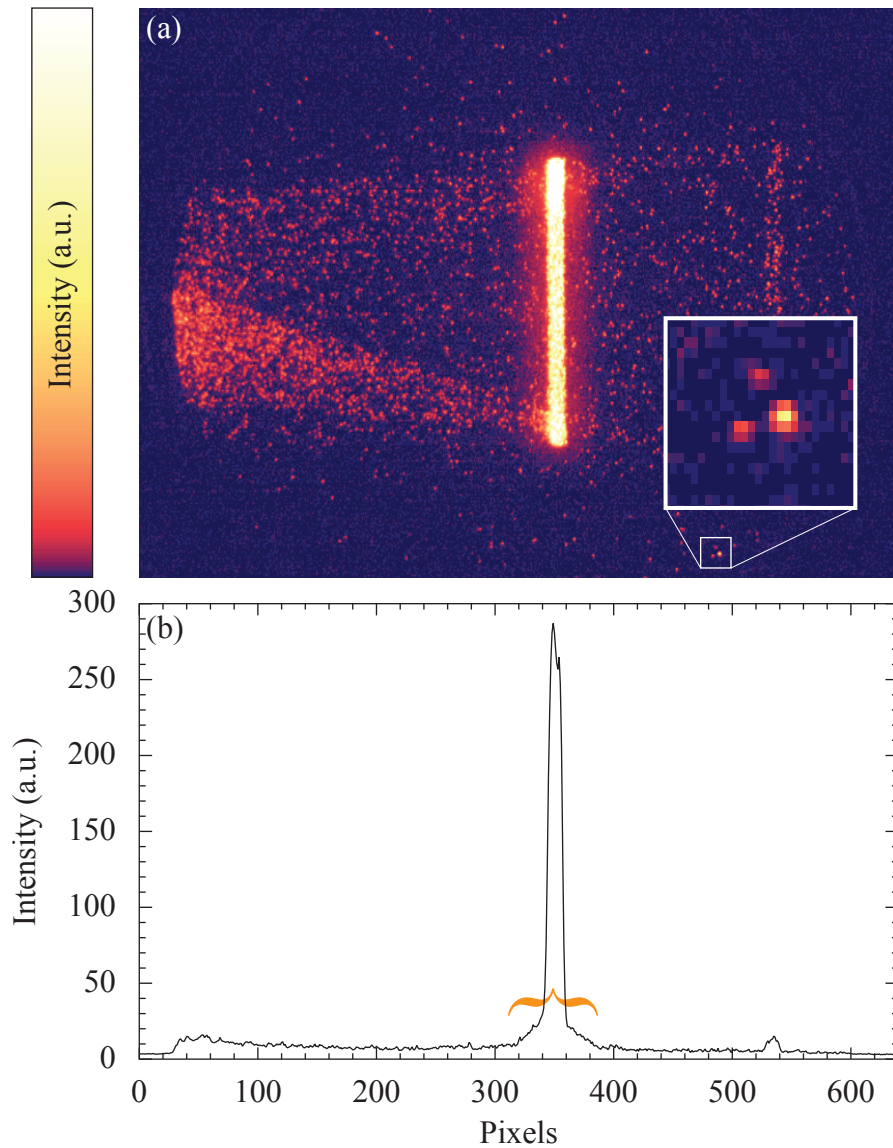


Figure 3.9: Gas cell photoemission image demonstrating the form of electron events. (a) entire image, with colour scale stretched such that the “tail” from electron events, when integrated over many counts, is visible as a faint halo around the main spectral feature. Numerous single-electron events are visible on the detector screen, with three showing different intensity levels highlighted in the inset. (b) integration across the detector, with an orange brace marking the “tails” around the main spectral feature.

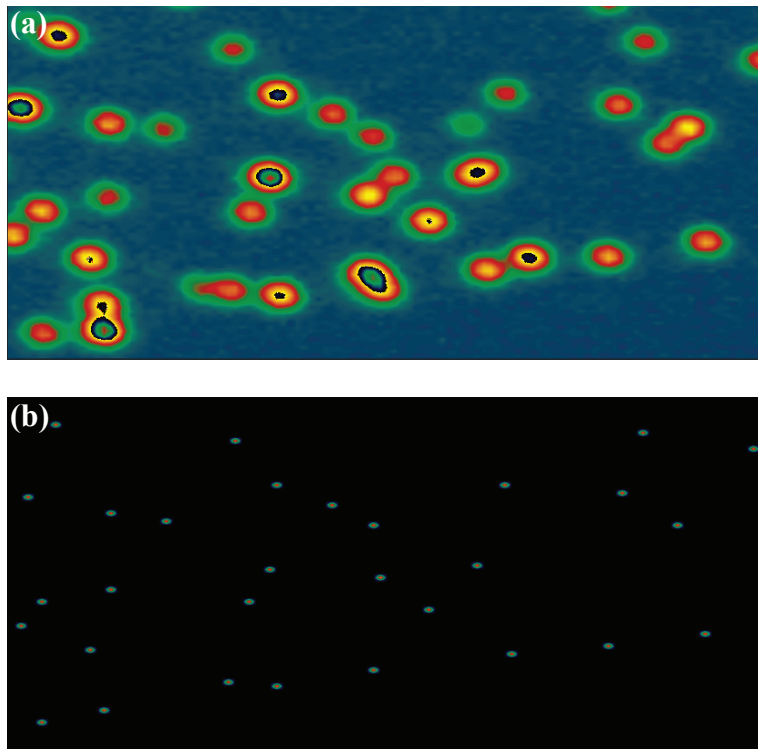


Figure 3.10: A zoom-in on a group of events before (a) and after (b) the application of a single-event filter.

3.3. Event counting

(thought to be a speck of dust). For these reasons the tails must be due to either the multichannel plate or the phosphor screen.

Regardless of their origin, the presence of these “tails” can cause spurious data, especially when trying to characterize a Fermi edge or spectral feature shape. In order to eliminate this problem, a single event filter was developed and applied to single images taken with fast acquisition times, such that few events were recorded to overlap. This routine would transform the image into islands of equal value for everything above a given threshold, and then further reduce it to single values of 1 at the centre of mass of each island. The results of this filter are illustrated in Fig. 3.10. Although occasional events were missed, either because they were too faint or because two events touched, this filter effectively reduced the camera image to a map of where each electron fell. Unfortunately, although the filter itself was reasonably fast, getting images from the camera itself proved to be a major bottleneck: with reasonable count rates the camera could not provide images fast enough, and camera dead-time accounted for a reasonable fraction of total experiment time. Given that many ARPES experiments are limited by sample life, this technique was not an option. Instead the camera was able to threshold multiple exposures and sum them at the hardware level, before sending a final image representing these multiple exposures. Given the correct choice of dwell time per exposure (such that not too many tail features overlapped) and threshold (such that only the tails were removed) the final image sent by the camera would be free of tails, and, with high enough statistics, the differing relative brightness of each electron event would average out.

All data presented in this thesis (with the exception of that to illustrate the tails) was taken such that the problem of tails was eliminated through camera thresholding. It is important, especially if detailed information about spectral shape is desired, to verify on a sample image that each exposure taken will be in the non-overlap regime and have the proper threshold applied.

3.4 Functional forms and a comparison of different measures

Sometimes, for clarity, it is best to simply set out the functional forms used. The Gaussian form used is as follows:

$$G(x) = \frac{A}{\sigma\sqrt{2\pi}} e^{-\frac{(x-x_0)^2}{2\sigma^2}}, \quad (3.4)$$

which is centred at x_0 , has area A (set to unity, based on step size, when doing a numeric convolution), and has standard deviation σ . For a Gaussian, σ is related to the FWHM and half width at half maximum (HWHM) according to

$$\begin{aligned} \text{FWHM} &= 2\sqrt{2\ln 2} \sigma \approx 2.35 \sigma \\ \text{HWHM} &\approx 1.18 \sigma \\ \sigma &\approx 0.426 \text{ FWHM} \\ \sigma &\approx 0.847 \text{ HWHM}. \end{aligned} \quad (3.5)$$

The Lorentzian form used is as follows:

$$L(x) = \frac{A}{\pi} \frac{\Gamma/2}{(x-x_0)^2 + (\Gamma/2)^2}, \quad (3.6)$$

which is centred at x_0 , has area A , and has FWHM Γ (the standard deviation of a Lorentzian is undefined).

Although a true convolution was used in this chapter, an energy resolution rule of thumb exists: often, to get a rough estimate of instrumental energy resolution, the width of a (low-temperature) Fermi function from 10% to 90% is taken to be the FWHM resolution. Convoluting a Gaussian with a step edge shows that, for a Gaussian, this is not a bad approximation. For a Gaussian with FWHM= 1, 90%/10% happens at ± 0.544 , for a difference of ~ 1.09 (an overestimation of $\sim 9\%$). However, the same treatment with a Lorentzian (which has much larger tails) results in ± 1.54 , for a difference of ~ 3.08 and an overestimation by a factor of 3. This is illustrated in Fig. 3.11.

3.4. Functional forms and a comparison of different measures

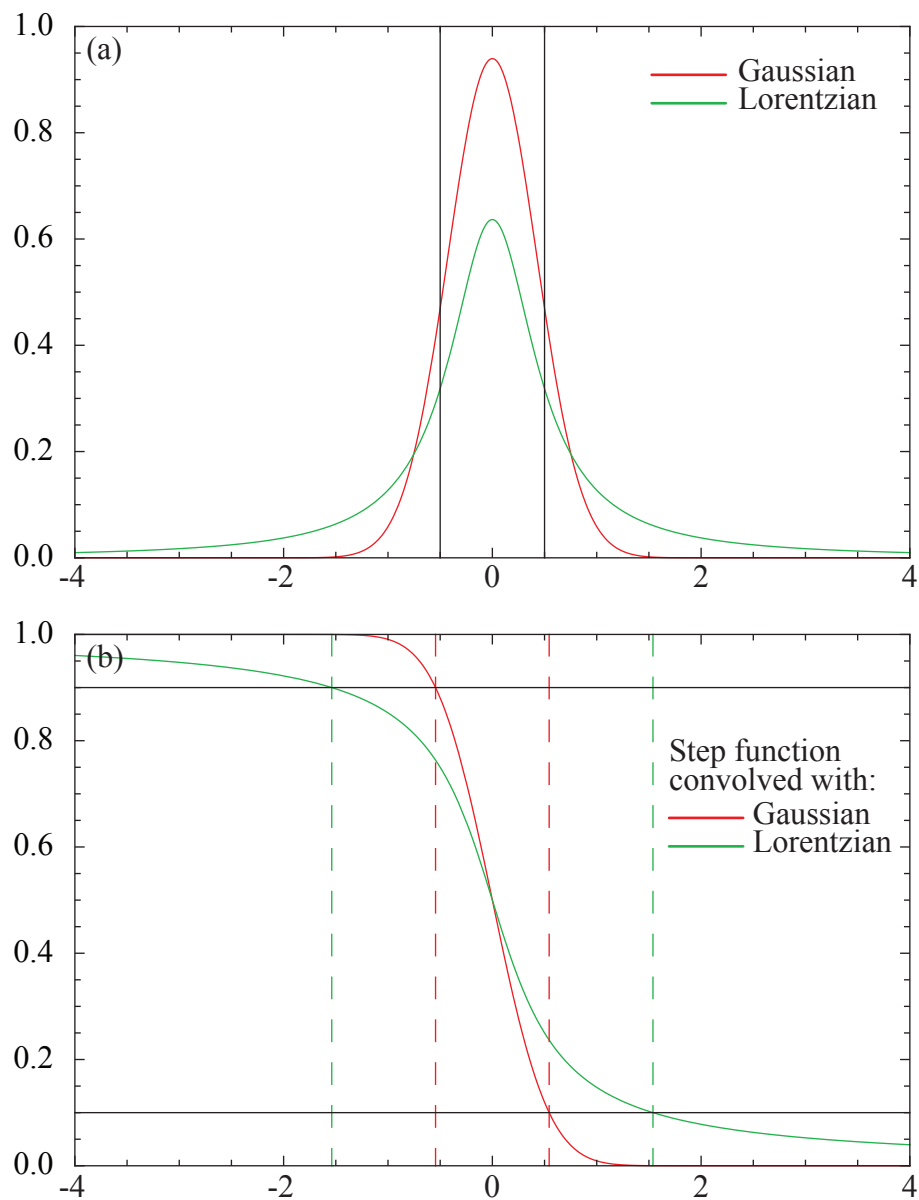


Figure 3.11: A comparison of Gaussian (red) and Lorentzian (green) functions. (a) Gaussian and Lorentzian functions with unit area and FWHM, with the FWHM outlined in black. (b) the results of convolving these functions with a unit step function, with lines marking 10% and 90% height.

Chapter 4

ARPES on Sr_2RuO_4

Since its discovery [13], superconductivity in Sr_2RuO_4 has received enormous attention in the attempt to understand not only the superconducting but also the normal state from which superconductivity arises. In the study of the normal state a unified picture of the Fermi surface (FS) was obtained from bulk-sensitive de Haas–van Alphen (dHvA) measurements [14, 54, 55], surface-sensitive angle-resolved photoemission spectroscopy (ARPES) [56], and local-density approximation (LDA) band structure calculations [17, 57]. Agreement with the latter could only be obtained with the inclusion of spin–orbit (SO) coupling, establishing its importance in the description of the low-energy electronic band structure¹⁵. This agreement between bulk and surface probes was not easily reached – ARPES initially revealed a different electronic structure than the bulk [56, 58], a result explained by a surface reconstruction also observed via low-energy electron diffraction (LEED) [59–61]. However, in our own ARPES measurements here at the University of British Columbia (UBC) with improved angular resolution and vacuum conditions, we began to regularly detect additional dispersive features not explained by this model – a result also found in another recent ARPES study that presented no definitive explanation but suspected a surface state driven by electronic interactions [16]. As in the case of topological insulators, the presence of SO coupling raises the possibility that these features may be due to novel topological states, Dirac or Rashba-type, that might exist on the (001) cleaving surface of Sr_2RuO_4 in the normal state (in addition to the chiral superconductivity topological edge-states detected below T_c on the side surfaces [62]). These new revelations and possibilities demanded that

¹⁵SO coupling may also lie at the root of the larger question regarding the nature of the pairing in Sr_2RuO_4 , which is explored in more detail in Chapter 5.

this simple model of surface reconstruction be revisited.

In this chapter I will first discuss these additional features in contrast to those attributed to the previously accepted electronic structure from a bulk and reconstructed surface in § 4.1, before detailing the efforts made by our group to unravel their nature. These efforts included high-resolution mapping to determine the extent of previously unnoticed features and their characteristics, discussed in § 4.1.1; ruling out the possibility of a relationship to ruthenium metal inclusions¹⁶ discussed in § 4.1.2; time resolved surface degradation discussed in § 4.1.3; the use of polarized light to determine the symmetry of the underlying wave-functions discussed in § 4.1.4; and finally a comparison to related folding in the Bi-cuprates in discussed § 4.1.5. These efforts were combined with the examination of a variety of different possible structural distortions through LDA bulk and slab band structure calculations discussed in § 4.2. The culmination of these efforts allowed us to rule out novel phases driven by electronic interactions such as Dirac and Rashba-type states or surface magnetism and instead conclude that a surface reconstruction was still responsible for the additional features but that this reconstruction was not limited to the surface layer alone. We found that there exists a progressive reconstruction whereby both the surface and (at a minimum) the sub-surface layer both undergo similar reconstructions, differing in magnitude as the crystal structure relaxes progressively toward that of the bulk. This work resulted in a publication [6] that drew on many aspects of the work presented here but left out much detail in the avenues explored for brevity’s sake.

4.1 Bulk band structure, Fermi surface, and “extra” bands

The bulk crystal structure of Sr_2RuO_4 is precisely known from x-ray [63], as well as both single-crystal [64] and powdered [65–67] neutron diffraction. Sr_2RuO_4 is the single-layer member of its perovskite family (SrRuO_3 being

¹⁶The so-called 3K phase – a common growth defect.

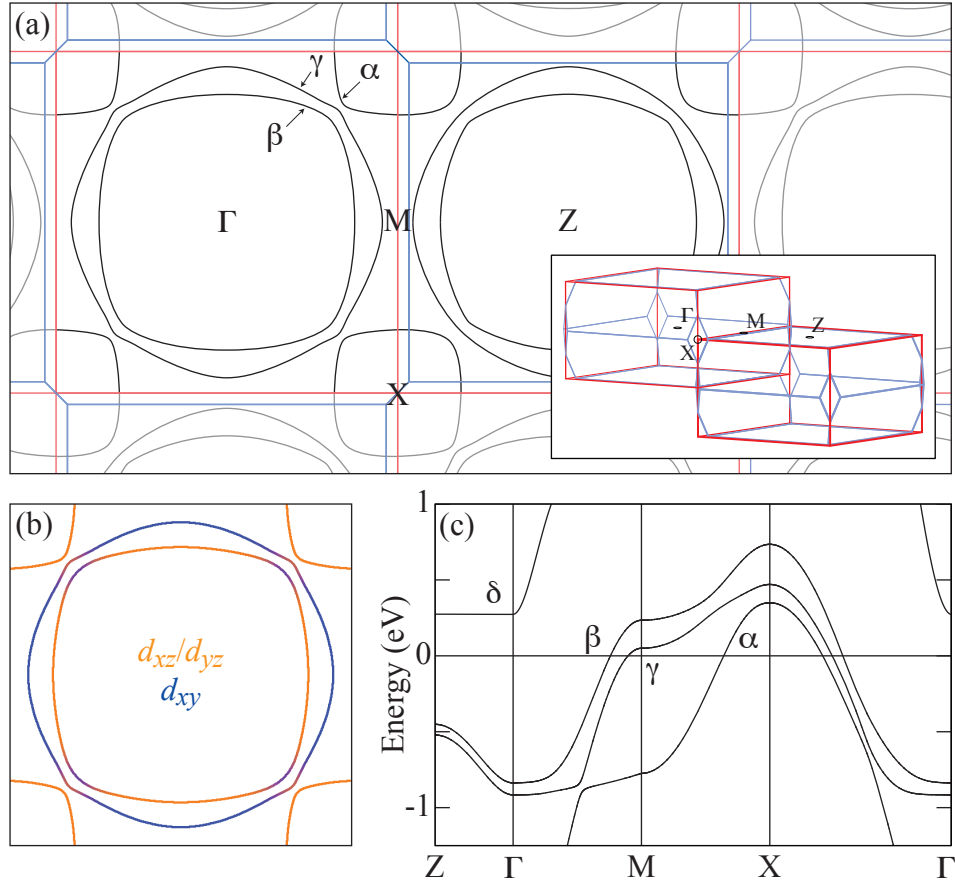


Figure 4.1: The near-FS bulk band structure of Sr_2RuO_4 from LDA+SO, with α , β , γ , and δ bands as well as Γ , M , X and Z BZ positions labelled. (a) the $k_z = 0$ FS across multiple BZs in black, with the primitive and conventional BZ boundaries shown in blue and red, respectively; the inset shows the shapes of the primitive BCT and conventional unit cell in 3D momentum space. (b) orbital character of the α , β , and γ bands at the $k_z = 0$ crossing. (c) band dispersions along the high-symmetry cuts through momentum space.

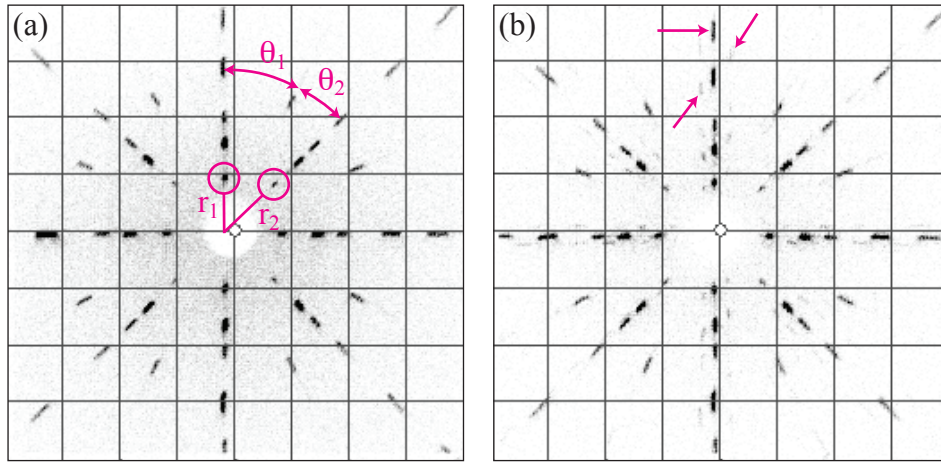


Figure 4.2: Laue diffraction pattern for sample alignment on Sr_2RuO_4 . Panel (a) shows a single crystal aligned with the a and b axis horizontal and vertical. This orientation will produce ARPES oriented similar to Fig. 4.3 (for example). To achieve this orientation (as opposed to 45° rotated) note that $r_1 < r_2$ and $\theta_1 > \theta_2$. Panel (b) shows a multi-faceted crystal, with additional diffraction patterns visible, as indicated with arrows. Such a sample should not be used.

the infinite-layer and $\text{Sr}_3\text{Ru}_2\text{O}_7$ the bi-layer compound). It has a single layer of (vertically) distorted oxygen octahedra centred on ruthenium atoms, with strontium in the gaps formed by their apical oxygen. These layers are offset-stacked, forming a natural (and charge-neutral) cleavage plane in between the Sr–O layers, which is sketched in Fig. 4.15.

The near-FS bulk electronic structure derives from the Ru t_{2g} orbitals, and is occupied by four electrons per unit cell. The quasi-1D d_{xz} and d_{yz} bands hybridize at their crossings to create the electron-like β and hole-like α pockets, while the roughly circular γ derives from the quasi-2D d_{xy} band. Just above the Fermi energy at the Γ point there lies the δ pocket of $d_{x^2-y^2}$ character, as illustrated in Fig. 4.1. Because of the body-centred tetragonal (BCT) crystal structure, the primitive Brillouin zone (BZ) unit cell has an offset stacking as illustrated in Fig. 4.1 (blue); however, for simplicity a conventional cubic BZ (red) is generally used, which results in neighbouring cells having different k_z values in the same $k_x - k_y$ plane. [For example, at $k_z = 0$ we find the Γ point at $(0, 0)$ and the Z point at $(2\pi, 0)$.] In this thesis I will use the conventional unit cell, as is done in most published works on Sr_2RuO_4 .

Although, in the bulk, there is no tilting or rotation of the oxygen octahedra (which would be seen by diffraction experiments) those in the surface layer are known to rotate about the c -axis, which causes a $(\sqrt{2} \times \sqrt{2})R45^\circ$ reconstruction of the primitive cell, as seen by surface-sensitive experiments such as ARPES [6, 56, 58, 68, 69] and LEED [59–61, 70, 71]. Additionally, it is likely that there are dimensional distortions along the c -axis in (at least) the topmost layer. As always, estimates of the true value for all these dimensions vary.

ARPES experiments were performed at the University of British Columbia using our SPECS Phoibos 150 analyzer and the 21.22eV He I spectral line from a monochromatized UVS300 discharge lamp, over a variety of polarizations. For dispersion mappings typical energy resolution is measured as 9 meV and angular resolution as 0.4° over a window of $\sim 14.5^\circ$ (equivalent to $\sim 0.04 \frac{\pi}{\sqrt{2}a}$). For Fermi surface mapping typical energy resolution was measured to be 17meV and angular resolution 0.1° over a window of $\sim 29^\circ$

(equivalent to $\sim 0.01 \frac{\pi}{a}$). Samples were examined for defects and oriented using Laue diffraction (see Fig. 4.2) and cleaved in situ. During measurement orientation was controlled by our two-rotation-axis cryogenic manipulator (rotation available parallel and perpendicular to analyzer entrance slit), with temperatures held between 5 and 10 K and pressures varied in the $5 - 9 \times 10^{-11}$ mbar range. The high-quality single crystals used in this study were grown by the floating zone method with Ru self-flux [72, 73] (see also § 4.1.2).

4.1.1 Additional features found

We begin our description of the new features with a brief review of the FS one would expect to measure based on the previously accepted electronic structure from a bulk and reconstructed surface. In Fig. 4.3(a) these bands are shown as calculated by LDA+SO; these predictions has been verified by both ARPES [56] and dHvA [14, 54, 55, 74, 75]. This is a portion of the same FS, as shown earlier in Fig. 4.1. If the oxygen octahedra are rotated, as has been observed for the surface layer of Sr_2RuO_4 by LEED [59, 60], this causes a $(\sqrt{2} \times \sqrt{2})R45^\circ$ reconstruction of the BZ [shown in Fig. 4.3(b) for a 5.5° rotation, which demonstrates the observed surface topology using bulk LDA calculations]. This reconstruction causes folded replicas (dotted line) of each original unfolded band (solid line) to appear mirrored across the new BZ boundary (dashed line). Because of the shallow dispersion at $(\pi, 0)$ (and points related by symmetry), this modulation also changes the topology of the γ sheet from circular electron-like to lobed hole-like. In these panels we also begin using the subscript s to refer to surface-like states, b to refer to bulk-like states, and primes to indicate folded bands. Measuring with ARPES, one might expect a superposition of panels (a) and (b), as shown in panel (c); with sufficient resolution, bands from both surface and bulk would be visible as an apparent doubling for the case of unfolded bands (and unfolded bands only, as there should exist no folded bulk bands).

In panel (d) we present a FS map over the entire upper right quadrant of the BZ from a pristine cleave of Sr_2RuO_4 , obtained by integrating ARPES

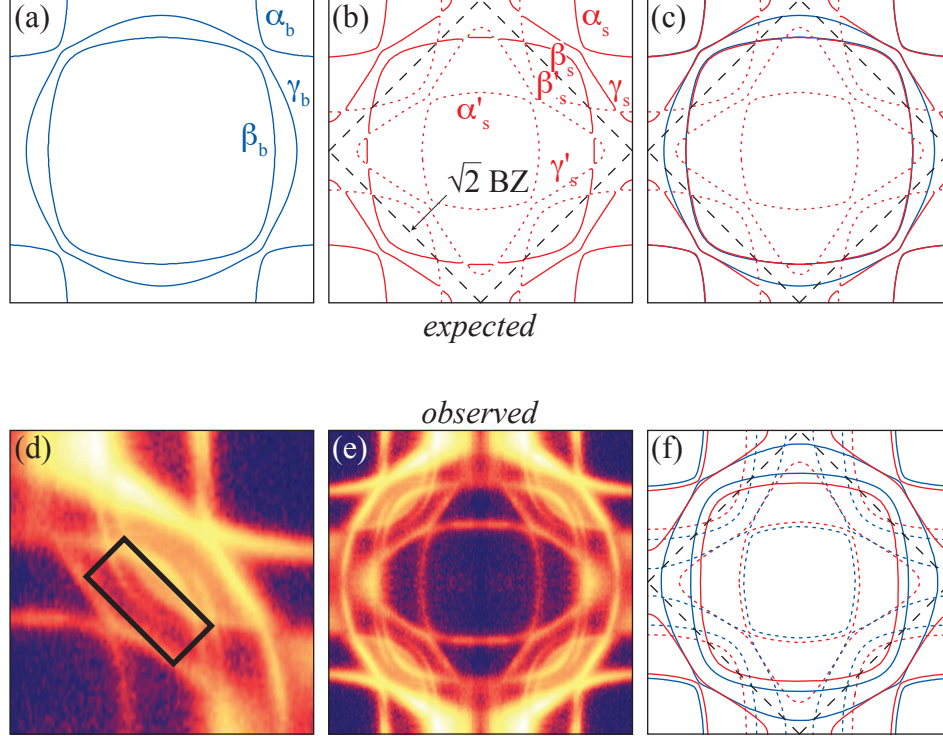


Figure 4.3: (a–c) The previously expected FS of Sr_2RuO_4 as would be measured by ARPES based on LDA+SO at $k_z = 0$. The FS of the (a) undistorted bulk and (b) bulk with RuO_6 octahedra rotated 5.5° causing a $(\sqrt{2} \times \sqrt{2})R45^\circ$ reconstruction (new BZ – dashed; unfolded FS – solid; folded replica FS – dotted) should combine to give (c). (d) shows the upper right quadrant of the FS as measured by ARPES, in p -polarization (parallel to incidence/emission plane), on a fresh low-temperature cleave. (e) reconstructs the entire FS by folding this image, while (f) shows a phenomenological FS based on (e), Figs. 4.4, 4.8, and 4.9. The most obvious outstanding unexplained feature, the double-folded β band, is highlighted with a rectangle in (d).

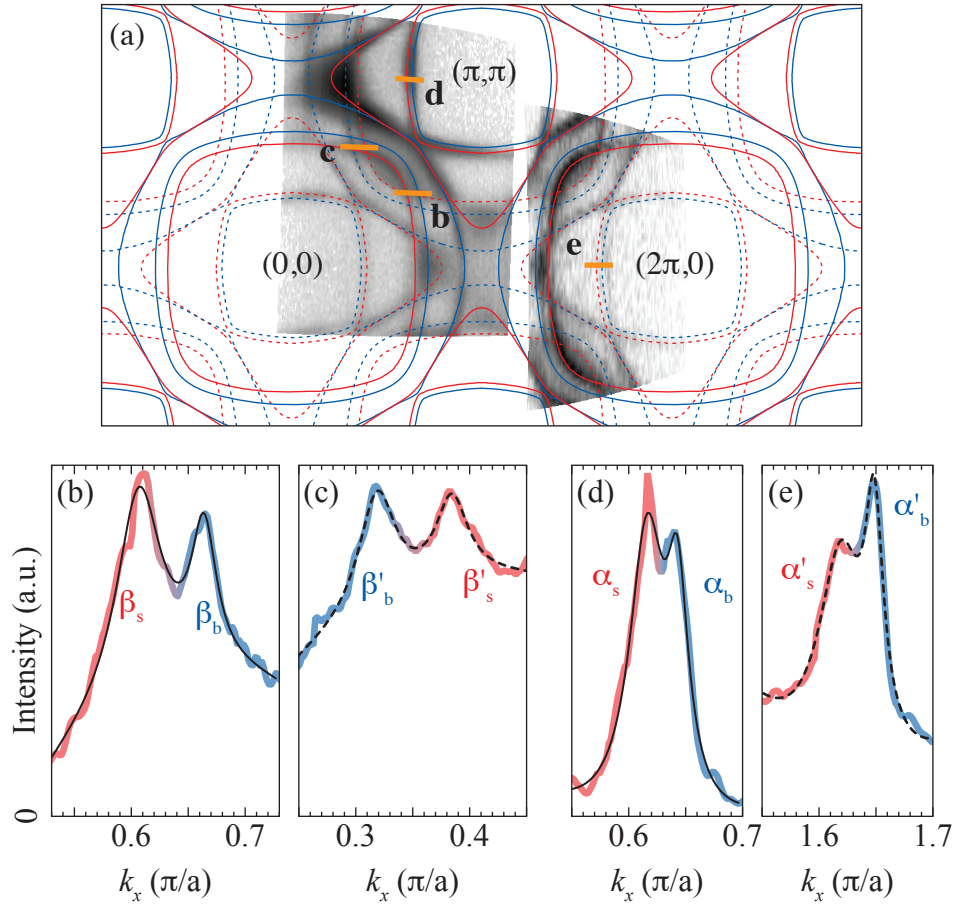


Figure 4.4: (a) Sr₂RuO₄ FS maps (greyscale) marking the location of MDC cuts at the Fermi energy, showing clear doubling in the (b) β sheet, (c) its folded replica β' , (d) α , and (e) folded α' . (b–e) Data is shown in colour, with red and blue referring to surface and bulk-like features, respectively, while fit results (see text) are shown in black (dashed lines for folded bands).

intensity over a 7meV region. This data set was taken in less than 3 hours after the cleave, during which time the sample was maintained at low temperature in ultra-high vacuum (6×10^{-11} mbar) and no significant aging was observed. The data was integrated over a 7 meV region around the Fermi energy and transformed into k -space without symmetrization. The size of the BZ was then determined from a wider-angle-scan which included data across more than one complete BZ at lower resolution and statistics, allowing the high-resolution image to be cropped and reflected about $(-\pi, 0)$ – $(\pi, 0)$ and $(0, -\pi)$ – $(0, \pi)$ to reproduce the entire BZ as shown in panel (e). The analyzer entrance slit was oriented horizontally with respect to the final image, giving greater angular resolution in that direction. One can immediately see an apparent doubling of many features, as well as γ bands with similar topology to both γ_b and γ_s [with γ_s showing clearly near $(0, \pi)$ and γ_b near $(\pi, 0)$ owing to varying matrix element dependence]. Much of this FS could be understood using the existing model of photoemission from both bulk and a reconstructed surface layer. However, contrary to this explanation, the folded β' is clearly doubled as well, with both a β'_b and β'_s visible, as highlighted with a rectangle in panel (d). We will show in Fig. 4.4 (and additionally in Fig. 4.8) that in fact *all* bands are doubled – both unfolded *and* folded – which cannot be explained by the simple model of a reconstructed surface. These observed doublings are indicated in a phenomenological FS plot in panel (f), where we mark the position of all features visible to ARPES, based on all data collected.

In Fig. 4.4 we confirm the doubling of features with momentum distribution curves (MDCs) obtained by integrating a 10 meV region just above E_F : panels (b–e) show the doubling of β , β' , α , and α' , respectively, observed at the k -locations indicated in the alignment FS of (a). Note that the splitting between α'_s and α'_b is more clearly resolved in the second BZ [Fig. 4.4(e)], perhaps because of matrix element effects and/or the higher effective angular resolution in the second BZ. By performing a least-squares fit to two Lorentzian peaks with a second-order polynomial background (black curves), we can estimate the observed splittings as 0.057, 0.065, 0.027, and $0.029 \pm 0.003 \frac{\pi}{a}$ for β , β' , α , and α' , respectively. Although it is difficult to

compare these values directly, because of the slight difference in angles and k -space locations between them, we note that the splittings between β_s/β_b and β'_s/β'_b are very close and approximately double those between α_s/α_b and α'_s/α'_b , which are almost identical.

These doublings – particularly the existence of α'_b , β'_b , and γ'_b (demonstrated later) – do not fit into the previous model of a bulk and reconstructed surface. In the rest of this section we will explore the dependence of these features on the absence/presence of the 3K phase in §4.1.2, their degradation over time in §4.1.3, their polarization dependence in §4.1.4, and we will compare them to similar features in the Bi-cuprates in §4.1.5.

4.1.2 Exploring the 3K phase

The high-quality Sr_2RuO_4 crystals used in this work were grown using the coating zone method [73]. This method involves melting one end of a feed rod manufactured from RuO_2 and SrCO_3 powders in an image furnace, seeding this molten zone with an existing Sr_2RuO_4 single crystal, and then passing it slowly through the furnace while rotating the seed crystal and feed rods in opposite directions. Thus, a narrow molten zone travels along the feed rod, where it solidifies as a single crystal with the same orientation as the seed. The quality of the resulting crystal relies heavily on a nearly endless variety of growth parameters, including stoichiometry of the feed rod; growth atmosphere temperature, pressure, and composition; rotation and draw rates of both seed and feed rods; as well as melt temperature and size – in addition to endless possible post-processing operations. Crystal growth is its own field of research.

Of the observed defects that may be present in Sr_2RuO_4 crystals, the one that has arguably the greatest effect on its electronic structure is the so-called 3K phase, which is caused by small (on the order of microns) Ru metal inclusions embedded in the final crystal. In order to compensate for the relative volatility of Ru, higher-than-stoichiometric quantities are used in the growth rod. This can result in a gradient of Ru concentration in the melt, which produces pure Sr_2RuO_4 near the outer edges of the final rod

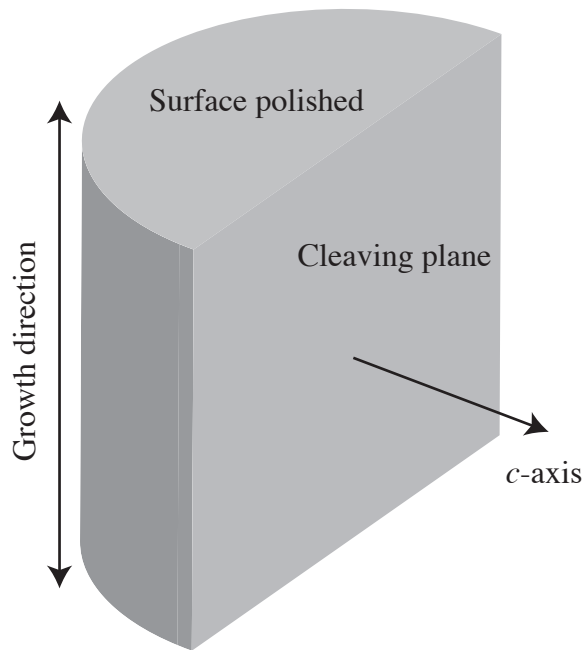


Figure 4.5: Orientation of the Sr_2RuO_4 single crystal that was polished to produce pieces with and without the presence of the 3K phase. The original growth rod was cut with a saw perpendicular to the growth direction and cleaved along the c -axis to mark that direction before polishing.

and a eutectic mix of Sr_2RuO_4 and Ru metal lamellae in the centre. These lamellae are approximately $1\mu\text{m}$ thick and on the order of $10\mu\text{m}$ in plane. The lamellae also tend to order into stripes, which can have long-range order over distances of millimetres, although the orientation with respect to the crystal axis of the underlying Sr_2RuO_4 is not unique and is known to vary within single-crystal samples [76]. In Sr_2RuO_4 samples with a high concentration of Ru metal¹⁷ lamellae, the superconducting temperature is enhanced from a sharp transition at 1.5 K to a broad transition up to 3.5 K, although the method of this enhancement remains unresolved [72, 76–78].

In order to ensure that the features observed in §4.1.1 were not somehow reliant on the presence or absence of the 3K phase, it was necessary to measure samples where the presence and quantity of 3K phase was known. It is possible to directly observe the 3K phase on polished samples using polarized light microscopy. In order to facilitate performing measurements on samples that would be identical other than the inclusion of 3K phase, we polished a cleaved growth rod end-on (on a face perpendicular to the growth direction, as shown in Fig. 4.5). The sample was glued to a polishing jig with crystal bond, which allowed the pressure used to be fine-tuned while holding the sample precisely perpendicular to the lapping surface. After polishing with progressively finer alumina grit suspended in water (down to $0.3\mu\text{m}$) the 3K phase became visible, as shown in Fig. 4.6. As expected, the Ru metal inclusions were concentrated toward the centre of the growth rod. This allowed the sample to be split into pieces and measured both with and without the 3K phase, as marked in Fig. 4.6.

In Fig. 4.7 we present ARPES FS data taken on these pieces. These data sets were taken in under 4.5 hours from the cleave in vacuum of $6 \times 10^{-11}\text{mbar}$, during which time no significant aging was observed. These FS images were generated by integrating a 4 meV region near the Fermi energy and transforming this data into k -space. In these images we can clearly see the presence of the mysterious doubling in both the pure and 3K phase samples, ruling out the possibility that the 3K phase is responsible. In fact, it is difficult (or perhaps impossible, although this has not been fully

¹⁷ $T_{c \text{ Ru}} = 0.49 \text{ K}$.

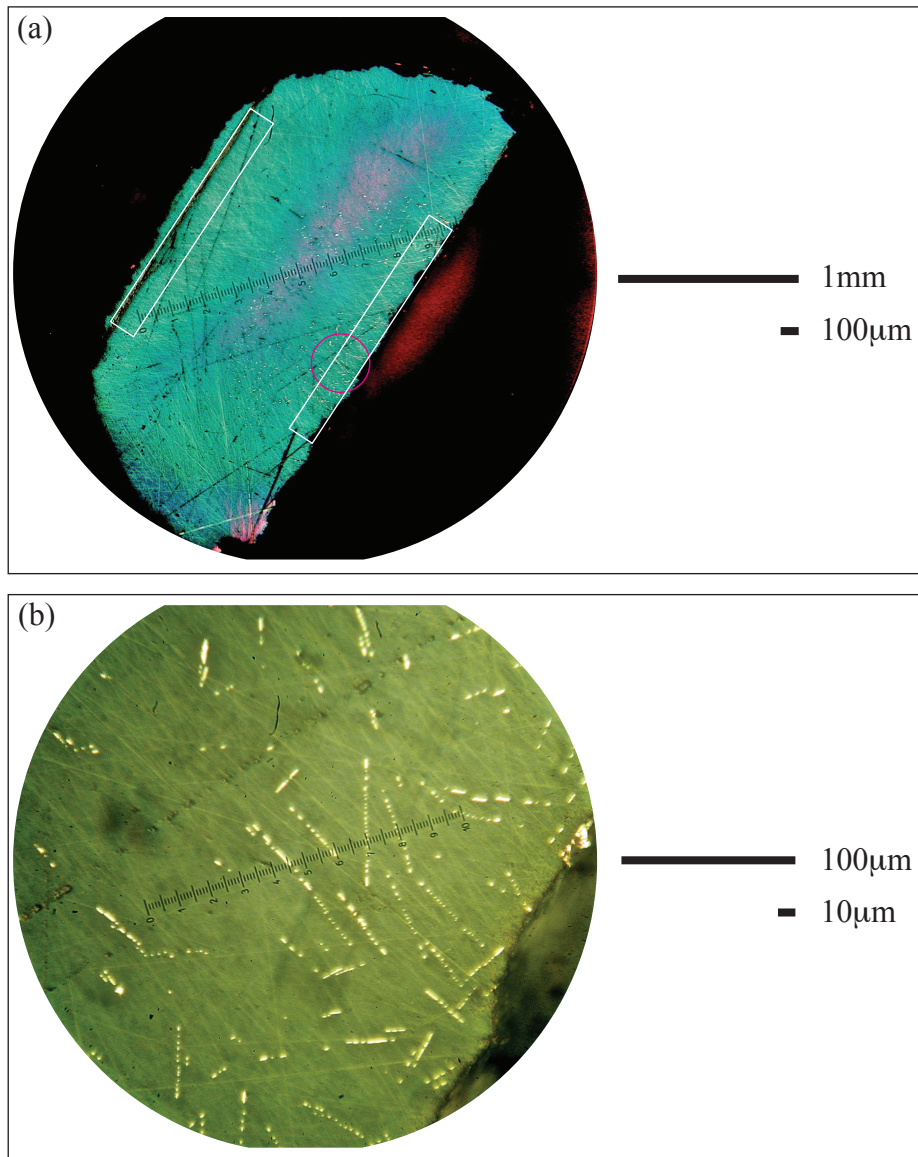


Figure 4.6: Polarized light microscopy image of the 3K phase (bright spots) in Sr_2RuO_4 , showing (a) the entire polished face and (b) a zoom-in on the region marked by a pink circle in (a). The locations of samples cleaved for measurements with and without 3K phase are marked in white on panel (a). Colour in these images is due to the use of a birefringent wave plate to increase contrast; under normal light the crystal is black.

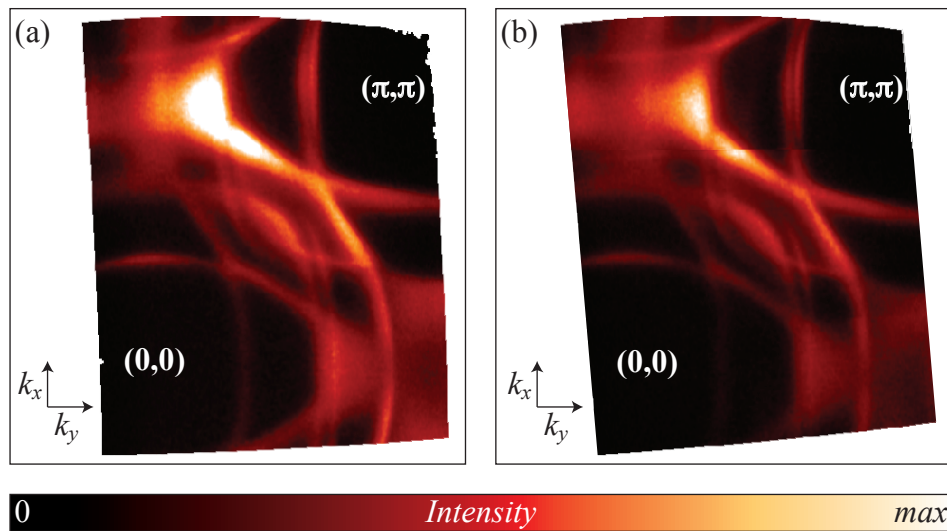


Figure 4.7: FS map of Sr_2RuO_4 as measured by ARPES on fresh samples both (a) without and (b) with the presence of the 3K phase. The discontinuity in (b) was caused by a discontinuity in the ϕ ($\sim k_y$) motion of the manipulator, not the sample; it was not reproduced in a smaller subsequent sweep through that region alone.

explored) to tell samples with or without the 3K phase apart using ARPES (at least at the quantity of ruthenium metal inclusions tested here). Despite the observed null-effect of the 3K phase on the existence of these features, all ARPES data presented in this thesis (aside from Fig. 4.7) was taken on samples inspected and known not to contain any 3K phase, lest it have some other unnoticed effect.

4.1.3 Time-dependent surface degradation and dispersion analysis

Thus far, with a doubling observed for all α and β bands, given no dependence on the 3K phase, and in light of the bulk magnetism of many Ru-oxides, one might be drawn to the possibility of Rashba-type effects [16] or even surface ferromagnetism [59]. If any of these were the case, one would expect that – under surface degradation – the surface states’ splitting would shrink and/or the intensity would decay uniformly over time for all of them, eventually revealing the underlying bulk electronic structure.

In Figs. 4.8 and 4.9 we show the results of such a time-dependent experiment performed over 16 hours on the band dispersion along the $(0, 0) - (\pi, \pi)$ direction, where all features and their folded replicas are visible simultaneously. This sample was maintained at 9.5 K while raising the base pressure to about 8.5×10^{-11} mbar. The time evolution of MDCs over the first 14 hours, integrated over 4 meV just above E_F in 100-minute intervals, is presented in Fig. 4.8(a). Panel (b) shows the location of the cut on the alignment FS, while (c,e,g) and (d,f,g) present the MDC, band map, and band map zoomed to the near- E_F region for the first and last 100-minute intervals. Fig. 4.9 shows the entire band map for each of these intervals, as well as an additional one showing the near-saturation of further degradation. While some features remain at a similar level of intensity during the degradation, others age and have their intensity suppressed, without any overall change in slope or shape. Particularly, comparing the panels representing the first and last 100-minute intervals in both Fig. 4.8 and Fig. 4.9, we can infer that (i) *all* bands and their folded replicas are doubled for a total of 12 bands

4.1. Bulk band structure, Fermi surface, and “extra” bands

(as labelled), including the γ bands not previously demonstrated in Fig. 4.4 and (ii) based on the observed difference in degradation rate, the electronic states do not all originate from the very same surface layer and can instead be classified as surface- (fast degradation) or bulk-like (slow degradation).

4.1. Bulk band structure, Fermi surface, and “extra” bands

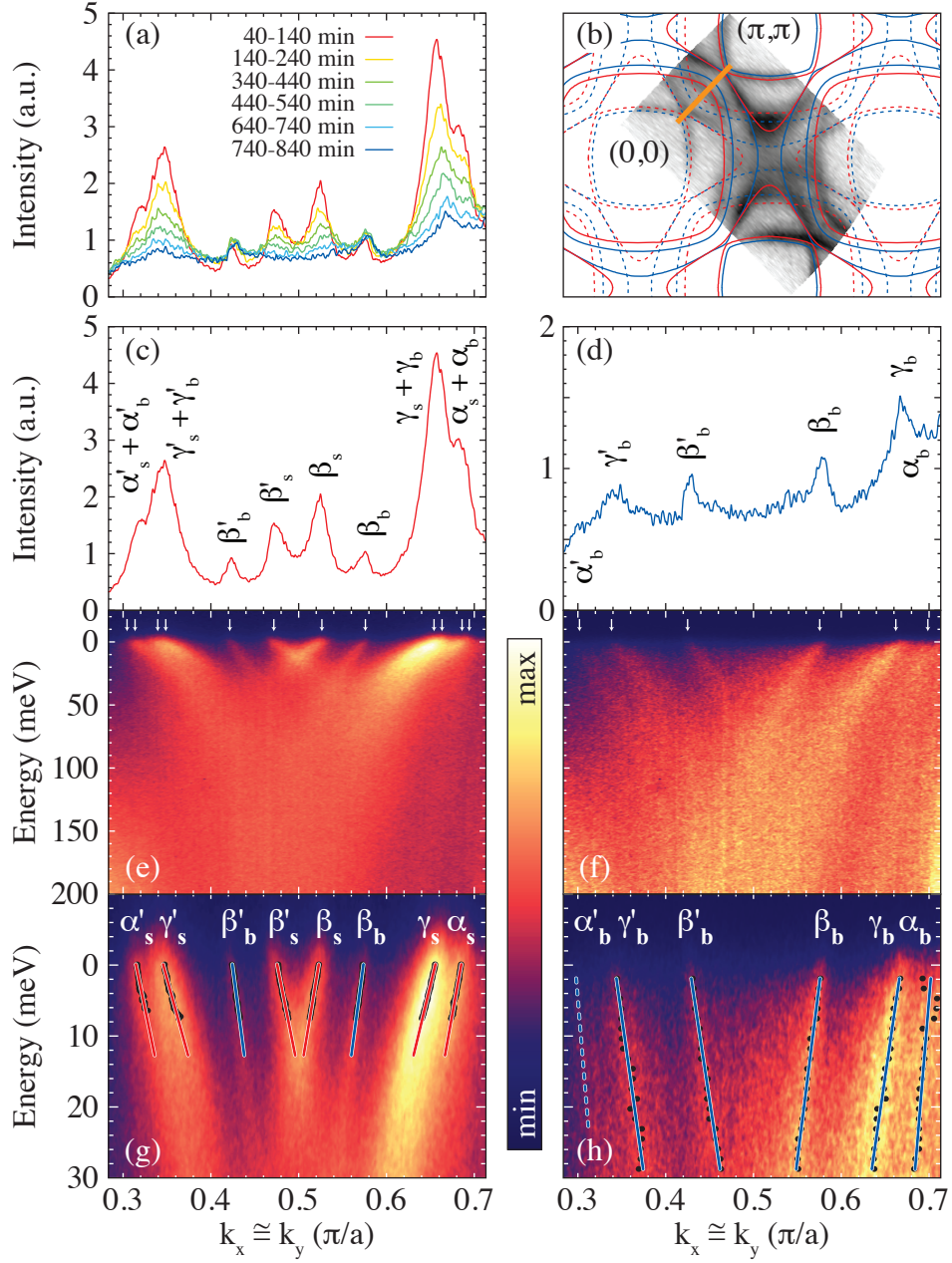


Figure 4.8: (a) time evolution of a 45° MDC cut at E_F ; its location is marked on the alignment FS in (b). (c,e,g) plot of MDC at E_F , band map of features on a large energy range, and zoom-in on the Fermi crossings, respectively, for the first 100 minutes after cleave; (d,f,h) the same for the final 100 minutes of acquisition. In (g,h), MDC maxima (black circles) and MDC-dispersion fits (blue – bulk; red – surface) are also shown. 78

4.1. Bulk band structure, Fermi surface, and “extra” bands

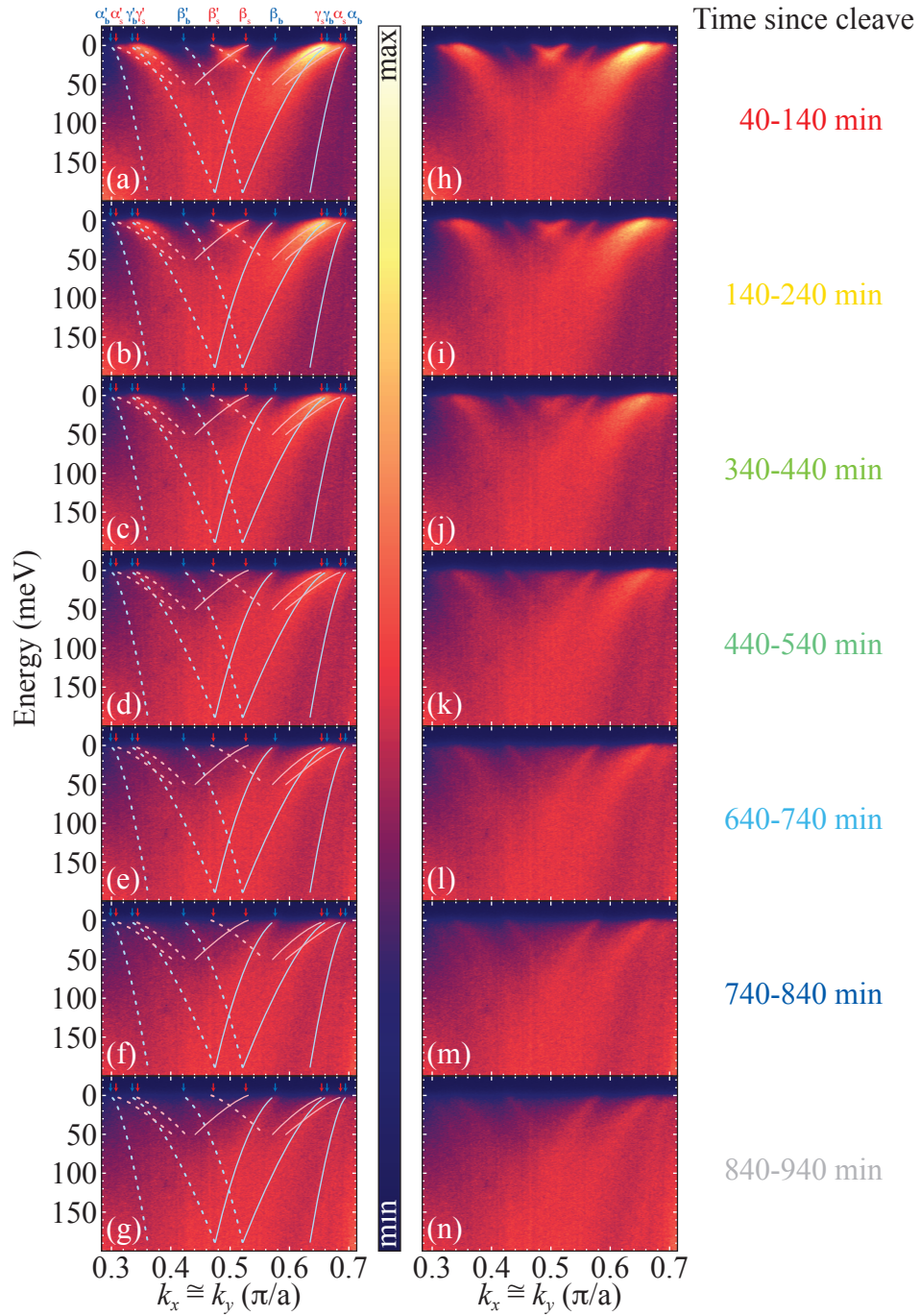


Figure 4.9: Band maps for all data in Fig. 4.8 both with guides to the eye (a–g) and without (h–n). Shown in (g,n) is an additional band map, which was omitted from Fig. 4.8 for clarity, as it is almost identical to (f,m). 79

Band	$n_e^{\text{LDA+SO}}$	$v_F^{\text{LDA+SO}}$ (eV Å)	n_e^{ARPES}	v_F^{ARPES} (eV Å)	$v_F^{\text{LDA+SO}}/v_F^{\text{ARPES}}$	n_e^{dHvA}
α_s, α'_s	1.668 ± 0.007	2.30 ± 0.01	1.721 ± 0.040	0.56 ± 0.05	4.1 ± 0.4	–
β_s, β'_s	0.864 ± 0.006	2.14 ± 0.01	0.757 ± 0.020	0.59 ± 0.05	3.6 ± 0.3	–
γ_s, γ'_s	1.340 ± 0.011	2.18 ± 0.02	1.396 ± 0.060	0.42 ± 0.05	5.2 ± 0.6	–
Total	3.872 ± 0.014	–	3.874 ± 0.120	–	–	–
α_b, α'_b	1.740 ± 0.003	2.14 ± 0.02	1.760 ± 0.040	1.30 ± 0.60	1.6 ± 0.8	1.781
β_b, β'_b	0.967 ± 0.022	2.60 ± 0.25	0.903 ± 0.020	0.80 ± 0.10	3.3 ± 0.5	0.921
γ_b, γ'_b	1.252 ± 0.014	2.21 ± 0.07	1.280 ± 0.060	0.76 ± 0.10	2.9 ± 0.4	1.346
Total	3.959 ± 0.026	–	3.943 ± 0.120	–	–	4.048

Table 4.1: Carrier concentrations counting electrons, $n_e = 2 \times A_{\text{FS}}/A_{\text{BZ}}$ (with 2 accounting for the spin degeneracy), and Fermi velocities along the $(0,0) \rightarrow (\pi,\pi)$ direction, v_F , as determined by our ARPES and LDA+SO slab calculations for surface- and bulk-like electronic structure. ARPES-FS volume estimates are from the phenomenological FS in Fig. 4.3; LDA+SO results were obtained for the 24 meV shifted chemical potential to match the average electron counting of surface and sub-surface FSs as determined by ARPES. The dHvA results from Ref. 55, representative of the bulk Luttinger’s counting, are also shown.

4.1. Bulk band structure, Fermi surface, and “extra” bands

These observations can be made more quantitative by doing an MDC-dispersion fit analysis, which allows us to distinguish between surface and bulk-like bands based on their remarkably different Fermi velocity v_F (see Tab. 4.1). While the fresh data in Fig. 4.8(g) are dominated by the surface α_s/α'_s , β_s/β'_s , and γ_s/γ'_s , with the addition of the well-separated β_b/β'_b pair, the aged data of Fig. 4.8(h) show only the much steeper bulk-like α_b/α'_b , β_b/β'_b , and γ_b/γ'_b (α'_b , although visible, could not be fit and is shown with a dashed line as a guide to the eye).

Since all s states are suppressed evenly and independently from the b states, we must conclude that no electronic interaction – ferromagnetism or Rashba coupling – is responsible for the apparent band doubling. Similarly, we must also rule out possible surface patches with different electronic structure or effective doping. The most natural explanation would be that the top surface layer is heavily modulated by the rotation of the RuO_6 octahedra and is responsible for all the s states, while the sub-surface layer is also modulated in a similar yet weaker fashion and is responsible for the b states; this lesser modulation would be enough to break the symmetry of the BZ and cause a visible folding but not enough to strongly modify FS topologies and volumes. Measured FS volumes [Fig. 4.3(c,d)] support this model: as shown in Tab. 4.1, while the s FS electron counting is somewhat reduced ($n_e^s \simeq 3.87$), the b FS electron counting is much closer to the dHvA results, adding up to $n_e^b \simeq 3.94$, i.e., almost four electrons, as expected in the Ru t_{2g} orbitals (this still seems to suggest the possibility that these near-surface layers are slightly hole-doped, possibly owing to the cleaving-induced Sr-vacancies revealed by scanning tunnelling microscopy [79]). Finally photoemission from a second layer, also folded but otherwise similar to the bulk, could even explain the so-called shadow band that remained after high-temperature cleaving had suppressed the surface states, in the original work uniting the dHvA and ARPES pictures of the FS of Sr_2RuO_4 [56].

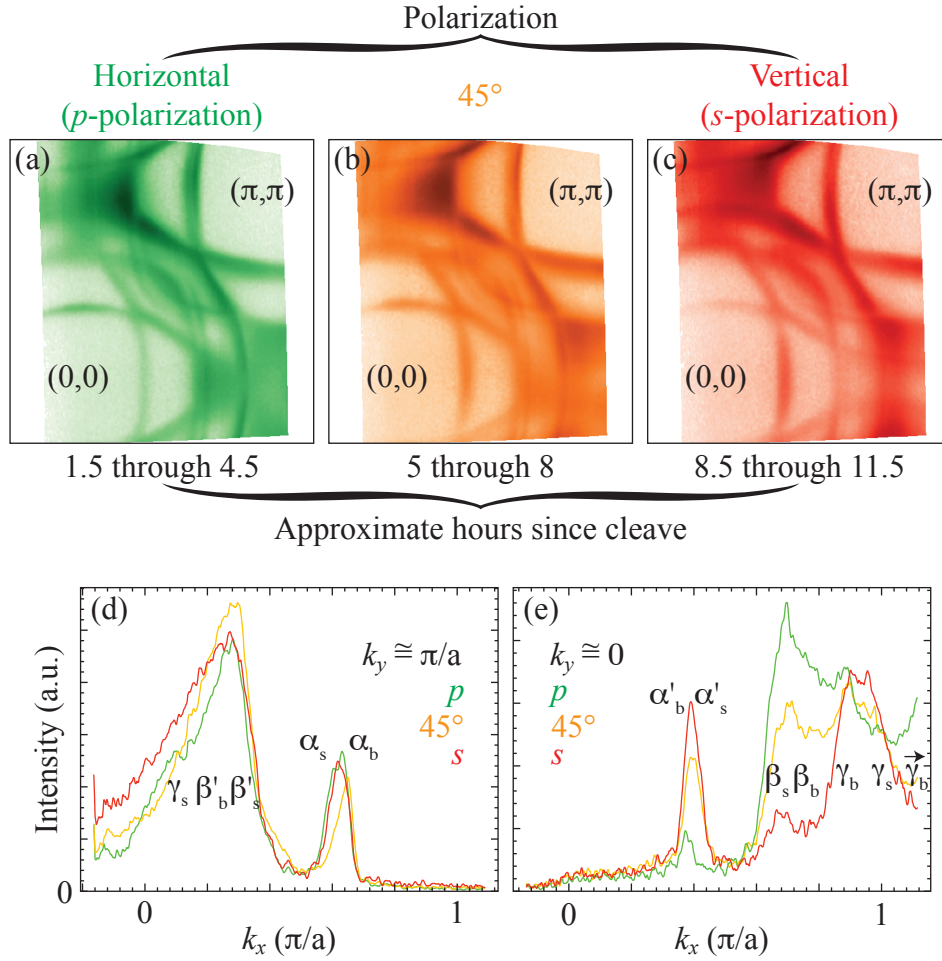


Figure 4.10: The FS of Sr_2RuO_4 , as measured by ARPES using light in (a) p -polarization, (b) intermediate 45° polarization, and (c) s -polarization. Panel (d) shows the high-symmetry cut from these FSs along $k_y = \pi/a$, while panel (e) shows the high-symmetry cut along $k_y = 0$, with locations where features cross these cuts marked. Acquisition times after the cleave are noted, with the sample held between 5 and 6 K in 6×10^{-11} mbar vacuum.

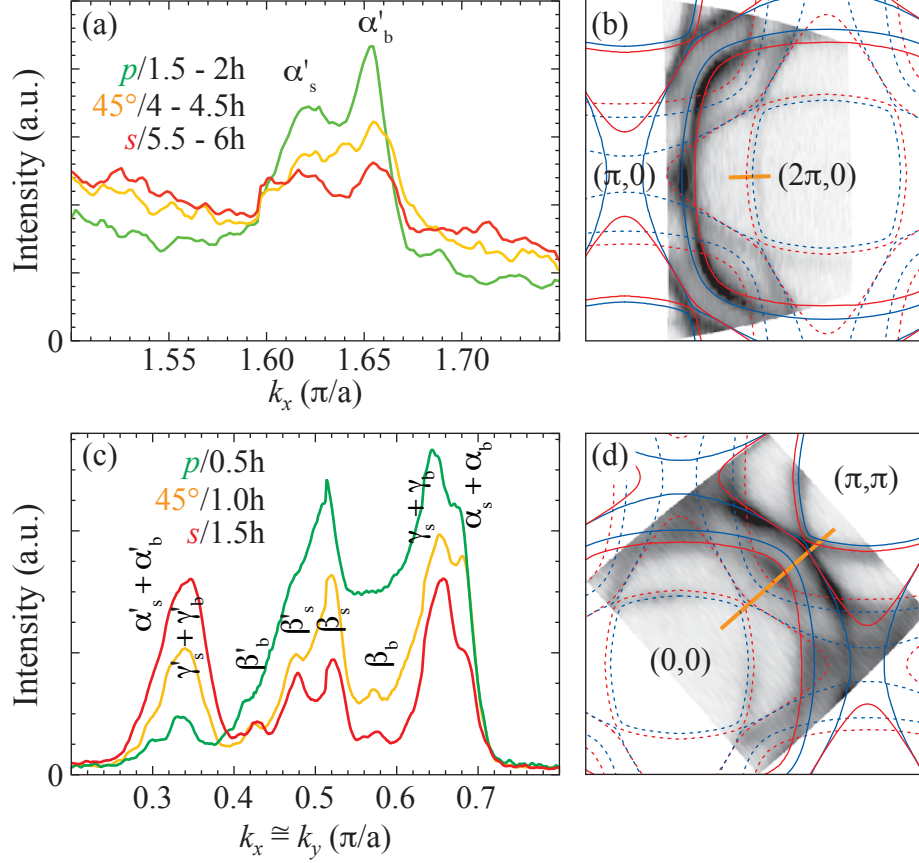


Figure 4.11: Polarization dependence of (a) the folded α' pocket in the second BZ, as marked in the alignment FS (b), as well as (c) a cut slightly offset from the $(0, 0) \rightarrow (\pi, \pi)$ high-symmetry direction, which crosses all bands, as marked in the alignment FS (d). Acquisition time for each cut in (a) was ~ 30 minutes, with the time since the cleave noted; the sample was held between 9 – 18 K in 8×10^{-11} mbar vacuum. For (c) acquisition time was on the order of minutes owing to higher intensity, and the sample was held at 5.6 K in 4×10^{-11} mbar vacuum.

4.1.4 Polarization dependence

Given the persistence of the b states compared with the s states in the time-dependent surface degradation measurements, it is certain that the b states originate from below the surface. However, it is difficult to definitively determine the source of the folding in the b states. There are two possible scenarios (given that the bulk is known not to reconstruct): either a reconstruction exists in the sub-surface layer, or bulk photoemission is scattering off a reconstructed surface. In the latter case the surface must retain enough of its structural modulation to continue to perform this scattering function, despite its being degraded enough to completely suppress photoemission. In the next two sections, first here through polarization dependence and then through a comparison with the Bi-cuprates, we explore the feasibility of the bulk-scattering scenario.

It is possible to measure the symmetry of the underlying wave-functions for various features by examining their ARPES intensity as a function of light polarization. Because of the monochromator between the He lamp and chamber, all light used in our lab at UBC is linearly polarized. This polarization can be changed by rotating the entire lamp and monochromator. Any detected electrons cannot have an odd final state with respect to the plane defined by the analyzer slit and the incoming photon. For this reason, using photons with p -polarization (electric field parallel, and hence even, to incidence/emission plane) will allow the detection of even (with respect to the incidence/emission plane) initial states; similarly, using s -polarization (from *senkrecht*, German for perpendicular) will allow the detection of odd initial states. The effects are the most drastic along high-symmetry directions, where the initial state is likely to be of pure even or odd character.

In principle, from the LDA calculations, it is possible to determine not only the band structure but also the orbital character and hence polarization dependence that should be measured by ARPES in any geometry. Unfortunately, for this work on Sr_2RuO_4 , because of orbital character mixing between bands as well as uncertainty in the k_z position of the measurement, I was unable to make such rigorous advances on the nature of these

additional bands using their polarization dependence. Additionally, the process of changing polarization is time consuming because the rotation must be slow in order to minimize the gyroscopic forces on the bearings in the turbo pumps. This time delay means that polarization-dependent measurements are often, effectively, also time-dependent measurements. Depending on sample temperature and chamber pressure, this may also have a large effect, owing to sample degradation. Nevertheless, from the polarization data presented in this section it becomes clear that the polarization dependence of both halves of many splittings are *independent* from each other. Likewise, the polarization dependence of the folded (primed) bands is often different from that of the primary (unprimed) bands. Their underlying wave-functions must therefore be of different character, either because they originate from either the surface or sub-surface (which may have different k_z locations) or because they are originating from k points on opposite sides of a mirror-plane (and are thus an initial state effect, rather than scattering through a reconstructed surface layer).

In Fig. 4.10 we present high-statistic FS measurements, integrated in a 7 meV region near the Fermi energy, for both p - and s -polarization as well as an intermediate polarization at 45° . Additionally, we highlight momentum distribution curve (MDC) cuts along the two high-symmetry locations accessed during this FS scan. Unfortunately, despite good vacuum and low temperature, some slight sample degradation during this time is visible as a general blurring of features in the s -polarization data. However, some information on the polarization dependence is still clear. In panel (d) we see that there is not strong polarization dependence in the $(0, \pi) \rightarrow (\pi, \pi)$ cut, although it appears that the b half of the splitting may be stronger in the α band at p -polarization, with both equally strong in s -polarization. In panel (e) we note strong polarization dependence, including the following characteristics: overall enhancement of both halves of the folded α' band in s -polarization, while in p -polarization α'_b appears stronger than α'_s (which may not appear at all in this polarization); overall enhancement of both halves of the β band in p -polarization, while in s -polarization only β_s appears strongly; an increase in γ_s while γ_b appears to maintain equal inten-

sity. In both these sets we see different polarization dependence for different halves of each splitting.

In Fig. 4.11 we present high-statistic MDC cuts integrated 6 meV near the Fermi energy, on which only a fast FS was taken for alignment purposes. This method allowed for quicker measurements with less opportunity for sample degradation. Unfortunately, for panel (a), helium flow problems resulted in warmer sample temperatures and higher pressures (see caption), and longer acquisition times were required owing to the relatively low intensity of the bands; therefore some sample degradation cannot be ruled out. Nevertheless in Fig. 4.11 panel (a) we see [similar to panel (e) from Fig. 4.10] that α'_b appears stronger than α'_s under p -polarization, but unlike in Fig. 4.10 we do not note an overall enhancement of both halves of the splitting in s -polarization. This could be due to either sample degradation or the differing location in k -space. In Fig. 4.11 panel (c) we cut across all bands and see a large polarization dependence. Most notable is that in s -polarization there is symmetry between the primary bands (unprimed) and their folded replicas (primed) and that, overall, the intensity of the folded replicas are strongly reduced under p -polarization, while the primary (unprimed) bands are mostly enhanced. However, there are exceptions to this trend – notably β_b and β'_b , which, while they still show a great difference between s - and p -polarization, show the opposite enhancement/reduction between folded and primary. Also, while an overall effect is clear, the overlap of b and s in the α and γ bands makes it difficult to discern which components of these peaks might be enhanced or reduced.

As we conclude the examination of the polarization data, two things are evident. First, the polarization dependence of each half of the splittings (b vs. s) can be different for some bands. This supports the hypothesis that they may originate from the surface and sub-surface layer, as the underlying wave-functions in this case would have slightly different structure, especially with respect to k_z (which is poorly defined for a single layer). Additionally the polarization dependence of both halves of each folding (primed vs. unprimed) also shows different polarization dependence in many places. This suggests the bands must be of differing origin – i.e., not simply replicas

scattered through a reconstructed surface layer.

4.1.5 A comparison with folded features in the cuprates

While the results of surface degradation and polarization dependence are strong evidence against the diffraction of bulk photoelectrons by the surface layer, it is nevertheless important to explore the parallel between the additional features observed in Sr_2RuO_4 and the diffraction proposed at one time to occur in the Bi-cuprates. There, two sets of unexpected features are detected in addition to the single band of the ideal CuO_2 square plane [80]: these have been referred to in the literature as “shadow bands” and “umklapp bands” [33]. It is the umklapp bands that were initially suspected to be due to the diffraction of the CuO_2 -plane photoelectrons travelling through the modulated BiO surface layer, since they appeared to exhibit multiple positive and negative high-order replicas, consistent with a diffraction scenario. However, this was later shown not to be the case: all crystal planes present the same incommensurate modulations as the BiO planes, and the umklapp bands therefore stem from initial states *intrinsic* to the modulated CuO_2 plane and not from *extrinsic* photoelectron diffraction [81–84]. Additionally, it is not with the umklapp but with the shadow bands that the sub-surface folded bands in Sr_2RuO_4 share their form of reconstruction. Importantly, contrary to the umklapp bands, these shadow bands in Bi-cuprates were deemed inconsistent with a photoelectron diffraction scenario; by analogy, the same would hold for Sr_2RuO_4 . While initially attributed to antiferromagnetic fluctuations giving rise to a $(\sqrt{2} \times \sqrt{2})\text{R}45^\circ$ larger unit cell and a correspondingly folded Brillouin zone [80], the shadow bands in Bi-cuprates were shown to arise from the presence of two structurally inequivalent Cu atoms per orthorhombic unit cell [81–84].

4.2 LDA calculations and structural distortions

In order to explore the possibility of the additional features being due to a structural distortion in both the surface and sub-surface layers, a variety

of LDA calculations were performed both with and without SO coupling using the linearized augmented-plane-wave method in the WIEN2k package [85]. As discussed earlier, it is known that oxygen octahedra in the surface layer rotate about the c -axis, which causes a $(\sqrt{2} \times \sqrt{2})R45^\circ$ reconstruction of the primitive cell as seen by surface-sensitive experiments such as ARPES [6, 56, 58, 68, 69] and LEED [59–61, 70, 71]. Additionally, it is likely that there may be dimensional distortions along the c -axis in (at least) the topmost layer. It is also known that the bulk crystal does not undergo such a reconstruction, as this is not detected in any x-ray [63] or neutron diffraction experiments (on either single-crystals [64] or powders [65–67]), nor is the resultant reconstruction of the BZ seen in dHvA measurements [14, 54, 55]. However, the precise nature of the sub-surface layers is not known, and is difficult to probe directly, although ARPES may come close in that it can be sensitive to a superposition of the electronic structure of surface, sub-surface, and bulk-like layers.

If the sub-surface layer were to undergo a similar rotation to that of the surface, one would expect that photoemission from that layer would display folded replicas in the same manner – thus explaining all visible features. However, as shown by bulk calculations, simply modulating the same structural distortion cannot entirely explain the features as observed. Namely, the change in volume of the β splitting (distance between β_s and β_b seen, for example, in Fig. 4.3 or 4.4) is not reproduced. It is possible that the surface itself, owing to the disruption of the periodic potential seen by electrons, either alone or in combination with a structural distortion, may cause these discrepancies. For this reason slab calculations are necessary in order to model the existence of the vacuum, surface, and sub-surface layers and any possible interplay between them. In such calculations the unit cell is expanded along the c -axis to include multiple, possibly different, atomic layers and a layer of vacuum is also included. In this manner one can simulate both surfaces with a bulk-like layer, at the cost of finite size effects (for the bulk-like layers) and computational time because of the increased number of atoms (which scales non-linearly). In order to decide on the parameters to be used for the computationally expensive slab calculations, in particu-

lar the unknown sub-surface layer, a series of comparatively fast bulk LDA calculations were performed, both with and without SO coupling. I will first discuss the results of these preliminary calculations in §4.2.1, before describing the slab choice (§4.2.2) and finally the results (§4.2.3) of those calculations.

4.2.1 Preliminary bulk calculations

In order to determine the structure to use for slab calculations, in particular the sub-surface layer, LDA bulk band structure calculations were performed for varying rotations of the oxygen octahedra as well as a possible buckling mode. Additionally, the effects of adding Coulomb repulsion U were examined. This allowed the exploration of a wide parameter space without the computational cost of many slab-based calculations.

As Ru oxygen octahedra rotation is known to occur in the surface layer, a range of crystal structures with different rotations (unit cell dimensions kept constant) were studied with bulk LDA+SO calculations. The structure can be visualized in Fig. 4.15, keeping in mind that it is a bulk calculation with all layers rotated. In Fig. 4.12(a) we see that, for rotations under $\sim 3^\circ$, no significant change in Fermi surface volume (average 3%) is observed, with, in particular, no change in the topology of the γ Fermi surface. [Correspondingly the γ band Van Hove singularity at the M point remains above the Fermi level in Fig. 4.12(b).] For rotations above $\sim 5.5^\circ$ the topology of the γ band changes to match that of the surface, and $\sim 7.5^\circ$ introduces also the δ band at Γ/X . Comparing these calculations to experiments [for example, Fig. 4.3(f), and values in Tab. 4.1] then suggests that any sub-surface rotation should be $\lesssim 3^\circ$, while the surface rotation should be $\gtrsim 5^\circ$. (As discussed below, the δ crossing moves above the Fermi level with the inclusion of U , so $\sim 7.5^\circ$ is not a hard upper limit.)

While tilting of the oxygen octahedra occurs in the related family of compounds with Ca substitution, $\text{Ca}_{2-x}\text{Sr}_x\text{RuO}_4$, it is known from the symmetry of the Sr_2RuO_4 surface that no tilting of the octahedra occurs [60, 71], as moving the in-plane (with Ru) O atoms out of plane would change the

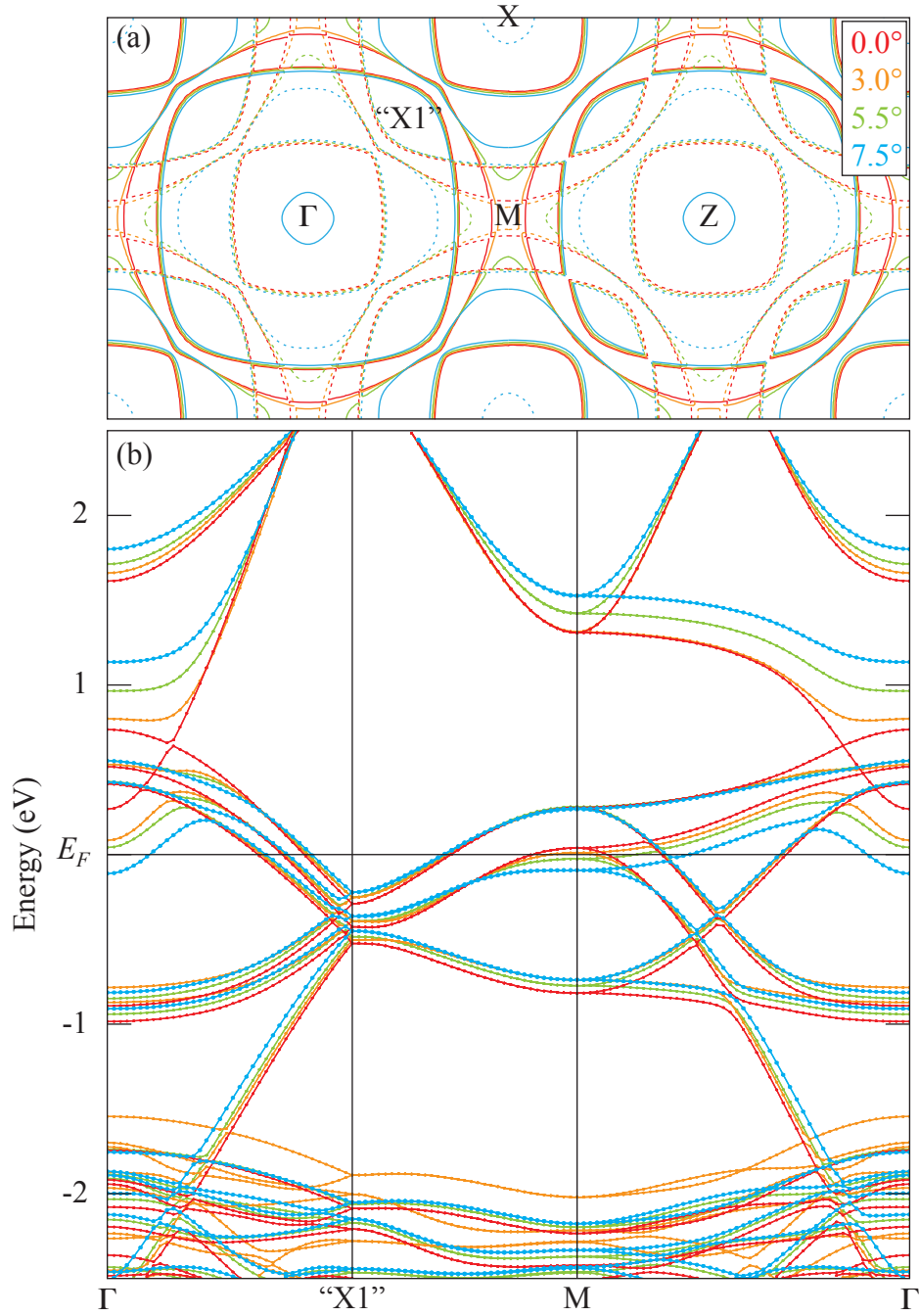


Figure 4.12: (a) Fermi surface and (b) high-symmetry cut from bulk LDA+SO band structure calculations for Sr_2RuO_4 , with incremental rotations of the oxygen octahedra. Primary bands are shown solid, with their folded replicas shown dotted in (a). 90

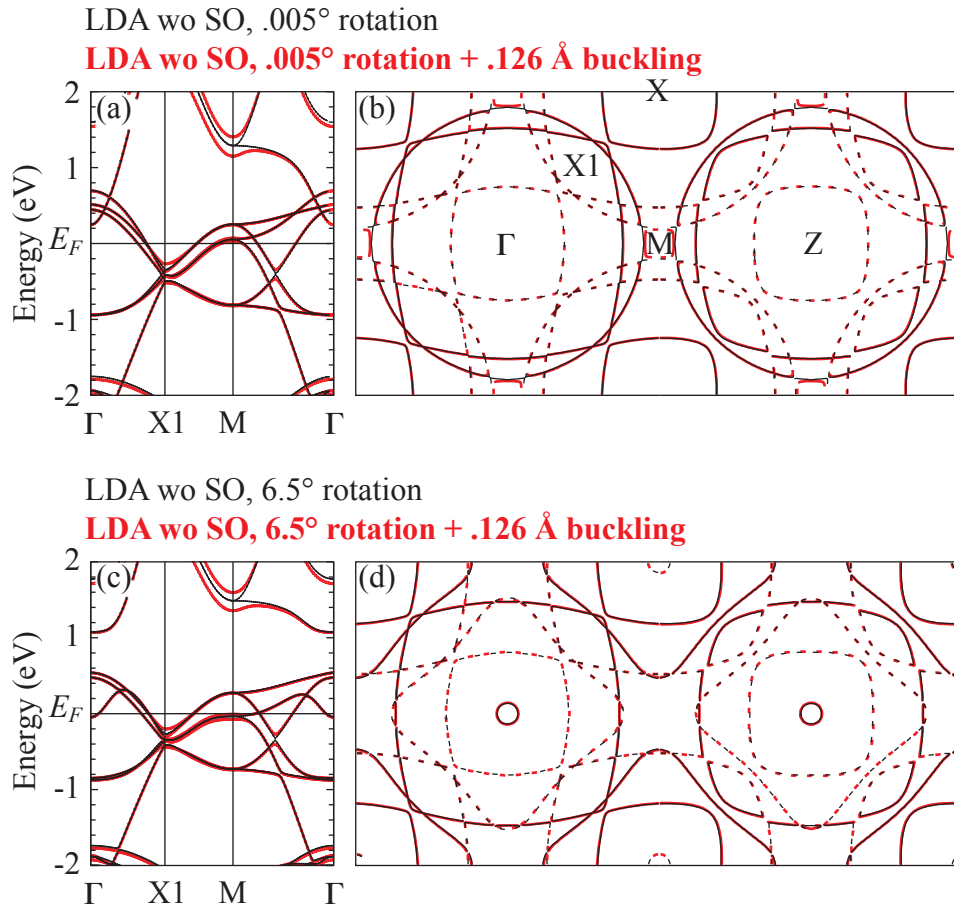


Figure 4.13: (a) high-symmetry cut and (b) Fermi surface from bulk LDA (without SO) band structure calculations, both with (red) and without (black) elongation of alternate oxygen octahedra. (c,d) show the same but with additional rotation of the oxygen octahedra. Primary bands are shown solid, with their folded replicas shown dotted in (b,d).

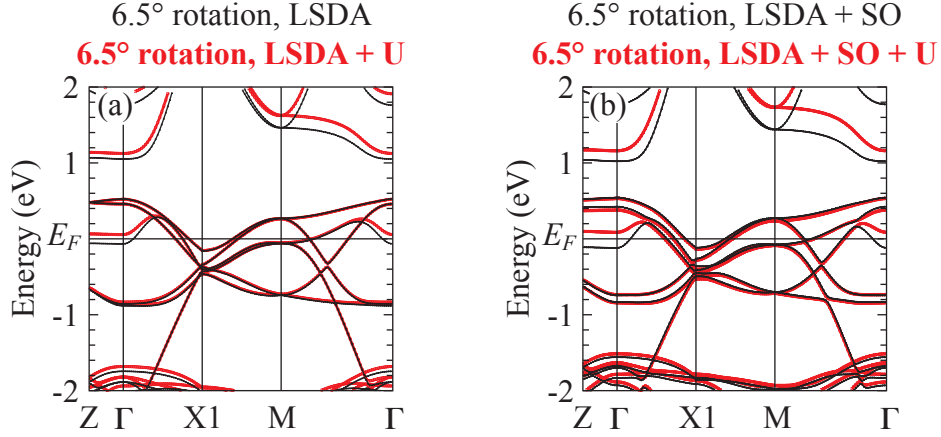


Figure 4.14: High-symmetry cut from bulk LSDA band structure calculations showing the effect of adding an effective electronic interaction of 1 eV (red), compared to 0 eV (black) both without (a) and with (b) SO.

symmetry group. However, a c -axis distortion of the apical O, either uniformly or as a buckling mode, is not similarly restricted. To explore this possibility, calculations were performed where the Ru oxygen bond lengths were distorted along the c -axis by ± 0.063 Å. This is a rather large number, as the uniform (not as a buckling mode) c -axis elongation of this bond length observed to occur at the surface by LEED is ~ 0.0141 Å. Despite the introduction of this rather large buckling, only small effects were observed on the LDA band structure near the Fermi energy, as shown in Fig. 4.13 (a,b) for both the case of non-rotated¹⁸ octahedra and octahedra with a 6.5° rotation. The only observable effect was the lifting of certain degeneracies – for example, the γ - γ' intersection along $X1 \rightarrow M$. For this reason further calculations exploring the effects of a buckling mode were not performed, and it was not considered in slab calculations.

The final bulk calculations discussed here involve the inclusion of electronic interactions via an on-site Coulomb interaction U and exchange interaction J , for an effective interaction $U - J$ [86–88] using the local-spin-

¹⁸Nominally undistorted; however, the symmetry was pre-broken by introducing a $.005^\circ$ rotation, so the symmetry remained the same with the introduction of buckling.

density approximation (LSDA). Although ab-initio methods for calculating these interactions have been proposed [89], often the more empirical method of varying the effective interaction until good agreement with experiment is found has been used (for example, in related Sr_2RhO_4 [57]). Here we sought merely to explore the effect of adding such an effective interaction, before investing computation resources with more costly LSDA calculations and determining the best value to use for the interaction. Accordingly we chose the rather large effective coupling of 1 eV (compared with, for example, related Sr_2RhO_4 , where an effective coupling of 0.3 eV – 0.5 eV was used [57]). The results of these LSDA calculations for a bulk crystal structure with oxygen octahedra rotated 6.5° , both with and without the inclusion of SO, for effective coupling 1 eV and 0 eV are shown in Fig. 4.14. Here it can be seen that the effect is on overall bandwidth, which, near the Fermi energy, causes little change other than eliminating the δ crossing at the Γ point by moving it above the Fermi level. Because adding U had little overall effect slab calculations were not performed with the inclusion of electronic interactions under this scheme.

4.2.2 Slab choice

The exact slab structure chosen for the LDA+SO slab calculations is presented in detail in Fig. 4.15. The surface layer was chosen to exactly match that measured by LEED, which includes a slight elongation as well as a 7.46° rotation of the oxygen octahedra, and, based on the preceding bulk calculations, should be expected to match the overall band structure of the surface well. However, as discussed earlier, the exact nature of the sub-surface layer is unknown and cannot be probed accurately. From the preceding discussion it appears that any sub-surface rotation should be $\lesssim 3^\circ$. Since the choice of any finite small rotation in the sub-surface layer would thus be largely arbitrary, and unnecessary in order to simply introduce a folding because of the nature of the calculations, we chose to use a pure bulk-like structure for the inner three layers as the simplest possible model. This also allowed the realization – with only five layers – of a bulk-like region with large size

4.2. LDA calculations and structural distortions

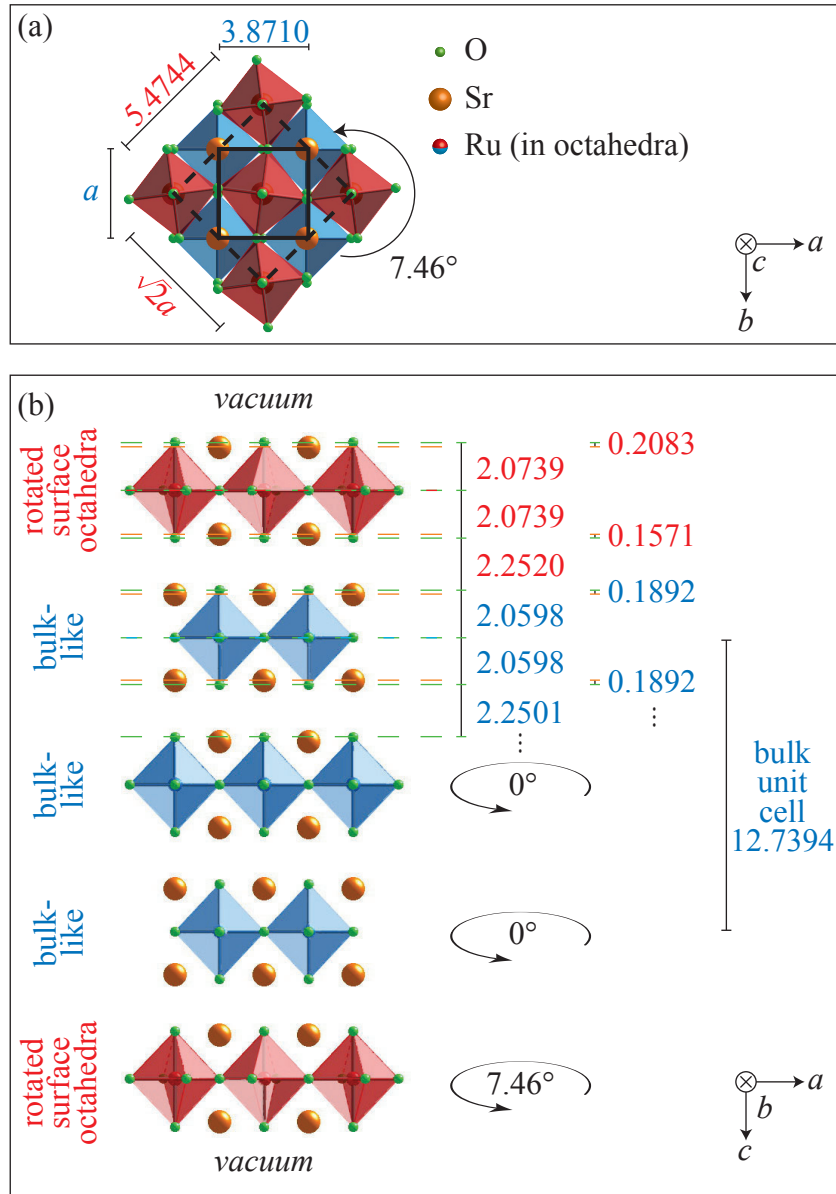


Figure 4.15: Atomic positions in the five-layer slab used for LDA+SO calculations, with rotated octahedra and modified c -axis dimensions for surface (red) and bulk-like layers (blue). All dimensions in Å. Panel (a) shows the surface viewed from the vacuum, with bulk primitive cell shown with solid lines and $(\sqrt{2} \times \sqrt{2})R45^\circ$ reconstructed shown with dashed lines. Panel (b) illustrates c -axis dimensions for both bulk and surface layers, viewed from the side.

compared with the surface-like region. To include a sub-surface layer with a different (and arbitrary) rotation would necessitate 10 layers to have a similar ratio of surface-like to bulk-like layers.

4.2.3 Slab results

The results of the slab calculations are presented in Fig. 4.16. In addition to allowing us to study both the structural reconstruction as well as effects due to broken symmetry in proximity to the surface in a self-consistent way we are able us to estimate the surface/bulk character of the resulting band structure by projecting the corresponding wave-functions onto the Ru orbitals for each layer. This method was used to colour the band structure red and blue for surface and bulk-like layers, respectively. As the ARPES measured FS shows a slight hole doping (see Tab. 4.1) a variety of chemical potential shifts, panels (d–g), were considered with the constant energy contour at 24 meV binding energy chosen for a final comparison, panel (a). This corresponds to a FS with an averaged electron counting $n_e \simeq 3.91$ to match the s – b averaged value experimentally observed by ARPES and, as shown in Tab. 4.1, also closely matches the relative doping measured between layers (with s containing slightly fewer electrons). From the colourized band structure hybridization between layers does occur at some k -points, where sheets can be seen to change character, and although somewhat complicated by hybridization gaps appearing at all crossings, these calculations show good overall agreement with the phenomenological FS concerning the splitting, topology, and volume of the various bands (Tab. 4.1), as well as – and most importantly – the surface vs. bulk-like assignment of all detected features¹⁹. These calculations validate the explanation of a progression of structural distortions from surface to bulk, with a corresponding progression of electronic states.

¹⁹The appearance of the δ_s pocket of $d_{x^2-y^2}$ character at $(0,0)$ and (π,π) , which experimentally is found just above E_F [58] and not observed to cross, would lift above the FS with the addition of an electronic interaction term U , as seen in §4.2.1, but this would require more computationally expensive LSDA.

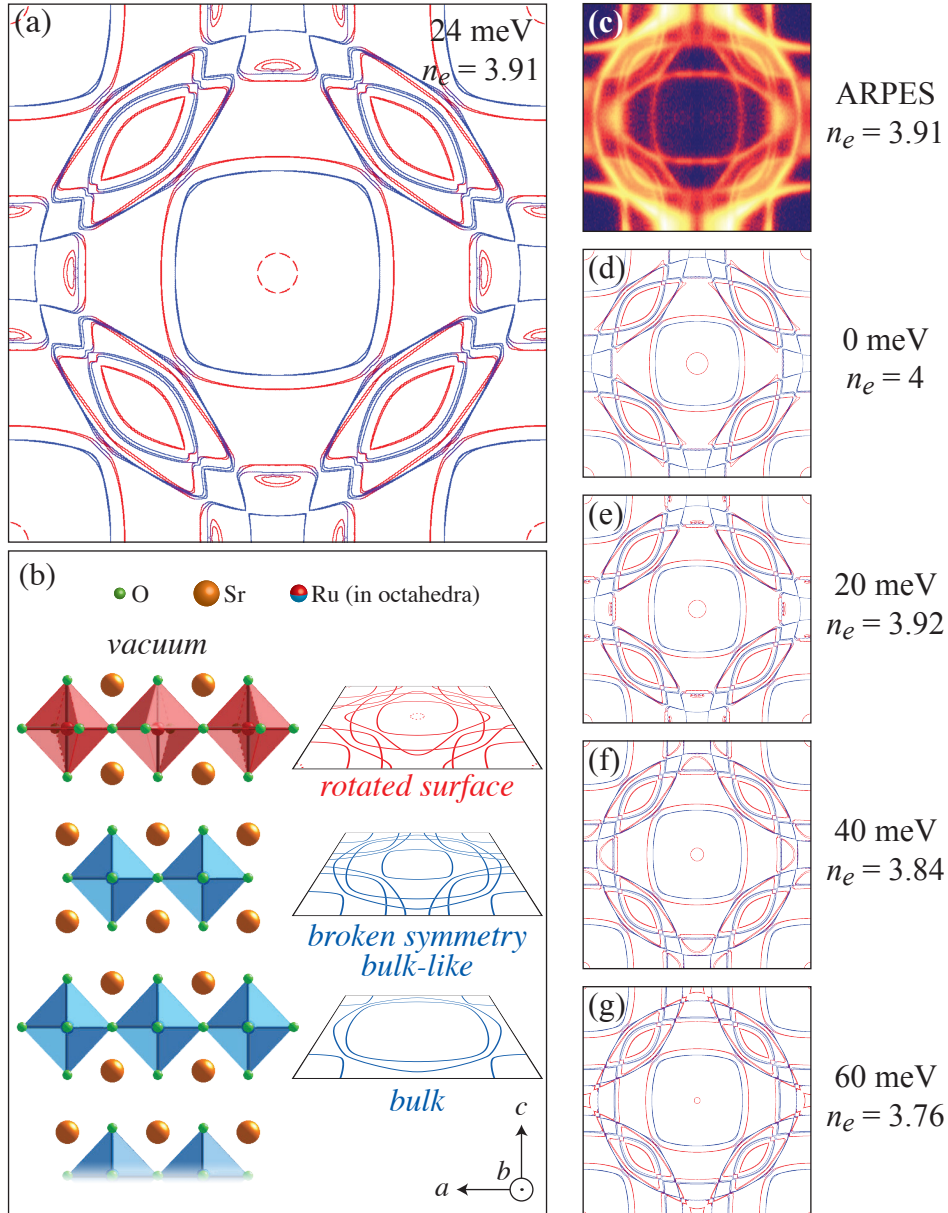


Figure 4.16: (a) FS obtained from the LDA+SO slab calculations by shifting the chemical potential 24 meV down in energy to match the slight average hole doping observed by ARPES. Surface and bulk character are shown in red and blue, respectively. (b) partial structure of Sr_2RuO_4 slab with FS sketches showing the corresponding surface and bulk-like FS derived from (a). (c) FS as measured by ARPES, for comparison. (d-g) FS from slab calculations for shifts of 0→60 meV.

4.3 Conclusions

To conclude, by means of ARPES and LDA+SO slab calculations we have been able to unravel a surface-to-bulk progression of the electronic structure in Sr_2RuO_4 . We find that a $(\sqrt{2} \times \sqrt{2})\text{R}45^\circ$ reconstruction of surface and sub-surface layers provides a consistent explanation of all detected dispersive features in terms of a progression of electronic states induced by structural instabilities, with no evidence for novel phases driven by topological bulk properties, ferromagnetic ordering, or the interplay between SO coupling and the broken symmetry of the surface. This layer-by-layer approach provides the most detailed information on FS volumes, Fermi velocities, as well as many-body renormalizations $v_F^{\text{ARPES}}/v_F^{\text{LDA+SO}}$, for both surface and bulk-like bands (Tab. 4.1). In analogy with the recent work on underdoped cuprates [84, 90], which found evidence for the enhancement of electronic correlations and ordering tendencies in the surface and sub-surface region, this study of Sr_2RuO_4 also highlights the significantly more correlated character of the top surface layer bands, which might thus more strongly benefit from an LDA+SO+U description [57].

It is likely that similar phenomena may occur, yet unnoticed, in other systems. This possibility should be considered whenever analyzing data from a surface-sensitive technique like ARPES, especially as resolution and the ability to resolve features advance.

Chapter 5

CPS-ARPES on Sr_2RuO_4

Sr_2RuO_4 is a well-known candidate for spin-triplet superconductivity [91]. This came after a flurry of experimental activity observed, in rapid succession, spontaneous internal magnetic fields in the superconducting state, by muon spin-relaxation experiments, indicating a p -wave state [92]; a square flux-line lattice, by neutron scattering experiments, indicating that pairing occurs in the 2D γ band [93]; and no change in spin susceptibility passing through the superconducting transition temperature, through ^{17}O Knight shift measurements, indicating spin-triplet pairing [94]. Following this the description of superconductivity in Sr_2RuO_4 was thought to be complete – it became a hallmark spin-triplet chiral p -wave superconductor, the 2D analogue of superfluid ^3He [95]. However, despite the apparent existence of such a pairing, some later experiments have failed to support this conclusion, suggesting that this description alone may not be sufficient. While the additional superconducting transition in magnetic fields (expected as a result of the multi-component order parameter in spin-triplet superconductivity) has been measured in specific heat [96], DC magnetization [97], and AC susceptibility [98], there is an extreme, and puzzling, sensitivity to the angle of the field with respect to the ab -plane – it is observed only for angles $\lesssim 1^\circ$ [99]. Additionally, under similar conditions, the upper critical field is found to be strongly suppressed [100]. This strange behaviour cannot be explained within a theoretical model using spin-triplet superconductivity alone [91].

A solution to this conflict is offered by relativity and the spin-orbit (SO) interaction, which blurs the distinction between singlet and triplet and could facilitate mixed-parity pairing [17, 101, 102]. However, thus far, experimental confirmation has been largely circumstantial, limited to measurements of the band structure itself [17]. In this work we aim to directly probe the exis-

tence of mixing between spin and orbital quantum numbers. We do this by performing spin- and angle-resolved photoemission spectroscopy (SARPES) and using the angular momentum inherent in circularly polarized light along with final state selection rules to generate spin-polarized photoemission from the mixed states (CPS-ARPES).

In this chapter we will first review and expand on the theoretical prediction of SO-entangled bands in Sr_2RuO_4 by Haverkort *et al.* [17] and the implication for the single-particle states, in § 5.1. In § 5.2 we will then confirm these predictions using CPS-ARPES performed at the Swiss Light Source Complete Photoemission Experiment (COPHEE) endstation. Following this we briefly discuss the ramifications this entanglement must have on the superconducting state and its description in this material in § 5.3. We find that the presence of SO coupling must drive the superconducting state in Sr_2RuO_4 to be even more unconventional than generally assumed, with strong momentum-dependent entanglement between the spin and orbital sectors; this leaves a classification in terms of spin eigenstates meaningless.

5.1 Single-particle predictions – entanglement at the Fermi energy

The bulk band structure of Sr_2RuO_4 was calculated using the tight-binding (TB) linear muffin-tin orbital (LMTO) code [103], which was tested against that calculated with full-potential linearized augmented-plane-wave method using with WIEN2k [85]. The TB parameters were extracted from the TB-LMTO results using the order-N muffin-tin orbital (NMTO) method [104] on the minimal basis of oxygen p and ruthenium d orbitals. Atomic spin-orbit coupling was then added as a local term in the tight-binding Hamiltonian, the results of which show excellent agreement with calculations performed using relativistic local-density approximation (LDA)+SO calculations in WIEN2k. In this manner the effects of the SO interaction can be easily studied on their own.

In Sr_2RuO_4 the relativistic SO coupling is relatively small ($\zeta \approx 93$ meV)

5.1. Single-particle predictions – entanglement at the Fermi energy

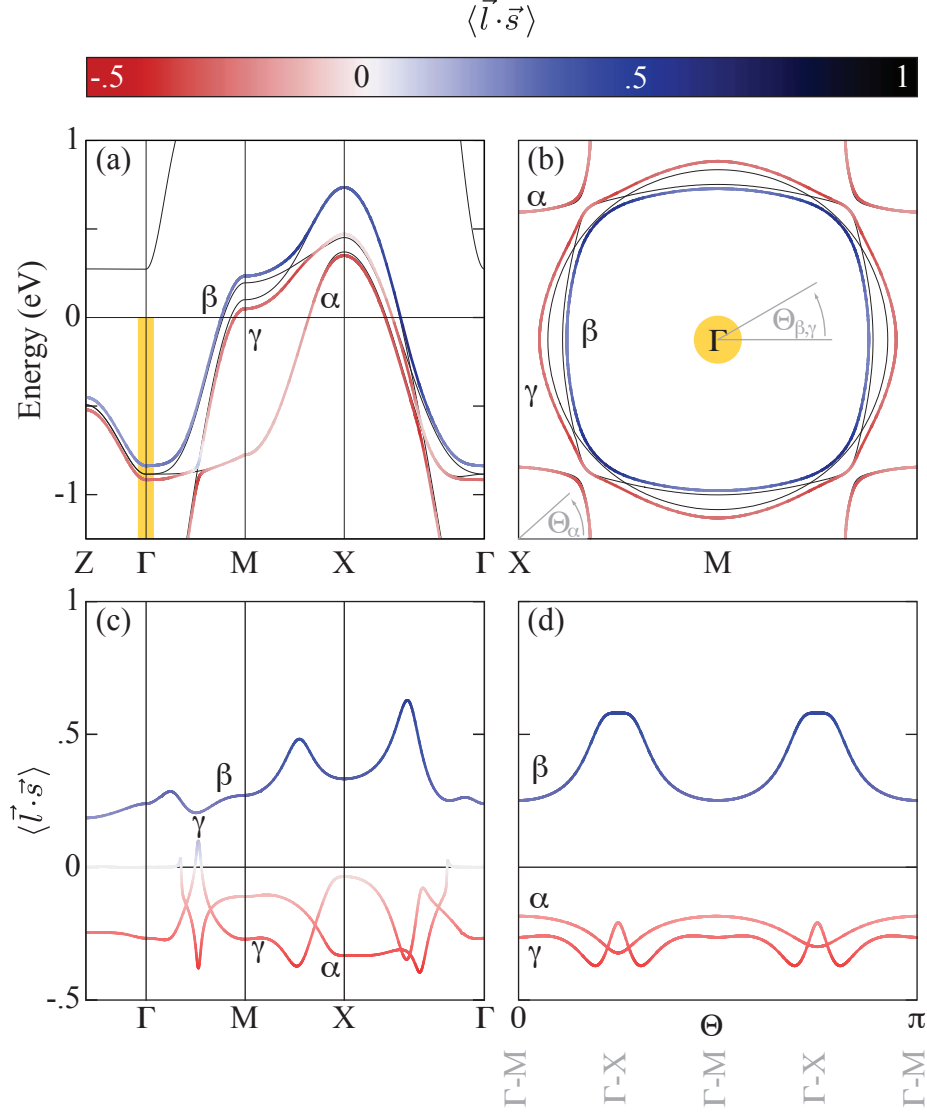


Figure 5.1: The band structure of Sr_2RuO_4 (a) along high-symmetry directions and (b) at the Fermi energy for $k_z = 0$. $\langle \vec{l} \cdot \vec{s} \rangle$ for LMTO/NMTO+SO is shown via the colour scale at top using thick lines, while that without SO is shown underneath in fine black. The value of $\langle \vec{l} \cdot \vec{s} \rangle$ is shown in panels (c) and (d), and the location of CPS-ARPES measurements performed is highlighted yellow in (a) and (b).

5.1. Single-particle predictions – entanglement at the Fermi energy

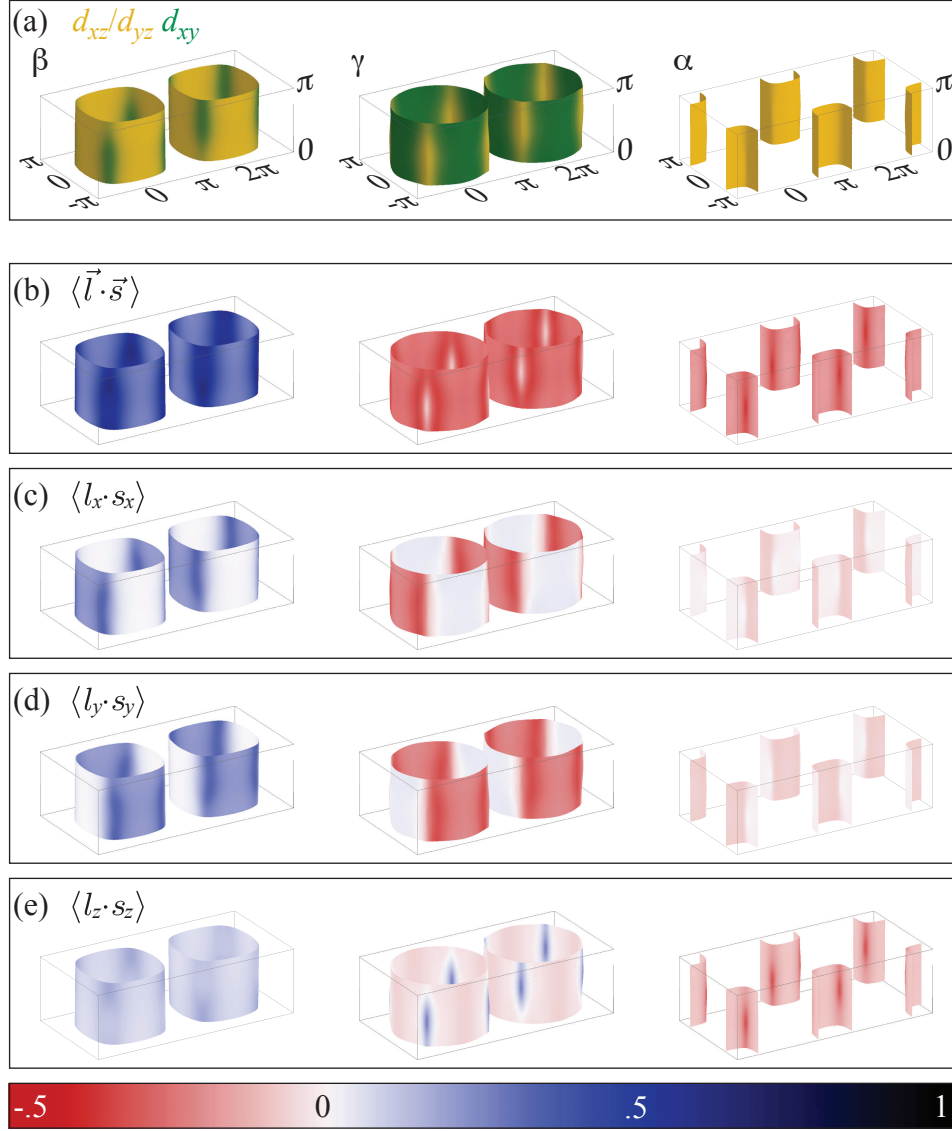


Figure 5.2: Orbital character (a), expectation value of $\langle \vec{l} \cdot \vec{s} \rangle$ (b), and its components (c–e) around the Fermi surface sheets of Sr_2RuO_4 , as calculated by LMTO/NMTO+SO. The extended zone scheme is used to illustrate the conventional BZ inside the fundamentally body-centred tetragonal (BCT) unit cell.

5.1. Single-particle predictions – entanglement at the Fermi energy

with respect to the bandwidth (~ 1.5 eV). Nevertheless its influence always becomes important whenever two non-relativistic bands would be degenerate, either by symmetry or accidentally. In Sr_2RuO_4 this happens at several places in the Brillouin zone (BZ), as demonstrated in Fig. 5.1(a,b) where we show a comparison of the band structure and Fermi surface calculated both with and without SO coupling included. For example, by symmetry the d_{xz} and d_{yz} bands would be degenerate along the entire momentum path from Γ to Z. Additionally there are accidental degeneracies along the path Γ to X where the bands of d_{xz} , d_{yz} , and d_{xy} all cross – the location of which varies with k_z but often occurs at the Fermi level, which can be seen in Fig. 5.2 panel (a), where the Fermi sheets change orbital character. At all these locations SO coupling leads to a splitting of the bands and a non-trivial entanglement between the spin and orbital character, as shown via the expectation value of $\vec{l} \cdot \vec{s}$ (where \vec{l} is the orbital and \vec{s} the spin angular momentum operator, and which is zero when spin and orbit are independent) near these crossings in Fig. 5.1 panels (c) and (d). If this mixing existed at a few isolated k -points on the Fermi surface, one could imagine ignoring SO coupling, but the importance of SO coupling is not limited to these would-be degeneracies. The SO interaction can be enhanced by correlations that either reduce the bandwidth or, as suggested in Ref. 57, increase the SO splitting in a mean-field approach if they span the Fermi level. As seen in Fig. 5.1(a), despite the large bandwidth, the bands are often separated by energies small compared with the SO interaction of ≈ 93 meV, which indicates that SO coupling may be important everywhere. In Fig. 5.2 we see that this is, in fact, the case – in panel (b) we see that $\langle \vec{l} \cdot \vec{s} \rangle$ is non-zero around almost the entire Fermi surface sheet. Although there is a small region near the corners of the γ band where $\langle \vec{l} \cdot \vec{s} \rangle = 0$, we see in panels (c–e) that it is not because \vec{l} and \vec{s} are independent from each other at that location but rather because the individual non-zero components sum to zero. Overall we find that LMTO/NMTO+SO predicts a strong entanglement between the spin and orbital quantum numbers on the entire Fermi surface, for all three bands, everywhere in k -space.

5.2 Measuring spin-orbital entanglement

SARPES measures the spin polarization of photoemitted electrons, while the SO-induced splitting in Sr_2RuO_4 is inherently not spin polarized, owing to an occupation of two degenerate states with opposite (pseudo) spin²⁰. For this reason the angular momentum of circularly polarized light, carefully selected initial states, and final state selection rules were used together in order to transform SO splitting into spin-polarized photoemission, in a similar manner to that done on GaAs [105].

5.2.1 States measured

In order to pioneer this technique on Sr_2RuO_4 we measured the SO splitting at the Γ point, or $\vec{k} = (0, 0, 0)$, as indicated in Fig. 5.3. This allows us to use both the experimental geometry and initial-state wave-functions that are the most straightforward to understand, leading to a clear-cut proof of the SO entanglement in these bands. At this point in k -space non-relativistic band structure calculations predict two degenerate bands of d_{xz} and d_{yz} orbital character. Here the other bands are far enough away in energy that they can be ignored in the following discussion, which we will do by considering only the Ising part of the SO interaction. This breaks the degeneracy by hybridizing these bands and the electron spin into two states, with a predicted $\zeta_{eff} \sim 90$ meV splitting between them: a higher-energy state with the z components of orbital and spin angular momentum parallel [$d_{+1_z}^{\uparrow z}, d_{-1_z}^{\downarrow z}$, illustrated in panel (b)], and a low-energy state where they are antiparallel [$d_{-1_z}^{\uparrow z}, d_{+1_z}^{\downarrow z}$, illustrated in panel (c)]. Here $d_{+1_z} \equiv \sqrt{1/2}(-d_{xz} - id_{yz})$ has $m_{\ell_z} = 1$, while $d_{-1_z} \equiv \sqrt{1/2}(d_{xz} - id_{yz})$ has $m_{\ell_z} = -1$, and \uparrow_z represents spin.

Optical selection rules dictate that both $\Delta\ell = \pm 1$ and $\Delta m_l = \pm 1$. For d orbitals the change in ℓ will strongly favour the $d \rightarrow p$ transition over $d \rightarrow f$ owing to cross-section at the used photon energies, while the change

²⁰The Kramers degeneracy states that a state at $+\mathbf{k}$ with (pseudo) spin up is equivalent to the state at $-\mathbf{k}$ with (pseudo) spin down. The Kramers degeneracy, together with the inversion symmetry in the crystal structure of Sr_2RuO_4 (which equates $+\mathbf{k}$ with $-\mathbf{k}$), results in the existence of degenerate states with opposite (pseudo) spin at every \mathbf{k} -point.

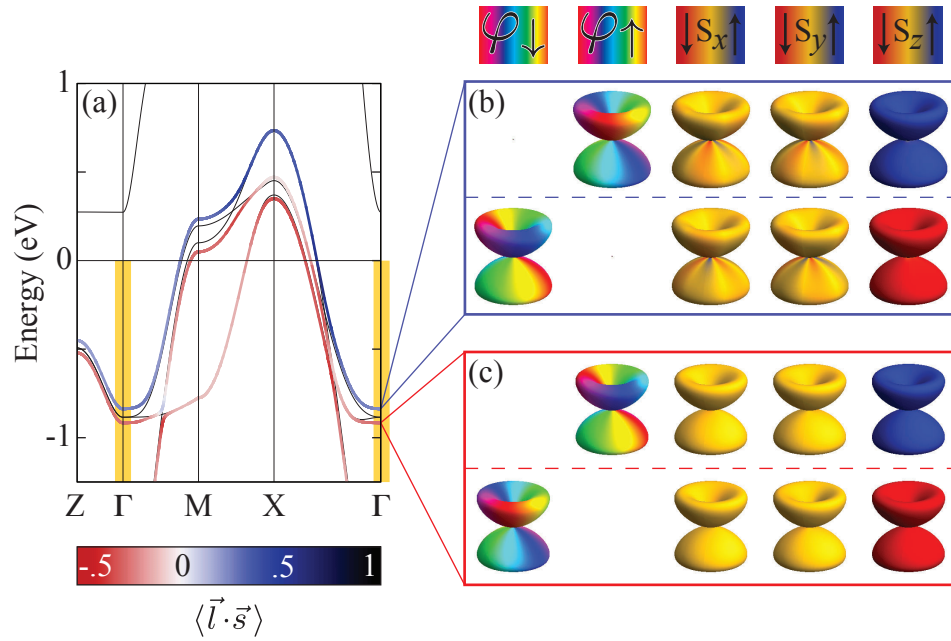


Figure 5.3: (a) the band structure of Sr_2RuO_4 , as in Fig. 5.1, with the eigenstates measured by CPS-ARPES illustrated in real space in panels (b) and (c). These illustrations show, for both halves of the Kramers degenerate pair, from left to right, the phase of both spin parts of the wave-function ($\varphi_{\downarrow}/\varphi_{\uparrow}$, quantized in the z direction) and spin expectation values in the x , y , and z directions as calculated by LMTO/NMTO+SO.

in m_l will depend on polarization. A circularly polarized photon travelling along the z direction could be either circular plus (\oplus) or minus (\ominus). When a \oplus (\ominus) photon is absorbed by the high-energy parallel $d_{+1z}^{\uparrow z}, d_{-1z}^{\downarrow z}$ state m_{l_z} must increase (decrease) by one; but as $m_{l_z} = 2$ is forbidden in the strongly favoured p transition, electrons from the $d_{-1z}^{\downarrow z}$ ($d_{+1z}^{\uparrow z}$) will dominate, resulting in \downarrow_z (\uparrow_z) spin polarization. Similarly, using \oplus (\ominus) light will result in photoemission with the opposite, \uparrow_z (\downarrow_z), spin polarization from the low energy antiparallel state $d_{-1z}^{\uparrow z}, d_{+1z}^{\downarrow z}$. This is illustrated in Appendix C, Fig. C.3.

5.2.2 ARPES results

When observed with regular, spin-integrated, angle-resolved photoemission spectroscopy (ARPES) the energy distribution curve (EDC) from these two states at the Γ point shows both predicted features as a broad hump with width ~ 400 meV, as shown in Fig 5.4 using data taken at the University of British Columbia (UBC). That the individual states cannot be resolved despite an energy resolution five times greater than the predicted splitting indicates that the states have a broad fundamental lineshape. However, as we will demonstrate, it is still possible to measure a splitting between these two states because of their fundamentally different character using CPS-ARPES.

5.2.3 CPS-ARPES results

SARPES data was taken at the Paul Scherrer Institute using the Swiss Light Source COPHEE endstation, with $\sim 1^\circ$ angular resolution²¹ and energy resolution ~ 100 meV. Samples were cleaved in situ with base pressures in the 10^{-9} mbar range at low temperature (40 K). Owing to the relatively high temperature and pressure, no features associated with the reconstructed surface [6, 56] were observed. In order to compensate for the observed strong circular dichroism on this material, all measurements were repeated using both circular plus and minus light, and the cross-polarization \tilde{P}^\otimes was

²¹Equivalent to $\sim 0.1 \frac{\pi}{a}$ at 24 eV and $\sim 0.2 \frac{\pi}{a}$ at 56 eV photon energy.

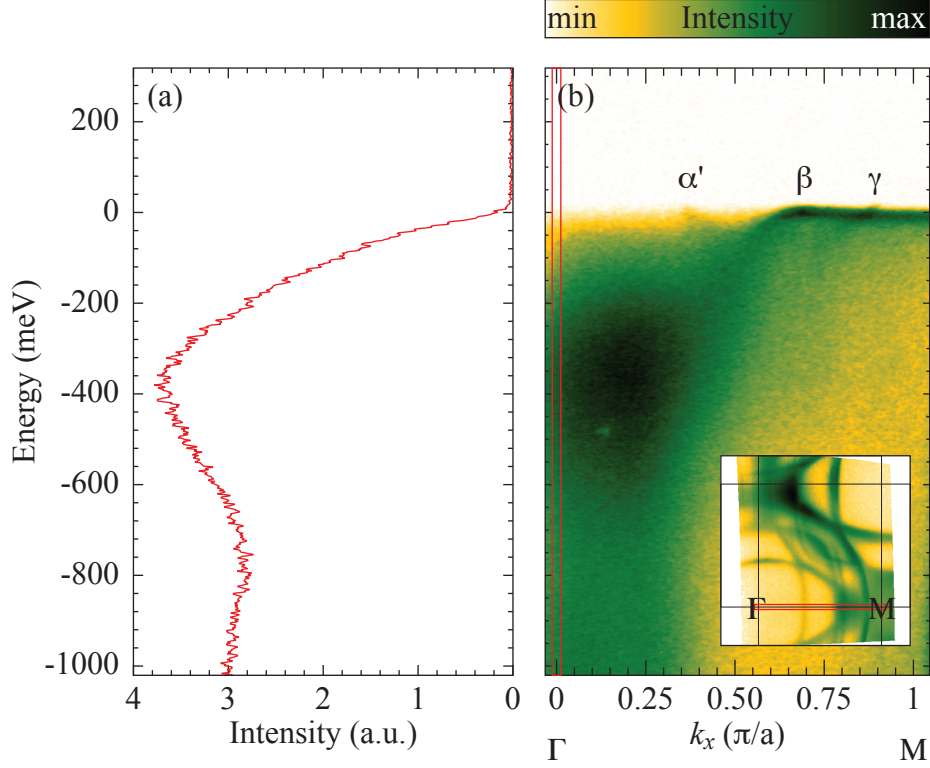


Figure 5.4: Spin-integrated ARPES on 5.2 K Sr_2RuO_4 at the Γ point, performed at UBC using 21.22 eV He I spectral line, with energy resolution of ~ 17 meV and angular resolution equivalent to $\sim 0.01 \frac{\pi}{a}$. (a) shows an EDC integrated over $\sim 0.03 \frac{\pi}{a}$ around the Γ point, as marked in the band map (b). In (b) the location of the band map is marked in the Fermi surface map in the inset. Note that this sample, cleaved at low temperature and ultra-high vacuum conditions, shows clear evidence of the reconstructed surface (as seen by the folded α' band), while those on which CPS-ARPES was performed did not. In either case no additional folded features will appear in an EDC at the Γ point, owing to the nature of the folding, which maps the X point (which has no features in that energy range) to the Γ point.

5.2. Measuring spin-orbital entanglement

calculated using the geometric formula

$$\tilde{P}^{\otimes} S_{\text{Motts}} = \frac{\sqrt{I_L^{\oplus} I_R^{\ominus}} - \sqrt{I_R^{\oplus} I_L^{\ominus}}}{\sqrt{I_L^{\oplus} I_R^{\ominus}} + \sqrt{I_R^{\oplus} I_L^{\ominus}}} \quad (5.1)$$

for each of the Mott polarimeter pairs. (Here S_{Motts} is the Sherman function, an empirically determined measure of the efficiency of a Mott pair, while I is the measured intensity for the left, L , and right, R , halves of the Mott pair using circular plus, \oplus , and minus, \ominus , light.) With the effects of dichroism eliminated the cross polarization will be equivalent to the true incoming electron polarization P given by

$$P = \frac{I_{\uparrow} - I_{\downarrow}}{I_{\uparrow} + I_{\downarrow}}; \quad (5.2)$$

however, we will continue to use \tilde{P}^{\otimes} everywhere the measured cross polarization was used. The total intensity from all detectors and light polarizations (I_T) was used with the measured cross polarizations to reconstruct the spin intensities according to $I_{\uparrow} = I_T(1 + \tilde{P}^{\otimes})/2$, $I_{\downarrow} = I_T(1 - \tilde{P}^{\otimes})/2$ for all three spatial dimensions and transformed into crystal coordinate directions according to the experimental geometry. Aspects of raw data analysis are presented in more detail in Appendix C, § C.1.

When the two states discussed in § 5.2.1 are observed with CPS-ARPES two distinct features, split in the z direction only, become apparent. This splitting was observed with both 24 eV (shown in Fig. 5.5) and 56 eV photons over two energy ranges (shown in Figs. 5.6 and 5.7). Estimating the splitting directly from the z direction curves [panel (e)] in each data set yields estimates of 83 meV, 101 meV, and 110 meV (respectively) for an average of 98 ± 14 meV. However owing to the experimental geometry (light incident at 45° relative to the analyzer), photons cannot be incident directly along the z direction (additionally there is a node in the final state preventing the experiment from being performed in the second Brillouin zone (BZ) with normal incident light and 45° emission). The result is that with equal probability the photons will interact either with m_{l_z} , resulting in spin-polarized

5.2. Measuring spin-orbital entanglement

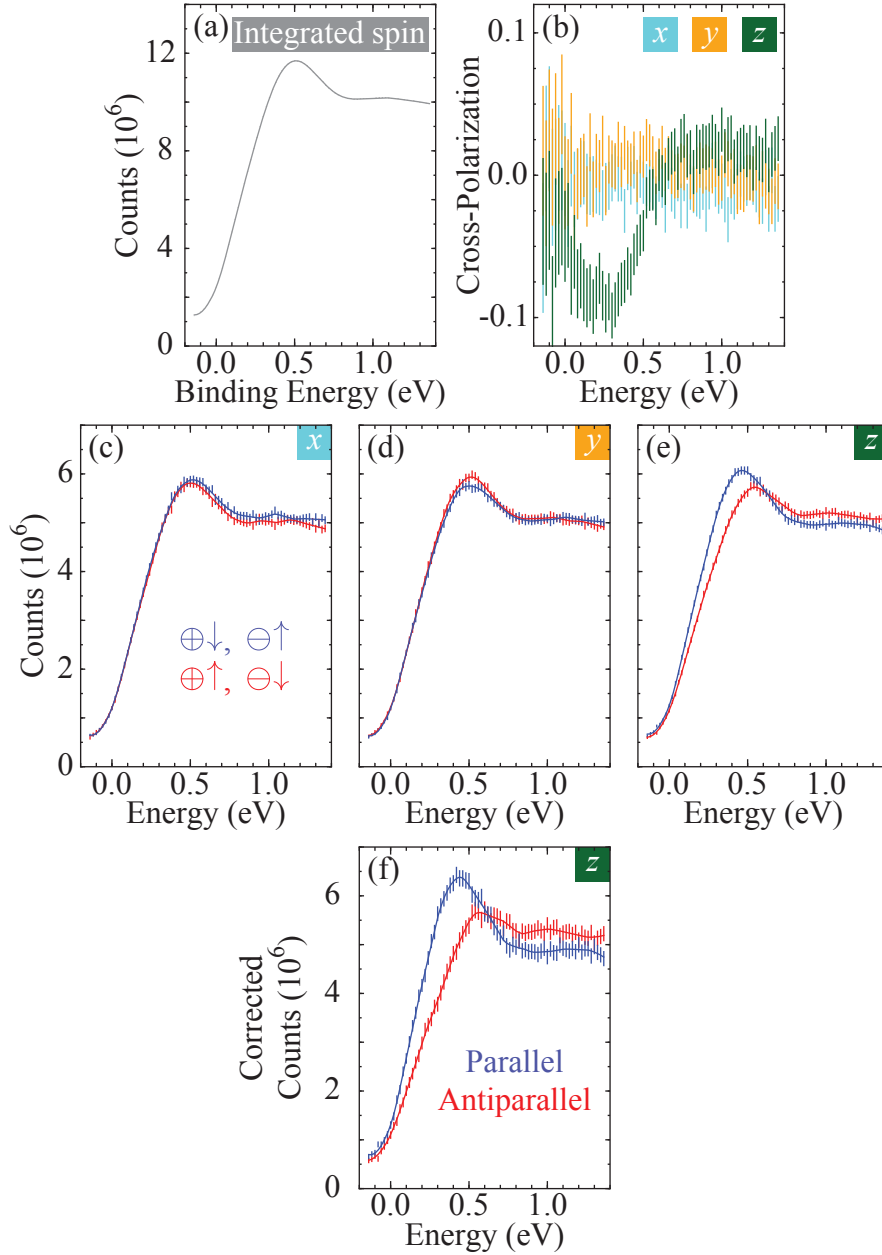


Figure 5.5: CPS-ARPES on Sr₂RuO₄ using 24 eV photon energy at the Γ point, measuring the states as highlighted in Fig. 5.3. (a) total intensity, (b) cross-polarization, and spin intensities (c–e) relative to the crystal coordinate directions. (f) shows the state intensity required to give the results in (e), corrected for photons incident at 45° and assuming no background. Error bars represent statistical uncertainty plotted at 95% confidence, with locally weighted [106] fits shown.

5.2. Measuring spin-orbital entanglement

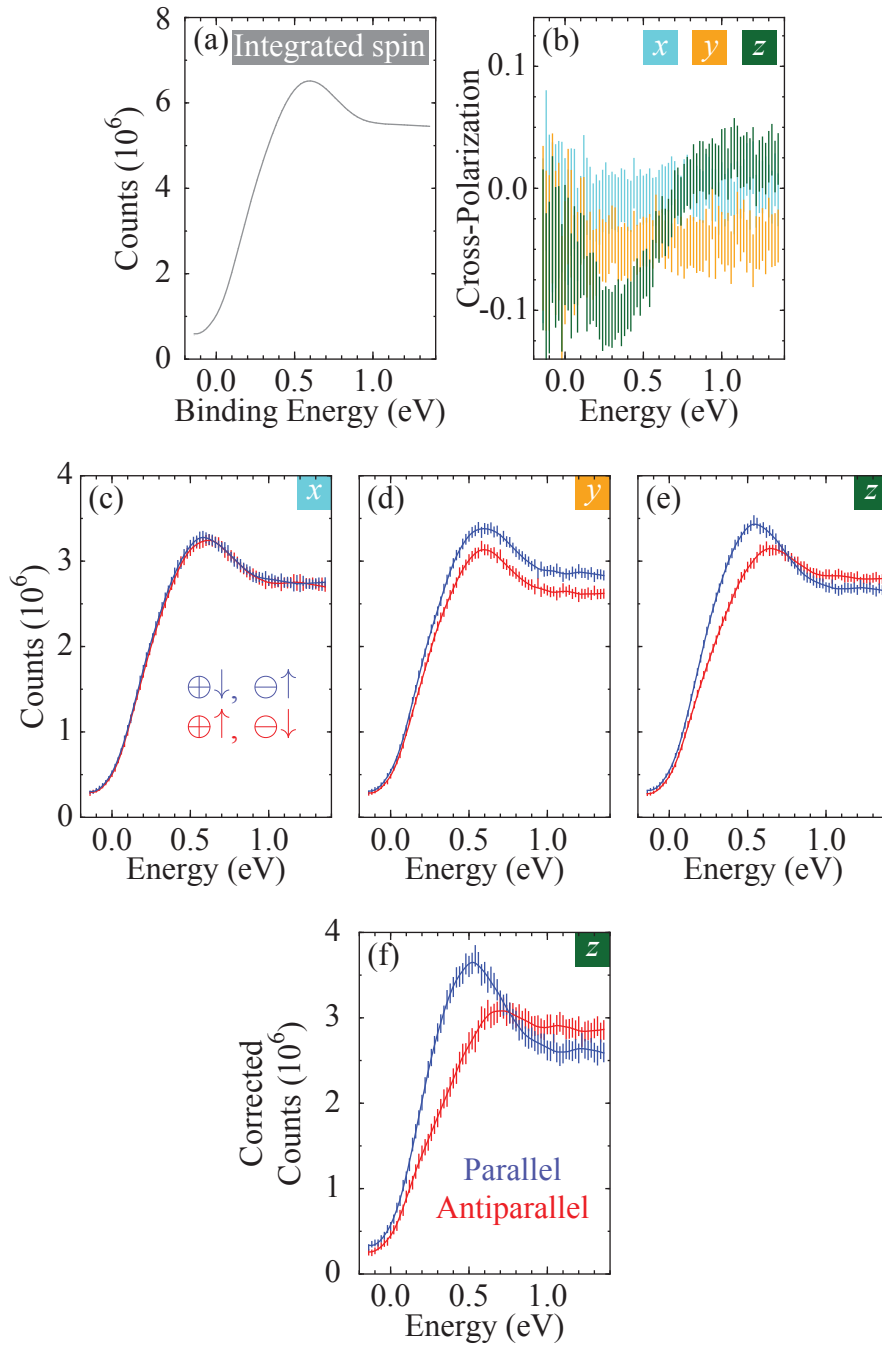


Figure 5.6: CPS-ARPES on Sr_2RuO_4 as in Fig. 5.5 but using 56 eV photon energy.

5.2. Measuring spin-orbital entanglement

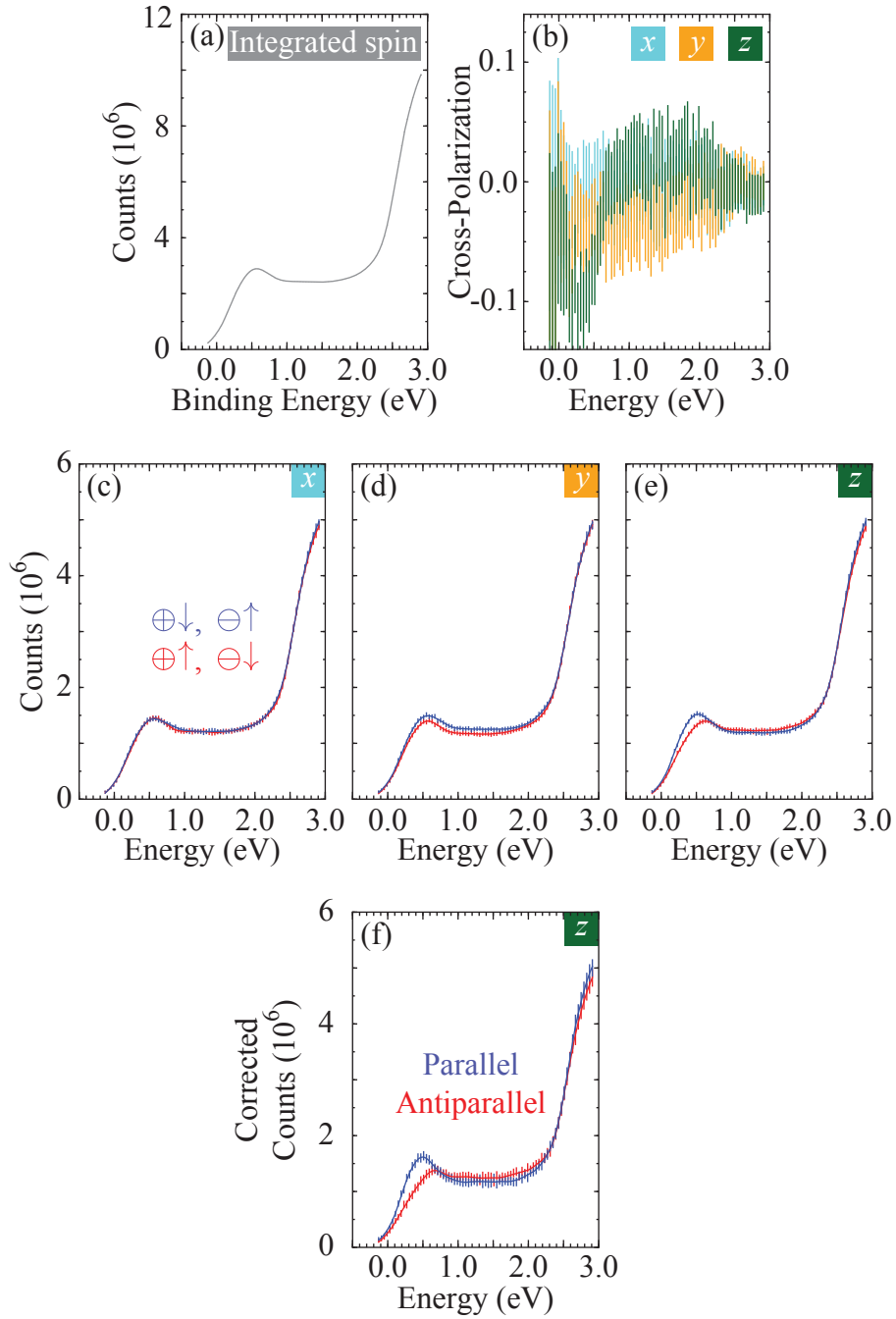


Figure 5.7: CPS-ARPES on Sr₂RuO₄ as in Figs. 5.5 and 5.6 but using 56 eV photon energy and over a greater energy range than that shown in Fig 5.6. (This represents a second data set, not the same data rescaled.)

5.2. Measuring spin-orbital entanglement

photoemission as described above, or with m_{l_x} , resulting in non-polarized photoemission (which will be measured as either \uparrow or \downarrow with equal probability from both parallel and antiparallel states). Therefore, in the z direction, the spin intensity (I) measured for the $(\oplus\downarrow, \ominus\uparrow)$ configuration will be given by

$$I_{\oplus\downarrow, \ominus\uparrow} = \frac{I_{\text{parallel}}}{2} + \frac{I_{\text{parallel}}}{4} + \frac{I_{\text{antiparallel}}}{4} \quad (5.3)$$

(and opposite for $I_{\oplus\uparrow, \ominus\downarrow}$). Here I_{parallel} and $I_{\text{antiparallel}}$ represent the total photoemission intensity given off by the states discussed in §5.2.1; the single term on the left represents the spin-polarized photoemission described above (divided by two due to half photons interacting with m_{l_z}), while the two terms on the right represent the non-spin polarized photoemission (divided by four due to half photons interacting with m_{l_x} , and half of those being measured as either up or down). This dilution causes a decrease in the observed splitting, which can be corrected for by taking

$$I_{\text{parallel}} = (3I_{\oplus\downarrow, \ominus\uparrow} - I_{\oplus\uparrow, \ominus\downarrow})/2 = I_T(1 - 2\tilde{P}^{\otimes})/2 \quad (5.4)$$

(and opposite for $I_{\text{antiparallel}}$) to recover the intensities from each state; this assumes that all observed intensity is from only these two states with no background. Such a correction is shown in panel (f) in each figure and results in splitting estimates of 125 meV, 184 meV, and 172 meV (respectively) for an average of 160 ± 30 meV. These limits represent an upper (160 ± 30 meV) and lower bound (98 ± 14 meV) on the splitting between these two states, which shows good agreement with the predicted splitting of $\zeta_{\text{eff}} \sim 90$ meV.

The possible enhancement of the energy splitting is another reminder of the importance of electronic correlations in this material. Most importantly, however, the existence of these two states, from which spin-polarized photoemission can be generated using circularly polarized light in the z direction only, is a clear confirmation of the theoretical prediction of SO coupling in Sr_2RuO_4 and its consequences for the entangled nature of the wave-functions.

5.3 Implications for pairing

To understand the impact of this entanglement on the description of superconductivity in this material, we must look at the basic building blocks of the Cooper pair. Cooper assumed the two-particle wave-function describing a Cooper pair to be of the form $\Psi(\mathbf{r}_1, \sigma_1, \mathbf{r}_2, \sigma_2) = \varphi(\mathbf{r}_1 - \mathbf{r}_2) \phi_{\sigma_1, \sigma_2}^{\text{spin}}$, assuming the momentum of the Cooper pair to be zero and where the spin part can be either singlet:

$$\phi_{\sigma_1, \sigma_2}^{\text{spin}} = \sqrt{\frac{1}{2}} (|\uparrow\downarrow\rangle - |\downarrow\uparrow\rangle) \quad (5.5)$$

(total spin $S = 0$) or triplet:

$$\phi_{\sigma_1, \sigma_2}^{\text{spin}} = \begin{cases} |\uparrow\downarrow\rangle \\ \sqrt{\frac{1}{2}} (|\uparrow\downarrow\rangle + |\downarrow\uparrow\rangle) \\ |\uparrow\uparrow\rangle \end{cases} \quad (5.6)$$

($S = 1$) [107, 108]. This allows one to classify superconductors in singlet or triplet paired states. However, a fundamental assumption to this description is that one can write the wave-function of each electron as a simple product of spatial and spin parts:

$$\psi(\mathbf{k}, \sigma) = \varphi(\mathbf{k}) \phi_{\sigma}^{\text{spin}}. \quad (5.7)$$

However, this separation into a product of independent charge and spin functions cannot be used when SO coupling is important; instead, the general equation becomes

$$\psi(\mathbf{k}, \sigma) = c_{\uparrow} \varphi_{\uparrow}(\mathbf{k}) \phi_{\uparrow}^{\text{spin}} + c_{\downarrow} \varphi_{\downarrow}(\mathbf{k}) \phi_{\downarrow}^{\text{spin}}, \quad (5.8)$$

with \uparrow and \downarrow specifying the spin, c_{\uparrow} and c_{\downarrow} eigenstate-dependent pre-factors, and φ_{\uparrow} and φ_{\downarrow} two independent wave-functions. In locations with strong mixing between φ_{\uparrow} and φ_{\downarrow} , it is not possible to use a description in terms of spin eigenstates.

In Fig. 5.8 we illustrate orbitals in real space showing spin character

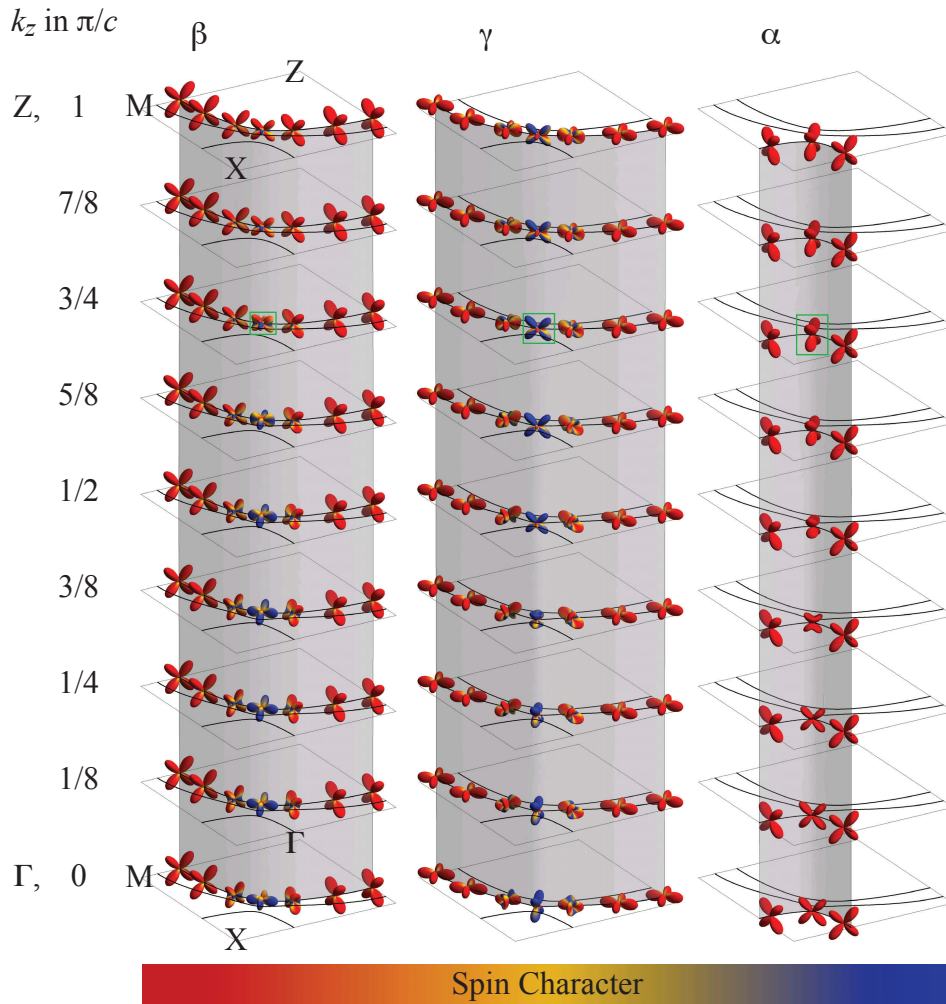


Figure 5.8: Orbitals illustrated in real space showing spin character in Sr_2RuO_4 for a variety of momentum space locations on the Fermi surface sheets as calculated by LMTO/NMTO+SO. Spin character is shown by colouring the orbitals according to spin character in the z direction for one half of the Kramers degenerate pair – all orbitals are degenerate with a second state that has opposite character. More detail is presented in Fig. 5.9 for the orbitals along the diagonal at $k_z = 3/4\pi/c$ – those highlighted here in green.

5.3. Implications for pairing

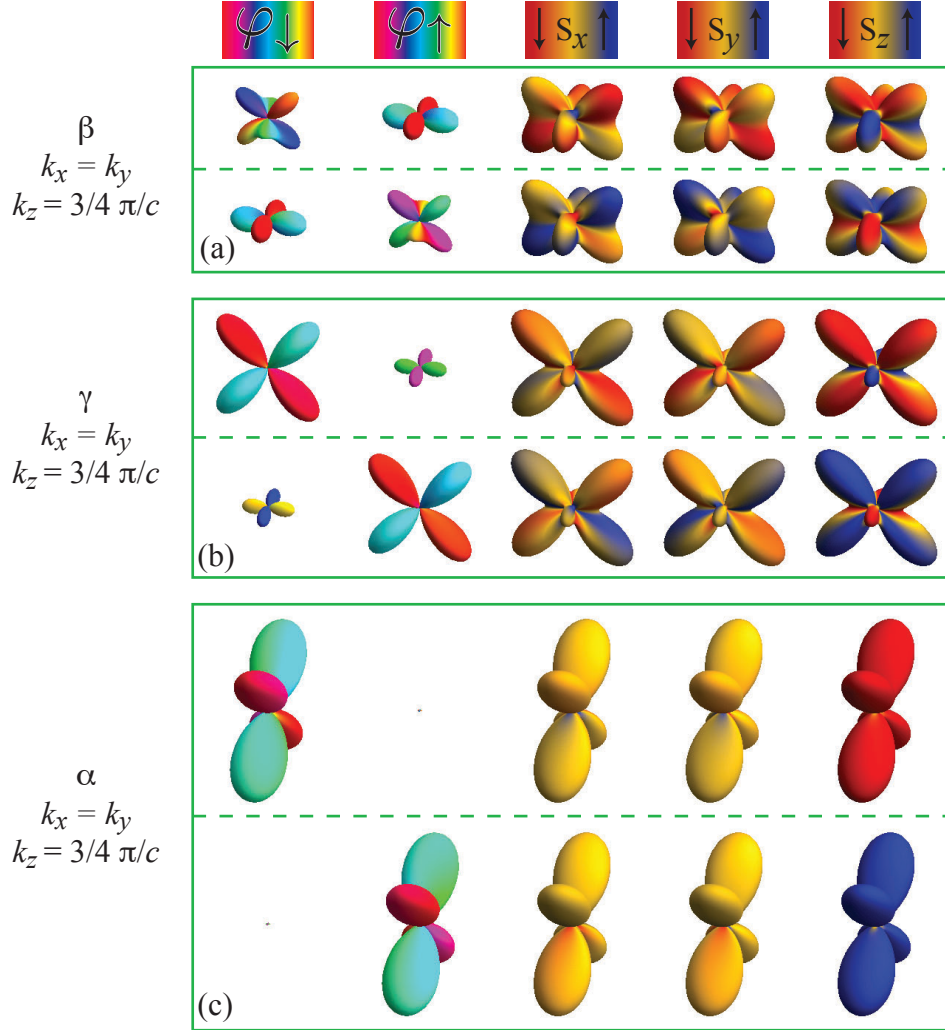


Figure 5.9: Orbitals illustrated in real space along the zone diagonal at $k_z = 3/4 \pi/c$, as highlighted in Fig. 5.8; (a–c) show the β , γ , and α bands, respectively. Here both halves of the Kramers degenerate pair are illustrated, showing, from left to right, the phase of both spin parts of the wave-function ($\varphi_{\downarrow}/\varphi_{\uparrow}$, quantized in the z direction) as well as spin expectation values in the x , y , and z directions. Note that the illustrations of spin character should not be interpreted to mean that these states could alternatively be represented by a single wave-function, as the phase information in φ_{\downarrow} and φ_{\uparrow} has been lost.

5.3. Implications for pairing

for a variety of momentum space locations on the Fermi surface sheets of Sr_2RuO_4 for one quarter of the BZ. Along the edges of the zone, e.g., near the intersections with $\Gamma \rightarrow \text{M}$ or $\text{Z} \rightarrow \text{M}$, we find that the orbitals do not show strong mixing, and we notice also that in these areas the β and α bands are of d_{xz}/d_{yz} orbital character, while the γ band is of d_{xy} character, as expected. At these locations the wave-function could be well approximated by a simple product of spatial and spin parts, as in Eq. 5.7. However, close to the zone diagonal, e.g., near the intersections of the sheets with $\Gamma \rightarrow \text{X}$ or $\text{Z} \rightarrow \text{X}$, this is not the case; here we find strong mixing in orbital character for all bands and, in the γ and β bands, also mixing in spin character. Orbitals from a selection of these locations with strong mixing, those directly along the zone diagonal at $k_z = 3/4\frac{\pi}{c}$, are chosen for a more detailed illustration in Fig. 5.9. In Fig. 5.9 we explicitly see how, for the γ and β that show strong spin mixing, this is a direct consequence of the fact that the wave-function cannot be split into independent charge and spin parts and can only be represented by Eq. 5.8.

As discussed earlier, Cooper took the momentum of a pair to be zero and the spin part to be either singlet or triplet. Even in cases where the wave-function cannot be separated into spin and spatial components as in Eq. 5.7, we can still work out the interaction of the spin between the canonical two states at \mathbf{k} and $-\mathbf{k}$ – and therefore whether the spin states are singlet/triplet or something else. We will follow this interaction, written as

$$H_{\text{int}}^{k,-k} \propto \vec{s}_{\mathbf{k}} \cdot \vec{s}_{-\mathbf{k}} \quad (5.9)$$

where \vec{s} is the spin operator, between these two states around the Fermi surface sheets for all three bands in Fig. 5.10. Regardless of the pairing glue in Sr_2RuO_4 , this total spin of the pair should be conserved. This is the case whether it be phonons or even a magnetic interaction, which fundamentally results from the Coulomb interaction.

In Fig. 5.10 we see that, between states at \mathbf{k} and $-\mathbf{k}$, spin does occasionally form a singlet/triplet system – for example, in the α band at $\Theta = 0, \pi/2$, and π . However, it does not do so elsewhere. For the β and γ bands we find

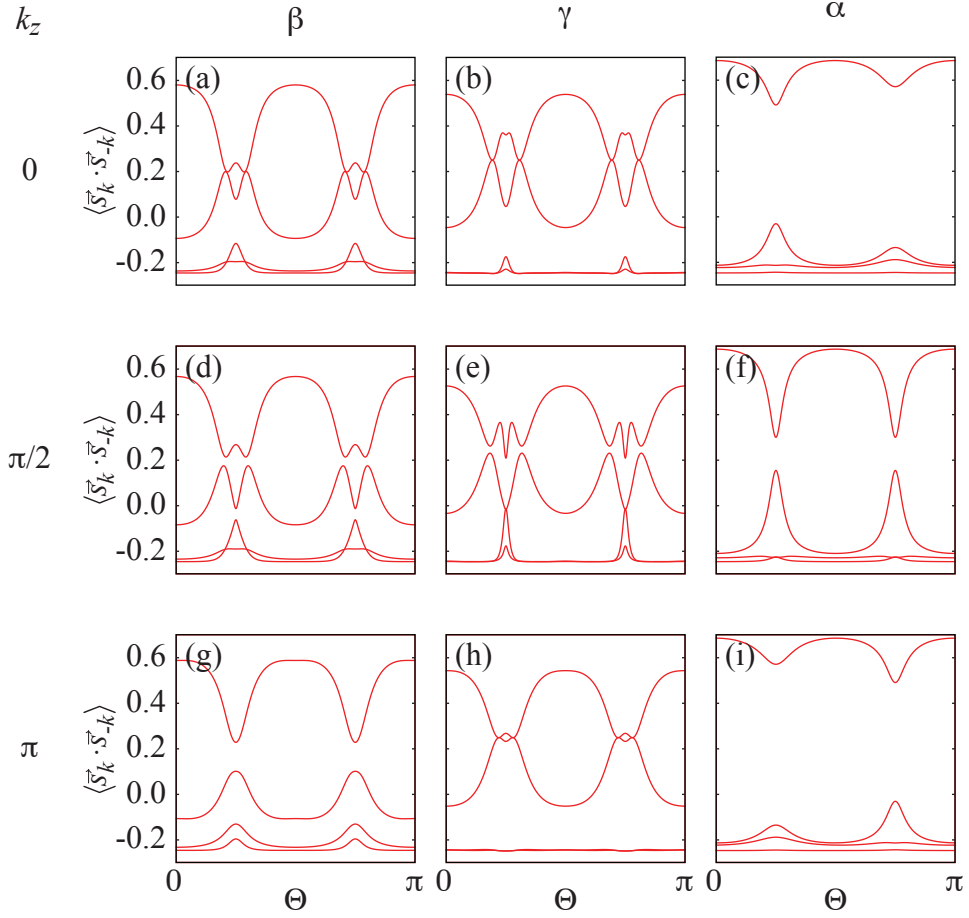


Figure 5.10: $\langle \vec{s}_{\mathbf{k}} \cdot \vec{s}_{-\mathbf{k}} \rangle$ around the Fermi surface sheets in Sr_2RuO_4 , as calculated by LMTO/NMTO+SO, for β (a,d,g), γ (b,e,h), and α (c,f,i) bands at $k_z = 0$ (a–c), $\pi/2$ (d–f), and π (g–i). The value of \mathbf{k} in the xy -plane is defined using Θ as in Fig. 5.1.

that occasionally there exists two doublets, but most often two singlets and a doublet. Overall, in all bands, we find that there exists much \mathbf{k} -dependent mixing between singlet/triplet, doublet/doublet, and other spin configurations rendering a description in terms of spin eigenstates meaningless.

5.4 Conclusion

In conclusion we have shown that Sr_2RuO_4 , a known unconventional superconductor, may well be much more unconventional than has been assumed so far. The theoretically predicted entanglement of spin and orbital descriptions has been experimentally confirmed with SARPES using circularly polarized light. This means that the states at the Fermi energy cannot be written as a simple product of charge and spin functions, resulting in a situation where one cannot build normal Cooper pairs in terms of pure spin singlet or triplet states. In the future it would be highly desirable to calculate the superconducting gap function using the relativistic LDA eigenstates and possible realistic superconducting pairing interactions. Such a description, by allowing mixed states, could reconcile the experimental results that suggest that the superconducting state in Sr_2RuO_4 cannot be purely triplet in character.

Chapter 6

Conclusion

This thesis covered many details over a range of topics, here we will recapitulate the main conclusions and their context.

The ARPES system at UBC

A state of the art angle-resolved photoemission spectroscopy (ARPES) system has been constructed and characterized here at the University of British Columbia (UBC). It has already begun producing publication-quality data on a wide variety of systems [6, 84, 109–111], and will continue to do so into the future.

Spectral Function Analysis

ARPES, by measuring the spectral function, provides access to an extremely rich data source. Not only can fundamental elements like the electronic band structure be resolved, but it is also possible to learn about the many-body electronic interactions in a system.

We have shown that none of the renormalizations measured in the quasi-particle dispersion necessarily scale linearly with the dimensionless coupling found in the Hamiltonian, as is often assumed in the interpretation of ARPES results. It should therefore be expected that in many real-world systems $\lambda_{\text{eff}} \neq \lambda$. This helps explain some of the exceedingly large renormalization values sometimes reported in ARPES literature [9–12], which, for example, have been as high as 30 (in Ref. 10). Understanding the mechanisms by which such renormalizations do not necessarily imply unphysically large couplings is a key step toward the correct interpretation of these results.

Additionally, we have developed and thoroughly tested a variety of methods that can be applied to determine the self-energy of the underlying interactions from the spectral function. A key difference between this and previous works along a similar vein, is the assessment of how our methods perform in the presence of a momentum-dependent self-energy. This is an important distinction as, while momentum independence is often assumed, it is unlikely to occur in real-world materials; at best it will be a question of *how much* momentum dependence exists. Further, it is not possible to know with certainty that a self-energy is momentum independent from simple lineshape alone – a Lorentzian form is a necessary, but not sufficient, condition. We show that by comparing quasiparticle renormalizations it is possible to determine the degree of momentum dependence in the vicinity of the quasi-particle peak. Additionally, we developed and presented two independent methods of determining the self-energy: Kramers–Kronig bare-band fitting (KKBF), which can find the self-energy if the momentum dependence is not too strong; and a lineshape ratio-based method, which will correctly produce the *form* of the self-energy regardless of its momentum-dependence anywhere the lineshape is Lorentzian.

These methods show promise for future ARPES studies, such as those led by B. Ludbrook on MgB₂, which is currently in preparation for publication. In this material, a multi-gap superconductor [112], it is thought that a strongly momentum-dependent electron-phonon coupling may be responsible for the differing gap sizes measured for each of the two bulk bands. Such a coupling would surely cause momentum-dependence in the self-energy of the quasiparticle excitations as well. This makes the use of our newly developed methods, which explicitly account for possible momentum-dependence, particularly valuable. Confidently determining the self-energy of the quasiparticle excitations in MgB₂ may help unlock the mystery of how the otherwise-conventional superconductivity in this material could be different between its two bands.

ARPES on Sr_2RuO_4

With the advancement of the ARPES technique a new set of features was recently discovered in data on Sr_2RuO_4 [6, 16, 113]; these features could not be explained by the existing model of surface reconstruction, and appeared to show a splitting that could be indicative of a wide variety of phenomena. Through extensive ARPES measurements on these newly discovered features, and a comparison against both bulk and slab local-density approximation (LDA) calculations with the inclusion of spin-orbit (SO) coupling, we have shown that the structural reconstruction observed on the surface must progressively relax into the bulk; this causes a corresponding progression in the electronic band structure, which explains all features and their observed characteristics. In addition to the implications for the study of Sr_2RuO_4 it is likely that, in other materials with a surface reconstruction, a similar progression of states may exist. In much the same way that ARPES results on Sr_2RuO_4 were originally resolved as being due to a surface reconstruction [56], this work demonstrates that it is now necessary to consider also the structure of the sub-surface layers. Such considerations will become ever more important as advancements continue in both the resolution of ARPES systems as well as the level of detail with which materials are studied.

In addition to demonstrating the existence of a progression of electronic structure from the surface to the bulk, this work also provides the most detailed information yet presented on Fermi surface volumes and velocities for both the surface and sub-surface layers, as well as the many body renormalization of these velocities as compared to LDA. The progression of renormalizations, in particular, demonstrates a strong enhancement of electronic correlations in the surface layer. This may be due to reduced dimensionality, and similar enhancements have recently been observed in other materials as well – for example the underdoped cuprates [84, 90].

The morals of this story also show strong ties to the rapidly advancing field of interface-physics, by demonstrating that the effects of the surface interface propagate over multiple layers and that its reduced dimensionality

strongly enhances the electronic correlations. By exploiting and combining such effects through engineered interfaces and layers, the field of interface-physics shows promise as an avenue for the future development of next-generation electronic devices in much the same way that semiconductors revolutionized and brought about the electronics we enjoy today.

CPS-ARPES, Spin-orbit coupling, and superconductivity in Sr_2RuO_4

Problems exist in the current struggle to classify the superconductivity in Sr_2RuO_4 , specifically the spin-configuration of the paired electrons. While some experiments show that Sr_2RuO_4 is a chiral p -wave spin-triplet superconductor [92–94], others cannot be fully explained by such a description [96–98] – specifically regarding the spin-triplet nature of the pairing interaction. The SO interaction, expected to be significant for a heavy transition metal like ruthenium, offers a possible resolution to this conflict by coupling the spin and motion of electrons in the lattice. While the band-structure predictions of SO coupling have previously been confirmed for Sr_2RuO_4 [17], the actual coupling of spin and orbital descriptions has not. It is this entanglement between spin and orbital motion that we probed directly and confirmed with circularly polarized photon spin- and angle-resolved photoemission spectroscopy (CPS-ARPES).

By confirming this coupling between the spin and orbital motion of the electrons we directly show that the usual method of writing the electronic wave-function as product of independent spin and spatial parts is invalid. This interferes with the first steps of writing a Cooper pair under the normal description. Additionally, we calculate the spin-eigenstates for the canonical pair of electrons around the Fermi surface, for all bands, using the full SO description and show that the available spin-eigenstates vary continuously between singlet-triplet, doublet-doublet, and other spin configurations. This shows that attempting to classify the pairing in Sr_2RuO_4 as “spin-triplet” is not actually meaningful, and that the pairing must instead be even *more* unconventional than is generally assumed. Moving forward, it would be

highly desirable to calculate superconducting properties using possible realistic pairing interactions and the full relativistic LDA+SO eigenstates. By allowing mixed and transitory states, such a description provides more spin configurations than the traditional singlet–triplet eigenstates, as well as a means for the apparent spin-state of the pair to change; neither of these things are possible using the regular formulation. This could reconcile the conflicting experimental results on the pairing in Sr_2RuO_4 , and pave the way for its complete description. Such calculations, led by M. W. Haverkort, are already underway.

These results on Sr_2RuO_4 directly probing the coupling of spin to orbit should be expected to apply also to other $4d$ and heavier transition metal oxides, for example the Iridates, although less so to the $3d$ group.

Bibliography

- [1] C. N. Veenstra, G. L. Goodvin, M. Berciu, and A. Damascelli, “Elusive electron–phonon coupling in quantitative analyses of the spectral function,” *Phys. Rev. B*, vol. 82, p. 012504, Jul 2010.
- [2] C. N. Veenstra, G. L. Goodvin, M. Berciu, and A. Damascelli, “Spectral function tour of electron–phonon coupling outside the Migdal limit,” *Phys. Rev. B*, vol. 84, p. 085126, Aug 2011.
- [3] G. L. Goodvin and M. Berciu, “Momentum average approximation for models with electron–phonon coupling dependent on the phonon momentum,” *Phys. Rev. B*, vol. 78, p. 235120, Dec 2008.
- [4] M. Berciu and G. L. Goodvin, “Systematic improvement of the momentum average approximation for the Green’s function of a Holstein polaron,” *Phys. Rev. B*, vol. 76, p. 165109, Oct 2007.
- [5] M. Berciu, “Green’s function of a dressed particle,” *Phys. Rev. Lett.*, vol. 97, p. 036402, Jul 2006.
- [6] C. N. Veenstra, Z.-H. Zhu, B. Ludbrook, M. Capsoni, G. Levy, A. Nicolaou, J. A. Rosen, R. Comin, S. Kittaka, Y. Maeno, I. S. Elfimov, and A. Damascelli, “Unravelling the surface-to-bulk progression of the electronic structure in Sr_2RuO_4 ,” *ArXiv e-prints*, 1205.4248, May 2012.
- [7] A. Damascelli, “Probing the electronic structure of complex systems by ARPES,” *Physica Scripta*, vol. T109, p. 61, 2004.
- [8] A. Migdal, “Interactions between electrons and lattice vibrations in a normal metal,” *Sov. Phys. JETP*, vol. 34, no. 6, p. 996, 1958.

- [9] A. Lanzara, P. V. Bogdanov, X. J. Zhou, S. A. Kellar, D. L. Feng, E. D. Lu, T. Yoshida, H. Eisaki, A. Fujimori, K. Kishio, J.-I. Shimoyama, T. Noda, S. Uchida, Z. Hussain, and Z.-X. Shen, “Evidence for ubiquitous strong electron–phonon coupling in high-temperature superconductors,” *Nature*, vol. 412, p. 510, 2001.
- [10] A. Kaminski, M. Randeria, J. C. Campuzano, M. R. Norman, H. Fretwell, J. Mesot, T. Sato, T. Takahashi, and K. Kadowaki, “Renormalization of spectral line shape and dispersion below T_c in $\text{Bi}_2\text{Sr}_2\text{CaCu}_2\text{O}_{8+\delta}$,” *Phys. Rev. Lett.*, vol. 86, p. 1070, Feb 2001.
- [11] T. K. Kim, A. A. Kordyuk, S. V. Borisenko, A. Koitzsch, M. Knupfer, H. Berger, and J. Fink, “Doping dependence of the mass enhancement in $(\text{Pb,Bi})_2\text{Sr}_2\text{CaCu}_2\text{O}_8$ at the antinodal point in the superconducting and normal states,” *Phys. Rev. Lett.*, vol. 91, no. 16, p. 167002, 2003.
- [12] N. Mannella, W. L. Yang, X. J. Zhou, H. Zheng, J. F. Mitchell, J. Zaanen, T. P. Devereaux, N. Nagaosa, Z. Hussain, and Z.-X. Shen, “Nodal quasiparticle in pseudogapped colossal magnetoresistive manganites,” *Nature*, vol. 438, p. 474, 2005.
- [13] Y. Maeno, H. Hashimoto, K. Yoshida, S. Nishizaki, T. Fujita, J. G. Bednorz, and F. Lichtenberg, “Superconductivity in a layered perovskite without copper,” *Nature*, vol. 372, p. 532, 1994.
- [14] C. Bergemann, A. P. Mackenzie, S. R. Julian, D. Forsythe, and E. Ohmichi, “Quasi-two-dimensional Fermi liquid properties of the unconventional superconductor Sr_2RuO_4 ,” *Advances in Physics*, vol. 52, no. 7, p. 639, 2003.
- [15] N. J. C. Ingle, K. M. Shen, F. Baumberger, W. Meevasana, D. H. Lu, Z.-X. Shen, A. Damascelli, S. Nakatsuji, Z. Q. Mao, Y. Maeno, T. Kimura, and Y. Tokura, “Quantitative analysis of Sr_2RuO_4 angle-resolved photoemission spectra: Many-body interactions in a model Fermi liquid,” *Phys. Rev. B*, vol. 72, p. 205114, Nov 2005.

- [16] V. B. Zabolotnyy, E. Carleschi, T. K. Kim, A. A. Kordyuk, J. Trinkauf, J. Geck, D. Evtushinsky, B. P. Doyle, R. Fittipaldi, M. Cuoco, A. Vecchione, B. Behner, and S. V. Borisenko, “Surface and bulk electronic structure of the unconventional superconductor Sr_2RuO_4 : unusual splitting of the β band,” *New Journal of Physics*, vol. 14, no. 6, p. 063039, 2012.
- [17] M. W. Haverkort, I. S. Elfimov, L. H. Tjeng, G. A. Sawatzky, and A. Damascelli, “Strong spin–orbit coupling effects on the Fermi surface of Sr_2RuO_4 and Sr_2RhO_4 ,” *Phys. Rev. Lett.*, vol. 101, p. 026406, Jul 2008.
- [18] T. Valla, A. V. Fedorov, P. D. Johnson, and S. L. Hulbert, “Many-body effects in angle-resolved photoemission: Quasiparticle energy and lifetime of a Mo(110) surface state,” *Phys. Rev. Lett.*, vol. 83, p. 2085, Sep 1999.
- [19] Z.-X. Shen, A. Lanzara, S. Ishihara, and N. Nagaosa, “Role of the electron–phonon interaction in the strongly correlated cuprate superconductors,” *Phil. Mag. B*, vol. 82, p. 1349, September 2002.
- [20] M. L. Kubic, “Interplay of electron–phonon interaction and strong correlations: the possible way to high-temperature superconductivity,” *Phys. Reports*, vol. 338, no. 1–2, p. 1, 2000.
- [21] G. Mahan, *Many-Particle Physics*. Plenum, 2nd ed., 1981.
- [22] G. Grimvall, *The Electron–Phonon Interaction in Metals*. Elsevier, 1981.
- [23] A. A. Kordyuk, S. V. Borisenko, A. Koitzsch, J. Fink, M. Knupfer, and H. Berger, “Bare electron dispersion from experiment: Self-consistent self-energy analysis of photoemission data,” *Phys. Rev. B*, vol. 71, p. 214513, Jun 2005.

- [24] F. Giustino, M. L. Cohen, and S. G. Louie, “Small phonon contribution to the photoemission kink in the copper oxide superconductors,” *Nature*, vol. 452, p. 975, 2008.
- [25] D. Reznik, G. Sangiovanni, O. Gunnarsson, and T. P. Devereaux, “Photoemission kinks and phonons in cuprates,” *Nature*, vol. 455, p. E6, 2008.
- [26] R. Heid, K.-P. Bohnen, R. Zeyher, and D. Manske, “Momentum dependence of the electron–phonon coupling and self-energy effects in superconducting $\text{YBa}_2\text{Cu}_3\text{O}_7$ within the local density approximation,” *Phys. Rev. Lett.*, vol. 100, p. 137001, Mar 2008.
- [27] R. Heid, R. Zeyher, D. Manske, and K.-P. Bohnen, “Phonon-induced pairing interaction in $\text{YBa}_2\text{Cu}_3\text{O}_7$ within the local-density approximation,” *Phys. Rev. B*, vol. 80, p. 024507, Jul 2009.
- [28] S. Johnston, F. Vernay, B. Moritz, Z.-X. Shen, N. Nagaosa, J. Zaanen, and T. P. Devereaux, “Systematic study of electron–phonon coupling to oxygen modes across the cuprates,” *Phys. Rev. B*, vol. 82, p. 064513, Aug 2010.
- [29] P. Monthoux, “Migdal’s theorem and the pseudogap,” *Phys. Rev. B*, vol. 68, p. 064408, Aug 2003.
- [30] R. J. Wojciechowski, “Migdal’s theorem in heavy Fermion systems,” *Physica B*, vol. 259–261, p. 498, 1999.
- [31] C. Grimaldi, L. Pietronero, and S. Strässler, “Nonadiabatic superconductivity: Electron–phonon interaction beyond Migdal’s theorem,” *Phys. Rev. Lett.*, vol. 75, p. 1158, Aug 1995.
- [32] T. Valla, A. V. Fedorov, P. D. Johnson, B. O. Wells, S. L. Hulbert, Q. Li, G. D. Gu, and N. Koshizuka, “Evidence for quantum critical behavior in the optimally doped cuprate $\text{Bi}_2\text{Sr}_2\text{CaCu}_2\text{O}_{8+\delta}$,” *Science*, vol. 285, no. 5436, p. 2110, 1999.

- [33] A. Damascelli, Z. Hussain, and Z.-X. Shen, “Angle-resolved photoemission studies of the cuprate superconductors,” *Rev. Mod. Phys.*, vol. 75, p. 473, Apr 2003.
- [34] J. C. Campuzano, M. R. Norman, and M. Randeria, *Photoemission in the High T_c Superconductors*, vol. II, pp. 167–265. Berlin: Springer, 2004.
- [35] A. Kaminski and H. M. Fretwell, “On the extraction of the self-energy from angle-resolved photoemission spectroscopy,” *New J. Phys.*, vol. 7, p. 98, 2005.
- [36] E. G. Maksimov, M. L. Kubic, and O. V. Dolgov, “Bosonic spectral function and the electron–phonon interaction in HTSC cuprates,” *Adv. Cond. Mat. Phys.*, 2010. Article ID 423725.
- [37] M. Randeria, A. Paramekanti, and N. Trivedi, “Nodal quasiparticle dispersion in strongly correlated d -wave superconductors,” *Phys. Rev. B*, vol. 69, p. 144509, Apr 2004.
- [38] P. Werner and A. J. Millis, “Efficient dynamical mean field simulation of the Holstein-Hubbard model,” *Phys. Rev. Lett.*, vol. 99, p. 146404, Oct 2007.
- [39] A. Knigavko and J. P. Carbotte, “Effects of finite bandwidth on spectroscopic characteristics of normal metals,” *Phys. Rev. B*, vol. 72, p. 035125, Jul 2005.
- [40] E. Cappelluti and L. Pietronero, “electron–phonon renormalization in small Fermi energy systems,” *Phys. Rev. B*, vol. 68, p. 224511, Dec 2003.
- [41] B. Lau, M. Berciu, and G. A. Sawatzky, “Single-polaron properties of the one-dimensional breathing-mode Hamiltonian,” *Phys. Rev. B*, vol. 76, p. 174305, Nov 2007.
- [42] T. Holstein, “Studies of polaron motion,” *Ann. Phys.*, vol. 8, p. 325, 1959.

- [43] M. Eschrig and M. R. Norman, “Effect of the magnetic resonance on the electronic spectra of high- T_c superconductors,” *Phys. Rev. B*, vol. 67, p. 144503, Apr 2003.
- [44] Z. Li, D. Baillie, C. Blois, and F. Marsiglio, “Ground-state properties of the Holstein model near the adiabatic limit,” *Phys. Rev. B*, vol. 81, p. 115114, Mar 2010.
- [45] A. Alvermann, H. Fehske, and S. A. Trugman, “Polarons and slow quantum phonons,” *Phys. Rev. B*, vol. 81, p. 165113, Apr 2010.
- [46] M. Capone, S. Ciuchi, and C. Grimaldi, “The small-polaron crossover: Comparison between exact results and vertex correction approximation,” *Europhys. Lett.*, vol. 42, no. 5, p. 523, 1998.
- [47] M. Capone, W. Stephan, and M. Grilli, “Small-polaron formation and optical absorption in Su–Schrieffer–Heeger and Holstein models,” *Phys. Rev. B*, vol. 56, p. 4484, Aug 1997.
- [48] F. Marsiglio, “Pairing in the Holstein model in the dilute limit,” *Physica C*, vol. 244, pp. 21–34, 1995.
- [49] G. Lepage, “A new algorithm for adaptive multidimensional integration,” *J. Comput. Phys.*, vol. 27, p. 192, 1978.
- [50] G. Lepage, “VEGAS: An adaptive multi-dimensional integration program,” *Cornell preprint CLNS*, vol. 80, p. 447, 1980.
- [51] M. Galassi, J. Davies, J. Theiler, B. Gough, G. Jungman, P. Alken, M. Booth, and F. Rossi, *GNU Scientific Library Reference Manual – Third Edition (v1.15)*. Network Theory Ltd, 2011.
- [52] C. Kim, W. Kyung, S. Park, C. Leem, D. Song, Y. Kim, S. Choi, W. Jung, Y. Koh, H. Choi, Y. Yoshida, R. Moore, Z.-X. Shen, and C. Kim, “Self-energy analysis of multiple-bosonic mode coupling in Sr_2RuO_4 ,” *Journal of Physics and Chemistry of Solids*, vol. 72, no. 5, p. 556, 2011.

- [53] C. B. Markwardt, “Non-linear least squares fitting in IDL with MPFIT,” *ArXiv e-prints*, 0902.2850, Nov. 2009.
- [54] A. P. Mackenzie, S. R. Julian, A. J. Diver, G. J. McMullan, M. P. Ray, G. G. Lonzarich, Y. Maeno, S. Nishizaki, and T. Fujita, “Quantum oscillations in the layered perovskite superconductor Sr_2RuO_4 ,” *Phys. Rev. Lett.*, vol. 76, p. 3786, May 1996.
- [55] C. Bergemann, S. R. Julian, A. P. Mackenzie, S. Nishizaki, and Y. Maeno, “Detailed topography of the Fermi surface of Sr_2RuO_4 ,” *Phys. Rev. Lett.*, vol. 84, p. 2662, Mar 2000.
- [56] A. Damascelli, D. H. Lu, K. M. Shen, N. P. Armitage, F. Ronning, D. L. Feng, C. Kim, Z.-X. Shen, T. Kimura, Y. Tokura, Z. Q. Mao, and Y. Maeno, “Fermi surface, surface states, and surface reconstruction in Sr_2RuO_4 ,” *Phys. Rev. Lett.*, vol. 85, p. 5194, Dec 2000.
- [57] G.-Q. Liu, V. N. Antonov, O. Jepsen, and O. K. Andersen., “Coulomb-enhanced spin-orbit splitting: The missing piece in the Sr_2RhO_4 puzzle,” *Phys. Rev. Lett.*, vol. 101, p. 026408, Jul 2008.
- [58] K. M. Shen, A. Damascelli, D. H. Lu, N. P. Armitage, F. Ronning, D. L. Feng, C. Kim, Z.-X. Shen, D. J. Singh, I. I. Mazin, S. Nakatsuji, Z. Q. Mao, Y. Maeno, T. Kimura, and Y. Tokura, “Surface electronic structure of Sr_2RuO_4 ,” *Phys. Rev. B*, vol. 64, p. 180502, Oct 2001.
- [59] R. Matzdorf, Z. Fang, Ismail, J. Zhang, T. Kimura, Y. Tokura, K. Terakura, and E. W. Plummer, “Ferromagnetism stabilized by lattice distortion at the surface of the p -wave superconductor Sr_2RuO_4 ,” *Science*, vol. 289, no. 5480, p. 746, 2000.
- [60] R. Matzdorf, Ismail, T. Kimura, Y. Tokura, and E. W. Plummer, “Surface structural analysis of the layered perovskite Sr_2RuO_4 by LEED $I(V)$,” *Phys. Rev. B*, vol. 65, p. 085404, Jan 2002.
- [61] R. G. Moore, V. B. Nascimento, J. Zhang, J. Rundgren, R. Jin, D. Mandrus, and E. W. Plummer, “Manifestations of broken symme-

Bibliography

- try: The surface phases of $\text{Ca}_{2-x}\text{Sr}_x\text{RuO}_4$,” *Phys. Rev. Lett.*, vol. 100, p. 066102, Feb 2008.
- [62] S. Kashiwaya, H. Kashiwaya, H. Kambara, T. Furuta, H. Yaguchi, Y. Tanaka, and Y. Maeno, “Edge states of Sr_2RuO_4 detected by in-plane tunneling spectroscopy,” *Phys. Rev. Lett.*, vol. 107, p. 077003, Aug 2011.
- [63] L. Walz and F. Lichtenberg, “Refinement of the structure of Sr_2RuO_4 with 100 and 295 K X-ray data,” *Acta Crystallographica Section C*, vol. 49, p. 1268, Jul 1993.
- [64] M. Braden, A. Moudden, S. Nishizaki, Y. Maeno, and T. Fujita, “Structural analysis of Sr_2RuO_4 ,” *Physica C: Superconductivity*, vol. 273, no. 34, p. 248, 1997.
- [65] Q. Huang, J. Soubeyroux, O. Chmaissem, I. Sora, A. Santoro, R. Cava, J. Krajewski, and W. P. Jr., “Neutron powder diffraction study of the crystal structures of Sr_2RuO_4 and Sr_2IrO_4 at room temperature and at 10 K,” *Journal of Solid State Chemistry*, vol. 112, no. 2, p. 355, 1994.
- [66] J. Gardner, G. Balakrishnan, and D. Paul, “Neutron powder diffraction studies of Sr_2RuO_4 and SrRuO_3 ,” *Physica C: Superconductivity*, vol. 252, no. 34, p. 303, 1995.
- [67] J. J. Neumeier, M. F. Hundley, M. G. Smith, J. D. Thompson, C. Allgeier, H. Xie, W. Yelon, and J. S. Kim, “Magnetic, thermal, transport, and structural properties of $\text{Sr}_2\text{RuO}_{4+\delta}$: Enhanced charge-carrier mass in a nearly metallic oxide,” *Phys. Rev. B*, vol. 50, p. 17910, Dec 1994.
- [68] A. Liebsch, “Comment on ‘Fermi surface, surface states, and surface reconstruction in Sr_2RuO_4 ’,” *Phys. Rev. Lett.*, vol. 87, p. 239701, Nov 2001.

- [69] A. Damascelli, K. M. Shen, D. H. Lu, and Z.-X. Shen, “Damascelli *et al.* reply:,” *Phys. Rev. Lett.*, vol. 87, p. 239702, Nov 2001.
- [70] R. G. Moore, M. D. Lumsden, M. B. Stone, J. Zhang, Y. Chen, J. W. Lynn, R. Jin, D. Mandrus, and E. W. Plummer, “Phonon softening and anomalous mode near the $x_c = 0.5$ quantum critical point in $\text{Ca}_{2-x}\text{Sr}_x\text{RuO}_4$,” *Phys. Rev. B*, vol. 79, p. 172301, May 2009.
- [71] R. G. Moore, *Manifestations of Broken Symmetry: The Surface Phases of $\text{Ca}_{2-x}\text{Sr}_x\text{RuO}_4$* . PhD thesis, University of Tennessee, 2006.
- [72] T. Ando, T. Akima, Y. Mori, and Y. Maeno, “Upper critical fields of the 3-K superconducting phase of Sr_2RuO_4 ,” *Journal of the Physical Society of Japan*, vol. 68, no. 5, p. 1651, 1999.
- [73] Z. Mao, Y. Maeno, and H. Fukazawa, “Crystal growth of Sr_2RuO_4 ,” *Materials Research Bulletin*, vol. 35, no. 11, p. 1813, 2000.
- [74] S. Julian, A. Mackenzie, G. Lonzarich, C. Bergemann, R. Haselwimmer, Y. Maeno, S. NishiZaki, A. Tyler, S. Ikeda, and T. Fujita, “Normal state, superconductivity and quasiparticle Fermi surface of the strongly correlated oxide Sr_2RuO_4 ,” *Physica B: Condensed Matter*, vol. 259261, no. 0, p. 928, 1999.
- [75] C. Bergemann, J. Brooks, L. Balicas, A. Mackenzie, S. Julian, Z. Mao, and Y. Maeno, “Normal state of the unconventional superconductor Sr_2RuO_4 in high magnetic fields,” *Physica B: Condensed Matter*, vol. 294295, no. 0, p. 371, 2001. Proceedings of the Sixth International Symposium on Research in High Magnetic Fields.
- [76] Y. Maeno, T. Ando, Y. Mori, E. Ohmichi, S. Ikeda, S. NishiZaki, and S. Nakatsuji, “Enhancement of superconductivity of Sr_2RuO_4 to 3 K by embedded metallic microdomains,” *Phys. Rev. Lett.*, vol. 81, p. 3765, Oct 1998.
- [77] S. Kittaka, H. Yaguchi, and Y. Maeno, “Large enhancement of 3-K phase superconductivity in the Sr_2RuO_4 –Ru eutectic system by

- uniaxial pressure,” *Journal of the Physical Society of Japan*, vol. 78, no. 10, p. 103705, 2009.
- [78] S. Kittaka, H. Taniguchi, S. Yonezawa, H. Yaguchi, and Y. Maeno, “Higher- T_c superconducting phase in Sr_2RuO_4 induced by uniaxial pressure,” *Phys. Rev. B*, vol. 81, p. 180510, May 2010.
- [79] Y. Pennec, N. Ingle, I. Elfimov, E. Varene, Y. Maeno, A. Damascelli, and J. Barth, “Cleaving-temperature dependence of layered-oxide surfaces,” *Phys. Rev. Lett.*, vol. 101, p. 216103, 2008.
- [80] P. Aebi, J. Osterwalder, P. Schwaller, L. Schlapbach, M. Shimoda, T. Mochiku, and K. Kadowaki, “Complete Fermi surface mapping of $\text{Bi}_2\text{Sr}_2\text{CaCu}_2\text{O}_{8+x}(001)$: Coexistence of short range antiferromagnetic correlations and metallicity in the same phase,” *Phys. Rev. Lett.*, vol. 72, p. 2757, Apr 1994.
- [81] A. Mans, I. Santoso, Y. Huang, W. K. Siu, S. Tavaddod, V. Arpiainen, M. Lindroos, H. Berger, V. N. Strocov, M. Shi, L. Patthey, and M. S. Golden, “Experimental proof of a structural origin for the shadow Fermi surface of $\text{Bi}_2\text{Sr}_2\text{CaCu}_2\text{O}_{8+\delta}$,” *Phys. Rev. Lett.*, vol. 96, p. 107007, Mar 2006.
- [82] K. Nakayama, T. Sato, T. Dobashi, K. Terashima, S. Souma, H. Matsui, T. Takahashi, J. C. Campuzano, K. Kudo, T. Sasaki, N. Kobayashi, T. Kondo, T. Takeuchi, K. Kadowaki, M. Kofu, and K. Hirota, “Shadow bands in single-layered $\text{Bi}_2\text{Sr}_2\text{CuO}_{6+\delta}$ studied by angle-resolved photoemission spectroscopy,” *Phys. Rev. B*, vol. 74, p. 054505, Aug 2006.
- [83] P. D. C. King, J. A. Rosen, W. Meevasana, A. Tamai, E. Rozbicki, R. Comin, G. Levy, D. Fournier, Y. Yoshida, H. Eisaki, K. M. Shen, N. J. C. Ingle, A. Damascelli, and F. Baumberger, “Structural origin of apparent Fermi surface pockets in angle-resolved photoemission of $\text{Bi}_2\text{Sr}_{2-x}\text{La}_x\text{CuO}_{6+\delta}$,” *Phys. Rev. Lett.*, vol. 106, p. 127005, Mar 2011.

- [84] J. A. Rosen, R. Comin, G. Levy, D. Fournier, Z.-H. Zhu, B. Ludbrook, C. N. Veenstra, D. Wong, P. Dosanjh, Y. Yoshida, H. Eisaki, L. Petaccia, and A. Damascelli, “Evidence for charge-density-wave in underdoped Bi2201 from ARPES and LEED,” *ArXiv e-prints*, 1111.2673, Nov. 2011.
- [85] P. Blaha, K. Schwarz, G. K. H. Madsen, D. Kvasnicka, and J. Luitz, *An Augmented Plane Wave Plus Local Orbitals Program for Calculating Crystal Properties*. Technical University of Wien, Vienna, 2001. Edited by K. Schwarz.
- [86] V. I. Anisimov, J. Zaanen, and O. K. Andersen, “Band theory and Mott insulators: Hubbard U instead of Stoner I ,” *Phys. Rev. B*, vol. 44, p. 943, Jul 1991.
- [87] V. I. Anisimov, I. V. Solovyev, M. A. Korotin, M. T. Czyżyk, and G. A. Sawatzky, “Density-functional theory and NiO photoemission spectra,” *Phys. Rev. B*, vol. 48, p. 16929, Dec 1993.
- [88] I. V. Solovyev, P. H. Dederichs, and V. I. Anisimov, “Corrected atomic limit in the local-density approximation and the electronic structure of d impurities in Rb,” *Phys. Rev. B*, vol. 50, p. 16861, Dec 1994.
- [89] M. Cococcioni and S. de Gironcoli, “Linear response approach to the calculation of the effective interaction parameters in the LDA + U method,” *Phys. Rev. B*, vol. 71, p. 035105, Jan 2005.
- [90] H.-H. Wu, M. Buchholz, C. Trabant, C. Chang, A. Komarek, F. Heigl, M. Zimmermann, M. Cwik, F. Nakamura, M. Braden, and C. Schler-Langeheine, “Charge stripe order near the surface of 12-percent doped $\text{La}_{2x}\text{Sr}_x\text{CuO}_4$,” *Nat. Commun.*, vol. 3, p. 1023, 2012.
- [91] Y. Maeno, S. Kittaka, T. Nomura, S. Yonezawa, and K. Ishida, “Evaluation of spin-triplet superconductivity in Sr_2RuO_4 ,” *Journal of the Physical Society of Japan*, vol. 81, no. 1, p. 011009, 2012.

- [92] G. M. Luke, Y. Fudamoto, K. M. Kojima, M. I. Larkin, J. Merrin, B. Nachumi, Y. J. Uemura, Y. Maeno, Z. Q. Mao, Y. Mori, H. Nakamura, and M. Sigrist, “Time-reversal symmetry-breaking superconductivity in Sr_2RuO_4 ,” *Nature*, vol. 394, p. 558, 1998.
- [93] T. M. Riseman, P. G. Kealey, E. M. Forgan, A. P. Mackenzie, L. M. Galvin, A. W. Tyler, S. L. Lee, C. Ager, D. M. Paul, C. M. Aegerter, R. Cubitt, Z. Q. Mao, T. Akima, and Y. Maeno, “Observation of a square flux-line lattice in the unconventional superconductor Sr_2RuO_4 ,” *Nature*, vol. 396, p. 242, 1998.
- [94] K. Ishida, H. Mukuda, Y. Kitaoka, K. Asayama, Z. Q. Mao, Y. Mori, and Y. Maeno, “Spin-triplet superconductivity in Sr_2RuO_4 identified by ^{17}O knight shift,” *Nature*, vol. 396, p. 658, 1998.
- [95] M. Rice, “Superconductivity: An analogue of superfluid ^3He ,” *Nature*, vol. 396, p. 627, 1998.
- [96] K. Deguchi, M. A. Tanatar, Z. Mao, T. Ishiguro, and Y. Maeno, “Superconducting double transition and the upper critical field limit of sr_2ruo_4 in parallel magnetic fields,” *Journal of the Physical Society of Japan*, vol. 71, no. 12, p. 2839, 2002.
- [97] K. Tenya, S. Yasuda, M. Yokoyama, H. Amitsuka, K. Deguchi, and Y. Maeno, “Unusual magnetic response in superconducting mixed state of Sr_2RuO_4 ,” *Journal of the Physical Society of Japan*, vol. 75, no. 2, p. 023702, 2006.
- [98] H. Yaguchi, T. Akima, Z. Mao, Y. Maeno, and T. Ishiguro, “Detailed study of the AC susceptibility of Sr_2RuO_4 in oriented magnetic fields,” *Phys. Rev. B*, vol. 66, p. 214514, Dec 2002.
- [99] Z. Q. Mao, Y. Maeno, S. NishiZaki, T. Akima, and T. Ishiguro, “In-plane anisotropy of upper critical field in Sr_2RuO_4 ,” *Phys. Rev. Lett.*, vol. 84, p. 991, Jan 2000.

- [100] S. Kittaka, T. Nakamura, Y. Aono, S. Yonezawa, K. Ishida, and Y. Maeno, “Angular dependence of the upper critical field of Sr_2RuO_4 ,” *Phys. Rev. B*, vol. 80, p. 174514, Nov 2009.
- [101] J. J. Deisz and T. E. Kidd, “Quantum many-body calculation of mixed-parity pairing in the Sr_2RuO_4 superconductor induced by spin-orbit coupling,” *Phys. Rev. Lett.*, vol. 107, p. 277003, Dec 2011.
- [102] C. M. Puetter and H.-Y. Kee, “Identifying spin-triplet pairing in spin-orbit coupled multi-band superconductors: application to Sr_2RuO_4 ,” *ArXiv e-prints*, 1101.4656, Jan. 2011.
- [103] O. K. Andersen, “Linear methods in band theory,” *Phys. Rev. B*, vol. 12, p. 3060, Oct 1975.
- [104] O. K. Andersen and T. Saha-Dasgupta, “Muffin-tin orbitals of arbitrary order,” *Phys. Rev. B*, vol. 62, p. R16219, Dec 2000.
- [105] D. T. Pierce and F. Meier, “Photoemission of spin-polarized electrons from GaAs,” *Phys. Rev. B*, vol. 13, p. 5484, Jun 1976.
- [106] W. Cleveland, “Robust locally weighted regression and smoothing scatterplots,” *Journal of the American Statistical Association*, vol. 74, p. 829, 1979.
- [107] J. Bardeen, L. N. Cooper, and J. R. Schrieffer, “Theory of superconductivity,” *Phys. Rev.*, vol. 108, p. 1175, Dec 1957.
- [108] J. F. Annett, *Superconductivity, Superfluids, and Condensates*. Oxford University Press, New York, 2004.
- [109] Z.-H. Zhu, G. Levy, B. Ludbrook, C. N. Veenstra, J. A. Rosen, R. Comin, D. Wong, P. Dosanjh, A. Ubaldini, P. Syers, N. P. Butch, J. Paglione, I. S. Elfimov, and A. Damascelli, “Rashba spin-splitting control at the surface of the topological insulator Bi_2Se_3 ,” *Phys. Rev. Lett.*, vol. 107, p. 186405, Oct 2011.

- [110] R. Comin, G. Levy, B. Ludbrook, Z.-H. Zhu, C. N. Veenstra, J. A. Rosen, Y. Singh, P. Gegenwart, D. Stricker, J. N. Hancock, D. van der Marel, I. S. Elfimov, and A. Damascelli, “Na₂IrO₃ as a novel relativistic mott insulator with a 340 meV gap,” *Phys. Rev. Lett.*, vol. 109, p. 266406, Dec 2012.
- [111] Z.-H. Zhu, C. N. Veenstra, G. Levy, A. Ubaldini, P. Syers, N. P. Butch, J. Paglione, M. W. Haverkort, I. S. Elfimov, and A. Damascelli, “Layer-by-layer entangled spin-orbital texture of the topological surface state in Bi₂Se₃,” *ArXiv e-prints*, 1212.4845Z, Dec. 2012.
- [112] S. Souma, Y. Machida, T. Sato, T. Takahashi, H. Matsui, S.-C. Wang, H. Ding, A. Kaminski, J. C. Campuzano, S. Sasaki, and K. Kadowaki, “The origin of multiple superconducting gaps in MgB₂,” *Nature*, vol. 423, no. 6935, p. 65, 2003.
- [113] S. Liu, H. Weng, D. Mou, W. Zhang, Q. Wu, J. He, G. Liu, L. Zhao, H. Liu, X. Jia, Y. Peng, S. He, X. Dong, J. Zhang, Z. Q. Mao, C. Chen, Z. Xu, X. Dai, Z. Fang, and X. J. Zhou, “Fermi surface sheet-dependent band splitting in Sr₂RuO₄ revealed by high-resolution angle-resolved photoemission spectroscopy,” *Phys. Rev. B*, vol. 86, p. 165112, Oct 2012.
- [114] J. J. More, *The Levenberg-Marquardt Algorithm Implementation and Theory*, vol. 630 of *Lecture Notes in Mathematics*. Springer, 1978.
- [115] J. H. Dil, “Spin and angle resolved photoemission on non-magnetic low-dimensional systems,” *Journal of Physics: Condensed Matter*, vol. 21, no. 40, p. 403001, 2009.
- [116] F. Meier, J. H. Dil, and J. Osterwalder, “Measuring spin polarization vectors in angle-resolved photoemission spectroscopy,” *New Journal of Physics*, vol. 11, no. 12, p. 125008, 2009.

Appendix A

Spectral function analysis

This appendix focuses on details of spectral function analysis left out of the main body of text.

A.1 Calculating renormalizations from perturbation theory

Starting from the Hamiltonian, Eq. 2.2,

$$\mathcal{H} = \sum_{\mathbf{k}} \varepsilon_{\mathbf{k}}^b c_{\mathbf{k}}^\dagger c_{\mathbf{k}} + \Omega \sum_{\mathbf{Q}} b_{\mathbf{Q}}^\dagger b_{\mathbf{Q}} + \sum_{\mathbf{K}, \mathbf{Q}} \frac{g_{\mathbf{Q}}}{\sqrt{N}} c_{\mathbf{K}-\mathbf{Q}}^\dagger c_{\mathbf{K}} (b_{\mathbf{Q}}^\dagger + b_{-\mathbf{Q}}), \quad (\text{A.1})$$

which for momentum \mathbf{k} has a zeroth-order ground state $\langle \mathbf{k} |_0$ consisting of a single electron $c_{\mathbf{k}}^\dagger |0\rangle$ with energy $\varepsilon_{\mathbf{k}}^b$, we find that the first-order perturbation energy is 0 owing to a lack of phonons:

$$E_1(\mathbf{k}) = \langle 0 | c_{\mathbf{k}} \sum_{\mathbf{K}, \mathbf{Q}} \frac{g_{\mathbf{Q}}}{\sqrt{N}} c_{\mathbf{K}-\mathbf{Q}}^\dagger c_{\mathbf{K}} (b_{\mathbf{Q}}^\dagger + b_{-\mathbf{Q}}) c_{\mathbf{k}}^\dagger |0\rangle = 0. \quad (\text{A.2})$$

The first-order ground state adds a single phonon:

$$C_{1\Omega} = \sum_{\mathbf{L}} \langle 0 | c_{\mathbf{k}-\mathbf{L}} b_{\mathbf{L}} \frac{\sum_{\mathbf{K}, \mathbf{Q}} \frac{g_{\mathbf{Q}}}{\sqrt{N}} c_{\mathbf{K}-\mathbf{Q}}^\dagger c_{\mathbf{K}} (b_{\mathbf{Q}}^\dagger + b_{-\mathbf{Q}})}{\varepsilon_{\mathbf{k}}^b - \varepsilon_{\mathbf{k}-\mathbf{L}}^b - \Omega} c_{\mathbf{k}}^\dagger |0\rangle \quad (\text{A.3})$$

$$C_{1\Omega} = \sum_{\mathbf{L}} \frac{g_{\mathbf{L}}}{\sqrt{N}(\varepsilon_{\mathbf{k}}^b - \varepsilon_{\mathbf{k}-\mathbf{L}}^b - \Omega)} \quad (\text{A.4})$$

$$|\mathbf{k}\rangle_1 = c_{\mathbf{k}}^\dagger |0\rangle + \sum_{\mathbf{L}} \frac{g_{\mathbf{L}}}{\sqrt{N}(\varepsilon_{\mathbf{k}}^b - \varepsilon_{\mathbf{k}-\mathbf{L}}^b - \Omega)} c_{\mathbf{k}-\mathbf{L}}^\dagger b_{\mathbf{L}}^\dagger |0\rangle, \quad (\text{A.5})$$

A.2. Kramers–Kronig bare-band fitting

which gives the second-order correction to the ground-state energy:

$$E_2(\mathbf{k}) = \langle \mathbf{k} |_0 \sum_{\mathbf{L}, \mathbf{M}} \frac{g_{\mathbf{M}}}{\sqrt{N}} c_{\mathbf{L}-\mathbf{M}}^\dagger c_{\mathbf{L}} (b_{\mathbf{M}}^\dagger + b_{-\mathbf{M}}) | \mathbf{k} \rangle_1 \quad (\text{A.6})$$

$$E_2(\mathbf{k}) = \frac{1}{N} \sum_{\mathbf{L}} \frac{g_{\mathbf{L}-\mathbf{k}} g_{\mathbf{k}-\mathbf{L}}}{\varepsilon_{\mathbf{k}}^b - \varepsilon_{\mathbf{k}-\mathbf{L}}^b - \Omega}. \quad (\text{A.7})$$

This, changing the sum to an integral over all possible phonon momenta, becomes (for example, in 3D):

$$E_2(\mathbf{k}) = \frac{1}{(2\pi)^3} \int_{-\pi}^{\pi} \int_{-\pi}^{\pi} \int_{-\pi}^{\pi} \frac{g_{\mathbf{L}-\mathbf{k}} g_{\mathbf{k}-\mathbf{L}}}{\varepsilon_{\mathbf{k}}^b - \varepsilon_{\mathbf{k}-\mathbf{L}}^b - \Omega} \partial k_x \partial k_y \partial k_z. \quad (\text{A.8})$$

In 1D this integral can be solved exactly and was presented in a simplified form to show the band for both models as predicted by perturbation theory in Eqs. 2.8 and 2.9. However, for higher dimensions it was evaluated numerically.

In multiple dimensions, deterministic algorithms for numerical integration can require large calculation times and often provide no estimate for the error associated with the calculation. For these reasons Monte-Carlo integration was chosen to integrate Eq. A.1. Code to evaluate the integral found in Eq. A.1 and also provide an estimate of the error using the GNU scientific library [51] implementation of the VEGAS Monte Carlo integration algorithm [49, 50]²² is provided in § D.1.

A.2 Kramers–Kronig bare-band fitting

The method outlined here varies slightly from techniques previously described in the literature, which generally reduce the functional form for ε_k^b substantially in order to facilitate an exact solution for $A(k, \omega)$ as they often deal with data very close to the Fermi energy over a small range [23, 33–35].

²²This was a relatively new feature in version 1.15, released only two months before submission of the manuscript [2].

A.2. Kramers–Kronig bare-band fitting

In our analysis we have instead expanded everything about k_m , essentially using a new linear approximation for ε_k^b on each momentum distribution curve (MDC) slice. Although our method has the disadvantage that it does not work as well near the zone boundary where the band velocity goes to zero (other methods that make a second-order approximation can successfully predict and fit the non-Lorentzian shape in this region and may continue to work in this regime), ours has the distinct advantage that it works over a much larger energy range and allows fitting based on an infinite variety of bare-band models (so long as they are differentiable). Most importantly, by its form it also explicitly shows that the self-energies are evaluated along the k_m path in the case where there is global momentum dependence in the self-energy. One might imagine that for the analysis of a particular experiment one may have reasons to choose one method over another, or perhaps even a hybrid of the two. Here we will describe the idea of a Kramers–Kronig bare-band fitting (KKBF) as implemented for our method; its application to other methods is similar.

KKBF is a technique whereby a Lorentzian fit is first performed on every slice of constant energy, $\tilde{\omega}$, according to Eq. 2.13. The values of k_m and Δk_m from the fits can provide the self-energies for every $(\tilde{\omega}, k_m)$ point, within the limitations above, if the bare-band ε_k^b is known. As an analytic complex function the real and imaginary parts of the self-energy are Kramers–Kronig (KK) related:

$$\Sigma'_{\text{KK}}(k, \omega) = \pm \frac{1}{\pi} \mathcal{P} \int_{-\infty}^{\infty} \partial \xi \frac{\Sigma''_{\text{MDC}}(k, \xi)}{\xi - \omega}. \quad (\text{A.9})$$

It is possible to “fit” the bare-band parameters by choosing them such that $\Sigma'_{\text{MDC}} \equiv \tilde{\omega} - \varepsilon_{k_m}^b$ and $\Sigma''_{\text{MDC}} \equiv -v_{k_m}^b \Delta k_m$ are self-consistent with Σ'_{KK} and Σ''_{KK} . Since neither the Kramers–Kronig relationships (Eq. A.9) nor the MDC relationships (Eq. 2.15) are sensitive to a constant offset in both the real self-energy and bare-band, this is unconstrained by the method and both Σ' and ε_k^b are free. In our study we have simply made the calculation of differences between Σ_{KK} and Σ_{MDC} insensitive to a constant offset and set the final offset to zero by hand at the end to allow comparison.

A.2. Kramers–Kronig bare-band fitting

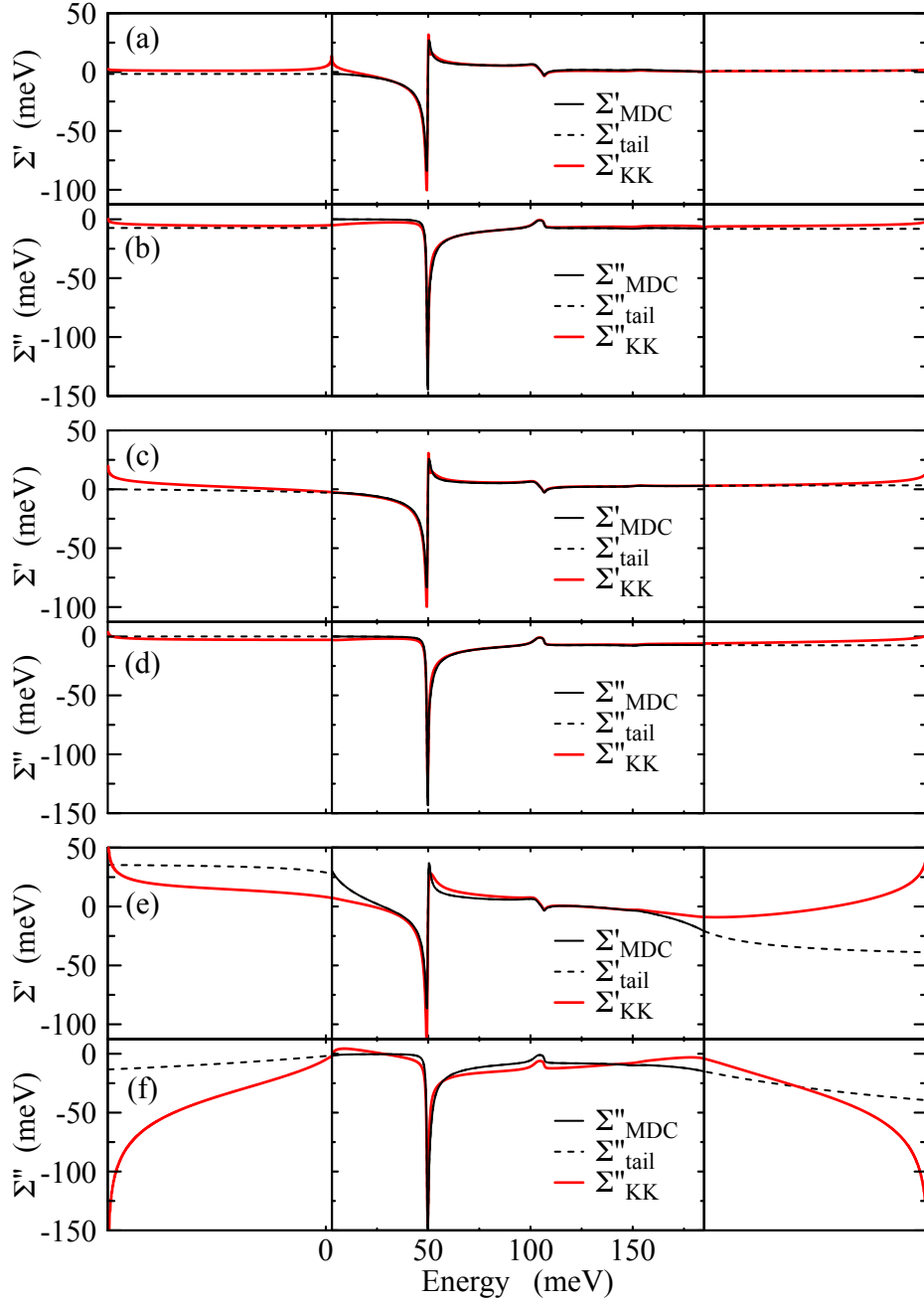


Figure A.1: Self-energies as defined in Fig. 2.10 for the MA⁽¹⁾ Holstein problem with $\Omega = 50$ meV and $\lambda = 0.15$, with extrapolated tails for Σ_{MDC} and the KK transform shown. Panels (a) and (b) have the bias used in fitting the tails set too small, (e) and (f) have the bias set too large, and (c) and (d) have it set just right.

A.2. Kramers–Kronig bare-band fitting

In our implementation of this idea, a simple third-order polynomial was used to fit the bare-band with an initial guess found by fitting MDC peak maxima. We then used the Levenberg–Marquardt algorithm [114] as implemented in the mpfit package for IDL [53] to vary band parameters. We found that the standard sum-of-squares minimization on the differences between Σ_{KK} and Σ_{MDC} did not perform as well as a concave-down function, as it placed too much weight on outlying points far away. In order to evaluate the integrals in Eq. A.9 with a finite region of data, tails were extrapolated before a Fourier-based transform was performed (the tails were then discarded, leaving the analysis of MDC and KK curves only within the data region). These tails were extrapolated by fitting an inverse polynomial to each side of the data, weighing the fit for each side’s tail with an exponentially decaying bias parameter. A bias parameter of zero would weigh the entire curve equally, while a large bias parameter would concentrate only near that data edge.

It is possible for problems such as tails, overweighted outliers, and unconstrained offsets to compound each other. An unconstrained constant offset in Σ'_{MDC} and ε_k^b leads toward a tendency for a small linear offset in both, which, when Kramers–Kronig transformed, will distort Σ''_{KK} most visibly near the edges of the data, where it can interfere with a good fit of the tails. This in turn can lead to inaccuracies at these edges, which, if overweighted, can distort the bare-band fit itself. This runaway condition results in a fit that gets progressively worse through iterations and will never find the correct bare-band. In practice we found that the tail bias parameter as well as the concavity of the function used to process errors must be carefully adjusted by hand in order to prevent this problem, which can be accomplished simply by looking at whether or not the tail approximation continues to appear reasonable through successive iterations.

In Fig. A.1 we show some typical examples of how the tail bias parameter can affect the fitting; each pair of panels represents the final “solution” of the entire band minimization problem using a given tail bias. Plots like these form the guide to be used when adjusting the bias parameters by hand while looking for the best solution. In panels (a) and (b) the tail bias is too small,

A.2. *Kramers–Kronig bare-band fitting*

and so the found tail is the best approximation that fits the whole curve. In panel (b) this causes a discontinuity for the low-energy tail right at the boundary, which in turn causes a cusp in the KK transform visible in (a). Despite this, the overall fit is not too bad, with reasonable general agreement between MDC and KK self-energies, meaning the found bare-band is likely close to the real solution. In panels (c) and (d) the tail bias is good, which results in a realistic fit at all boundaries and a good agreement between MDC and KK self-energies, giving confidence that the found bare-band is accurate. In panels (e) and (f) the tail bias is too strong, which results in a tail fit depending too much on the data right at the edges. This results in a KK transform poor enough to throw off the band fitting entirely resulting in a found bare-band that is likely not close to the true band, shown by generally poor agreement between MDC and KK self-energies.

Appendix B

ARPES data preparation

In order to analyze angle-resolved photoemission spectroscopy (ARPES) data, our group wrote a full object-oriented software suite in the Interactive Data Language (IDL), with many command-driven tools but with a graphical user interface (GUI) for most steps. This effort was undertaken largely by Giorgio Levy, Jonathan Rosen, and me. Each of us developed much of our own code regarding data management and workflow, with many core routines (or pieces of them) shared and often co-authored.

In order to transform the raw detector image into an intensity map over angle and energy, we generally followed a workflow as illustrated in Fig. B.1 to prepare ARPES data²³. It is this data-preparation workflow that will be discussed here. Along with the data of interest, reference gold and slit-array images are also taken. The slit-array image is used to correct distortions in and characterize the angular direction of the image (described in § B.1), while the gold image is used to define the Fermi energy and correct distortions in the energy direction (described in § B.2). Finally, in order to transform the angular data into momentum space, a Fermi surface map is created from a series of images (all themselves slit and gold corrected) taken for varying sample angles. This Fermi surface map is used to characterize any offset angles from sample mounting as well as the sample work function to allow emission angle and kinetic energy to be accurately related to the electron's origin in energy-momentum space, described in § B.3.

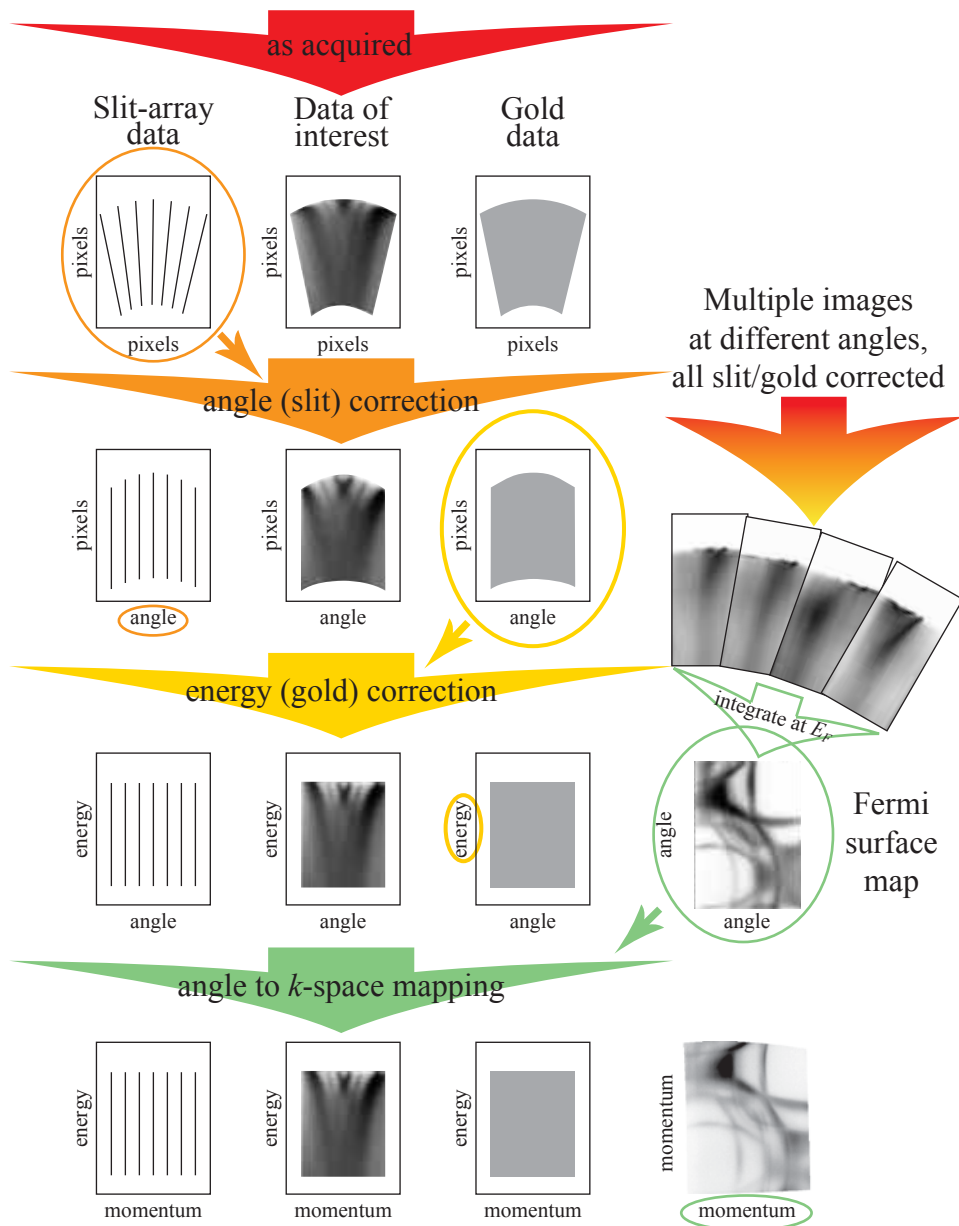


Figure B.1: An illustration of the ARPES data-preparation workflow to bring the raw image into energy–momentum space.

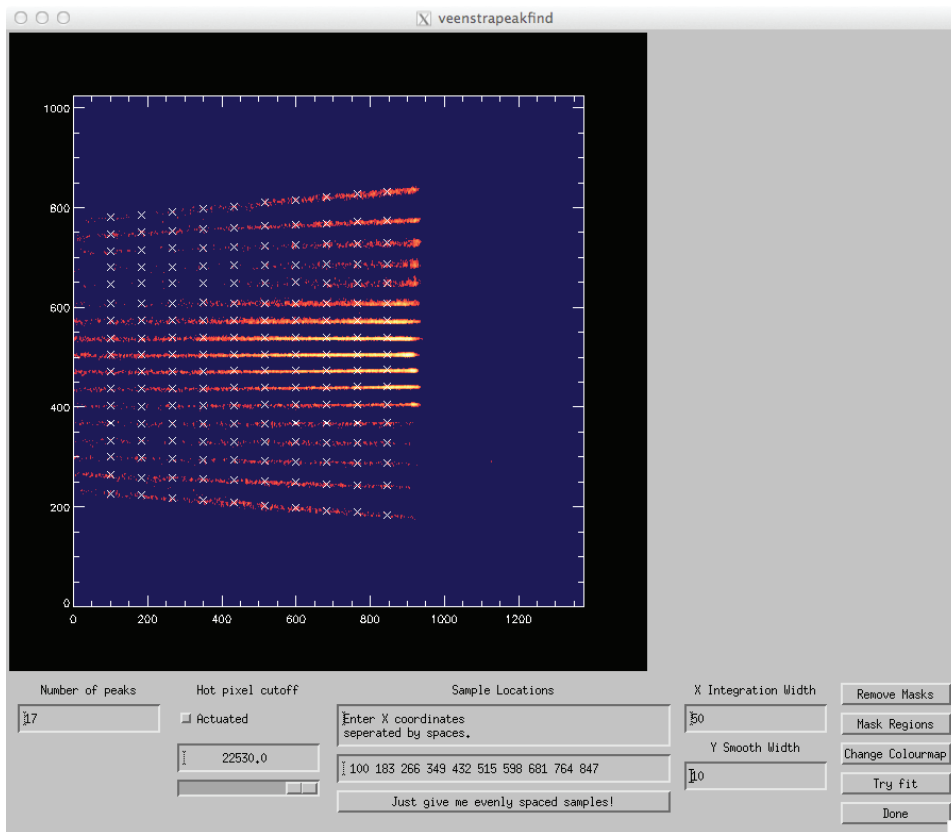


Figure B.2: A screen shot of IDL while defining peak positions in preparation for correcting angular distortions.

B.1 Angle (slit) correction

By inserting a slit-array between the sample and the analyzer (see Fig. 3.1) an image with lines evenly spaced in $\tan(\theta)$ can be taken. The first step to transform the raw detector image into energy–momentum space is to use this slit-array image to characterize any distortions in the angular direction and warp the image to correct for them. Peak locations are first determined at a variety of energy slices along the image²⁴, which are then fit to determine a smooth form for each line. These lines, along with the image data to be corrected, are then forced to have the correct spacing by individually warping each 1D energy slice. The use of a 1D transform prevents mixing in the direction the transform does not define and also allows attention to be paid to making sure the total intensity of each slice remains constant, as no readily available 2D warping routines have this feature²⁵.

B.2 Energy (gold) correction

After correcting the angular distortions and establishing the angular axis, a similar procedure is applied in the energy direction using data taken on polycrystalline gold. By fitting a Fermi edge to each constant angle slice and performing a polynomial fit to the resultant Fermi edge locations, the form of the Fermi edge constant-energy contour can be found. The chemical potential is then set to this location and, since a warping cannot be defined

²³This workflow is most relevant for quasi-2D systems, such as Sr_2RuO_4 , where the location in k_z is not of paramount importance owing to the small k_z dispersion.

²⁴Depending on data quality, defining the peak positions in an efficient manner can be non-trivial. While the peak location may be “obvious” to a human, writing an algorithm that can quickly and reliably locate each peak with minimal human intervention in noisy data is non-trivial. Instead of a standard least-squares fit to a fence of many peaks, which would have many parameters requiring good initialization guesses, data is smoothed over a region and primary peak locations selected based on topographic prominence.

²⁵2D image warping routines are, in general, designed explicitly not to conserve total intensity, instead keeping local intensity the same. This is because if you warp a photograph, you expect the colours not to change – but in our case we *do* want the local intensity to change to reflect the conservation of intensity overall.

by a single constant-energy contour²⁶, each momentum distribution curve (MDC) slice in the image is shifted so that the Fermi edge is straight. The scale of the energy axis is taken from the analyzer pass energy.

B.3 Angle to k -space mapping

After transforming all data into energy–angle space, the final step is to convert emission angle to the crystal momentum of the electron initial state. If the crystal were aligned perfectly, this would be straightforward, as the momentum in vacuum, determined from emission angles and kinetic energy, can be transformed from detector space to crystal space according to the known sample-holder geometry²⁷. However, the small offset angles acquired when mounting the sample must be taken into account.

To solve this problem and determine the offset angles, a large number of scans are taken at a variety of sample geometries, usually by incrementing the cryostat angle across its full range of travel in the direction perpendicular to the analyzer entrance slit. This data set can be integrated in a window near the Fermi energy, and a Fermi surface map generated using assumed offset angles and work function. These assumed parameters can then be varied until the Fermi surface map generated has the correct size and symmetries around $k_x = k_y = 0$. The GUI developed to perform and test these transforms for different conditions is shown in Fig. B.3. In addition to drawing grid lines whose spacing can be chosen based on the known reciprocal lattice size, it is possible to overlay images on top of the transformed data – in this case the results of a band structure Fermi surface calculation.

²⁶The Fermi edge could be swept across the detector, by changing the kinetic energy of the analyzer, to generate constant energy contours at any location – but there is no reason to assume that any warping present would be the same for different analyzer settings.

²⁷Straightforward for the in-plane k_x and k_y directions, where momentum is conserved during photoemission owing to symmetry. The k_z value of the initial state in crystal space is much harder to define, as this direction is not conserved, and calculating it requires knowledge of the inner potential. At a synchrotron the k_z dispersion can be measured by varying photon energy continuously, and the inner potential inferred. However, using spectral lines as a light source does not provide enough data points to do this. Generally the k_z location is either inferred from a comparison with band structure calculations, or a quasi-2D material is selected in which case the exact k_z location is not important.

B.3. Angle to k -space mapping

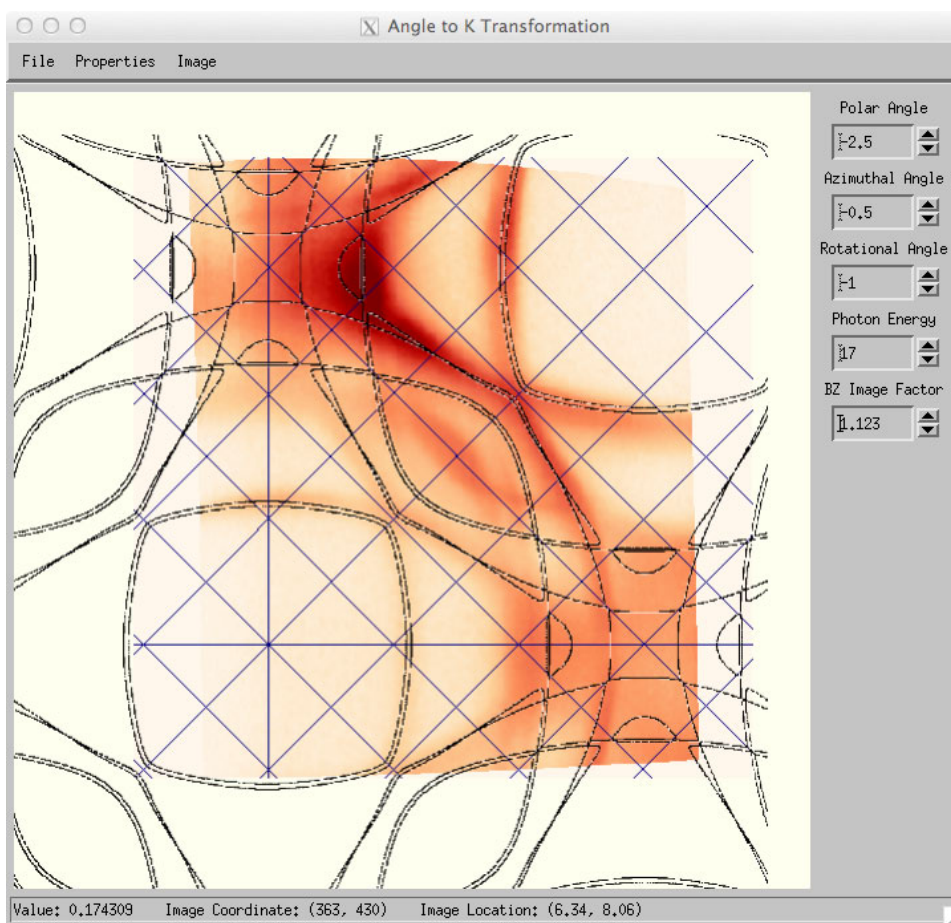


Figure B.3: A screen shot of the GUI from which offset angles are chosen. This drives the angle-to-momentum space transformation. Note the “photon energy” label is a misnomer and should more properly be “photon energy minus work function”.

B.3. Angle to k -space mapping

It is also possible to display composite images folded along high-symmetry directions (not shown). With careful consideration, angles defined in this manner are likely accurate to better than 0.75° . Once the offset angles for a given sample are defined, the angular direction can be transformed into momentum space and is ready for more meaningful analysis.

Appendix C

CPS-ARPES data preparation

Here we will go over some details of circularly polarized photon spin- and angle-resolved photoemission spectroscopy (CPS-ARPES) omitted from Chapter 5 for the sake of readability. A discussion on the experimental setup and how the relative spin intensities in each direction are produced from the raw detector data is found in § C.1. § C.2 explores how the shape of the “wobble” measured in polarization is related to the shape and splitting of the underlying peaks and why direct estimates based on the width of the wobble alone will fail. For further information about spin- and angle-resolved photoemission spectroscopy (SARPES) as an experiment, as well as a discussion of some results relating to Rashba splitting and topological insulators, both the review by Dil [115] as well as that by Meier, Dil, and Osterwalder [116] are highly recommended.

C.1 How polarization is measured

The analyzer/detector at the Complete Photoemission Experiment (COPHEE) endstation is roughly similar to ours at the University of British Columbia (UBC), with the exception that instead of a 2D detector, there is a hole that permits energy- and angle-filtered electrons to pass through and be focused and accelerated into a Mott detector array to discriminate spin²⁸.

²⁸Alternatively, the electrons can also be directed to a series of channeltron detectors, in cases where spin resolution is not required, such as data taken for sample alignment purposes. It should also be noted that the Mott detector array coordinate system is rotated with respect to that of the sample.

C.1. How polarization is measured

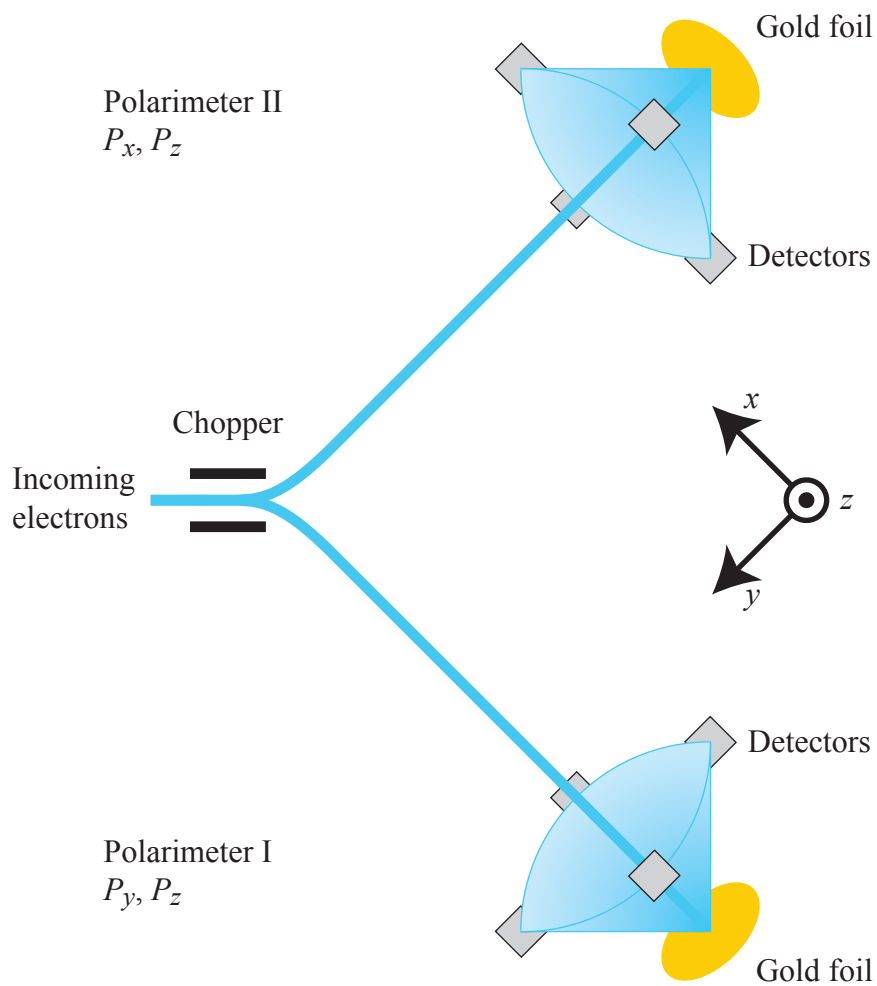


Figure C.1: Illustration of the Mott detector setup at COPHEE. Electrons are discriminated in angle and energy by a hemispherical analyzer before being split between two pairs of Mott polarimeters at right angles, for a total of eight detectors.

C.1. How polarization is measured

The Mott detector array consists of two sets of Mott detector pairs at 90° to each other; electrons are directed toward one or the other by a chopper operating at 2 Hz, as illustrated in Fig. C.1 [115, 116]. This results in a total of eight detectors, with the polarization in one direction (z) theoretically overdetermined, although during the measurements presented here one pair of z detectors was malfunctioning.

The electron polarization P measured in any given direction, is simply the normalized difference in intensity between electrons measured as spin “up” (I_\uparrow) and “down” (I_\downarrow) and is given by

$$P = \frac{I_\uparrow - I_\downarrow}{I_\uparrow + I_\downarrow}, \quad (\text{C.1})$$

i.e., a stream of pure “up” electrons would have $P = 1$ and pure “down” would have $P = -1$ regardless of the overall intensity. Mott scattering is inherently not very efficient at sorting spin²⁹. The scattering asymmetry, A , between the intensities I_L and I_R in any given detector pair is given by

$$A = \frac{I_L - I_R}{I_L + I_R} = PS, \quad (\text{C.2})$$

where P is the electron polarization and where S , the Sherman function, is 0.068 at COPHEE³⁰ – i.e., each Mott pair is 6.8% efficient at sorting (detected) electrons left or right based on their incoming spin polarization.

Additionally, we observe a strong circular dichroism – the overall intensity varies depending on light polarization, with similar magnitude to the already small variations from electron polarization. For this reason a combination of measurements with opposite light polarizations is needed. Here

²⁹Although inefficient, using Mott scattering is the best available method of sorting electron spin – an inhomogeneous magnetic field, i.e. a Stern Gerlach experiment, does not work for charged particles.

³⁰The Sherman “function” is a function of the scattering energy, quality of the foil, and detector geometry; for our purposes it is an empirically determined constant.

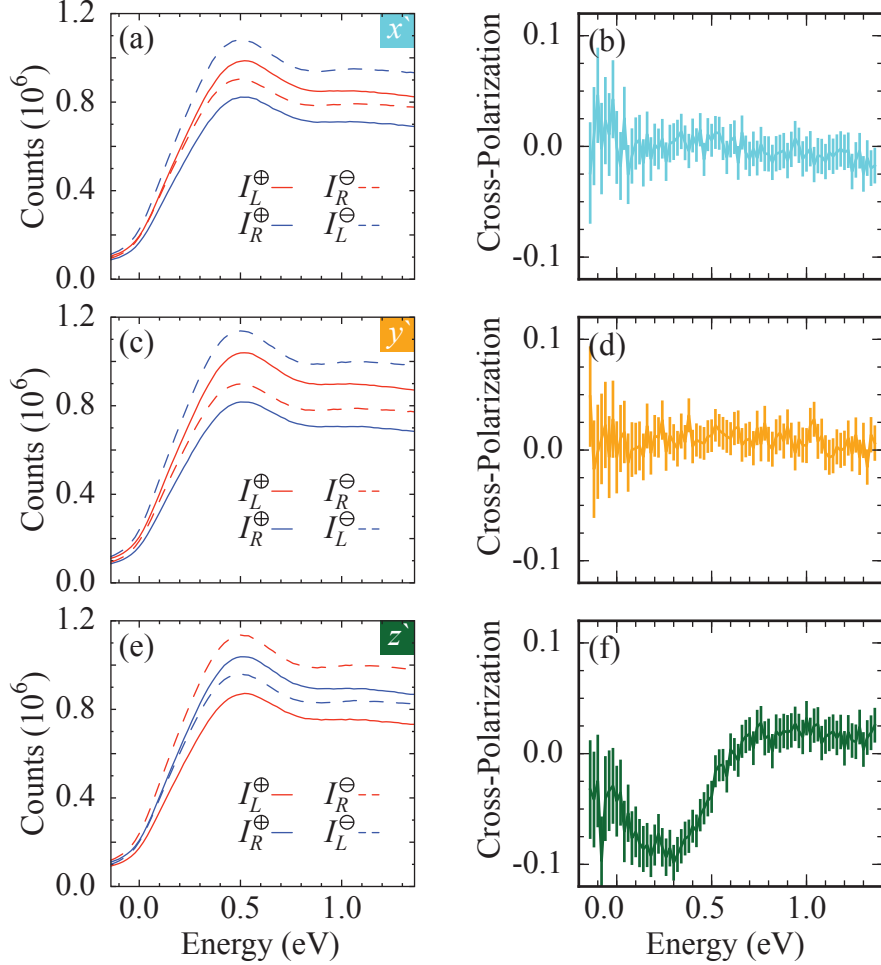


Figure C.2: Raw detector data from CPS-ARPES measurement on Sr_2RuO_4 at the Γ point using 24 eV photon energy. (a,c,e) show the intensity at each left (L) / right (R) half of the (x , y , z) detector pairs for both circular plus (\oplus) and minus (\ominus) light, which is transformed using the cross-asymmetry to find the electron polarization for each pair in detector space (b,d,f). These twelve data sets are used to produce the polarization and spin intensities in Fig. 5.5; note that, in this geometry, changing from detector to sample coordinate systems mixes x and y only. Error bars represent statistical uncertainty plotted at 95% confidence.

C.1. How polarization is measured

we use the geometric cross-asymmetry, \tilde{A}^\otimes , defined as

$$\tilde{A}^\otimes = \frac{\sqrt{I_L^\oplus I_R^\ominus} - \sqrt{I_R^\oplus I_L^\ominus}}{\sqrt{I_L^\oplus I_R^\ominus} + \sqrt{I_R^\oplus I_L^\ominus}}. \quad (\text{C.3})$$

Using the geometric cross-asymmetry \tilde{A}^\otimes has the advantage that it can correct for both circular dichroism as well as detector efficiencies, assuming the intensity at each detector can be written in the following form:

$$\begin{aligned} I_L^\oplus &= D^\oplus E_L \uparrow, & I_R^\oplus &= D^\oplus E_R \downarrow, \\ I_L^\ominus &= D^\ominus E_L \downarrow, & I_R^\ominus &= D^\ominus E_R \uparrow. \end{aligned} \quad (\text{C.4})$$

Here D^\oplus and D^\ominus are multiplicative factors representing the circular dichroism, E_L and E_R represent possibly different linear detector efficiencies, while \uparrow and \downarrow represent the photoemitted states in which we are interested – those that (may) change scattering probability with light polarization. It should be noted that the sometimes-used arithmetic cross-asymmetry, given by $((I_L^\oplus + I_R^\ominus) - (I_R^\oplus + I_L^\ominus)) / ((I_L^\oplus + I_R^\ominus) + (I_R^\oplus + I_L^\ominus))$, does not have this property – it will correct for *either* $D^\oplus \neq D^\ominus$ or $E_L \neq E_R$ but not both at the same time.

The 12 raw energy distribution curves (EDCs) (3 directions \times 2 detectors \times 2 light polarizations) gathered at the Γ point by sweeping the analyzer kinetic energy and used to generate the polarization, total intensity, and spin intensities in Fig. 5.5 are presented in Fig. C.2. Here the strong circular dichroism can be seen as the difference in average value between the data taken with \oplus and \ominus , with \ominus showing greater intensity overall³¹. Possibly differing detector efficiencies can be seen as well, with the L , L , and R detectors returning a consistently higher number of counts in the x , y , and

³¹Note that this scaled difference in intensity between \oplus and \ominus was also seen to exist on polycrystalline copper, so some of the intensity difference could also be from the intensity of light produced by the beamline undulator for different polarizations, but this will be corrected for in the cross-asymmetry in both cases. Possible accidental photon energy shifts also associated with changing light polarization were evaluated on the same polycrystalline copper sample, and this was not found to occur.

z directions, respectively. Finally, it can be readily seen that all curves (by eye) appear to be almost identical rescalings of the same curve – it is for this reason that such high count rates are necessary in order to properly determine the slight difference between them and why, despite having $\sim 10^6$ counts, the error in polarization still ends up being substantial. Finally, once the cross polarizations in each direction are determined, the associated spin intensities can be worked out by rearranging Eq. C.1 with $I_T = I_\uparrow + I_\downarrow$ to get

$$\begin{aligned} I_\uparrow &= I_T(1 + \tilde{P}^\otimes)/2, \\ I_\downarrow &= I_T(1 - \tilde{P}^\otimes)/2. \end{aligned} \tag{C.5}$$

C.2 Polarization from a toy model – what’s in a wiggle?

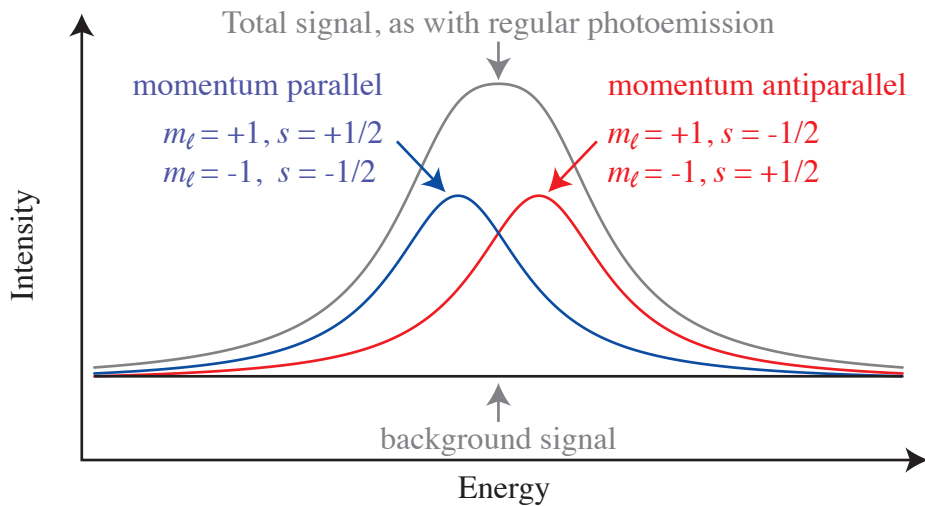
Looking at the cross-polarization in Fig. C.2(f), one might estimate the width of the “wiggle” to be ~ 500 meV. That the estimate of splitting between these two states ends of being a factor of five or so lower than that may then initially come as a surprise. For this reason we will consider here, for a toy model where all parameters are controlled, the appearance of the “wiggle” that would be measured in polarization as a function of peak width, splitting, and background intensity for both Lorentzian and Gaussian lineshapes.

Our model, as the states measured in Chapter 5, consists of a pair of spin-orbit (SO) split states, where the splitting between the two states is (usually) not sufficiently large compared with peak width to resolve each individually with regular photoemission³², as illustrated in Fig. C.3. In Fig. C.3 we see that the width of the “wiggle” is actually comparable to the width of the splitting, but we will soon see that this is only a coincidence for the particular parameters used.

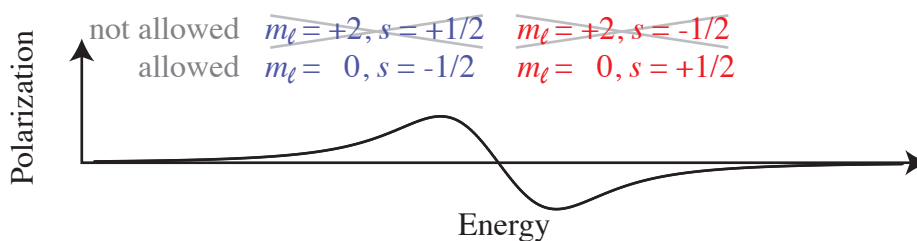
Varying the shape of the measured polarization as a function of peak

³²Why you cannot resolve each peak, whether because of a fundamental broadening or simply instrumental resolution, is not important.

(a) Unpolarized light



(b) Circ+ light ($m_\ell \rightarrow m_\ell + 1$)



(c) Circ- light ($m_\ell \rightarrow m_\ell - 1$)

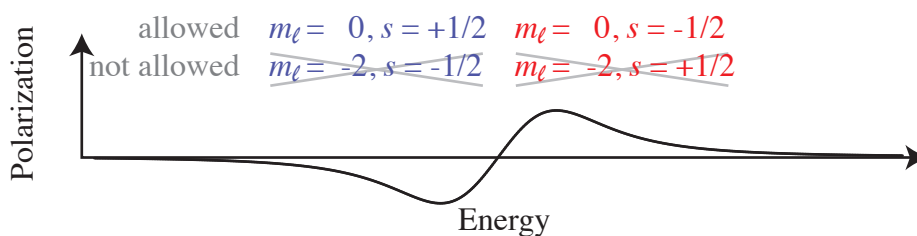


Figure C.3: Spin-polarized photoemission from a simple SO-split system showing (a) total intensity from all sources and polarization measured using circular plus (b) or minus (c) light.

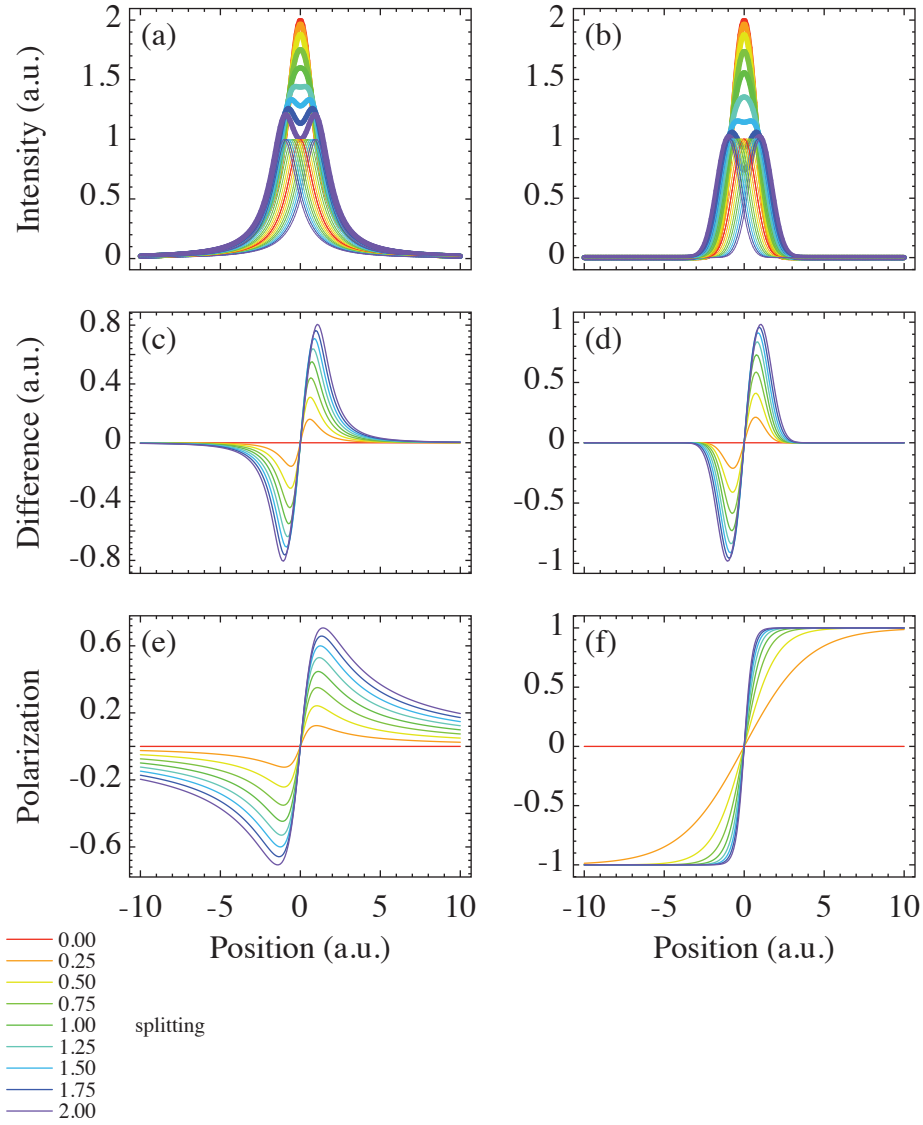


Figure C.4: Peak splitting simulation example, varying the splitting in a background-free environment, for Lorentzian (a,c,e) and Gaussian (b,d,f) lineshapes of constant unit width. (a,b) show the original peaks (thin lines) and sum (thick lines), while (c,d) show the difference of the two peaks. (e,f) show the polarization – i.e., the normalized difference (difference divided by sum).

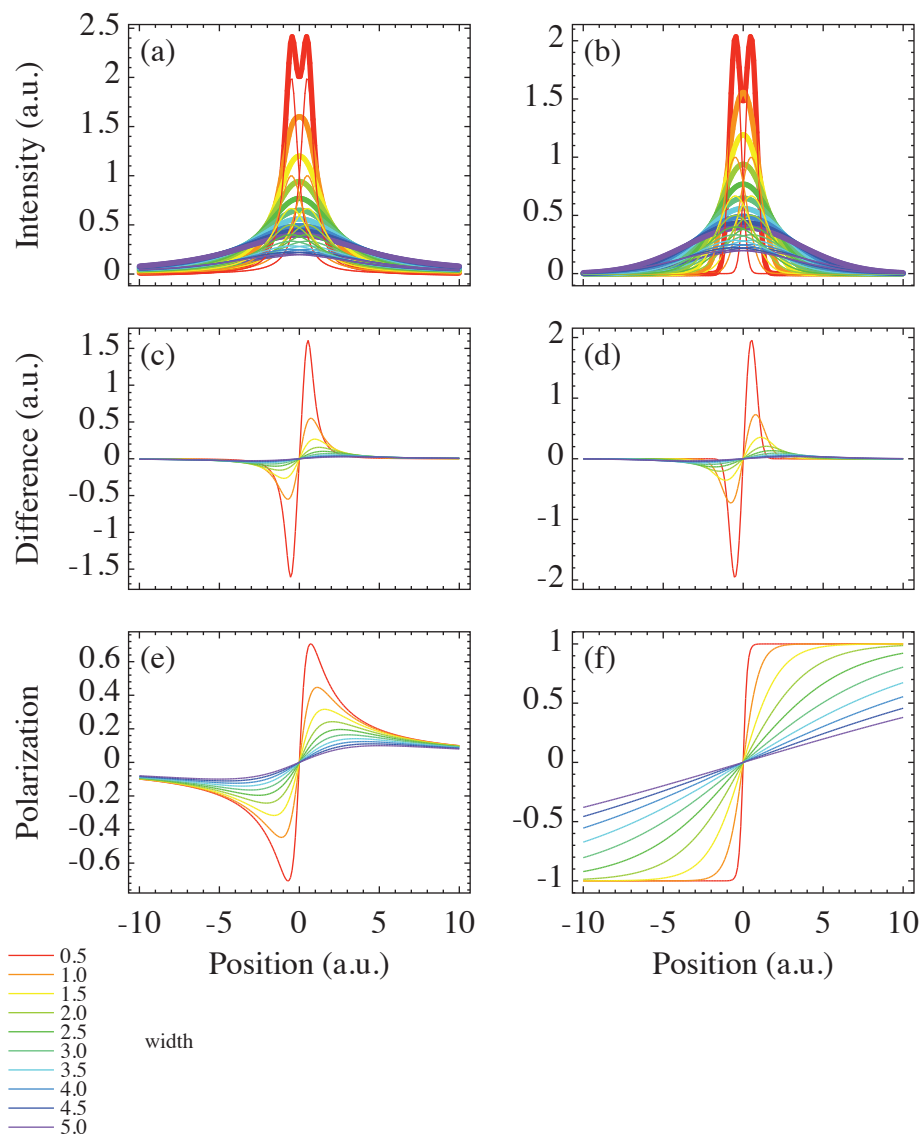


Figure C.5: Peak splitting simulation example, varying the peak width in a background-free environment, for Lorentzian (a,c,e) and Gaussian (b,d,f) lineshapes of constant unit splitting. (a,b) show the original peaks (thin lines) and sum (thick lines), while (c,d) show the difference of the two peaks. (e,f) show the polarization – i.e., the normalized difference (difference divided by sum).

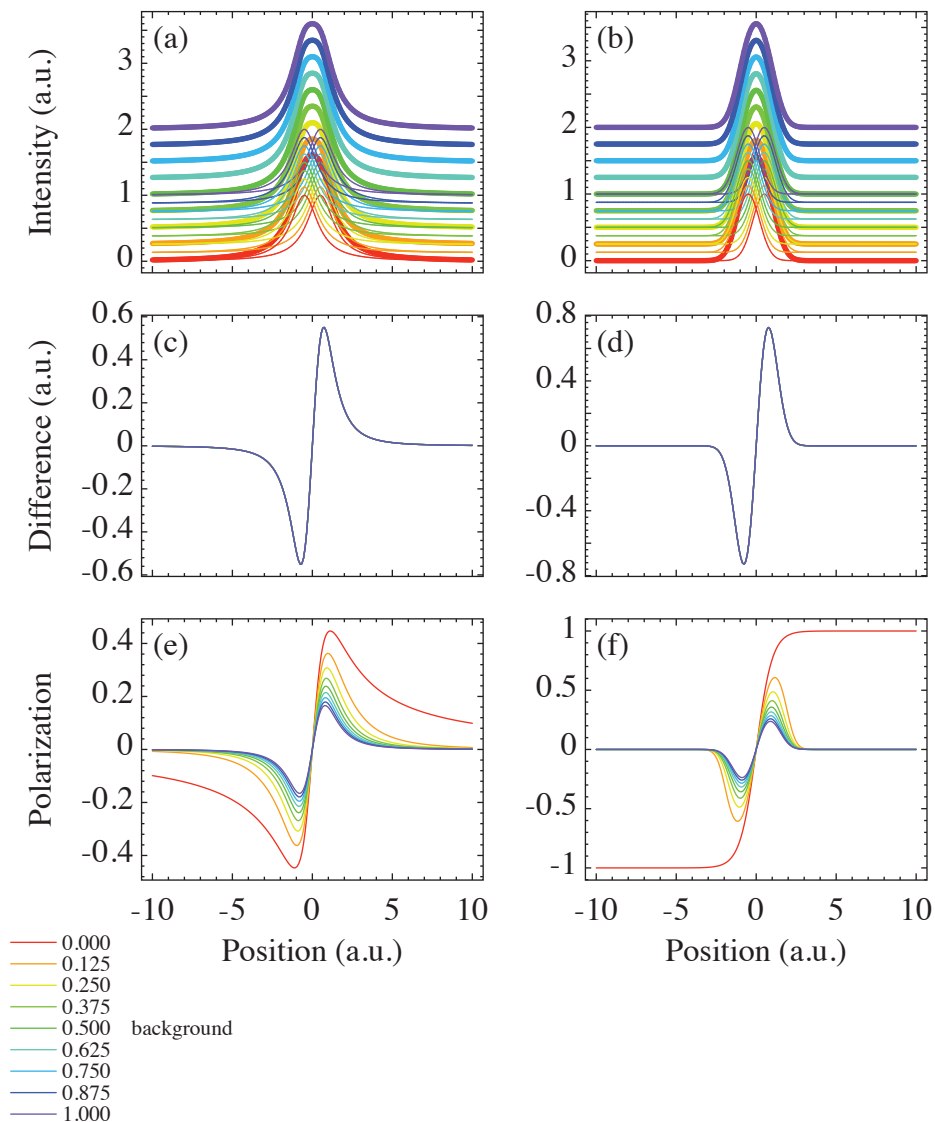


Figure C.6: Peak splitting simulation example, varying background, for Lorentzian (a,c,e) and Gaussian (b,d,f) lineshapes of constant unit width and splitting. (a,b) show the original peaks (thin lines) and sum (thick lines), while (c,d) show the difference of the two peaks. (e,f) show the polarization – i.e., the normalized difference (difference divided by sum).

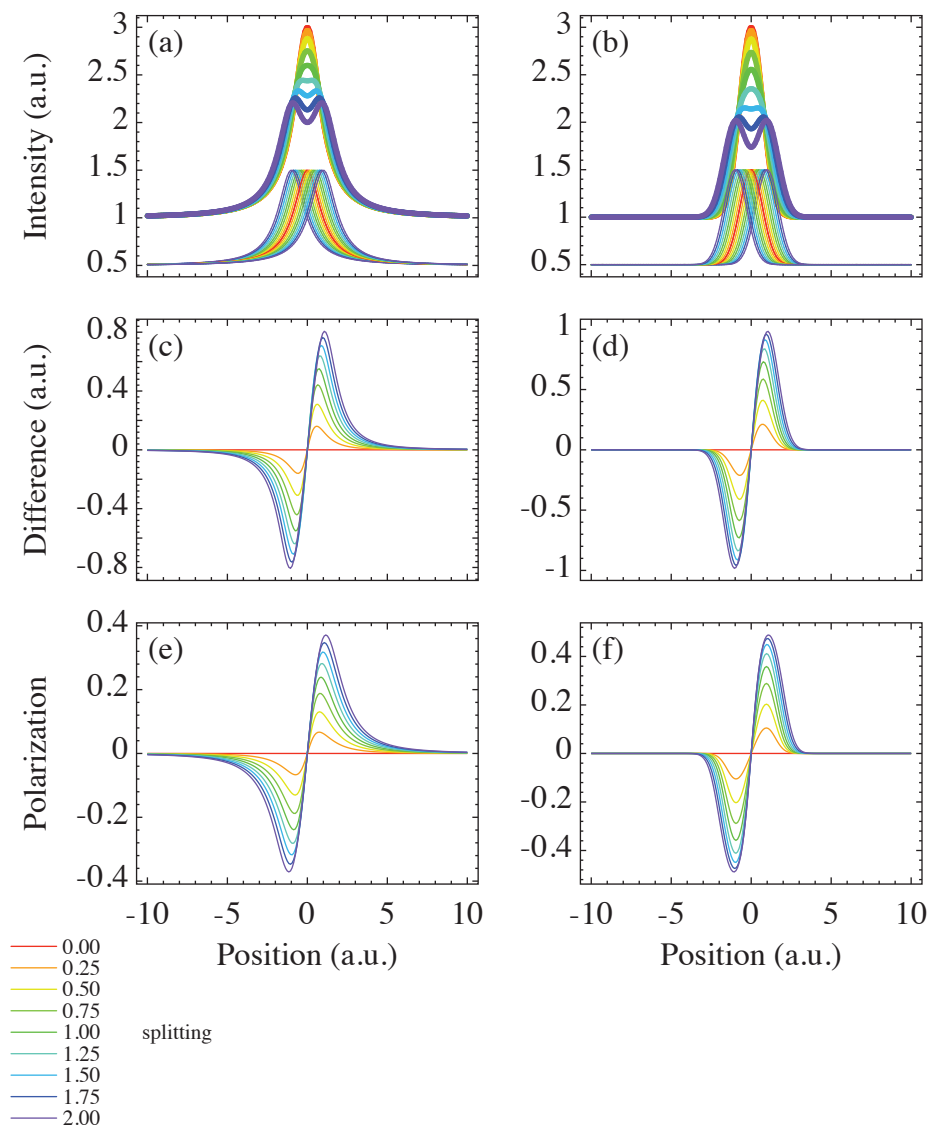


Figure C.7: Peak splitting simulation example, varying splitting with a background of 0.5, for Lorentzian (a,c,e) and Gaussian (b,d,f) lineshapes of constant unit width. (a,b) show the original peaks (thin lines) and sum (thick lines), while (c,d) show the difference of the two peaks. (e,f) show the polarization – i.e., the normalized difference (difference divided by sum).

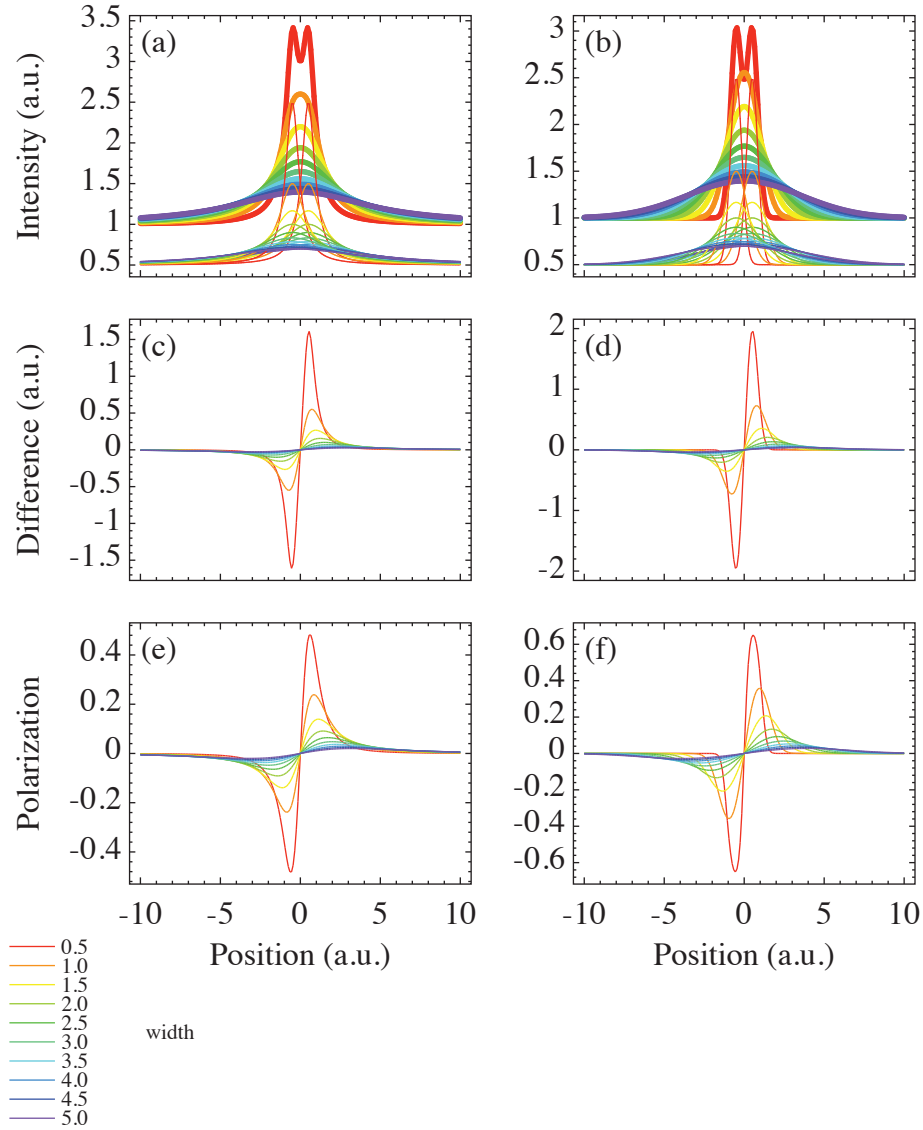


Figure C.8: Peak splitting simulation example, varying width with a background of 0.5, for Lorentzian (a,c,e) and Gaussian (b,d,f) lineshapes of constant unit splitting. (a,b) show the original peaks (thin lines) and sum (thick lines), while (c,d) show the difference of the two peaks. (e,f) show the polarization – i.e., the normalized difference (difference divided by sum).

C.2. Polarization from a toy model – what’s in a wiggle?

shape, background levels, and width is shown in Figs. C.4–C.8. In the first cases, as we vary both splitting (Fig. C.4) and width (Fig. C.5), the polarization behaves vastly differently between peak shapes. In the Lorentzian case, where the intensity drops off slowly as $1/x^2$, the peak shape takes on a wiggle; conversely in the Gaussian case, where the peak shape drops off quickly as e^{-x^2} , the polarization asymptotically approaches 1 and -1 at the extremes. This difference, due to the tails and in limits that would not be possible to measure experimentally owing to zero intensity, changes quickly in the presence of a background intensity, as shown in Fig. C.6, where a background is slowly added. This causes the polarization to quickly become a wiggle in both cases (and, in fact, any case where the intensity in the peaks goes to zero). Figs. C.7 and C.8 show the same progressively changing splitting and width as Fig. C.4 and C.5 only with a background intensity, closer to what might be expected in a real experiment. Fig. C.7 shows that (in the parameter regime shown where the peaks overlap strongly), as splitting is increased, most of the modulation is not in the shape or width of the wiggle but in its amplitude, while Fig. C.8 shows that changing peak shape (rather than splitting) can strongly change both the amplitude as well as the shape and width of the wiggle. In fact, for the case of two Lorentzians with equal area and width with no background, it is possible to solve exactly for the width (defined as the distance from maxima to minima), amplitude (max to min), and the slope in the middle of the wiggle in the polarization:

$$\text{Width} = \sqrt{\text{FWHM}^2 + \text{Splitting}^2} \quad (\text{C.6})$$

$$\text{Amplitude} = 2 \frac{\text{Splitting}}{\sqrt{\text{FWHM}^2 + \text{Splitting}^2}}. \quad (\text{C.7})$$

$$\text{Slope}_0 = 4 \frac{\text{Splitting}}{\text{FWHM}^2 + \text{Splitting}^2}. \quad (\text{C.8})$$

In this case, and where the splitting is small compared with the peak widths, the amplitude of the wiggle and slope in the middle scale linearly with splitting, while the width is a constant. Given these simple forms, a natural temptation would be to combine these easily measured quantities to re-

C.2. Polarization from a toy model – what’s in a wiggle?

trieve the splitting (for example, as $\text{Width} \cdot \text{Amplitude}/2$); however, this approximation fails quickly³³ for non-zero background.

While real-life cases of asymmetric lineshapes and non-constant backgrounds will complicate matters, in general it appears that – as a rough rule of thumb for peaks very broad compared with the splitting – the width of the splitting is related more strongly to the *amplitude* of the “wiggle” than to its width, although in a way that depends strongly on the background, peak form, and peak width. In general, making quantitative estimates of the magnitude peak splitting directly from the shape of the wiggle in polarization is not recommended; it must be combined with the measured total intensity.

³³This approximation fails faster than linearly with increasing background and would (for example) underestimate the splitting by a factor of 2 for peaks with a splitting of 0.1, full width at half maximum (FWHM) 2 and area 1 once the background had reached 0.1.

Appendix D

Software routines

A large quantity of software was written for the analysis of both angle-resolved photoemission spectroscopy (ARPES) (138 000 lines of code³⁴), and circularly polarized photon spin- and angle-resolved photoemission spectroscopy (CPS-ARPES) data (2600 lines of code³⁵) in the Interactive Data Language (IDL). However, none of that code is reproduced here; the level of interdependency between routines and the fact that IDL is a proprietary language does not make that practical.

Here we include one routine – that written in C++ and used to perform the Monte Carlo integration using the GNU scientific library [51] VEGAS [49, 50] algorithm. This is included because it is relatively short, is self-contained, requires only open-source libraries, and would be straightforward to modify in order to calculate the same integral based on a different coupling or bare-band. Evaluating such an integral with a deterministic integration engines, especially in three dimensions, is also liable to take a very long time.

D.1 Monte Carlo integration using the GNU VEGAS algorithm

The code works by evaluating both the bare-band and the band as predicted by perturbation theory for $\lambda = \Delta_\lambda$ at $\mathbf{k} = 0$ and $\mathbf{k} = \Delta_k$, where Δ_k was set

³⁴As counted by CLOC 1.56 and roughly divided as 20k managed by J. A. Rosen, 86k managed by G. Levy, 2k contributed by summer students, and 30k that I managed – although there has been a lot of intermingling, particularly between Levy and me, and Levy’s code base also includes some libraries modified to suit our own purposes. This total also includes some software for low-energy electron diffraction (LEED) and x-ray photoelectron spectroscopy (XPS) analysis.

³⁵Managed solely by me.

to 0.005 and Δ_λ was set to 0.005. Setting either of these values too high could result in an error because the band or renormalization can no longer be approximated as linear, and too low could result in an error because the renormalization becomes difficult to detect.

The main body of the code is **Integrator.cpp**, which relies on a definition for the coupling as provided by either **Holstein.cpp** or **Breathing.cpp**, using shared parameters found in **shared.h**. For speed, these are linked at compile time – an example **makefile** is included, which creates two binaries named Holstein and Breathing, as well as a bash script **do_them_all** to run all the calculations necessary to produce Figs. 2.7 and 2.8.

D.1.1 shared.h

```
//special variable types used by Integrator, Holstein and Breathing
struct model_params { double t; double Omega; double g2;
    size_t dimension; char cut; size_t monte_calls; size_t monte_warmups;
    double delta_k;};
struct integral_params { struct model_params params; double *k; };
```

D.1.2 Holstein.cpp

```
#include <iostream>
#include <fstream>
#include <stdio.h>
#include <string>
#include "shared.h"

using namespace std;

string modelname(){
    return "Holstein Polaron";
}
```

```
double numerator_1d (double l[1], double k[1], model_params params){
    return 1;
}
double numerator_2d (double l[2], double k[2], model_params params){
    return 1;
}
double numerator_3d (double l[3], double k[3], model_params params){
    return 1;
}
```

D.1.3 Breathing.cpp

```
#include <iostream>
#include <fstream>
#include <stdio.h>
#include <string>
#include <gsl/gsl_math.h>
#include "shared.h"

using namespace std;

string modelname(){
    return "Breathing Mode Coupling";
}

double numerator_1d (double l[1], double k[1], model_params params){
    return double(2) * gsl_pow_int(
        sin( (l[0] - k[0])/double(2) )
        , 2);
}
double numerator_2d (double l[2], double k[2], model_params params){
    return double(2) * gsl_pow_int(
        sin( (l[0] - k[0])/double(2) )
```

```
+
sin( (l[1] - k[1])/double(2) )
, 2);
}
double numerator_3d (double l[3], double k[3], model_params params){
    return double(2) * gsl_pow_int(
sin( (l[0] - k[0])/double(2) )
+
sin( (l[1] - k[1])/double(2) )
+
sin( (l[2] - k[2])/double(2) )
, 2);
}
```

D.1.4 Integrator.cpp

```
#include <iostream>
#include <fstream>
#include <stdio.h>
#include <string>
#include <gsl/gsl_math.h>
#include <gsl/gsl_monte.h>
#include <gsl/gsl_monte_vegas.h>
#include "shared.h"

using namespace std;

//function prototypes for what's in either Holstein or Breathing,
//depending on what compiled library is linked
string modelname();
double numerator_1d (double l[1], double k[1], model_params params);
double numerator_2d (double l[2], double k[2], model_params params);
```

D.1. Monte Carlo integration using the GNU VEGAS algorithm

```
double numerator_3d (double l[3], double k[3], model_params params);

//Inline functions for readability and changability but retaining speed

inline double bareband_1d (double k[1], model_params params){
    return -double(2)*(params.t)*( cos(k[0]) );
}
inline double bareband_2d (double k[2], model_params params){
    return -double(2)*(params.t)*( cos(k[0]) +cos(k[1]) );
}
inline double bareband_3d (double k[3], model_params params){
    return -double(2)*(params.t)*( cos(k[0]) + cos(k[1]) + cos(k[2]) );
}

//but use the above when concerned about speed
double bare_band (double k[], model_params params){

    double bareband_energy;

    switch (params.dimension) {
    case 1:
        bareband_energy = bareband_1d(k,params);
        break;
    case 2:
        bareband_energy = bareband_2d(k,params);
        break;
    case 3:
        bareband_energy = bareband_3d(k,params);
        break;
    }
}
```

```
    return bareband_energy;
}
```

```
inline double denominator_1d (double l[1], double k[1], model_params params){
    return (params.Omega) - bareband_1d(k,params) + bareband_1d(l,params);
}
```

```
inline double denominator_2d (double l[2], double k[2], model_params params){
    return (params.Omega) - bareband_2d(k,params) + bareband_2d(l,params);
}
```

```
inline double denominator_3d (double l[3], double k[3], model_params params){
    return (params.Omega) - bareband_3d(k,params) + bareband_3d(l,params);
}
```

```
//The meat of things
```

```
double integrate_this_1d (double l[1], size_t dim, void * p) {
    struct integral_params * i_params = (struct integral_params *) p;

    return numerator_1d( l, i_params->k, i_params->params )
        /
        denominator_1d( l, i_params->k, i_params->params );
}
```

```
double integrate_this_2d (double l[2], size_t dim, void * p) {
    struct integral_params * i_params = (struct integral_params *) p;

    return numerator_2d( l, i_params->k, i_params->params )
        /
        denominator_2d( l, i_params->k, i_params->params );
}
```

```
}
double integrate_this_3d (double l[3], size_t dim, void * p) {
    struct integral_params * i_params = (struct integral_params *) p;

    return numerator_3d( l, i_params->k, i_params->params )
        /
        denominator_3d( l, i_params->k, i_params->params );
}

void display_results(double result, double error){
    cout << "integral value : " << result;
    cout << "; estimated error : " << error << "\n";
}

double perturbation_energy (double k[], model_params params,
                            double *error, gsl_rng *r){

    //my variables
    double prefactor = gsl_pow_int( double(2) * M_PI , -params.dimension);
    //int monte_iterations_counter = 0;

    //gsl monte integral setup
    double res, err;
    double lb_1d[] = {-M_PI};
    double lb_2d[] = {-M_PI,-M_PI};
    double lb_3d[] = {-M_PI,-M_PI,-M_PI};
    double ub_1d[] = {M_PI};
    double ub_2d[] = {M_PI,M_PI};
    double ub_3d[] = {M_PI,M_PI,M_PI};
    double *lb;
    double *ub;
```

```
double chisq;
//cout << "" << gsl_rng_get(r) << "";
gsl_monte_vegas_state *s = gsl_monte_vegas_alloc(params.dimension);

integral_params int_params = {params,k};
gsl_monte_function integral;
integral.params= &int_params;
integral.dim=params.dimension;

// setup the integral differently in different dimensions...

switch (params.dimension) {
case 1:
    integral.f = &integrate_this_1d;
    //cout << "calculating perturbed band for k = "
    //      << k[0] << endl;
    lb=lb_1d;
    ub=ub_1d;
    break;
case 2:
    integral.f = &integrate_this_2d;
    //cout << "calculating perturbed band for k = "
    //      << k[0] << "," << k[1] << endl;
    lb=lb_2d;
    ub=ub_2d;
    break;
case 3:
    integral.f = &integrate_this_3d;
    //cout << "calculating perturbed band for k = "
    //      << k[0] << "," << k[1] << "," << k[2] << endl;
    lb=lb_3d;
    ub=ub_3d;
```

```
    break;
}

//cout << "warming-up integration grid" << endl;
gsl_monte_vegas_integrate (&integral, lb, ub,
    params.dimension, params.monte_warmups, r, s,
    &res, &err);
//cout << "  warm-up complete, ";
//display_results(res,err);
//cout << "converging..." << flush;
do
{
    // if (monte_iterations_counter == 1 )
    // {
    //   cout << "  err est off: chisq/dof= " << chisq << flush;
    // }
    gsl_monte_vegas_integrate (&integral, lb, ub,
        params.dimension, params.monte_calls/5, r, s,
        &res, &err);
    chisq = gsl_monte_vegas_chisq(s);
    //chisq per DOF.  Should be close to 1 or error is underestimated

    // if (monte_iterations_counter > 0)
    // {
    //   cout << " ... " << chisq << flush;
    // }
    // monte_iterations_counter=monte_iterations_counter+1;
}
while (fabs (chisq - 1.0) > 0.4);
//cout << "converged, ";
//display_results (res, err);
```

```
gsl_monte_vegas_free(s);

*error = - prefactor * params.g2 *err;
return - prefactor * params.g2 * res;

}

double perturbed_band (double k[], model_params params,
                      double *error, gsl_rng *r){
    return bare_band(k,params) + perturbation_energy(k,params,error, r);
}

inline double d2_from_points (double f_zero, double f_delta,
                              double delta){
    // assumes it's even about zero (ie - 1st deriv is zero)
    return double(2)*(f_delta - f_zero)/gsl_pow_2(delta);
}

double renorm_at_0 (model_params params,
                   double *error_in_renorm, gsl_rng *r){
```

```
double pert_0, pert_delta, pert_d2;
double bare_0, bare_delta, bare_d2;
double integral_error_0, integral_error_delta;
double renorm, error_in_d2, perror_in_d2;
double k0[params.dimension];
double kd[params.dimension];

//find second deriv bb and setup the k vectors
//depending on what slice you pick
//note that d2 is not strictly correct on the diagonals,
//but that's ok because the sqrt(2) or sqrt(3) cancels out in the ratio.
switch (params.dimension) {
case 1:
    k0[0]=double(0);
    kd[0]=params.delta_k;

    break;
case 2:
    k0[0]=double(0);  k0[1]=double(0);

    kd[0]=params.delta_k;
    switch (params.cut) {
    case 's':
        kd[1]=double(0);
        break;
    case 'd':
        kd[1]=params.delta_k;
        break;
    }
    break;
case 3:
    k0[0]=double(0);  k0[1]=double(0);  k0[2]=double(0);
```

```
kd[0]=params.delta_k;
switch (params.cut) {
case 's':
    kd[1]=double(0); kd[2]=double(0);
    break;
case 'd':
    kd[1]=params.delta_k; kd[2]=params.delta_k;
    break;
}
break;
}

bare_0      = bare_band(k0, params);
bare_delta  = bare_band(kd, params);
bare_d2     = d2_from_points(bare_0, bare_delta, params.delta_k);

pert_0      = perturbation_energy(k0, params, &integral_error_0, r);
pert_delta  = perturbation_energy(kd, params, &integral_error_delta, r);
pert_d2     = d2_from_points(pert_0, pert_delta, params.delta_k);

renorm = bare_d2/(pert_d2+bare_d2);

//simple multiplication was done to get d2 from delta
// - so the error scales
perror_in_d2 = fabs( (integral_error_0+integral_error_delta)
                    /(pert_delta-pert_0) );
error_in_d2 = fabs( pert_d2*perror_in_d2 );
//likewise for renormalization (but now the error is on dispersion)
*error_in_renorm = fabs( renorm * error_in_d2/(pert_d2+bare_d2) );

return renorm;
}
```

```
void cmd_error_message(char *argv[], double monte_calls,
    double delta_k, double lambda,
    double delta_omrat, double omrat_min,
    double omrat_max)
{
    cout << "You must supply at least 3 arguments:" <<
        "dimension (1,2,3) ; cut (to side or diag) ; filename"
        << endl;
    cout << " ie:      $ " << argv[0] <<
        " 2 side output.dat -option value" << endl;
    cout << "optional flags must go at the end and are:" << endl;
    cout << "    -monte_calls (currently " << monte_calls << " )" << endl;
    cout << "    -delta_k      (currently " << delta_k << " )" << endl;
    cout << "    -delta_lambda (currently " << lambda << " )" << endl;
    cout << "    -delta_omrat (currently " << delta_omrat << " )" << endl;
    cout << "    -omrat_min   (currently " << omrat_min << " )" << endl;
    cout << "    -omrat_max   (currently " << omrat_max << " )" << endl;
}

//main actually makes "figure 3" - slope of renormalization at k=0 lambda->0
int main (int argc, char *argv[])
{
    double t=1.0;
    double lambda=0.005; //the value to check renormalization at
    //double omrat=1.0;
    size_t dimension;
```

```
char cut;// = 's'; //"s" for side or "d" for diagonal
string outputfilename;

size_t monte_calls=500000;
size_t monte_warmups=10000;
double delta_k = 0.005;

double delta_omrat=0.02;
double omrat_min=0.02;
double omrat_max=2.001;

//read from the command line
if (argc < 4)
{
    cmd_error_message(argv, monte_calls, delta_k, lambda,
delta_omrat, omrat_min, omrat_max);
    return 1;
}
bool validarg;

validarg = ( sscanf(argv[1], "%zd", &dimension) == 1 );
cut = argv[2][0];
outputfilename = (string)argv[3];

if ( dimension > 3 || ! validarg ||
    (cut != 's' && cut != 'd') )
{
    cmd_error_message(argv, monte_calls, delta_k, lambda,
delta_omrat, omrat_min, omrat_max);
```

```
    return 1;
}

for (int i=4; i < argc; i=i+2)
{
    validarg=0;
    if (strcmp(argv[i], "-monte_calls") == 0 && (i+1) < argc )
{
    validarg = ( sscanf(argv[i+1], "%zd", &monte_calls) == 1 );
}
    if (strcmp(argv[i], "-delta_k") == 0 && (i+1) < argc )
{
    validarg = ( sscanf(argv[i+1], "%lf", &delta_k) == 1 );
}
    if (strcmp(argv[i], "-delta_lambda") == 0 && (i+1) < argc )
{
    validarg = ( sscanf(argv[i], "%lf", &lambda) == 1 );
}
    if (strcmp(argv[i], "-delta_omrat") == 0 && (i+1) < argc )
{
    validarg = ( sscanf(argv[i+1], "%lf", &delta_omrat) == 1 );
}
    if (strcmp(argv[i], "-omrat_min") == 0 && (i+1) < argc )
{
    validarg = ( sscanf(argv[i+1], "%lf", &omrat_min) == 1 );
}
    if (strcmp(argv[i], "-omrat_max") == 0 && (i+1) < argc )
{
    validarg = ( sscanf(argv[i+1], "%lf", &omrat_max) == 1 );
}
    if ( ! validarg )
{
    cmd_error_message(argv, monte_calls, delta_k, lambda,
```

```
    delta_omrat,omrat_min,omrat_max);
cout << "Your flag: " << argv[i] << endl;
return 1;
}

}
//monte_calls=monte_calls * dimension;
//done initializing command line arguments

//make a plot of slope of renormalization

double omrat, renorm, slope, r_error, s_error;

omrat=omrat_min;

cout << modelname() << " pertubation renormalization" << endl;
cout << " Dimension : " << dimension << endl;
cout << " Cut      : " << cut << endl;
cout << " t        : " << t << endl;
cout << " delta_lambda : " << lambda << endl;
cout << " delta_k      : " << delta_k << endl;
cout << " monte_warmups : " << monte_warmups << endl;
cout << " monte_calls  : " << monte_calls << endl;
cout << " delta_omrat  : " << delta_omrat << endl;
cout << " omrat_min    : " << omrat_min << endl;
cout << " omrat_max    : " << omrat_max << endl << endl;
cout << "Outputting to file: " << outputfilename << endl;

//open output file
ofstream output(outputfilename.c_str(),ios::ate);
output.precision(6);
```

```
output << "# " << modelname() << " in Dimension : " << dimension << endl;
output << "# Cut          : " << cut << endl;
output << "# t           : " << t << endl;
output << "# delta_lambda : " << lambda << endl;
output << "# delta_k      : " << delta_k << endl;
output << "# monte_warmups : " << monte_warmups << endl;
output << "# monte_calls  : " << monte_calls << endl;
output << "# omrat \t renorm_slope \t abs_error_in" << endl;

//random number generator for the loop
const gsl_rng_type *T;
gsl_rng *r;
gsl_rng_env_setup ();
T = gsl_rng_default;
r = gsl_rng_alloc (T);

//time junk for the loop
double ratiodone;
time_t started, finished, now, last, difference, future;
struct tm * timeinfo;
time(&started);
timeinfo = localtime(&started);
cout << "Started: " << asctime(timeinfo) << endl;
last=started;

//the loop
do
{
    double Omega=omrat*t*double(2);
    // omrat := Omega/2t

    double g2=lambda*t*Omega*double(dimension*2);
    // lambda := g^2 / 2 t D Omega
```

```
    model_params params={ t, Omega, g2 , dimension , cut ,
monte_calls , monte_warmups ,
delta_k };

    renorm = renorm_at_0(params,&r_error,r);
    slope = (renorm-double(1)) / lambda;
    s_error = r_error / lambda;

    output << omrat << "\t" << slope << "\t" << s_error << endl;

    ratiodone=(omrat-omrat_min+delta_omrat)/(omrat_max-omrat_min);
    cout << (int)( 100*ratiodone ) << "% done; ";
    cout << " omrat= " << omrat << ", slope= " << slope;
    //cout << ", %err= " << (100*s_error/slope);
    cout << ", abserr= " << s_error;
    time(&now);
    cout << ", took: " << difftime(now,last)/60 << "min";
    last=now;
    difference = now - started;
    future = now + difference*(1-ratiodone)/ratiodone;
    timeinfo = localtime(&future);
    cout << ", done " << asctime(timeinfo) << flush;

    omrat+=delta_omrat;
}
while (omrat <= omrat_max);

//free random number generator
gsl_rng_free(r);

//time junk
time(&finished);
```

```
timeinfo = localtime(&finished);
cout << "Finished: " << asctime(timeinfo) << endl;
cout << "Took: " << difftime(finished,started)/3600 << " hours" << endl;
output.close();

return 0;

}
```

D.1.5 makefile

```
#compiler
CPP = g++

#dirs
INC_DIR = /opt/local/include
LIB_DIR = /opt/local/lib
INC_DIR2 = /usr/local/include
LIB_DIR2 = /usr/local/lib

# flags
COMP_FLAGS = -Wall -Wno-unknown-pragmas -c -I$(INC_DIR) -I$(INC_DIR2)
LINK_FLAGS = -lgsl -lgslcblas -lm -L$(LIB_DIR) -L$(LIB_DIR2)

#sources
HOLST_OBJECT = Holstein.o
HOLST_SOURCE = Holstein.cpp

BREAT_OBJECT = Breathing.o
BREAT_SOURCE = Breathing.cpp

SHARED_OBJECT = Integrator.o
```

D.1. Monte Carlo integration using the GNU VEGAS algorithm

```
SHARED_SOURCE = Integrator.cpp

OBJECTS = $(HOLST_OBJECT) $(BREAT_OBJECT) $(SHARED_OBJECT)

Holstein: $(HOLST_OBJECT) $(SHARED_OBJECT)
$(CPP) $(LINK_FLAGS) $(HOLST_OBJECT) $(SHARED_OBJECT) -o Holstein

Breathing: $(BREAT_OBJECT) $(SHARED_OBJECT)
$(CPP) $(LINK_FLAGS) $(BREAT_OBJECT) $(SHARED_OBJECT) -o Breathing

Holstein.o: $(HOLST_SOURCE)
$(CPP) $(COMP_FLAGS) $(HOLST_SOURCE)

Breathing.o: $(BREAT_SOURCE)
$(CPP) $(COMP_FLAGS) $(BREAT_SOURCE)

Integrator.o: $(SHARED_SOURCE)
$(CPP) $(COMP_FLAGS) $(SHARED_SOURCE)

.PHONY clean:
rm -f *~ $(OBJECTS) Holstein Breathing

hctest: Holstein
./Holstein 1 s test.dat -monte_calls 50000

bctest: Breathing
./Breathing 1 s test.dat -monte_calls 50000
```

D.1.6 do.them.all

```
./Holstein 1 s 1Ds_Holstein.dat -monte_calls 5000000
./Holstein 2 s 2Ds_Holstein.dat -monte_calls 50000000
./Holstein 2 d 2Dd_Holstein.dat -monte_calls 50000000
./Holstein 3 s 3Ds_Holstein.dat -monte_calls 500000000
./Holstein 3 d 3Dd_Holstein.dat -monte_calls 500000000

./Breathing 1 s 1Ds_Breathing.dat -monte_calls 5000000
./Breathing 2 s 2Ds_Breathing.dat -monte_calls 50000000
./Breathing 2 d 2Dd_Breathing.dat -monte_calls 50000000
./Breathing 3 s 3Ds_Breathing.dat -monte_calls 500000000
./Breathing 3 d 3Dd_Breathing.dat -monte_calls 500000000
```